Imperial College London
Department of Physics

EVOLUTION AND DYNAMICS OF THE ION ENVIRONMENT AT COMET 67P/CHURYUMOV–GERASIMENKO

Zoë Maria Lewis

Submitted in part fulfilment of the requirements
for the degree of Doctor of Philosophy at
Imperial College London, 2025

I declare that the work presented in this thesis is my own, except where explicitly indicated otherwise. Information derived from the published and unpublished work of others has been acknowledged in the text and references are given in the list of sources.

Zoë Maria Lewis (2025)

Abstract

The cometary plasma environment is formed through the ionisation of the neutral gas coma, which is mostly water. Directly produced H_2O^+ can go on to interact with other neutral gas molecules to produce a rich and variable cometary ionosphere. However, the cometary ionosphere is not gravitationally bound, so the possibility for ion-neutral chemical reactions is counter-balanced by transport into space. This thesis focusses on the balance between these processes, by evaluating the response of the composition and density of the ionosphere to the changing plasma dynamics through a range of heliocentric distances. The work is underpinned by data from the Rosetta mission, which escorted comet 67P/Churyumov-Gerasimenko for two years.

Data from the Rosetta Orbiter Spectrometer for Ion and Neutral Analysis (ROSINA) Double Focussing Mass Spectrometer (DFMS) instrument is exploited using a multi-instrument approach. This allows assessment of the variation in high proton affinity ion species, primarily NH_4^+, which require ion-neutral interactions to be produced and are therefore particularly sensitive to ion transport. It is shown for the first time that the ion-neutral chemistry is more complex inside the diamagnetic cavity, a magnetic field-free region surrounding the nucleus at high activity.

A 1D fluid ionospheric model is built to test the impact of acceleration by an ambipolar electric field on the ionospheric composition, bulk velocity, and total density inside the diamagnetic cavity. The model is used to constrain the electric field strength through comparison with electron density data from the Rosetta Plasma Consortium (RPC) instruments. The study is then expanded to lower cometary activity, by adapting a 3D collisional test-particle model to simulate the reaction of cometary ions to electric and magnetic fields from a hybrid simulation. In doing so, we highlight potential improvements of hybrid simulations and advance our ability to explain the plasma density observed by Rosetta at 67P.

Dedicated to my grandpa, Christopher Lewis, who loved learning.

Acknowledgements

It's a common misconception that a PhD is a solitary thing. There are many people who have helped me and kept me company along the way, and I would like to take a moment to acknowledge them here.

First and foremost, I am deeply grateful to Marina for being such a kind, passionate and dedicated supervisor. She has pushed me out of my comfort zone, and I have gained so much confidence as a result. It has been a privilege to learn from her for the past few years and to have been a part of her cometary adventure. Thanks are also due to the rest of Marina's team at Imperial. To Arnaud, for all the thought-provoking discussions and reliable mathematical steering. And to Pete, for his support with the test particle modelling, of course, but also for advice and patience in the face of my naïve questions. I'd also like to thank my collaborators from the cometary community. In particular, thanks to Kathrin Altwegg and Martin Rubin, who kindly lent me their expertise in interpretation of the ROSINA data, and to Esa Kallio for providing runs of the hybrid simulation for Chapter 5. Sincere thanks also to my examiners, Geraint Jones and Lorenzo Matteini, for the time and care they gave to reading this thesis, and surprisingly enjoyable discussions in the viva.

No big project could be completed without a healthy dose of procrastination, and I have been lucky to do mine alongside some truly excellent people. Harry and Harley started with me on day one and have been sat beside me every day since. I can't imagine sharing this strange journey with anyone else. I'd also like to thank my office-mates - Adrian, Sophia, Ronan, and Joseph - and all the other lovely friends I've made at Imperial. Together they have made my time in London such a happy one, and our numerous crosswords, snack walks, and tea breaks have kept me sane through everything.

Finally, this ridiculous venture has been made possible by the love and support of my friends and family. A special mention goes to Ollie, who has valiantly taken up the task of believing in me when I forget to do it for myself. Last but not least, I would not have got this far without the steadfast encouragement of my mum and dad, who have been supporting me on this journey since I was just a little girl who really liked space.

I'm so grateful to you all.

Contents

List of Figures

List of Tables

CHAPTER 1

INTRODUCTION

Comets are small solar system bodies made of ice and dust. They are left over from the formation of the solar system 4.6 billion years ago and have existed relatively unchanged in the Kuiper Belt and Oort cloud ever since, due to the lack of solar energy reaching them. However, small collisions or gravitational influence from surrounding objects, such as Jupiter, occasionally pull them on a dramatic new trajectory around the Sun. The orbital paths these objects follow can be categorised based on their shape: elliptical, hyperbolic, or parabolic. Hyperbolic and parabolic comets will make only one pass through the inner solar system before being lost into space, while those following elliptical comets will have many perihelia throughout their lifetimes. The orbital periods of comets vary greatly: from Jupiter family comets which return to perihelion more frequently than every 20 years to those which take thousands of years to return to the night sky.

Perhaps the most recognisable feature of comets are the two tails, for example as visible in the remarkable image of Comet C/1995 O1 Hale-Bopp, Figure 1.1. The brighter of the two is the dust tail, formed of dust particles that are released with the ices sublimating from the surface. The dust particles scatter the Sun's light in all directions, producing a white light which trails behind the comet on its path through the solar system. The second tail is formed of ionised molecules, and is therefore influenced by the solar wind and directed anti-sunward

Figure 1.1: Comet C/1995 O1 Hale-Bopp, imaged on 14th March 1997 at European Southern Observatory (ESO), showing clearly the dust and ion tails. Credit: ESO/E. Slawik

(Biermann, 1951). This cometary plasma is made up of ions and electrons from the ionisation of the neutral coma and is a uniquely dynamic environment, changing dramatically with heliocentric distance. In many ways, it can be seen as a space plasma test laboratory with relevance to planets and other small bodies that interact with the solar wind.

Section 1.1 describes how our understanding of comets has evolved alongside scientific and technological progress. This paved the way for the most extensive cometary mission to date, Rosetta, on which the majority of the work in this thesis is founded. The motivations and timeline of the Rosetta mission will be set out in Section 1.2, followed by a presentation of the key instruments from which data will be used in this thesis (Section 1.2.1).

1.1 A brief history of comet exploration

Observations of comets are as old as human history itself, and appear in records dating as far back as ancient China in 613 BC (Ho, 2000). Of particular note is comet 1P/Halley, whose $\sim$ 76 year orbital period makes its apparition in the night sky an intriguing once-in-a-lifetime event. It even makes an appearance in the Bayeux tapestry, which depicts the

1066 Battle of Hastings, and another in the Eadwine Psalter, a 12th century book of Psalms [1]. An explanation for these intriguing (and often frightening) objects eluded astronomers until 1684, when Edmond Halley used the newly discovered laws of gravity to finally understand the periodicity and predict the next apparition of his eponymous comet. Though he didn't live to see it, his prediction was confirmed when the comet returned in 1758, and it became the first comet recognised as having a short orbital period, and whose return was successfully predicted - hence the alternative name, 1P, where the 'P' stands for periodic.

With improved telescopes in the 19th and early 20th centuries, a more detailed picture of cometary structure emerged. For example, during the 1835 apparition of 1P/Halley, the mathematician Friedrich Bessel observed and recorded streaming paths of ejected material (Bessel, 1836). Until the advent of The Space Age and the first cometary flybys, it was not possible to directly image the nucleus itself. However, it was recognised that the presupposition of the comet nucleus as a rocky body with some imbedded ice wouldn't provide enough gas to explain the observations of the coma and tail. Whipple (1950) suggested an alternative model of the nucleus as a mixture of ice and dust (the 'dirty snowball'), which became the accepted theory.

Interest in the cometary plasma environment also gained traction in the mid-20th century, alongside the solar-terrestrial environment and space plasma physics more generally. The anti-sunward direction of the ion tail provided evidence of the solar wind flow (Biermann, 1951) and its associated magnetic field (Alfvén, 1957). Following this, the first models of the comet-solar wind interaction were developed (e.g. Biermann *et al.*, 1967, Mendis and Ip, 1977). The Space Age provided the first opportunities to test these theories, and in 1985 the International Cometary Explorer (ICE) became the first spacecraft to make in situ measurements of a comet, flying through the tail of 21P/Giacobini-Zinner.

The return of 1P/Halley to perihelion in 1986 was unique, since for the first time humankind had the technological capability to get up close (see Figure 1.2). It was met by the so-called 'Halley Armada'—five spacecraft that made flybys in quick succession of each other. The two Vega spacecraft (of the Soviet space programme) made flybys at around 8000 km on

[1] in the Eadwine Psalter, the comet is described rather charmingly as a 'hairy star' that 'seldom reveals itself much during the year' but also as a 'portent' - a harbinger of doom.

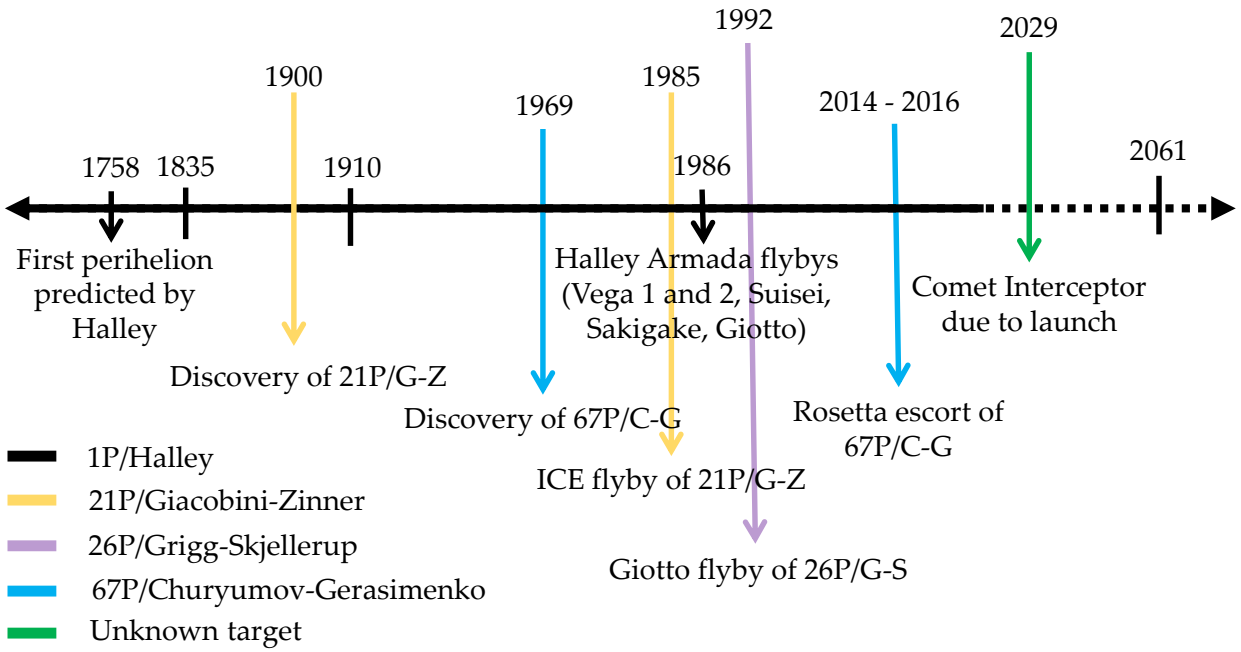

Figure 1.2: Timeline of cometary exploration, showing missions relevant to the cometary plasma environment. Black tick marks show the perihelia of 1P/Halley, approximately every 76 years.

the 6th and 9th of March, the Japanese craft Suisei at 1.5×10^5 km on the 8th and Sakigake at 7×10^6 km on the 11th. The closest approach was made by the European Space Agency's Giotto spacecraft at 600 km on 13th March 1986, becoming the first to take an image of a comet nucleus. The nucleus was revealed to be peanut-shaped, around 15 km long and very dark due to a covering of dust (Keller *et al.*, 1986).

The magnetometer on board Giotto made the first ever measurement of a **diamagnetic cavity**; a region surrounding the comet nucleus where the magnetic field drops to zero or nearly zero. The existence of this plasma region had been proposed before (Biermann *et al.*, 1967), but this was the first time it had been measured directly. The diamagnetic cavity is a key boundary which will be frequently referred to in this thesis, and Section 1.3.2 outlines the current understanding and the open questions which remain.

In the years following Giotto, more Jupiter-family comets were visited with the goal of making higher resolution images of the surface (e.g. of Comet 19P/Borrelly by Deep Space 1, Boice *et al.*, 2000) or performing sample return (from 81P/Wild by Stardust, Elsila *et al.*, 2009).

It became clear, however, that a longer mission would be necessary, and that a short flyby was simply not enough to capture the significant time evolution of these objects. Comets are initially relatively unchanged since the early solar system; to understand them is to understand the way in which material is processed over time by the environment of space. The most ambitious cometary mission to date, Rosetta, was therefore planned to undertake an escort, instead of a short flyby, allowing it to assess this evolution up close. A description of the mission and its key plasma instruments follows in Section 1.2.

Rosetta's final descent in September 2016 is hardly the end of the story. In June 2022, the European Space Agency adopted Comet Interceptor as its first F-class ('fast') mission (Jones *et al.*, 2024, Snodgrass and Jones, 2019). This mission will be novel in that the payload is spread across three spacecraft in order to take measurements from different locations within the comet environment. This will enable a more 3D picture of the cometary environment and solar wind interaction to be produced. The mission is also unique in that it will travel after launch to the gravitationally stable Lagrange point L2 and wait there for a suitable target to be identified. Ideally, this will be a 'dynamically new' comet: entering the inner solar system for the first time. Ground based observations from the new Vera Rubin telescope (Ivezić *et al.*, 2019) will be used to find such a target, as it will be able to see them from further away than has been previously possible.

1.2 The Rosetta mission

In this section, I will describe the timeline and technical scope for the Rosetta mission, which broke new ground in cometary science by escorting and landing on the surface of comet 67P/Churyumov–Gerasimenko during the main mission phase from 2014–2016. As well as inspiring a generation of young space scientists in Europe and beyond (myself included), Rosetta has transformed our view of comets and their evolution. Efforts to understand and explain the vast and rich dataset are still ongoing ten years later, and this thesis describes only a small piece of the fascinating puzzle.

Named after the Rosetta Stone, whose discovery enabled historians to decipher ancient

(a) The nucleus of Comet 67P, photographed by the Rosetta spacecraft. Credit: ESA/Rosetta/NAVCAM

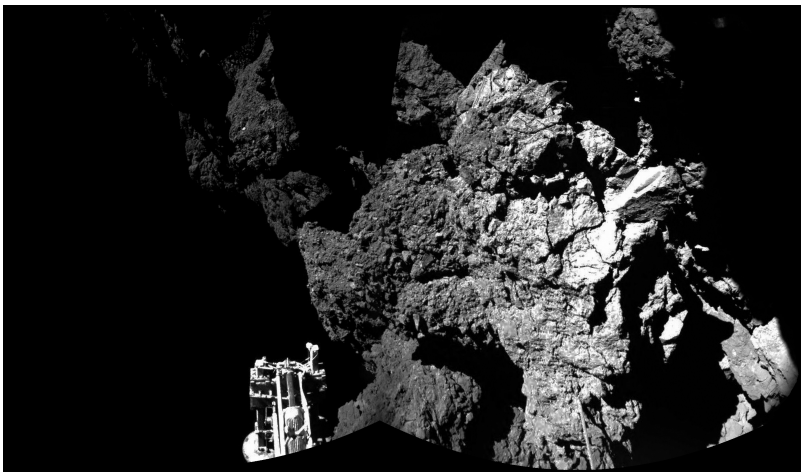

(b) The surface of comet 67P as seen by the camera on the Philae lander. One of the lander's feet can be seen in the foreground of the image. Credit: ESA/Rosetta/Philae/CIVA

Figure 1.3

Egyptian scripts, the Rosetta mission was one of the cornerstone missions of the European Space Agency Horizon 2000 programme (Glassmeier *et al.*, 2007b). Its goal was to enhance our understanding of the formation and composition of the early solar system by performing the first prolonged comet escort and landing. Comet 67P/Churyumov–Gerasimenko (hereafter referred to as 67P) was chosen as the target of this ambitious mission in 2003 after delays to the launch prevented travel to the original object (Comet 46P/Wirtanen, Taylor *et al.*, 2017). 67P is a 6.55-year period Jupiter family comet which was discovered in 1969 by Ukrainian astronomers Klim Ivanovich Churyumov and Svetlana Ivanovna Gerasimenko (Churyumov and Gerasimenko, 1972) and probably formed in the Kuiper belt. The spacecraft was launched by the Ariane 5 rocket from the Guiana Space Center in French Guiana on 2nd March 2004, making flybys of asteroids Steins (Accomazzo *et al.*, 2010) and Lutetia (Schulz *et al.*, 2012) before catching a first glimpse of 67P in March 2014. The on-board cameras captured thousands of images revealing a double lobed 'rubber duck' structure of the comet nucleus (see Figure 1.3a), thought to be from the fusing together of two different objects (Massironi *et al.*, 2015). On 12th November 2014 the Philae lander module was deployed, becoming the first human-made object to land on the surface of a comet and capturing images (e.g. Figure 1.3b) that became headline news globally.

Following the Philae landing, the Rosetta orbiter continued on a two-year escort of 67P,

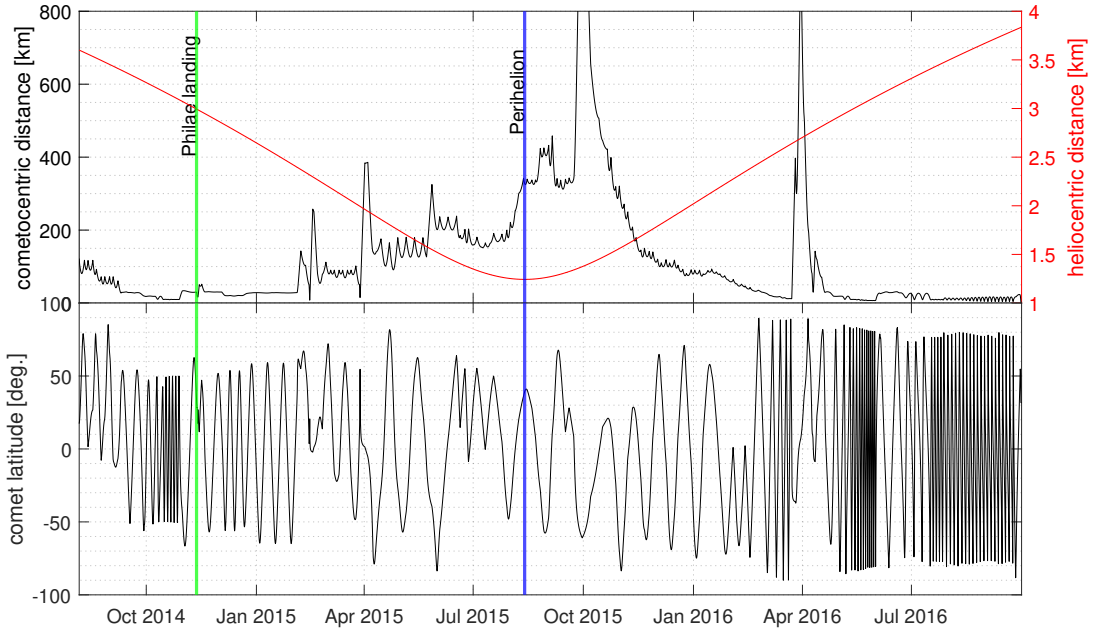

Figure 1.4: Overview of the Rosetta mission, showing spacecraft-comet distance (upper panel, black), comet-Sun distance (upper panel, red) and comet latitude of the sub-spacecraft point (lower panel, black). Key dates are shown by vertical lines: the Philae landing (green) and perihelion (blue).

from its rendezvous point at 3.6 au to perihelion at 1.24 au and back out to 3.8 au, where the mission ended. During the escort phase, the many spacecraft instruments captured an extensive dataset, covering a wide range of cometocentric as well as heliocentric distances (see Figure 1.4). In the following section (Section 1.2.1) I will describe the instruments from which data have been used in this thesis.

1.2.1 Instruments

The Rosetta orbiter carried a payload of eleven sets of scientific instruments, mounted on the spacecraft to 'look' towards the comet throughout the escort phase. The data I have used in this thesis to look at the plasma environment fall under two of these instrument suites: the Rosetta Orbiter Spectrometer for Ion and Neutral Analysis (ROSINA) and the Rosetta Plasma Consortium (RPC). The datasets are summarised in Table 1.1. Unless otherwise specified, data has been acquired via the Planetary Science Archive (Besse *et al.*, 2018).

Table 1.1: The datasets used in this thesis and the instruments that provided them.

Instrument	Measurement	Variable
ROSINA-DFMS	neutral composition	f_n
	ion composition	counts
ROSINA-COPS	neutral density	n_n
RPC-MAG	magnetic field	$\vec{B}$
RPC-LAP	electron number density	n_e
	electron temperature	T_e
	ion bulk velocity	u_i
	spacecraft potential	V_{SC}
RPC-MIP	electron number density	n_e
	electron temperature	T_e

ROSINA

ROSINA (Balsiger *et al.*, 2007) comprised the Double Focussing Mass Spectrometer (DFMS) and the COmet Pressure Sensor (COPS). A third instrument, the Reflectron Time-Of-Flight (RTOF) mass spectrometer experienced some technical failures during the mission (Gasc *et al.*, 2017b), and is therefore not used in this thesis, but some studies have been published with the limited data available (e.g. Hoang *et al.*, 2019).

ROSINA–DFMS was a mass spectrometer, capable of measuring the mass per charge ratio of both ion and neutral species, in high and low resolution modes. In neutral mode, the gas was ionised with an electron source before it could be analysed, and this feature was switched off during ion mode. A strong potential of $+200$ eV was also applied in neutral mode, to repel the cometary ions and ensure only the neutrals were measured. The instrument was therefore not able to measure both ions and neutrals simultaneously. The instrument's range was 12–150 atomic mass units per charge (m/z), though the actual mass range scanned at a given time changed to adjust to different conditions throughout the mission (i.e. scanning the higher masses only when close enough to perihelion when significant chemistry occurs).

The 'double focussing' name of the mass spectrometer refers to the addition of an electrostatic analyser to the traditional magnetic sector. This allows it to achieve a higher resolution by focussing based on kinetic energy as well as mass per charge ratio—minimising the spread in the peaks (Schlaeppi, 2011). Ions (or those created from the ionisation of neutrals in the

instrument's neutral mode) are accelerated by a potential V_{accel}, proportional to the mass per charge ratio, in order to make it through the electrostatic analyser within a 1 % energy range. They then pass through the magnetic sector to be filtered by mass per charge.

The two resolutions offered by DFMS (high resolution (HR) where $\frac{m}{\Delta m} > 3000$ and low resolution (LR) where $\frac{m}{\Delta m} \approx 500$) were also advantageous at different times. On the one hand, HR mode was able to distinguish between different species with the same integer mass per charge, and was therefore more useful at high outgassing when the counts were higher. On the other hand, the LR mode was more sensitive so able to detect a lower signal, albeit without mass separation at a given mass per charge.

DFMS led to many new discoveries, and the main results from the ion mode are discussed in Section 1.3.1. In neutral mode, a wide range of volatile molecules were detected (Le Roy *et al.*, 2015), including the basic amino acid glycine (Altwegg *et al.*, 2016) and molecular oxygen (Bieler *et al.*, 2015).

ROSINA–COPS comprised two pressure gauges, the 'nude gauge' and the 'ram gauge'. The nude gauge measured the total neutral particle density of the gas, while the ram gauge measures cometary gas flux via the ram pressure. They operate by ionising the incoming neutral gas with high energy electrons and then measuring the resulting ion current. Both gauges are mounted on the end of 25cm booms to avoid measuring reflection from the nearby hardware. The total neutral density, derived from ROSINA–COPS (n_{COPS}), needs to be corrected for the ion composition, as the efficiency of the detection process depends on the specific ions being measured. With correction factors β_n (given in Table 1.2) for each neutral species n of volume mixing ratio f_n, the total neutral density can be calculated as (Gasc *et al.*, 2017a):

$$n_n^{\text{tot}} = n_n^{\text{COPS}} \times \left(\sum_n \frac{f_n}{\beta_n} \right)^{-1}. \tag{1.1}$$

The neutral density allowed the comet outgassing to be assessed across the whole escort phase (see Section 2.1, Hässig *et al.*, 2015, Hansen *et al.*, 2016, Läuter *et al.*, 2019) as well as variations from the asymmetric nucleus shape.

Table 1.2: Correction factors for the neutral species measured by ROSINA-COPS, as applied in Equation 1.1. Credit: Gasc *et al.*, 2017b.

Neutral species	H_2O	CO	CO_2	O_2
β_n	0.893	0.952	0.704	0.990

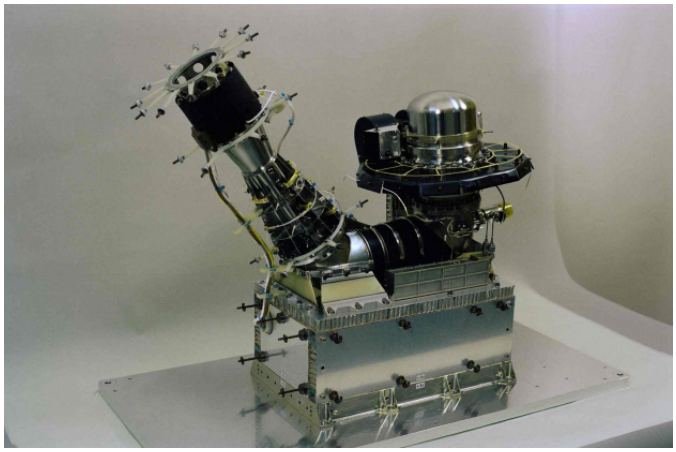

(a) The ROSINA-DFMS flight model. Credit: ESA/ Rosetta/ROSINA-UBern/BIRA/LATMOS/LMM/ IRAP/MPS/SwRI/TUB/UMich.

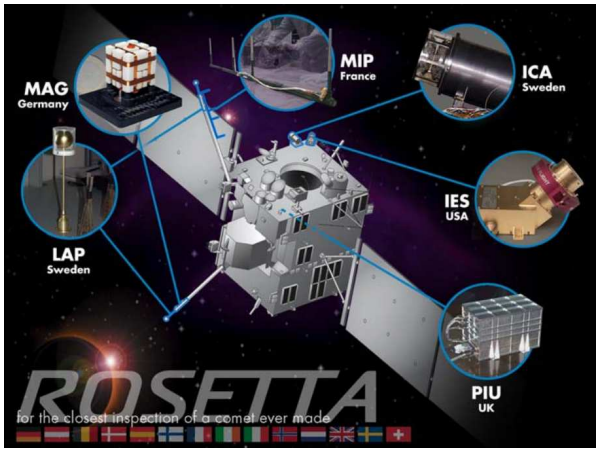

(b) The instruments of the Rosetta Plasma Consortium. Credit: Carr *et al.*, 2007.

Figure 1.5

Rosetta Plasma Consortium

The Rosetta Plasma Consortium (RPC) (Carr *et al.*, 2007) was a group of sensors designed to make in-situ measurements of key plasma properties in the cometary coma. This includes five sensors, linked by the Plasma Interface Unit (PIU, Carr *et al.*, 2007): the MAGnetometer (MAG, Glassmeier *et al.*, 2007a), LAngmuir Probe (LAP, Eriksson *et al.*, 2007), Mutual Impedance Probe (MIP, Trotignon *et al.*, 2007), Ion and Electron Sensor (IES, Burch *et al.*, 2007) and the Ion Composition Analyser (ICA, Nilsson *et al.*, 2007).

RPC–MAG (Glassmeier *et al.*, 2007a) was a fluxgate magnetometer, comprised of two sensors, inbound (IB) and outbound (OB) mounted along a 1.5 m boom. The IB sensor was 15 cm closer to the spacecraft than the OB sensor, therefore more affected by spacecraft noise. For this reason, we generally use data from the OB sensor only. The IB sensor is more commonly used to identify magnetic signals from the spacecraft itself, in order to clean the OB data. Both sensors had two modes, normal (1 Hz) and burst (20 Hz) mode to allow for different sampling rates at different locations. It measured the 3 components of the magnetic

field, with an accuracy of ± 3 nT per component and a range of ± 16384 nT. An important function of the magnetometer is to identify when Rosetta was inside the diamagnetic cavity, a region of negligible magnetic field surrounding the nucleus at high activity (see Section 1.3.2). The magnetic field is so consistently low in the diamagnetic cavity, and has fewer fluctuations, that MAG is calibrated by setting the mean field within the diamagnetic cavity to 0 nT (Goetz *et al.*, 2016b), removing any small offset.

RPC–LAP (Eriksson *et al.*, 2007), a pair of spherical Langmuir probes, measured the plasma number density, electron temperature and ion bulk velocity. It did this by making voltage 'sweeps', altering the bias potential (± 30 V) to find the voltage-current response of the plasma, and the resonant plasma frequency. LAP also measured the spacecraft potential by identifying the point at which the probe becomes positive with respect to the surrounding plasma, which is identifiable in the voltage-current characteristic from the probe, as the photoemission current decreases exponentially to zero once the photoelectrons begin to be attracted back to its surface. LAP only measured a fraction of the spacecraft potential, as it itself is located within the electron cloud around the spacecraft (Odelstad *et al.*, 2017).

RPC–MIP (Trotignon *et al.*, 2007) also measured key plasma properties such as the electron number density via the plasma frequency, and the electron temperature, by measuring the impedance between transmitting and receiving dipoles. MIP was blind to plasma with a Debye length that is greater than half the distance between the emitter and the receiver, so it operates in either Short or Long Debye Length mode (SDL or LDL), by using different emitters and receivers to adjust the distance between them (0.4 m–4 m). The range of electron number densities that could be measured also depended on the frequency of the alternating current applied. The limitations in its ability to measure a wide range of electron number densities is mitigated by cross-calibrating it with the RPC–LAP dataset (Johansson *et al.*, 2021). RPC–MIP also enabled the observation of a persistent population of cold electrons (Gilet *et al.*, 2020, Wattieaux *et al.*, 2020) as well as warm, newly-ionised photoelectrons (see Section 2.3.3).

RPC–IES (Burch *et al.*, 2007) consisted of two electrostatic analysers, one for ions and one for electrons. They used electric fields to guide particles of specific energies into the instrument, allowing energy spectra of the electrons and ions to be determined. The particle

fluxes can be used to determine the electron-impact ionisation frequency (Galand *et al.*, 2016), and Stephenson *et al.* (2023) used them to assess it over the whole escort phase (see Section 2.2.1). The suprathermal (high-energy) electron population (see Section 2.3.3) was also characterised by IES (e.g. Madanian *et al.*, 2016b).

RPC-ICA (Nilsson *et al.*, 2007) also used an electrostatic analyser to determine the 3D ion distribution functions as well as being able to separate between major ions from the solar wind (e.g. H^+, He^+, He^{++}) and cometary ionosphere. This allowed the deflection of the solar wind due to mass loading by the cometary ions to be observed (Behar *et al.*, 2016, see Section 2.3.1), as well as the bulk ion flow directions in and around the diamagnetic cavity (Bergman *et al.*, 2021a, see Section 1.3.3).

1.3 Introduction to the ion environment of 67P

The neutral gas, released by sublimation of ices from a comet's nucleus, is partially ionised (see Section 2.2.1), forming the **cometary ionosphere**. Unlike at planets, the cometary ionosphere is not gravitationally bound but is instead continuously produced and lost to space. The focus of this thesis is on these cometary ions and how they interact with their environment, which is a combination of other charged particles (the solar wind and cometary electrons), the neutral gas, and solar photons (see Figure 1.6).

The rest of this chapter is dedicated to describing the key topics and open questions that drive the aims of the thesis. I start with the observations and drivers of the ionospheric composition in Section 1.3.1. Section 1.3.2 then covers the diamagnetic cavity; a magnetic-field-free region which forms around the nucleus near perihelion and is an important boundary for the ion dynamics. Lastly, Section 1.3.3 describes how the ion dynamics at 67P evolved over the escort phase of Rosetta, highlighting the gaps in understanding that are addressed in subsequent chapters.

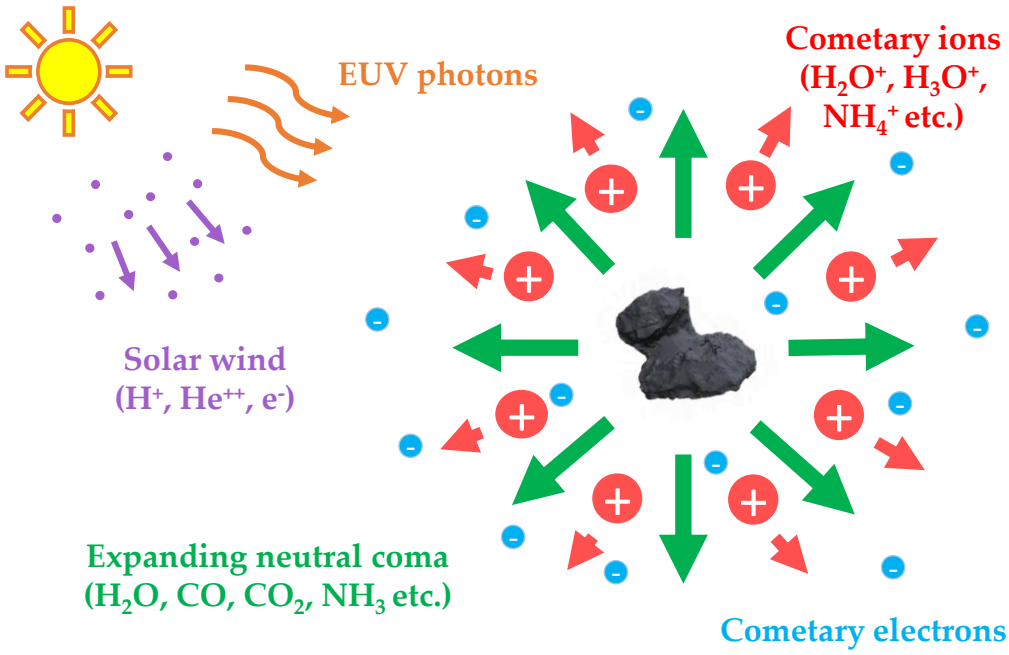

Figure 1.6: Formation of the cometary ionosphere, including the key plasma populations and neutral gases.

1.3.1 Ion composition

The neutral gas coma is mostly made up of water (see Section 2.1). In a cometary coma dense enough, H_2O^+ is quickly lost through the transfer of a proton to H_2O, forming H_3O^+:

$$H_2O + H_2O^+ \rightarrow H_3O^+ + OH. \tag{1.2}$$

This reaction happens so readily that H_3O^+ can often become the dominant ion species in the cometary coma (e.g. Murad and Bochsler, 1987, Heritier *et al.*, 2017a). H_3O^+ can then be lost to reactions with high proton affinity neutrals (Altwegg *et al.*, 1993, Vigren and Galand, 2013, Heritier *et al.*, 2017a). These are neutrals for which it is energetically favourable to 'steal' a proton from H_3O^+ , and this process can happen repeatedly for neutrals with increasing proton affinity until the terminal ion, with the highest proton affinity, is reached (NH_4^+, formed through the protonation of NH_3, Vigren and Galand, 2013):

$$NH_3 + H_3O^+ \rightarrow NH_4^+ + H_2O. \tag{1.3}$$

NH_4^+ can also be produced through interaction between NH_3 and other protonated versions of neutrals with proton affinity higher than water but lower than NH_3. Therefore, although H_3O^+ is usually the dominant ion species, when the coma is dense enough for ion-neutral chemistry to happen more readily, NH_4^+ can overtake it. Only a small mixing ratio of NH_3 in the neutral population is required for significant production of NH_4^+. The protonation process is described in more depth in Section 2.2.2.

The ROSINA–DFMS instrument (see Section 1.2.1), the highest resolution mass spectrometer ever flown in the solar system at the time, enabled the unambiguous detection of many ion species in the coma of 67P (Beth *et al.*, 2020). In this section I discuss the key published findings to date from the analysis of the high and low mass resolution data.

Fuselier *et al.* (2015) first analysed data from DFMS ion mode during the early section of the escort of 67P by Rosetta (October - December 2014), finding that at these heliocentric distances ($>$ 3.5 au) the solar wind could be seen to penetrate all the way down to the nucleus, i.e. no diamagnetic cavity had formed (see Section 1.3.2). The water production rate at $\sim$ 3.5 au was estimated to be 4×10^{25} s^{-1} (Gulkis *et al.*, 2015), around 1000 times less than the peak observed at perihelion. As a result, the ion-neutral chemistry taking place in the coma was considerably less complex than at lower heliocentric distances. The ion species detected at this time mainly had a low mass per charge ratio (14–18 uq^{-1}), but some peaks at higher masses (26-30, 44 uq^{-1}) were also observed. These represent the water group ions and the organic volatiles (CO, CO_2) respectively, released as neutrals from the comet surface and ionised. H_3O^+ and HCO^+ (19 and 29 uq^{-1}) were also observed as secondary ions, produced through ion-neutral chemistry. However, at this low outgassing the coma is too thin for the protonated high proton affinity ions (see Section 1.3.1) to be produced.

Near perihelion in summer 2015, many more ion species were detected, as documented in Heritier *et al.* (2017a) and Beth *et al.* (2020). The presence of these ions indicate significant ion-neutral chemistry happening in the coma, particularly those formed by the protonation of high proton affinity neutrals, such as H_2S, H_2CO, HCN, CH_3OH and NH_3. There only needs to be a small mixing ratio of these species in the neutral population for them to have significant influence on the ion composition. Detection of the terminal ion NH_4^+ was first reported by

Beth *et al.* (2016), using the high resolution mode of DFMS (Section 1.2.1) to distinguish it from H_2O^+, both with mass per charge ratios of 18. This was not possible at 1P/Halley with the Giotto HIS instrument (Balsiger, 1986).

Heritier *et al.* (2017a) defined an occurrence frequency (f_i) as:

$$f_i = \frac{\text{Number of times the ion species of mass/charge } i \text{ is detected}}{\text{Number of DFMS ion scans of mass/charge } i}. \tag{1.4}$$

A detection is defined as a spectral peak above the background noise level. Figure 1.7 shows the occurrence frequency for several protonated high proton affinity species against time. The coma is water-dominated near perihelion, so H_2O^+ is always present as it is produced directly through the photoionisation of water. H_3O^+ is also consistently identified, as it is produced through the efficient interaction of H_2O^+ with H_2O. The other ions are detected less frequently, but Figure 1.7 shows that their occurrence is correlated with higher neutral number densities and lower cometocentric distances.

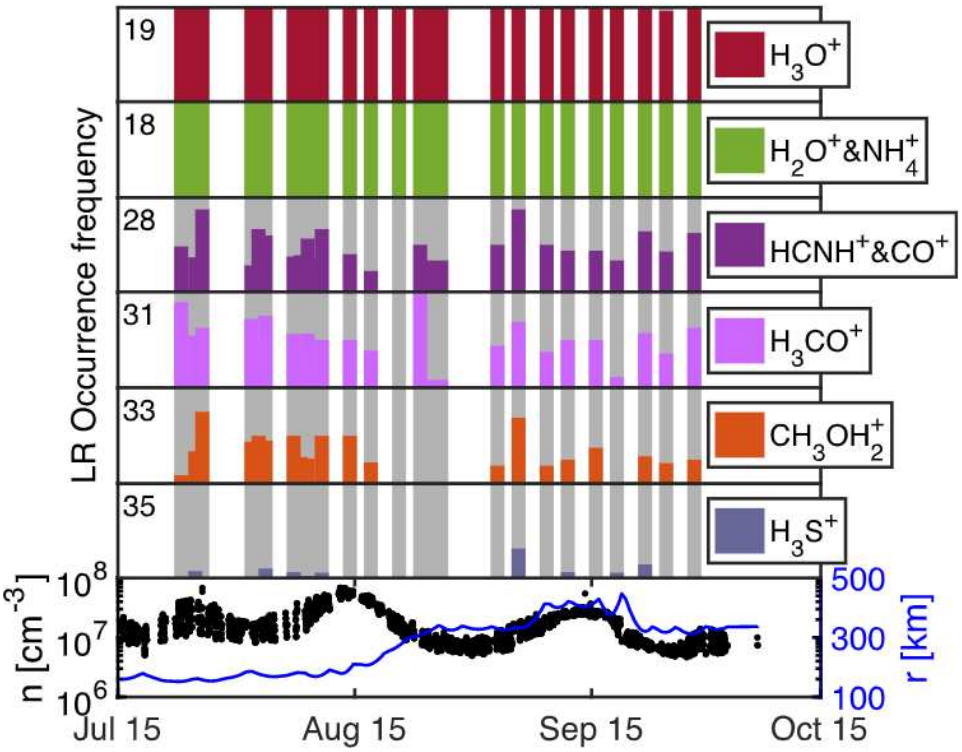

Figure 1.7: Occurrence frequencies from DFMS in low resolution mode for selected protonated high proton affinity neutrals against time for three months around perihelion. The bottom panel shows the COPS neutral density (black dots) and cometocentric distance (blue line). Credit: Heritier *et al.*, 2017a

In general, the ions with higher mass per charge ratios are detected less frequently than those that are lower (Heritier *et al.*, 2017a). This may be due to the effect of the negative spacecraft potential, accelerating the ions out of the energy acceptance window of the instrument (see Section 3.1.1).

1.3.2 The diamagnetic cavity

Prior to the first spacecraft missions to comet targets, an interface between the unmagnetised cometary plasma and the magnetised solar wind had been postulated (Biermann *et al.*, 1967). Mass loading of the solar wind with cometary ions (see Section 2.3.1), decelerates the solar wind, and for a comet with high enough outgassing, this presents enough of an obstacle to slow the solar wind from super- to sub-sonic, creating a **bow shock**. As the mass loading is a gradual process, this shock is considerably weaker than those at planets (Mach number ≈ 2). Bow shocks have been directly measured during flybys of several comets, including Halley (Neubauer *et al.*, 1986, Koenders *et al.*, 2013, Edberg *et al.*, 2023), but was missed by Rosetta at 67P, due to the spacecraft being too close to the nucleus near perihelion.

The frozen-in flux theorem states that strongly conducting fluids and their associated magnetic fields are tied together (Alfven, 1943), so the decelerated solar wind causes the magnetic field lines to drape around the comet (Figure 1.8). Eventually, the deceleration and deflection of the solar wind is enough that the solar wind plasma cannot reach the comet surface, so neither can the interplanetary magnetic field. This forms a magnetic cavity around the nucleus, as comets do not have an intrinsic magnetic field. The location of the cavity boundary was thought to originate from a balance between the thermal pressure from the cometary ionosphere and the magnetic pressure from the solar wind, much like that of Venus (Cravens, 1986). However, this simple picture was complicated by the first in-situ data from the flyby of 1P/Halley by the Giotto spacecraft in 1986.

The diamagnetic cavity is defined as a region of zero or nearly zero magnetic field surrounding a comet. The outer boundary of this region is called either the **contact surface** (mostly for 1P/Halley) or the **diamagnetic cavity boundary** (at 67P), and this can either refer to the location where the magnetic field magnitude ($|B|$) begins to decrease to zero,

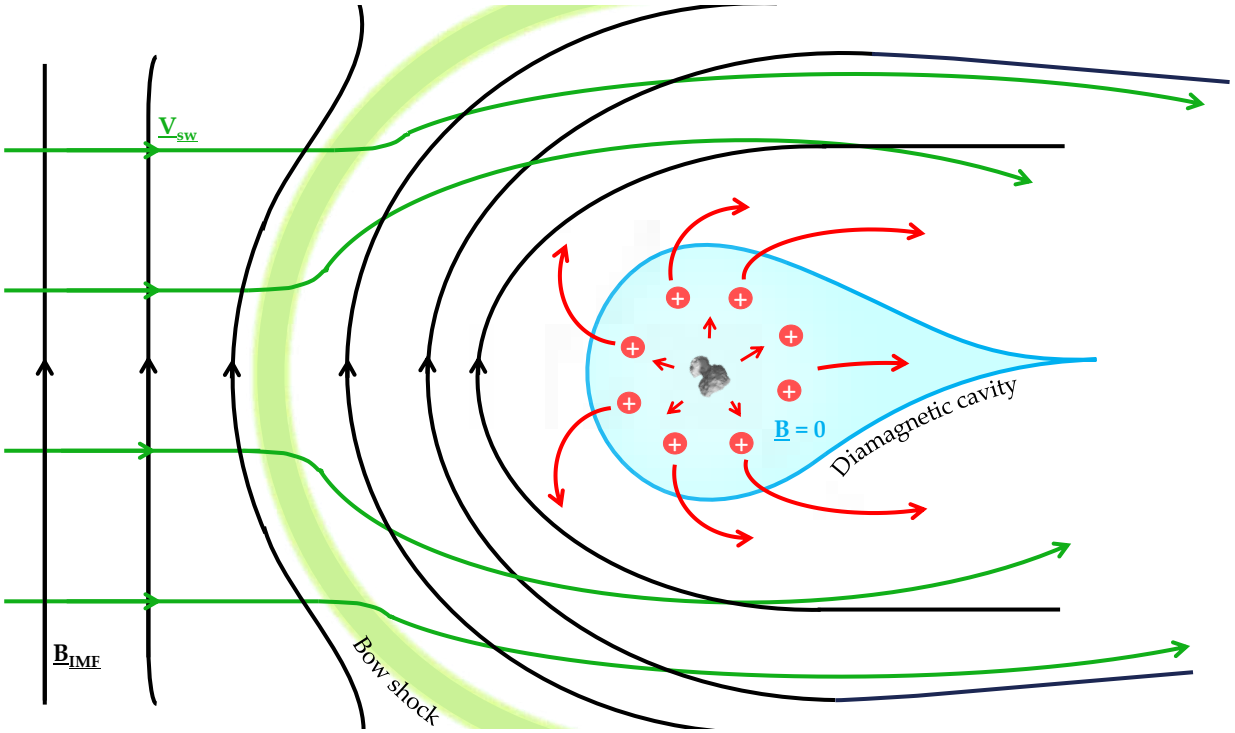

Figure 1.8: The deflection of the solar wind by a high outgassing comet, such as 1P/Halley, for the case where the solar wind flow is perpendicular to the interplanetary magnetic field. **Green lines** show the solar wind bulk velocity, and **black lines** show the magnetic field. The key plasma boundaries, diamagnetic cavity (**blue**) and bow shock (**light green**), are shown. Bulk flow of cometary ions is shown in **red** Features shown are not to scale.

or when it reaches its minimum value ($|B| \approx 0$). The region where the magnetic field is decreasing towards the nucleus is sometimes referred to as a boundary layer or transition region (Neubauer, 1988).

1P/Halley during the Giotto flyby

In the Giotto flyby of comet 1P/Halley, a diamagnetic cavity region was identified, as previously predicted by theory (Biermann *et al.*, 1967). The cavity region was found to be around 8500 km in width along the line of closest approach, 4760 km to the comet nucleus on the inbound journey and 3840 km outbound (Neubauer *et al.*, 1986). The magnetic field, in high temporal resolution, exhibits a steep drop from -20 nT to < 0.2–0.3 nT over 25 km (Neubauer, 1988). Cravens (1986) showed that the boundary could not be explained by a balance between the external magnetic pressure and internal pressure, as previously thought. Instead, they showed that the magnetic pressure gradient balances the ion-neutral drag force,

arising due to the flow of cometary neutral species past the stagnated ions (see Figure 1.9).

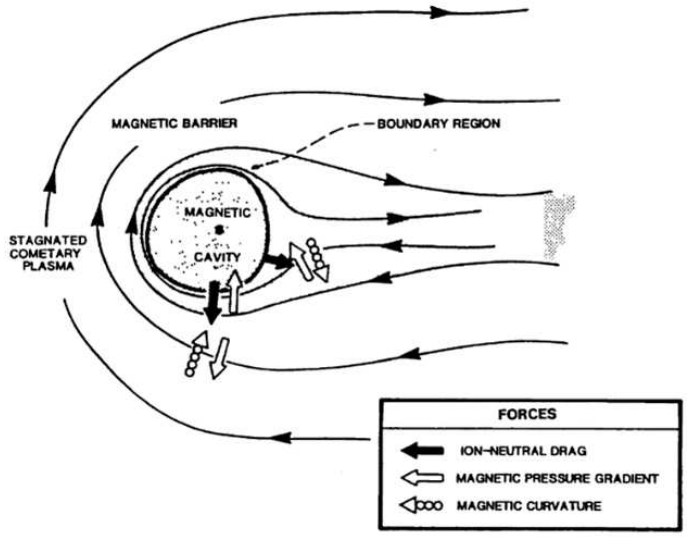

Figure 1.9: Illustration of the pressure balance at Halley, proposed in Cravens, 1986 to explain the existence of the diamagnetic cavity. Credit: Cravens, 1986

Balsiger (1986) derived the ion velocity profile in the radial direction from the Giotto Ion Mass Spectrometer (IMS) High Intensity Spectrometer (HIS) data, showing a discontinuity 4600 km from the nucleus in the plasma flow speed (from close to zero to 1 km s^{-1} as Giotto moved towards the nucleus into the diamagnetic cavity). This represents a transition from supersonic to subsonic plasma, indicative of an inner shock existing just inside the cavity boundary (Houpis and Mendis, 1980).

Goldstein *et al.* (1989) analysed the IMS–HIS data and observed a sharp spike in the ion density of water ions seen by IMS around the inner edge of the diamagnetic boundary. The spike was observed to be around 47 km in width and the ratio of heavy ions to water ions was also found to increase, indicating the importance of the chemical loss process due to differing recombination rates for different ions. Altwegg *et al.* (1993) re-analysed this dataset confirming the spike in the water ion density and showing an increase in the ion temperature in the region around the contact surface (4000–5000 km), as well as the changes in ion composition in more detail.

Cravens (1989) used a 1D magnetohydrodynamic (MHD) model (see Section 2.4) to show that the build-up of ionospheric plasma (pile-up) produces an ion-electron recombination layer between the inner shock and the contact surface. The increased plasma density in this

region increases the recombination rate such that flux of plasma transported there can be lost more quickly through recombination with neutrals.

While MHD modelling can successfully reproduce the large scale plasma boundaries for 1P/Halley during Giotto, the mean free path for collisions of the particles in the density peak (at the inner shock) is larger than the observed width of the peak (Goldstein *et al.*, 1989). In addition, MHD does not capture reflected ions at the cavity boundary moving antiparallel to the radial flow. This means that the small-scale structure of the contact surface can only be understood using kinetic models (Gombosi *et al.*, 1996).

The data gained from Giotto's short flyby of Halley was clearly not sufficient to understand the full picture, particularly features on smaller scales than the spatial resolution of the measurements, and the role of the inner shock on the kinetic scale. The Rosetta mission, escorting comet 67P at a relative speed of $1\ \mathrm{m\ s^{-1}}$, provided an opportunity to gather more data at higher spatial resolution, and to witness many diamagnetic cavity boundary crossings, albeit from a much less active comet (at perihelion $Q = 1 \times 10^{28}$ s^{-1}, compared to $Q = 9 \times 10^{29}$ s^{-1} for 1P/Halley, Moreels *et al.*, 1986). However, contrasting these observations with Giotto is particularly relevant, as the (yet unknown) target of the upcoming ESA Comet Interceptor mission (Snodgrass and Jones, 2019, Jones *et al.*, 2024) is likely to be closer in nature to the conditions encountered at 1P/Halley during the Giotto flyby.

67P during the Rosetta escort phase

Rosetta crossed over into the diamagnetic cavity of 67P a total of 713 times (Goetz *et al.*, 2016a), measuring clear periods of close to zero magnetic field with the RPC–MAG instrument (see Section 1.2.1, Glassmeier *et al.*, 2007a). Cavity signatures were identified while at heliocentric distances less than 2 au inbound and 2.4 au outbound (between April 2015 and February 2016), and when the outgassing was above 10^{27} s^{-1} (Goetz *et al.*, 2016a). An example of such a crossing is shown in Figure 1.10.

The boundary of the diamagnetic cavity was found at much larger cometocentric distances (50–400 km) than had been previously modelled based on the outgassing rate of 67P (Koenders *et al.*, 2015). This could be due to an underestimation of the gas production rate, and it

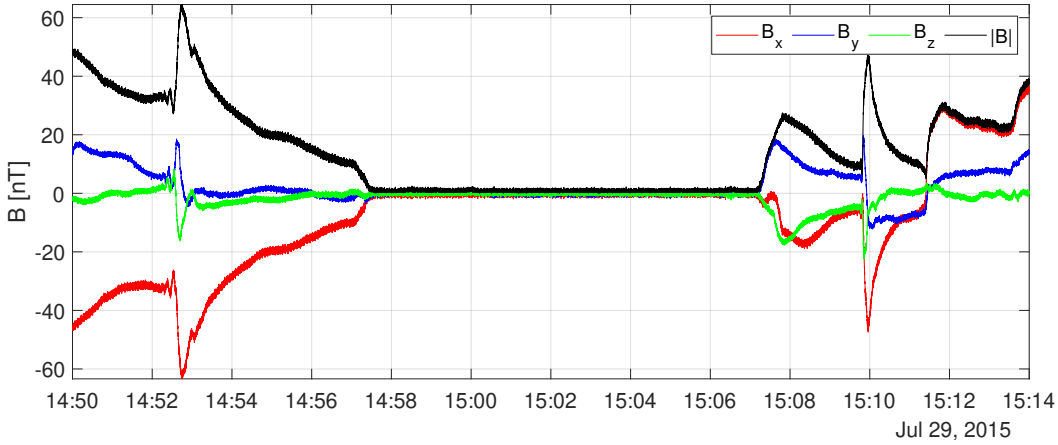

Figure 1.10: The components of the magnetic field from the RPC–MAG instrument on the 29th July 2015, showing a period of close to zero magnetic field. X, Y, and Z components are in the CSEQ coordinate System (cometocentric solar equatorial).

was shown that the measured production rate was not enough to explain the measured cavity boundary distance using previous models (Goetz *et al.*, 2016a). Anomalously high levels of gas and dust from outbursts were also ruled out by looking at images of the comet surface (from the Optical, Spectrocopic and Infrared Remote Imaging System instrument, OSIRIS, Keller *et al.*, 2007) at the same time as the magnetic field measurements were taken. Goetz *et al.* (2016a) also considered the possibility of a decrease in solar wind magnetic pressure causing the diamagnetic cavity to be drawn outwards. As the undisturbed solar wind was not able to be measured at Rosetta, the model outlined in Tao *et al.* (2005) was used to estimate solar wind conditions at 67P, extrapolated from Earth-based measurements. Goetz *et al.* (2016a) performed a superposed epoch analysis of the identified cavity crossings, showing that while some cavity observations do coincide with low solar wind magnetic pressure, this is not always the case, and in general an abnormally low magnetic pressure cannot account for the large diamagnetic cavity radius observed over months.

The diamagnetic cavity observations from Rosetta differ from those made by Giotto in that a large single region was not observed, rather a large number of shorter excursions into unmagnetised plasma, ranging from only a few seconds up to around 30 minutes (Goetz *et al.*, 2016a). They could be categorised into two groups: single and clustered events. The single events were characterised by longer durations and a return to background magnetic field

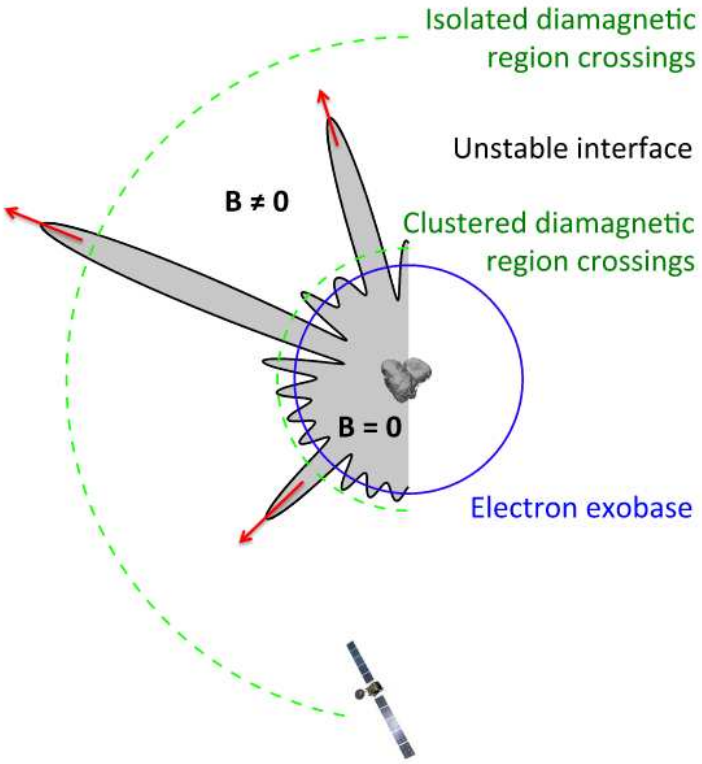

Figure 1.11: Possible configuration of magnetised and unmagnetised plasma regions, according to the RPC–MAG observations. Credit: Henri *et al.*, 2017

strength upon leaving the cavity. Clustered events happened when Rosetta moved in and out of the cavity several times in quick succession, and the magnetic field, though increased from zero, did not reach the background level between events. Due to the slow speed of Rosetta at this time, this is interpreted as the movement of the cavity boundary rather than the spacecraft itself travelling in and out of a stable region. Therefore, the diamagnetic cavity boundary at 67P appears to be relatively unstable, possibly due to Kelvin–Helmholtz instabilities driven by velocity shear between the two plasma populations at the cavity boundary. Rubin *et al.* (2012) applies an MHD model to the comet, showing how asymmetric neutral outgassing activity could drive this instability.

Henri *et al.* (2017) examined the plasma density within the unmagnetised regions more closely, finding that the clustered boundary crossings could be found to be near the limit of electron collisionality, known as the electron exobase. The solar wind electrons carry the interplanetary magnetic field (IMF) into the solar wind ion cavity, but, beyond the limit of the electron exobase (defined to be the cometocentric distance where the length scale is

equal to the mean free path of the electrons), collisions between the electrons and the radially expanding cometary neutrals become important. This friction couples the electrons to the outwards flowing neutrals, thus preventing the magnetic field from penetrating further and creating a field-free region, the boundary of such a region is closely tied to the location of the electron exobase. Local instabilities could extend sections of the cavity boundary, up to 10 times the distance of the electron exobase, as illustrated in Figure 1.11.

1.3.3 Changing ion dynamics over the escort phase

The simplest parameters we can use to describe the cometary ion population are the total ion density (which is approximately equal to the total electron density, quasi-neutrality is maintained in the plasma), and the ion bulk velocity. These parameters are inextricably linked, and the continuity equations which tie them together will be presented in full in Chapter 2. In this section, the aim is to describe the previous modelling which has been done in an effort to explain the ion measurements from the RPC instruments (Section 1.2.1).

The main challenge when trying to model the cometary ionosphere of 67P is that the input parameters (neutral outgassing, ionisation rate, etc.) vary so much throughout the escort phase of Rosetta. The same assumptions that can be applied at 3 au, for example, may not be valid near perihelion at 1.25 au.

For large heliocentric distances and close to the comet, Galand *et al.* (2016) demonstrated that a simple balance between the ionisation rate and radial ion transport was sufficient to explain the RPC–MIP and RPC–LAP electron density. For this low outgassing, the following conditions were determined to be valid:

(i) No attenuation of the incoming solar EUV (coma is optically thin),

(ii) No plasma loss through dissociative recombination.

Further to this, a simplifying assumption was made: that the cometary ions travel radially outwards at the same speed as the neutrals. Under these conditions the continuity equation

(Section 2.2) can be solved to find that the ion density n_i is simply

$$n_i = \frac{(\nu^{h\nu} + \nu^{e^-})n_n}{u_n}(r - r_c), \tag{1.5}$$

where u_n is the neutral speed, n_n is the neutral density from ROSINA-COPS (Section 2.1). $\nu^{h\nu}$ and ν^{e^-} are the photo and electron-impact ionisation frequencies, respectively, with the latter determined from RPC-IES observations (Section 2.2.1). r_c is the comet radius. Galand *et al.* (2016) demonstrated that this relation accurately reproduces the RPC plasma density measurements pre-perihelion at heliocentric distances < 3 au and below the cometocentric distance of Rosetta (< 20 km from the nucleus for the studied period).

Equation 1.5 predicts a peak in the density at $r = 2r_c$, around twice the comet radius of ~ 2 km. The physical explanation for this peak is that no ions are from the surface itself, so the density builds up once the gas is released and able to become ionised. After the peak, the transport becomes more efficient than the production and the density begins to drop off with increasing radial distance. The only opportunity Rosetta had to measure so close to the surface was during the final descent of the spacecraft on the 30th September 2016 at 3.8 au. As shown in Figure 1.12, this peak was indeed observed (Heritier *et al.*, 2017b).

In general, the model Equation 1.5 works well to explain the electron density at low outgassing post-perihelion (Heritier *et al.*, 2017b, Heritier *et al.*, 2018) as well as pre-perihelion (Galand *et al.*, 2016). The range of cometocentric distances probed by Rosetta at this time was usually within a few tens of kilometres from the surface, so the full parameter space was not explored, but there is good agreement over the regions analysed, which extended up to ~ 80 km post-perihelion (Heritier *et al.*, 2018).

At higher outgassing, the plasma density is no longer well constrained by the simple model (Vigren *et al.*, 2019). This is most likely due to the ions being accelerated by the ambipolar electric field (see Section 2.3.2) such that $u_i \neq u_n$ (e.g. Vigren *et al.*, 2017). However, it is not obvious what the radial profile of this electric field should be. Constraining this electric field, particularly within the diamagnetic cavity, is one of the aims of this thesis (see Chapter 4). Outside the diamagnetic cavity, the presence of the interplanetary magnetic field

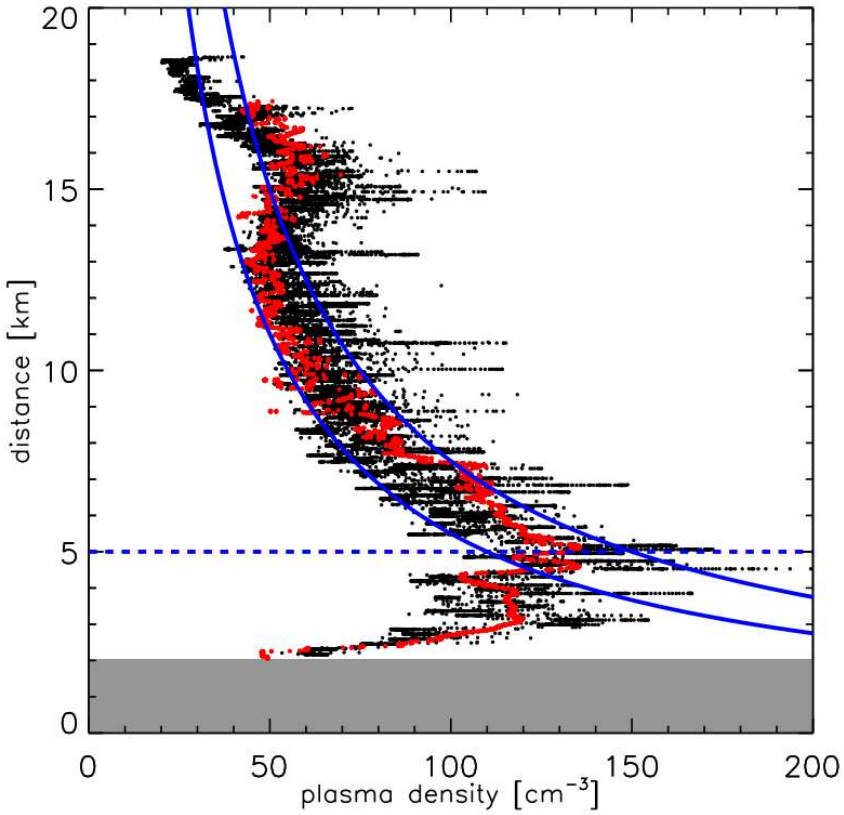

Figure 1.12: Vertical profile of the plasma density from Rosetta's final descent 30th September 2016. **Red**: MIP density, **Black**: cross-calibrated MIP/LAP dataset. **Blue lines:** 1/r vertical profiles. **Blue dotted line**: maximum of the density profile. Credit: Heritier *et al.*, 2017b

complicates the picture by introducing non-radial electric field contributions. In Section 2.3.1, each of these contributions to the electric field is described. Putting together this complex picture of the ion dynamics requires the ions to be treated kinetically (see Chapter 5).

Determination of the bulk ion velocity from Rosetta measurements is challenging. One method is described in Vigren *et al.* (2017) and involves the use of a combination of the current-voltage characteristics from RPC–LAP, and electron number densities from RPC-MIP (Section 1.2.1). For a Langmuir probe moving relative to a plasma that has a Maxwellian distribution and an ion drift $u_{i,D}$, the ion current (Fahleson, 1967) can be approximated as

$$I_i \approx \pi r^2 n_i e \sqrt{\frac{8k_B T_i}{\pi m_i} + u_{i,D}^2} \tag{1.6}$$

where n_i is the ion number density, r the radius of the probe, T_i the ion temperature and m_i the ion mass. The assumption of charge neutrality allows n_i to be replaced by the electron number density from RPC-MIP. An effective ion speed

$$u_{i,\text{eff}} = \sqrt{\frac{8k_B T_i}{\pi m_i} + u_{i,D}^2} \tag{1.7}$$

can then be derived using the current-voltage characteristic from LAP (dI_i/dU, where U is the applied voltage). This method does not allow the separation of the drift speed ($u_{i,D}$) from the thermal speed. For $u_{i,D}$ on the order of the neutral speed, 10^3 m s^{-1}, the thermal speed term is of comparable size for ion temperatures $\gtrsim$ 0.1 eV. The ion temperature is not well constrained, but values in the range 0.7–1.6 eV have been derived by Bergman *et al.* (2021a) using measurements from the ion composition analyser (RPC–ICA; Nilsson *et al.*, 2007).

This method was applied to a three day range in August 2015 by Vigren *et al.* (2017) and in November 2015 by Odelstad *et al.* (2018), finding effective ion velocities in the range 2–8 km s^{-1} at 200 km and 135 km, respectively. This range is higher than the 0.5–1 km s^{-1} neutral speed, and led to the conclusion that the ions and neutrals are decoupled and that the ions are accelerated by an electric field. In the same work, Vigren *et al.* (2017) also uses a simple flux conservation model, with the assumption of radial outflow, to estimate the ion speed. They find that the two methods produce similar values of u_i, but note that EUV

attenuation is neglected, as well as dissociative recombination. Neglecting the decrease in the photoionisation frequency is likely to result in overestimated values of u_i.

Another method that has been applied to derive the ion bulk speed is described in Bergman *et al.* (2021a) and uses RPC–ICA energy spectra fitted to drifting Maxwell–Boltzmann distributions for data from 88 diamagnetic cavity crossings. This fitting process allows the thermal and drift velocity components to be separated, and a bulk speed of 5–10 km s^{-1} was found, with a peak probability at 7 km s^{-1}

A key challenge when interpreting these calculated ion bulk speed measurements is the influence of the negative spacecraft potential on the ions detected (Odelstad *et al.*, 2017). RPC–LAP was positioned on a boom, and is therefore less strongly affected by this problem than RPC–ICA, which was positioned on the main body of the spacecraft. Low energy positively charged ions were accelerated towards the detector, resulting in the distortion of their energy spectra as measured by the instrument. Studies have been performed (e.g. Bergman *et al.*, 2020, Johansson *et al.*, 2020) using the Spacecraft–Plasma Interaction System (SPIS) to model this effect with the aim of correcting for it in the data. Bergman *et al.* (2021b) compared their derived ion temperature and velocity with results from the SPIS model to conclude that the effect on the measured speed would be fairly minimal (shifting the peak of the probability density function for $u_{i,D}$ to 6.9 km s^{-1}). However, other uncertainties remain, for example the variation in the spacecraft potential and the flow direction of the ions. The spacecraft potential distorts the measured direction of low energy ions from ICA, but higher energy cometary ions have been mostly observed in the radial direction (Nilsson *et al.*, 2017). Particle-In-Cell simulations have been used to correct for the spacecraft potential in ICA data by Bergman *et al.* (2021b), showing a surprising 'backstream' of ions towards the nucleus.

Despite these uncertainties, it is likely that, near perihelion, the cometary ions are indeed frequently travelling faster than the neutral population, suggesting the existence of a radial ambipolar electric field and a lack of collisional coupling between the ions and neutrals.

1.4 Motivations and objectives of the thesis

Section 1.3 introduced the understanding of the cometary ion environment so far, highlighting the progress made following the Rosetta escort. In this later stage of analysis from the mission, it is clear that we cannot build up a full picture with one dataset alone; we need a combination of multi-instrument analysis and modelling to make progress. In this Section, I discuss the specific motivations for each of the science objectives of the thesis, and what will be done to address them.

Firstly, I focus on the ionospheric composition, and what it can tell us about the dominant plasma processes in the coma. NH_4^+ is a key ion species, since it can only be formed through ion-neutral chemistry (i.e. not directly through ionisation). NH_3 has the highest proton affinity of the neutral species in the coma, so NH_4^+ is the terminal ion species; all proton transfer reaction pathways lead to it, and it is therefore a good tracer of how much ion-neutral chemistry took place before ions are lost through transport or through ion-electron dissociative recombination. The high mass resolution ion mode of DFMS allowed direct unambiguous detection of the NH_4^+ for the first time (Beth *et al.*, 2016), as well as the detection of other protonated high proton affinity species (Heritier *et al.*, 2017a; Beth *et al.*, 2020). However, the detections of NH_4^+ have not yet been assessed against datasets from other instruments. The goal of **Chapter 3** is to exploit the DFMS High Resolution ion mode dataset in depth over the 2-year escort phase of Rosetta, focussing on the presence of NH_4^+, to confirm its source in the coma, and to understand what factors drive its abundance.

- Exploit the ROSINA-DFMS dataset to assess the variation in NH_4^+ and other high proton affinity ion species over the escort phase.
- Compare the NH_4^+ dataset against neutral density from COPS, NH_3 mixing ratio from DFMS neutral mode, and spacecraft potential from RPC–LAP.
- Make a qualitative comparison of the ROSINA-DFMS NH_4^+ counts with the ion densities produced by the 1D ionospheric model from Heritier *et al.* (2018).

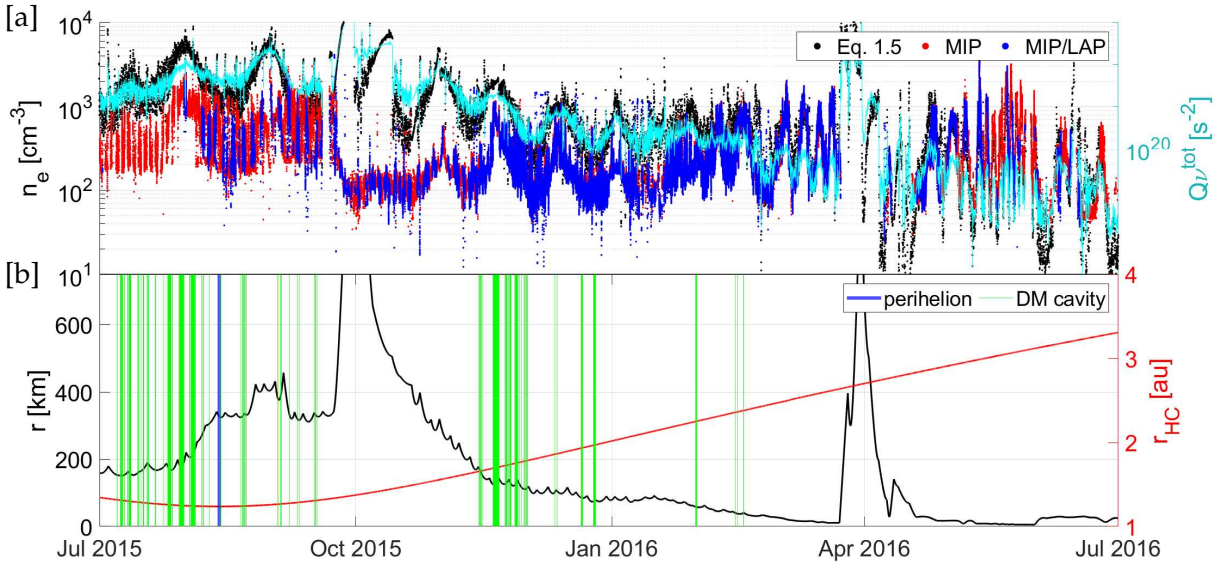

Figure 1.13: **[a]** Comparison of the **(black)** calculated plasma density from Equation 1.5, with the measured electron density from **(red)** RPC-MIP and **(blue)** the MIP/LAP combined dataset. **(cyan)** The ion production rate $Q\nu^{\mathrm{tot}}$ where Q is the total outgassing rate calculated COPS (see Equation 2.2) and ν^{tot} is the sum of the total photoionisation and electron-impact frequencies (Stephenson *et al.*, 2023, see Figure 2.5). Data are shown for July 2015 - July 2016. **[b]** (**black**) cometocentric distance, and (**red**) heliocentric distance. **Green** lines mark diamagnetic cavity crossings (Goetz *et al.*, 2016a, width of line not to scale) and **blue** line indicates perihelion in August 2015.

NH_4^+ was previously detected near perihelion (Beth *et al.*, 2016; Heritier *et al.*, 2017a). During this period, the outgassing of 67P was high enough to have a diamagnetic cavity formed (see Section 1.3.2). The plasma characteristics have been found to be systematically different inside the diamagnetic cavity, with less variation in the plasma density (Henri *et al.*, 2017) and ion bulk velocity (Odelstad *et al.*, 2018) than outside. Odelstad *et al.* (2018) found the ion bulk velocities to be mostly radial within the cavity, with enhanced dynamics outside. These observations have been supported by modelling, e.g. in Koenders *et al.* (2015). The effect of this different, unmagnetised plasma environment on the ion composition has however not yet been assessed.

- Compare detections of NH_4^+ inside and outside the diamagnetic cavity to determine whether the ion composition is affected by changing plasma dynamics.

Next, I turn to the processes driving the ion density and bulk velocity, which, as described in Section 1.3.3, have not yet been fully understood. Since cometary ions originate from neutral particles emanating from the surface, it is reasonable to initially assume that the ions share the same bulk velocity as the neutrals. This assumption has been demonstrated to accurately replicate the total plasma density observed by RPC–MIP and RPC–LAP at larger heliocentric distances, when comet activity was low and Rosetta was positioned within a few tens of kilometres from the nucleus (Galand *et al.*, 2016, Heritier *et al.*, 2018). However, inside the diamagnetic cavity, such a model does not apply, and it significantly overestimates the plasma density, indicating that the ions may be accelerated by an ambipolar electric field that does not affect the neutral particles. This process collisionally decouples the ions from the neutrals. Understanding the extent of this decoupling is crucial for understanding the behaviour of the cometary plasma, including the formation of the diamagnetic cavity boundary. However, this process remains poorly understood at present.

Determination of the ion bulk speed from the RPC data has resulted in values up to $10\ \mathrm{km\ s^{-1}}$ inside the diamagnetic cavity (Bergman *et al.*, 2021b), though their interpretation is complicated by, for example, the effect of the strongly negative spacecraft potential. The magnitude and functional form of the ambipolar electric field are also difficult to constrain. However, we know that at 67P, the ionospheric composition and density are inextricably linked to the plasma transport timescale (Beth *et al.*, 2019). With this in mind, the goal of **Chapter 4** is to model the ionosphere under different radial electric fields, to constrain the amount of transport that reproduces the plasma density observations from RPC inside the diamagnetic cavity.

- Build a 1D numerical model that includes acceleration by an imposed ambipolar electric field and collisions between the neutrals and the three main ion species: H_2O^+, H_3O^+, and NH_4^+.
- Compare the modelled electron density and ion composition measurements to constrain the amount of ion transport inside the diamagnetic cavity.

Outside the diamagnetic cavity, the non-zero magnetic field contributes motional (see Section 2.3.1) and polarisation (see Section 2.3.1) terms into the electric field, and the flow is no longer simply radial. One might expect that electric and magnetic fields are more likely to affect the ion velocity at low outgassing, when there is no diamagnetic cavity and the solar wind's influence extends all the way to the surface. However, the good agreement of the $u_i = u_n$ model (Equation 1.5) with the plasma density measurements is seemingly at odds with this.

As demonstrated in Vigren *et al.* (2019), a transition occurs during late February to early March 2016 where the assumptions of the simple model become valid (see Figure 1.13). Interestingly, the transition appears to coincide with the last observations of the diamagnetic cavity by RPC-MAG (Goetz *et al.*, 2016a) on 14th-17th February 2016. It is not known whether the diamagnetic cavity boundary lay below the spacecraft beyond these dates, but given the relatively short (and decreasing) distance of Rosetta from the comet nucleus it seems unlikely that the cavity persisted into March 2016.

Putting together this complex picture of the ion dynamics requires the ions to be treated kinetically, as in test-particle model and hybrid plasma simulations. **Chapter 5** aims to shed light on the effect of a more-complex 3D solar wind–comet interaction on the ionospheric composition and density, with a view to better interpret the RPC data for intermediate and low outgassing.

- Adapt the collisional test-particle electron model from Stephenson *et al.* (2022) to model the effect of the 3D electric and magnetic field structure on the cometary ion density, composition and bulk velocity.
- Validate the 1D approach against the full set of 3D collisions.
- Investigate and compare the effect of ion-neutral collisions on the ion chemistry and dynamics in 3D.
- Compare the plasma density from the 3D model against observations from RPC–MIP and RPC–LAP.

1.5 Structure of the thesis

Chapter 2 introduces the theory of the cometary ionosphere, starting from the continuity equation and bringing in the relevant elements of space plasma physics.

Chapters 3, 4, and 5 form the core research section of the thesis, and address the motivations and objectives presented in Section 1.4. **Chapter 3: 'Origin and trends in high proton affinity ion species'** presents my analysis of the ROSINA–DFMS high resolution ion dataset, focussing on NH_4^+ to identify its origin in the coma and whether it is affected by the presence of the diamagnetic cavity. In **Chapter 4: 'Constraining ion transport in the diamagnetic cavity'**, I describe the 1D ion acceleration model and use it to constrain the ambipolar electric field strength and ion bulk velocity in the diamagnetic cavity near perihelion. **Chapter 5: 'Modelling the ion dynamics in 3D'** then expands this into 3D, through ion test-particle modelling, to look at the impact of electric and magnetic fields on the cometary ion environment for lower outgassing.

Finally, **Chapter 6** summarises the findings of the thesis and suggests further studies that would be required to shed light on the open questions that remain.

CHAPTER 2

THE COMETARY PLASMA ENVIRONMENT

In Chapter 1, I discuss some of the key areas of study and previous work to understand the cometary ionosphere, outlining the open questions that will be addressed in this thesis. It is clear from the literature review that shedding light on the processes affecting the ion environment of comet 67P requires an arsenal of ionospheric and plasma physics methods, as well as a range of modelling approaches. In this chapter, I outline the relevant theory, bringing together fundamental equations and applying them to this unique environment.

First, in Section 2.1, I discuss the neutral coma of 67P, focussing on the key parameters that influence the ion environment. Section 2.2 presents the mathematical description of the cometary ion environment that is used for much of the modelling in Chapters 3 and 4. Section 2.3 describes the interaction of the cometary plasma with the solar wind, in particular the influence of electric and magnetic fields and the diamagnetic cavity. Finally, in Section 2.4 I discuss the different types of plasma models that have been applied to comets, how they apply in different regimes, and their advantages and limitations when used to understand the behaviour of the ions.

2.1 The neutral coma as an ion source

While the main focus of this thesis is the plasma environment, it is important to understand the neutral gas from which it originates. The ionosphere is only a small fraction of the total particle density (at most 0.01%) and the size and composition of the ion population is completely driven by the neutrals. In this section I present this neutral environment, discussing its density and composition (Section 2.1.1), as well as its bulk velocity (Section 2.1.2).

2.1.1 Neutral density and composition

One of the key differences between comets and planets is that comets don't have a strong enough gravitational field to hold an atmosphere under hydrostatic equilibrium. This means that the atmosphere is constantly leaving the surface and expanding into the vacuum of space. Fortunately, when the comet is close enough to the Sun, sublimation of ices from the nucleus provides a constant supply of new gas material which replenishes both the neutral coma and the ionosphere - at least until the nucleus mass has been completely depleted.

The number of molecules being ejected from the cometary nucleus per second is the total outgassing rate, Q. This outgassing rate varies as the nucleus travels around its highly eccentric orbit, experiencing varying levels of solar radiation. For comet 67P during the Rosetta escort phase, Q varied between 10^{26} s^{-1} and 10^{28} s^{-1} (Biver *et al.*, 2019).

For constant and radial neutral speed u_n, conservation of mass flux leads to the simplified Haser model (Haser, 1957), giving the neutral density at cometocentric distance r:

$$n_n(r) = \frac{Q}{4\pi u_n r^2} e^{-r/(\tau_n u_n)}. \tag{2.1}$$

where the exponential correction factor $\exp\left(-r/(\tau_n u_n)\right)$, where τ_n is the lifetime against dissociation and ionisation (e.g. Gombosi *et al.*, 1996), becomes important at large cometocentric distances ($r \gtrapprox 10^3$ km for the typical outgassing of 67P during the Rosetta mission). Locally, however, this term may be neglected, and $n_n \propto 1/r^2$ was observed to be a good fit to the ROSINA/COPS neutral density (Hässig *et al.*, 2015).

The Haser model assumes that the outgassing of the comet is spherically symmetric,

which is known not to be the case for 67P (Hansen *et al.*, 2016). The intriguing double-lobed shape of the nucleus (see Figure 1.3a) leads to enhanced surface area and therefore to more water production around the 'neck' area (the join between the two lobes). To take into account these variations, for data analysis purposes it is useful to define a local outgassing, Q^{local}, using the neutral density measured by COPS at a distance r above the surface,

$$\underbrace{n_n(r)}_{\text{from COPS}} = \frac{Q^{\mathrm{local}}}{4\pi u_n r^2}. \tag{2.2}$$

The composition and volatility of the surface is also non-uniform (Keller *et al.*, 2015), and the composition of the gas as measured by ROSINA-DFMS varied with latitude and season (Hansen *et al.*, 2016). All of this variation means that the neutral environment provides vital context for interpretation of the ion data.

Measurements of the neutral composition at comet 67P are provided by the DFMS instrument in neutral mode (see Section 1.2.1). The main species detected were water, carbon monoxide, carbon dioxide, methane, ammonia, and methanol (Hässig *et al.*, 2015). The relative abundances of these species were found to vary with heliocentric distance, but water is always the most abundant by a considerable margin (up to 99% of the total neutral gas, Biver *et al.*, 2019). The relative abundances of the other species were found to be consistent with the values measured in the coma of other comets (Hässig *et al.*, 2015), suggesting that 67P is a fairly typical comet in terms of its composition.

In Chapter 3, I discuss the production of the NH_4^+ ion, which, near perihelion, becomes the most dominant ion species close to the comet. This is the result of rapid protonation of NH_3: ammonia. Though ammonia makes up only a small fraction (around 0.01%) of the coma, it is interesting not only because it contributes so significantly to the ion composition, but also because it is a key ingredient in the formation of complex organic molecules. Moreover, glycine was detected in the coma (Altwegg *et al.*, 2016), which is the simplest amino acid and the only one able to form without the presence of liquid water. This suggests that comets could have played a role in the delivery of prebiotic molecules to the early Earth (Altwegg *et al.*, 2016).

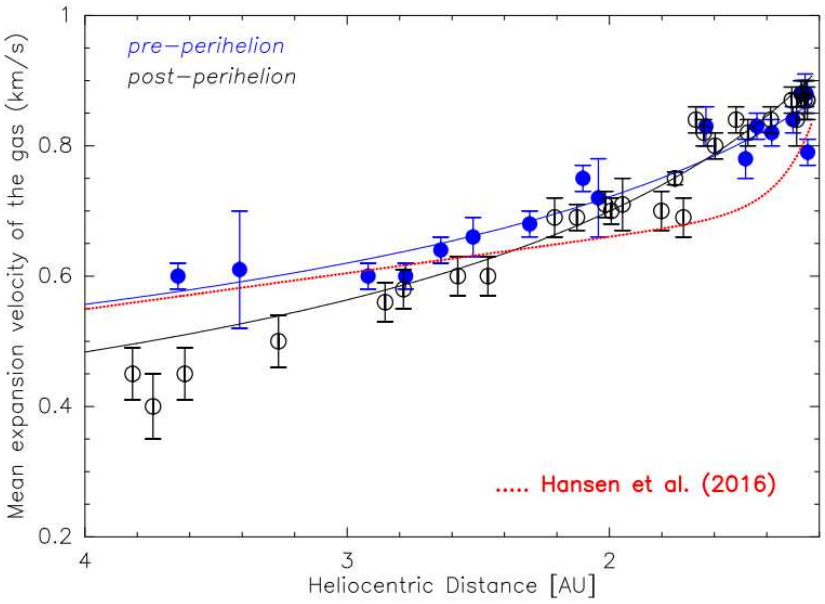

Figure 2.1: Neutral expansion velocity as a function of heliocentric distance during the escort phase of Rosetta, as determined by the MIRO instrument. Credit Biver *et al.*, 2019.

2.1.2 Neutral bulk velocity

The neutral speed u_n has been determined by the Microwave Instrument for the Rosetta Orbiter (MIRO), a submillimeter radio telescope on the Rosetta spacecraft. MIRO measured the Doppler shift of the water lines in the coma, and found that the neutral speed was typically $0.5 - 1$ km s^{-1} (Biver *et al.*, 2019). These data were fitted as a function of heliocentric distance (shown in Figure 2.1, alongside the earlier profile from Hansen *et al.*, 2016). Throughout this thesis, the Biver *et al.* (2019) parametrisations are used to determine the radial gas speed and are given by:

$$u_n(r_{hc}) = 0.94 r_{hc}^{-0.38} \text{ km s}^{-1} \tag{2.3}$$

pre-perihelion (before 14th August 2015) and

$$u_n(r_{hc}) = 1.01 r_{hc}^{-0.53} \text{ km s}^{-1} \tag{2.4}$$

post-perihelion, where r_{hc} is the heliocentric distance in au.

SECTION 2.1 KEY POINTS

- The number of neutral gas particles released per second from a comet nucleus is given by the **outgassing rate, Q**. For a given comet, the outgassing rate generally increases with decreasing heliocentric distance.
- The neutral gas coma is **mostly comprised of water**, with small but significant contributions from other gases such as NH_3.
- The outgassing rate can either be determined globally by remote sensing or can be calculated for the local environment using the density from the ROSINA-COPS instrument and the distance of the spacecraft from the nucleus.
- The bulk velocity of the gas escaping from the nucleus can be parametrised as a function of the heliocentric distance.

2.2 Formation of the cometary ionosphere

To understand the cometary ionosphere, we can mathematically formulate its sources and sinks into a set of continuity equations (e.g. Vigren and Galand, 2013). This aids in the interpretation of the RPC and ROSINA-DFMS electron and ion data, particularly since it is not possible to determine the density of each ion species directly from the ion mass spectra (see Section 1.2.1).

Consider an ion population j, travelling at bulk velocity $\vec{u}_j(\vec{r})$. The number density $n_j(\vec{r})$ of this species is governed by the continuity equation

$$\frac{\partial n_j(\vec{r},t)}{\partial t} + \nabla \cdot (n_j(\vec{r},t)\mathbf{u}_j(\vec{r})) = P_j(\vec{r},t) - R_j(\vec{r},t)n_j(\vec{r},t). \tag{2.5}$$

$P_j(r,t)$ is the production rate of the ion population j (in $\mathrm{cm}^{-3}\mathrm{s}^{-1}$), which comprises of the contributions from ionisation and ion-neutral chemistry:

$$P_j = P_j^{\text{ioni}} + P_j^{\text{chem}}. \tag{2.6}$$

Equivalently, $R_j(r,t)$ is the loss frequency of the ion population j (in s^{-1}), and comprises losses due to chemistry and dissociative recombination:

$$R_j = R_j^{\text{chem}} + R_j^{\text{DR}}. \tag{2.7}$$

Summing the density of all the ion species j together gives the total ion density n_i:

$$n_i(\vec{r},t) = \sum_j n_j(\vec{r},t). \tag{2.8}$$

Since the ion-neutral chemical reactions don't result in a net loss of plasma, only a transfer from one ion species to another, these terms cancel out for the total ion density,

$$\sum_j \left(P_j^{\text{chem}} - R_j^{\text{chem}} n_j\right) = 0 \tag{2.9}$$

and the continuity equation (Equation 2.5) becomes

$$\frac{\partial n_i(\vec{r},t)}{\partial t} + \nabla \cdot (n_i(\vec{r},t)\mathbf{u}_i(\vec{r})) = \sum_j P_j^{\text{ioni}}(\vec{r},t) - \left(\sum_j R_j^{\text{DR}}(\vec{r},t)\right) n_i(\vec{r},t). \tag{2.10}$$

The rest of this section describes the source and loss terms in more detail. I start with the ionisation: photoionisation and electron impact (Section 2.2.1). In Section 2.2.2, I discuss the ion-neutral chemistry and in Section 2.2.3, the ion-electron dissociative recombination. Finally, I present useful edge cases of the ion continuity equations applied in a 1D approximation (Section 2.2.4).

2.2.1 Ionisation

The two main ionisation sources for cometary ions are photoionisation and electron impact. At large cometocentric distances (> 1000 km, Simon Wedlund *et al.*, 2017), a significant number of ions are added through charge exchange between the cometary neutrals and the solar wind, however, this may be neglected at the location of Rosetta. Hence, the ionisation production rate is given by

$$P_j^{\text{ioni}} = (\nu_{n\to j}^{\text{photoioni}} + \nu_{n\to j}^{\text{e- impact}})n_n \tag{2.11}$$

where $\nu_{n\to j}^{\text{photoioni}}$ and $\nu_{n\to j}^{\text{e-impact}}$ are the photo- and electron-impact ionisation frequencies respectively. This is defined as the number of neutral molecules (n) per second that are photoionised to form ion species j by each ionisation source.

Photoionisation

All of the neutral species in the coma can be photoionised, but since water is the most abundant neutral species in the coma, the most important reaction:

$$\mathrm{H_2O} + \gamma \rightarrow \mathrm{H_2O^+} + \mathrm{e^-}. \tag{2.12}$$

For a photon γ to be capable of ionising water, it must exceed the ionisation threshold energy of 12.6 eV (Itikawa and Mason, 2005). These photons are in the Extreme Ultraviolet (EUV) part of the solar spectrum, $10 - 98$ nm, and most of the excess energy goes to the electrons that are produced - typically around 10 eV (Galand *et al.*, 2016). Further discussion of these newly-produced photoelectrons is given in Section 2.3.3.

The photoionisation frequency is calculated using the photoionisation cross sections for each neutral species $\sigma_{n\to j}^{\text{ioni}}(\lambda)$, combined with the attenuated solar EUV spectrum. At a location r and for wavelength λ, this is given by the Lambert-Beer law:

$$F(r,\lambda) = F(\infty,\lambda)\exp\left(-\underbrace{\sum_n \sigma_n^{\text{photoabs}}(\lambda)\int_\infty^{s(r)} n_n(s')\,ds'}_{\tau(\lambda,r)}\right) \tag{2.13}$$

where $F(\infty,\lambda)$ is the unattenuated solar flux adjusted to the heliocentric distance of the comet and $\tau(\lambda,r)$ is the optical depth. s is the distance of r along the line of sight from the Sun. The photoabsorption cross sections for each neutral species are given by $\sigma_n^{\text{photoabs}}(\lambda)$. Figure 2.3 shows the solar spectrum up to 100 nm for the 21st July 2015, taken from the TIMED/SEE experiment (Woods *et al.*, 2005), alongside the ionisation and absorption cross sections (σ^{ioni}

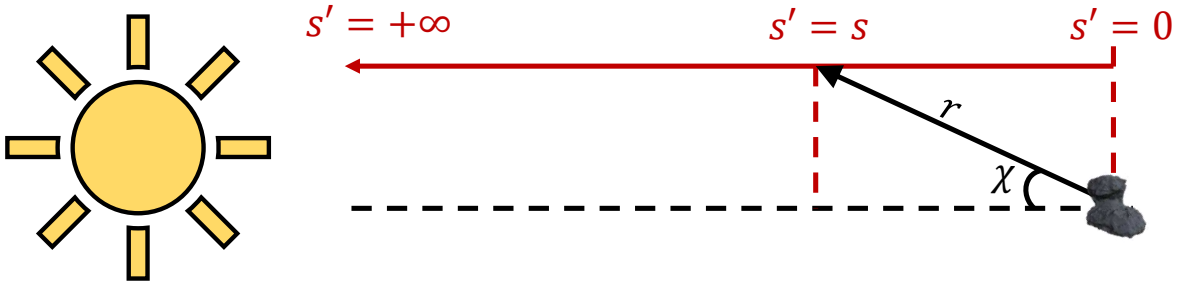

Figure 2.2: Illustration of how the column density of the cometary coma is calculated using Equation 2.14. s is the distance of point r from the comet along the line of sight of the sun. $s = r \cos \chi$.

and σ^{photoabs}) for water.

The optical depth $\tau(\lambda, r)$ is a dimensionless quantity and represents the amount by which solar flux of wavelength λ is attenuated by the local medium. An optical depth of 0 represents a medium that is completely transparent to all incoming flux, and a value of 1 represents a reduction in flux by a factor of $1/e$. At a comet, the attenuation is mostly due to the neutral gas coma (see Section 2.1), though attenuation by dust grains has been proposed as another factor (Johansson *et al.*, 2017).

Considering the neutral gas with the model of Haser (1957) (see Section 2.1.1), i.e. under spherical symmetry, allows an analytical solution to the optical depth to be derived (Beth *et al.*, 2016). First we define the column density $N_n(\chi, r)$ for solar zenith angle χ and cometocentric distance r:

$$N_n(\chi, r) = \int_s^\infty n_n(s')\, ds' \tag{2.14}$$

where s represents the path of the solar flux and is shown in Figure 2.2. Using Equation 2.2, the geometric relation $s = r \cos \chi$, and the fact that $r \sin \chi$ is constant for all r, we obtain

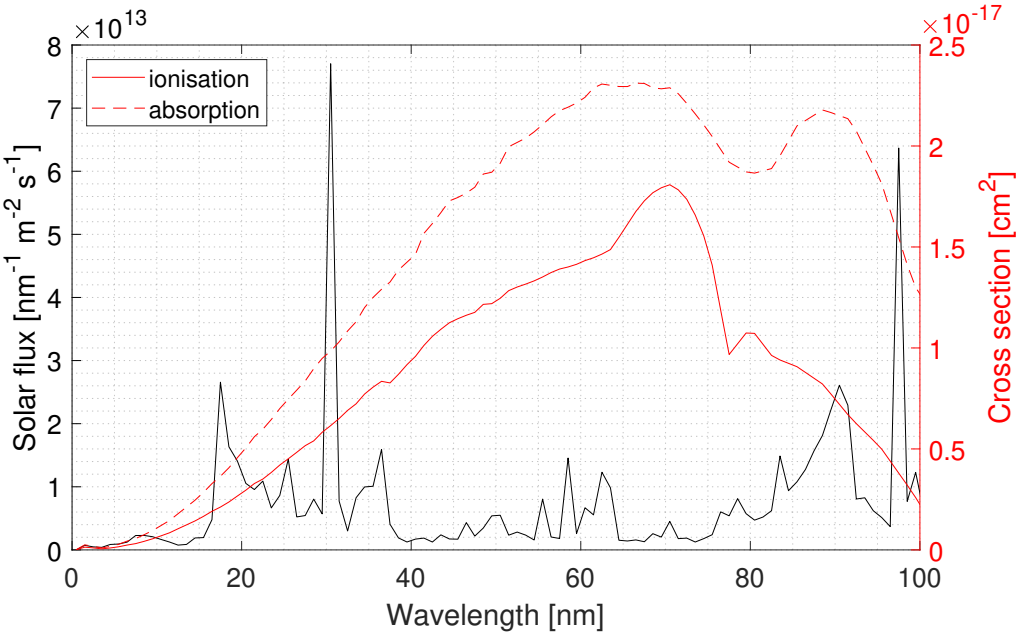

Figure 2.3: Solar flux at 1 au from the Sun, measured on the 21st July 2015 by the TIMED/SEE spacecraft **(black, left axis)**. Total photoionisation yielding H_2O^+ and photoabsorption cross section for H_2O **(red, right axis)**.

$$N_n(\chi, r) = \int_s^\infty \frac{Q}{4\pi u_n (s'^2 + r'^2 \sin^2(\chi'))}\, ds' \tag{2.15}$$

$$= \frac{Q}{4\pi u_n r^2 \sin^2(\chi))} \int_s^\infty \frac{1}{\frac{s'^2}{r'^2 \sin^2(\chi')} + 1}\, ds' \tag{2.16}$$

$$= \frac{Q}{4\pi u_n r^2 \sin^2(\chi))} \left[\frac{\pi}{2} - \arctan\left(\frac{s}{r\sin(\chi)}\right)\right] \tag{2.17}$$

$$= \frac{Q}{4\pi u_n r} \frac{\chi}{\sin(\chi)} \tag{2.18}$$

This expression (2.18) is valid for the dayside, i.e. where $0° < \chi < 90°$, but can be applied to the nightside by taking advantage of the spherical symmetry. For most of the Rosetta escort phase, Rosetta was in the terminator plane so $\chi \sim 90°$ is often a good approximation.

Once the attenuation of the solar flux has been determined, the photoionisation frequency can then be calculated,

$$\nu_{n\to j}^{\text{photoioni}} = \int_{\lambda^{min}}^{\lambda^{th}} \sigma_{n\to j}^{\text{ioni}}(\lambda) F(\infty, \lambda) e^{-\tau(\lambda, r)}\, d\lambda. \tag{2.19}$$

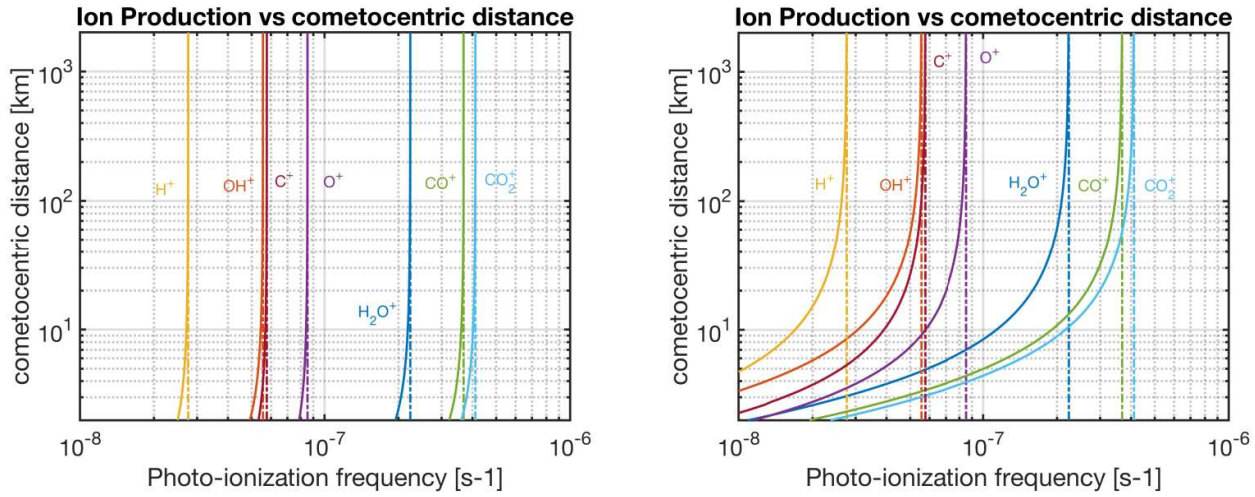

Figure 2.4: Photoionisation frequency for the products of photoionisation for H_2O, CO and CO_2 as a function of cometocentric distance, for two different outgassing rates: 10^{27} s^{-1} (**left**) and 3×10^{28} s^{-1} (**right**). Dotted lines show frequency from unattentuated solar flux. Credit: Heritier *et al.* (2017a)

Figure 2.4 shows example ionisation frequency profiles with cometocentric distance for medium (left) and high (right) outgassing rates. It is clear from this figure that the effect of photoabsorption may be neglected in the 10^{27} s^{-1} outgassing case. In the high outgassing case, there may be no attenuation at the spacecraft location if it is above 100 km (as it usually was near perihelion). However, models need to include it in order to build up the full picture of the ion environment.

Electron-impact ionisation

The second key process by which cometary neutrals can be ionised is by electron-impact ionisation. This is the process by which energetic electrons, exceeding the ionisation threshold for the neutral molecules, collide with them and release a secondary electron, e.g.,

$$e^- + H_2O \rightarrow H_2O^+ + e^- + e^-. \tag{2.20}$$

The electron-impact ionisation frequency is more complicated to derive than the photoionisation, since a single electron may retain energy and go on to cause more neutrals to become ionised (or excited). Conversely, an ionising photon is wholly absorbed by the neutral. Large electron-impact ionisation frequencies are associated with a significant population of

energetic electrons, such as those that have been accelerated by the solar wind (Madanian *et al.*, 2016a) or produced by absorption of X-rays at very large outgassing rates (such as 1P, Bhardwaj, 2003).

Photoionisation dominated near perihelion during the Rosetta escort phase, whereas electron impact was required to explain the electron density at larger heliocentric distance (Galand *et al.*, 2016, Heritier *et al.*, 2017b, Heritier, 2018). Stephenson *et al.* (2023) made the first assessment of the electron impact frequency across the whole mission, confirming that it does indeed dominate over photoionisation for large heliocentric distances. This was performed using measurements from RPC–IES (see Section 1.2.1) and calculated according to the equation

$$\nu_n^{\text{e-impact}} = \sum_j \int_{E_{\text{thresh}}}^{E_{\max}} \sigma_{n\to j}^{\text{e-impact}}(E)\ J(E)\ \mathrm{d}E \tag{2.21}$$

where j represents the different ion products resulting from the ionisation of neutral species n and $\sigma_{n\to j}^{\text{e-impact}}(E)$ is the electron-impact ionisation cross section at a given energy E. The integral goes from the threshold energy for each ionisation reaction E_{thresh}, to the maximum energy beyond which the electron flux is can be neglected E_{max}. $J(E)$ is the differential electron flux from RPC–IES (Burch *et al.*, 2007), and details of its derivation can be found in Stephenson *et al.* (2021). The electron-impact ionisation frequency derived is displayed in Figure 2.5 (black); it is highly variable, but it dominates over the photoionisation frequency (red) at large heliocentric distances particularly before April 2015 and after January 2016.

2.2.2 Ion-neutral chemistry

Equation 2.5 introduced the continuity equation for ion species j in the cometary coma. In this equation, the production term (Equation 2.6) comprised new ions from ionisation (covered in Section 2.2.1) and from ion-neutral chemistry. The production rate of ion population j at the neutral speed u_n due to ion-neutral chemistry is given by

$$P_j^{\text{chem}}(r) = \sum_{n,j'\neq j} k_{j',n\to j}^{\text{IN}} n_n(r) n_{j'}(r) \tag{2.22}$$

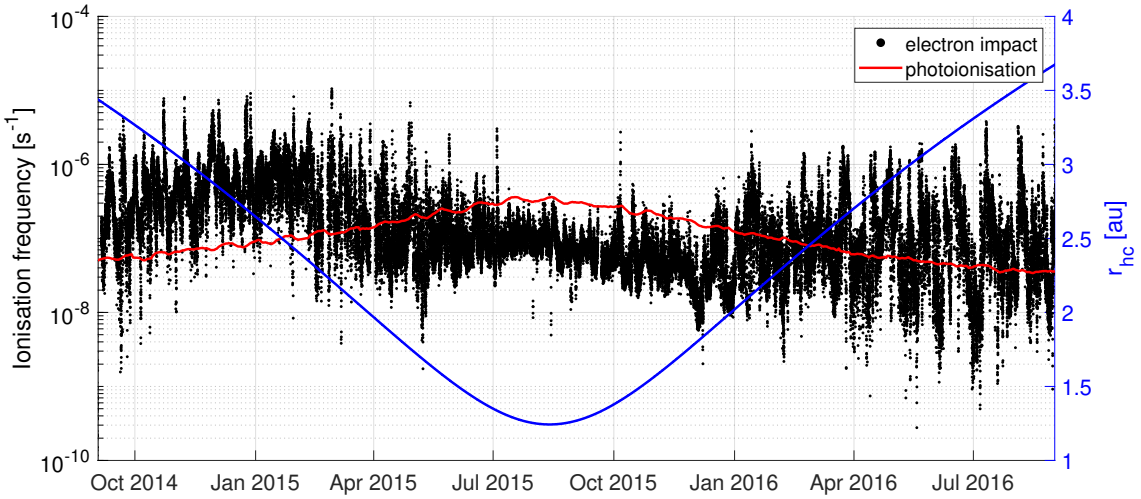

Figure 2.5: Photoionisation (**red**) and electron-impact ionisation (**black**) frequencies over the escort phase of Rosetta. Heliocentric distance given in blue. Reproduced from Stephenson *et al.*, 2023.

where $k^{\mathrm{IN}}_{j',n\to j}$ $[\mathrm{cm}^3\ \mathrm{s}^{-1}]$ is the reaction rate coefficient for ion-neutral chemical reactions between the ion species j' and the neutral species n, leading to the production of ion species j. Since the production of one ion species through ion-neutral chemistry results in the loss of another, there is an equivalent term in the loss rate ($\mathrm{R}_{\mathrm{j}}^{\prime\mathrm{chem}}$, see Equation 2.25).

The most common ion-neutral reaction type is protonation, which I introduced in Section 1.3.1. The production rate per unit volume of $\mathrm{H_3O^+}$ ions as a result of the protonation of neutral water (Equation 1.2) is given according to Equation 2.22 as:

$$\underbrace{P^{\mathrm{protonation}}_{\mathrm{H_3O^+}}(r)}_{[\mathrm{cm}^{-3}\ \mathrm{s}^{-1}]} = \underbrace{k^{\mathrm{IN}}_{(\mathrm{H_2O^+},\mathrm{H_2O}\to\mathrm{H_3O^+})}}_{[\mathrm{cm}^3\ \mathrm{s}^{-1}]} \cdot \underbrace{n_{\mathrm{H_2O}}(r)}_{[\mathrm{cm}^{-3}]} \cdot \underbrace{n_{\mathrm{H_2O^+}}(r)}_{[\mathrm{cm}^{-3}]} \tag{2.23}$$

The protonation reactions are exothermic - that is, they release an amount of energy given by the difference in the proton affinity of the two neutral species involved. The proton affinities of OH, $\mathrm{H_2O}$ and those cometary neutral species with higher proton affinity than water are given in Table 2.1. These values suggest that the protonation of water (Equation 1.2) would release 2.73 eV of energy. However, it is not entirely clear where this energy ends up. A reasonable assumption is that this energy is split between the neutral and ion products (OH and $\mathrm{H_3O^+}$ for reaction 1.2) in inverse proportion to their masses (Rees, 1989). Experimental

Table 2.1: Proton affinities for some relevant neutral species in the cometary coma (Hunter and Lias, 1998)

	Proton affinity [eV]
OH	6.14
H_2O	7.17
H_2S	7.32
H_2CO	7.40
HCN	7.40
CH_3OH	7.83
NH_3	8.86

studies performed by Lishawa *et al.* (1990) and Vančura and Herman (1991) found no evidence of a kinetic energy boost to the product ion, but the experiments were performed at higher energies than the typical cometary collisions we examine at comet 67P (> 1 eV compared to 0.1 eV). It is therefore likely that any effect of the released energy would fall within the error bars of the experiment. Cometary ionosphere models have typically neglected the extra energy, as they have been limited by their 1D nature (e.g. Vigren and Eriksson, 2017), and it has likewise been neglected in Chapter 4. This will be discussed further in Chapter 5 (Section 5.4).

The neutral species with the highest proton affinity in the cometary environment is NH_3 (see Table 2.1). This means that there is no neutral species that can be protonated by NH_4^+, and the only way for this species to be chemically lost is through dissociative recombination (see Section 2.2.3). The strong presence of NH_4^+ in the cometary ionosphere (Beth *et al.*, 2016, Heritier *et al.*, 2017a, Beth *et al.*, 2020), despite no direct ionisation pathway from the small fraction of NH_3 in the neutral gas, makes it a useful ion species to study the key plasma processes in the coma, and it will be the focus of Chapter 3.

A list of the ion-neutral reaction rate coefficients used for the ionospheric model used in Chapter 3 can be found in the appendix of Heritier *et al.* (2017a) or in Heritier (2018). The rates used in Chapter 4 is a subset of these, and is provided in Appendix A.

2.2.3 Electron-ion dissociative recombination

The other way that an ion of a particular species can be chemically lost is through ion-electron dissociative recombination (often abbreviated to DR herein). This is where an ion and electron join together to produce dissociated neutral molecules, for example,

$$\mathrm{H_2O^+ + e^- \rightarrow O + H_2}. \tag{2.24}$$

At low outgassing (large heliocentric distances) recombination has been found to be too insignificant a process to affect the overall plasma density (Galand *et al.*, 2016). This is due to the low densities of ions and electrons making collisions between them very rare. Closer to perihelion, the collision probability increases and recombination becomes more important (Heritier *et al.*, 2017a).

The recombination rate coefficient α_j^{DR} $[\mathrm{cm^3\ s^{-1}}]$ is dependent on the electron temperature (Rosen *et al.*, 2000). Putting together the loss frequency for ion species j through both ion-neutral chemistry and dissociative recombination, it follows that:

$$R_j(r) = \underbrace{\sum_{n,j' \neq j} k^{\mathrm{IN}}_{j,n \rightarrow j'} n_n(r)}_{\substack{\text{ion-neutral} \\ \text{chemistry}}} + \underbrace{\alpha_j^{\mathrm{DR}}(T_e)\ n_e(r)}_{\substack{\text{dissociative} \\ \text{recombination}}}. \tag{2.25}$$

2.2.4 The 1D case

Since close to the comet, the ions travel radially, the continuity equation (Equation 2.5) for ion species j is frequently solved in 1D, in which the divergence term is reduced to its radial component:

$$\frac{\partial n_j}{\partial t} + \frac{1}{r^2}\frac{\partial}{\partial r}(r^2 n_j u_j) = P_j - R_j n_j. \tag{2.26}$$

This simplified version of the equation allows us to consider some specific cases.

Transport-Ionisation balance

In the case where Rosetta was at large heliocentric distance ($\gtrsim 2$ au and $r \lesssim 80$ km) , the dissociative recombination timescale was slower than that of transport (Beth *et al.*, 2019, Galand *et al.*, 2016), allowing it to be neglected from the model. In addition, since the lower gas density resulted in an optically thin coma (see Section 2.2.1) the photoabsorption is negligible.

Considering the total ion density n_i in this field-free, chemistry-free case, then Equation 2.10 reduces to

$$\frac{1}{r^2}\frac{\partial}{\partial r}(r^2 n_i(r) u_i) = \nu^{\text{ioni}} n_n(r). \tag{2.27}$$

Assuming the ions travel at a constant velocity u_i, a constant total ionisation frequency ν^{ioni}, and the neutral density profile following Equation 2.2, the solution to Equation 2.27 is (Galand *et al.*, 2016, Vigren *et al.*, 2016, Heritier *et al.*, 2017b):

$$n_i(r) = \frac{Q\nu^{ioni}}{4\pi u_i u_n}\frac{r - r_c}{r^2}, \tag{2.28}$$

which is equivalent to Equation 1.5. This result tells us that in the case where $r >> r_c$, where r_c is the radius of the comet surface, then the plasma density should scale as $n_i(r) \propto r^{-1}$. The ion density at 67P was found to follow Equation 2.28 for low outgassing (Galand *et al.*, 2016, Heritier *et al.*, 2017b). When applied to higher outgassing levels, it results in an overestimation near perihelion (Vigren *et al.*, 2019). This can be attributed to the acceleration ions undergo by the ambipolar electric field (see Section 2.3.2) and is the focus of Chapter 4.

With the finite nucleus radius ($r_c \sim 2\,\text{km}$) taken into account in Equation 2.28, we find that the ionospheric density peaks at $r = 2r_c$ (Heritier *et al.*, 2017b). Below this peak the ionisation process has not had time to build up plasma, and it was observed during Rosetta's descent to its final resting place on the comet surface in September 2016 (Heritier *et al.*, 2017b).

Photochemical equilibrium

Another case we can consider is that of photochemical equilibrium, that is, when loss through dissociative recombination is significantly more efficient than that of transport. This was the case within the diamagnetic cavity of 1P/Halley during the Giotto flyby (Balsiger, 1986) where the outgassing ($\sim 7 \times 10^{29}$ s^{-1}) was high (Beth *et al.*, 2019).

In this case, the transport term in Equation 2.26 can be neglected leading to a balance of the ionisation and dissociative recombination terms:

$$\nu^{\text{ioni}} n_n(r) = \alpha_i^{DR} n_e(r) n_i(r). \tag{2.29}$$

Using Equation 2.2 for the neutral density ($n_n(r)$) and the quasi-neutrality of the plasma ($n_e(r) \approx n_i(r)$), we obtain (Cravens, 1987):

$$n_i(r) = \frac{1}{r}\sqrt{\frac{Q\nu^{\text{ioni}}(r)}{4\pi u_n \alpha^{DR}(T_e)}}. \tag{2.30}$$

The plasma density from Equation 2.30 agrees well with observations from Giotto during the flyby of 1P/Halley within the diamagnetic cavity (Rubin *et al.*, 2009, Beth *et al.*, 2019, Cravens, 1987).

SECTION 2.2 KEY POINTS

- The **sources** and **losses** of cometary ions can be expressed as a continuity equation for each species.
- The main source of cometary plasma is the ionisation of the neutral gas, either through **photoionisation** or **electron impact**.
- The sunlight is **attenuated** by the coma when it is **optically thick**, but this is minimal for low outgassing.
- New ion species can be formed through **ion-neutral chemical reaction**s. A key reaction type is **protonation**, which allows H_3O^+, and sometimes NH_4^+, to become the dominant ion species despite not being directly produced by ionisation.
- Plasma can be lost through **ion-electron dissociative recombination**, or through **transport**.
- The relative size of these source and loss terms lead to different ionospheric density profiles.
- In the inner coma of 1P/Halley during the Giotto flyby, the ionisation balanced the ion-electron dissociative recombination, and transport could be neglected - this is **photochemical equilibrium**.
- Transport is more important at 67P. For low outgassing, a balance between the ionisation and transport (neglecting recombination) can explain the plasma density.

2.3 Interaction between a comet and the solar wind

Our discussion has thus far ignored the influence of the wider space environment, considering only the cometary sources of plasma and the interactions between them. In this Section I address the solar wind's influence on the cometary system, starting with the effect of electric and magnetic fields on the single-particle motion of the ions (Section 2.3.1). Section 2.3.2 discusses the ambipolar electric field in more detail, as this is a key driver of the ion dynamics inside the diamagnetic cavity and will be the focus of Chapter 4. In Section 2.3.3 I cover the role of electrons in the comet ionosphere and the different populations based on their origins and energies. Finally, Section 2.4 outlines the types of plasma model that have been used to simulate the comet environment.

2.3.1 Electric fields experienced by the cometary ions

The electric field that arises in a plasma can be determined by rearranging the equation of motion for the electron population. This results in the relation known as the Generalised Ohm's Law (GOL, e.g. Cravens, 2004)

$$\vec{E} = -\vec{u_e} \times \vec{B} - \frac{1}{n_e e}\nabla p_e + \frac{m_e}{e}\vec{g} + \frac{m_e}{e}\sum_{t\neq e}\nu_{e,t}(\vec{u}_e - \vec{u}_t) - \frac{m_e}{e}\left(\frac{\partial \vec{u}_e}{\partial t} + (\vec{u}_e \cdot \nabla)\vec{u}_e\right) \tag{2.31}$$

where $\nu_{e,t}$ is the collision frequency between the electrons and other species t (both ions and neutrals). The gravitational term $\frac{m_e}{e}\vec{g}$ is small and can therefore be neglected.

With multiple ion species j, the mass-averaged velocity $\vec{u}$ can be defined as

$$\vec{u} = \frac{m_e n_e \vec{u_e} + \sum_j m_j n_j \vec{u_j}}{m_e n_e + \sum_j m_j n_j} \approx \vec{u_i}, \tag{2.32}$$

where $\vec{u_i}$ is the total mass-averaged bulk velocity of all the ion species. The current density $\vec{J}$ is then given by

$$\vec{J} = \sum_j e n_j Z_j \vec{u_j} - e n_e \vec{u_e} \tag{2.33}$$

with Z_J the charge number of ion species j. Using Equations 2.32 and 5.18, Equation 2.31 can be re-cast into a useful form

$$\vec{E} = \underbrace{-\vec{u} \times \vec{B}}_{\text{convective field}} + \overbrace{\frac{1}{n_e e}\vec{J} \times \vec{B}}^{\text{Hall term}} - \underbrace{\frac{1}{n_e e}\nabla p_e}_{\text{ambipolar term}} + \overbrace{\eta \vec{J}}^{\text{Ohmic term}} + \underbrace{\frac{m_e}{n_e e^2}\left(\frac{\partial \vec{J}}{\partial t} + \nabla \cdot (\vec{J}\vec{u} + \vec{u}\vec{J})\right)}_{\text{electron inertial term}} \quad (2.34)$$

where the Ohmic resistivity $\eta = (m_e \nu_e)/(n_e e^2)$, with ν_e the total electron momentum transfer collision frequency for all the ion and neutral species.

In a cometary context, the Ohmic and electron inertial terms are small compared to the others and can be neglected (Deca *et al.*, 2019). Inside the diamagnetic cavity, which appears close to the nucleus at high activity, there is a negligible magnetic field, thus only the ambipolar electric field term is relevant. Outside the diamagnetic cavity at high activity, and everywhere in the comet-solar wind interaction at lower outgassing, all three electric field terms need to be taken into account. In the following sections, the meaning and contribution of the motional, Hall and ambipolar electric fields are discussed (Section 2.3.1, 2.3.2 and 2.3.1, respectively).

Convective electric field

Sometimes called the motional electric field, the convective electric field ($\vec{E}_{\text{conv}}$) is associated with the motion of the solar wind in the comet reference frame. In the solar wind frame, this term in the GOL disappears following the Lorentz transformation:

$$\vec{E'} = \vec{E_{\text{conv}}} + \vec{u_{\text{SW}}} \times \vec{B_{\text{IMF}}} = \vec{0}. \quad (2.35)$$

Therefore while the solar wind particles do not experience this field directly, the cometary plasma is accelerated by it when it encounters the solar wind (see Figure 2.6). Since the newly produced cometary ions move slowly compared to the unaffected solar wind upstream of the comet (~ 1 km s^{-1} compared to $\sim 400 - 600$ km s^{-1}), the relative velocity is approximately the solar wind velocity $\vec{u}_{\text{sw}}$, and the cometary ions are subject to the electric field

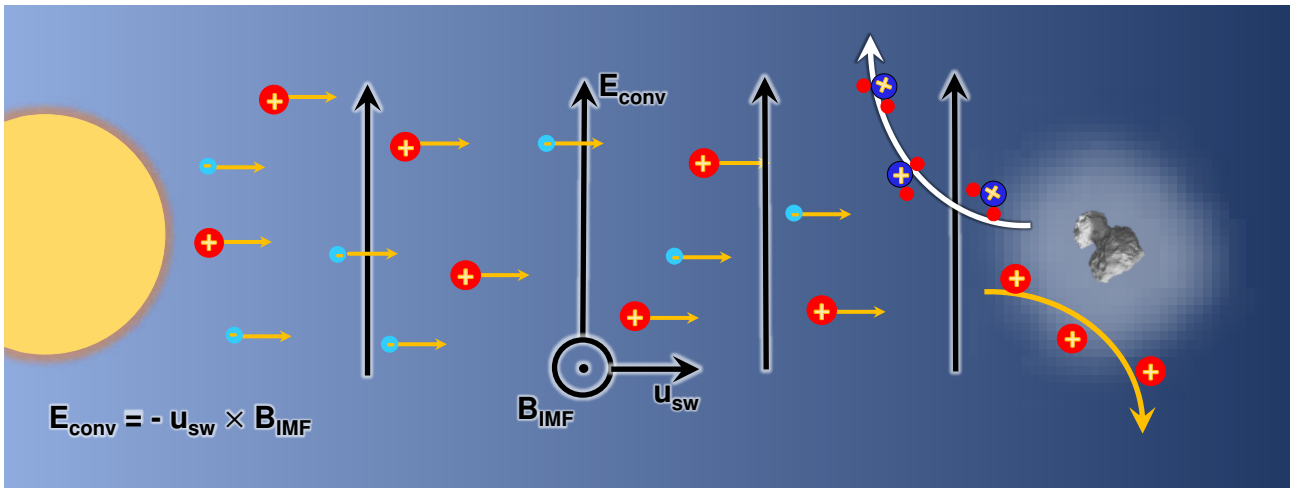

Figure 2.6: Schematic showing how solar wind creates a motional (convective) electric field and its impact on the cometary ions (shown as H_2O^+ ions). Red and light blue circles show the solar wind ions and electrons, respectively. Dark blue shows pick-up ions of cometary origin, initially travelling anti-cometward.

$$\vec{E}_{\rm conv} = -\vec{u}_{\rm SW} \times \vec{B}_{\rm IMF}. \tag{2.36}$$

The heavy cometary ions are accelerated along this electric field, as well as experiencing the IMF, and their motion gains an anti-sunward component (Nilsson *et al.*, 2015, Behar *et al.*, 2016). As the solar wind becomes mass-loaded with cometary ions, momentum is conserved by a slowing down of the solar wind ions and a deflection away from the comet-Sun line. Therefore the solar wind experiences the effect of the motional electric field indirectly.

Hall electric field

The Hall term in the GOL (Eq. 2.34) accounts for the current generated by the different electron and ion motion when the scale of the ion gyroradius is approached.

Polarisation electric field

Rather confusingly, the term 'polarisation electric field' is often used in a cometary plasma context to refer to the Hall effect arising from the different ion and electron trajectories (Nilsson *et al.*, 2018). In much of the general literature on space physics, 'polarisation field' is instead used to refer to the ambipolar term in Equation 2.34 (e.g. Cravens, 2004), but for

clarity we will stay in line with the cometary terminology in this thesis.

To understand where the polarisation field comes from, we must first consider the motion of charged particles in uniform electric and magnetic fields. In the solar wind context, these fields can represent the motional electric field (see Section 2.3.1) and interplanetary magnetic field, respectively. In the absence of any other external forces, the equation of motion is

$$m\frac{d\vec{v}}{dt} = q(\vec{v} \times \vec{B} + \vec{E}). \tag{2.37}$$

The velocity $\vec{v}$ of the charged particles can be decomposed into 3 parts: $\vec{v}_{\parallel}$ parallel to the magnetic field, a drift velocity $\vec{v}_d$ perpendicular to the magnetic field, and a time-varying gyration $\vec{v}_{\perp}(t)$. Considering only the drift component, Equation 2.37 reduces to

$$\vec{E} = -\vec{v_d} \times \vec{B}. \tag{2.38}$$

Taking the cross product with $\vec{B}$ to each side gives

$$\vec{E} \times \vec{B} = -(\vec{v_d} \times \vec{B}) \times \vec{B} \tag{2.39}$$

$$= (\vec{B} \cdot \vec{B})\vec{v_d} - (\vec{B} \cdot \vec{v_d})\vec{B} \tag{2.40}$$

$$= B^2\vec{v_d}. \tag{2.41}$$

The resulting drift velocity is then given by

$$\vec{v}_d = \frac{\vec{E} \times \vec{B}}{B^2}, \tag{2.42}$$

independent of the charges and therefore the same for both ions and electrons. However, the gyromotion does vary for each species, since the Larmour radius

$$r_L = \frac{mv_{\perp}}{|q||B|} \tag{2.43}$$

depends on the particle mass and the sense of the gyration depends on the particle charge. On scales much larger than the ion gyroradius, this difference in the particle trajectories can

be safely ignored. However this is frequently not the case in the cometary environment. For example Simon Wedlund *et al.* (2017) estimated the gyroradius of cometary ions at 1.3 au for comet 67P to be $(1.5 - 2) \times 10^4$ km, which is clearly significant when compared to the bow shock standoff distance of around 7×10^3 km. This means that, in this environment, the ions effectively move in the direction of the convective electric field of the solar wind, whereas the electrons experience an $\vec{E} \times \vec{B}$ drift. A similar situation arises at other unmagnetised bodies, such as Mars (Kallio and Jarvinen, 2012). This difference in the way the solar wind impacts the cometary ions and electrons sets up a charge separation, leading to the formation of the polarisation electric field (Nilsson *et al.*, 2018). This is illustrated, alongside the ambipolar and convective field components, in Figure 2.7.

2.3.2 Origin and impact of the ambipolar electric field

The ambipolar electric field term in the Generalised Ohm's Law (Equation 2.31),

$$\vec{E}_{\mathrm{amb}} = -\frac{1}{n_e e} \nabla p_e, \tag{2.44}$$

represents the response of the plasma to gradients in the electron pressure. These gradients set up a charge imbalance, counteracted by the ambipolar electric field to maintain quasi-neutrality on scales larger than the Debye length (see Figure 2.7). At planets, the charge imbalance can arise owing to the difference in the gravitational forces acting on electrons and ions (Collinson *et al.*, 2019). At comets, the gravitational force on individual particles is negligible, but an electron pressure gradient is still set up due to the difference in energy between the ions and electrons produced during photoionisation. The newly produced ions are relatively unchanged from the neutral outflow speed, leaving the photoelectron to absorb most of the excess energy from the ionisation process (this would be the incident solar photon energy - 12.6 eV for water). This gives the electrons higher kinetic energy than the ions, hence a outwardly-pointing radial electric field acts to maintain quasi-neutrality by restraining the electrons and accelerating the ions.

If the outgassing is high enough, electrons are efficiently cooled by collisions with the

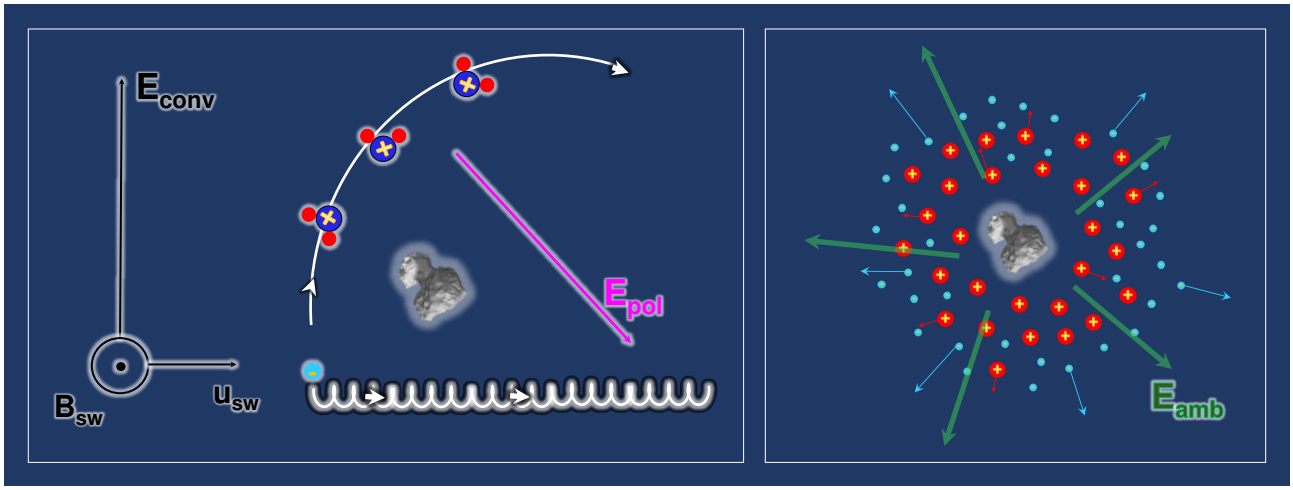

Figure 2.7: **(Left)** Diagram showing the different $\vec{E} \times \vec{B}$ drift motions of ions and electrons. (**right**) Schematic showing the direction of the ambipolar electric field (**green arrows**) to counteract the charge imbalance created by the different energies of the cometary ions (**red**) and photoelectrons (**blue**).

neutral molecules in the coma and this is enough to maintain quasi-neutrality without the need for an ambipolar electric field. It is likely to have been the case for comet 1P/Halley during the 1986 Giotto flyby, as demonstrated in Gan and Cravens (1990). However, the outgassing of comet 67P during the Rosetta mission was considerably lower than that of 1P/Halley during Giotto ($10^{26}-10^{28}$ s^{-1} compared to 10^{29} s^{-1}) and consequently the ambipolar electric field has a tangible impact on the cometary environment. One such impact is to keep cometary electrons 'trapped' in a region close to the nucleus (e.g. Deca *et al.*, 2017, Stephenson *et al.*, 2022), thereby increasing the efficiency of electron-neutral collisions and leading to a cold electron population (< 0.1 eV) observed by RPC–LAP and MIP (e.g. Eriksson *et al.*, 2017, Engelhardt *et al.*, 2018, Gilet *et al.*, 2020, Wattieaux *et al.*, 2020). In addition, solar wind electrons were found to have been accelerated towards the nucleus by such a field, detected as a suprathermal electron population (Madanian *et al.*, 2016a) and responsible for most of the ionisation (Stephenson *et al.*, 2023) and for generating aurora (Galand *et al.*, 2020, Stephenson *et al.*, 2021).

Determining the magnitude and functional form of the ambipolar electric field at a comet is not straightforward. At planets, the field acts against the difference in gravitational forces experienced by the ions and electrons, and can be determined analytically (this is the Pannekoek-Rosseland electric field, e.g. Rosseland, 1924), but cometary ionospheres

are not gravitationally bound. One way to constrain the field is to model how the total ion density might be influenced by varying electric field profiles. The modelling of this is the basis of Chapter 4, but at this point it is relevant to discuss the theoretical arguments for two functional forms of the electric field which have been proposed.

Vigren *et al.* (2015) derived an expression for the radial electric field ($\vec{E} = E(r)\,\vec{\hat{r}}$) by first enforcing $n_e \approx n_i \propto 1/r$. This arises from a field-free and chemistry-free model of the coma (Equation 1.5) , with a pure H_2O coma and the comet as a point source. T_e is also assumed to be constant. Under these assumptions, Equation 2.44 is reduced to

$$E(r) = -\frac{1}{qn_e(r)}\frac{dp_e(r)}{dr} = -\frac{k_B T_e}{qn_e(r)}\frac{d(n_e(r))}{dr} = \frac{k_B T_e}{qr}, \tag{2.45}$$

such that $E \propto 1/r$.

An argument can also be made for a $1/r^2$ dependence of the electric field by enforcing neutrality of the plasma (Beth and Galand, 2017) . Gauss's law under spherical symmetry gives

$$\frac{1}{r^2}\frac{d(E(r)r^2)}{dr} = \frac{n_i - n_e}{\epsilon_0} \tag{2.46}$$

which, assuming neutrality ($n_i = n_e$) leads to

$$E(r) = E(r_c)\frac{r_c^2}{r^2} \tag{2.47}$$

where $E(r_c)$ is the electric field strength at the comet surface. Beth and Galand (2017) derived an analytical model of the ion density for general electric field profiles $1/r^m$, arguing that $m > 1$ is required to avoid an unbounded potential at the surface. Both $1/r$ and $1/r^2$ profiles are modelled in Chapter 4.

2.3.3 Electron populations

Since quasi-neutrality holds in a plasma ($n_e \approx n_i$), the contribution of electrons is significant when it comes to ionospheric properties and dynamics. At a comet, they can be broadly

classified into three groups according to their temperature, which assists in identifying the predominant sources. The three populations of electrons can be categorised as follows:

- *Newly born, warm electrons* (5-15 eV) are those produced directly through photoionisation of the cometary neutrals, or as secondary electrons produced during electron-impact ionisation. Near perihelion, photoionisation is the primary source of warm electrons (Heritier, 2018), whereas at lower heliocentric distances, warm electrons have more likely been heated by accelerated solar wind electrons (Stephenson *et al.*, 2023).

  Since the excess energy after photoionisation (see Section 2.2.1) is $E_{h\nu} - E_{\text{ioni}}$ (where $E_{h\nu}$ is the photon energy and E_{ioni} is the ionisation energy of the neutral), the average energy of the photoelectrons depends on the incoming solar flux as well as the neutral composition. The dominant neutral species at 67P near perihelion is water, which has an ionisation energy of 12.5 eV, and in an optically thin coma (negligible attenuation of the solar flux due to photoabsorption, Section 2.2.1) this leads to photoelectrons of ~ 10 eV on average (Huebner *et al.*, 1992, Vigren and Galand, 2013). Those electrons released by electron-impact ionisation are also around $10\ \mathrm{eV}$ on average (Galand *et al.*, 2016).

- *Cold electrons* ($\lesssim 1$ eV) are those which have been cooled through collisions with neutrals. The cold electron population becomes more significant with increasing outgassing activity as the probability of collision increases (Eriksson *et al.*, 2017, Engelhardt *et al.*, 2018, Gilet *et al.*, 2020). Odelstad *et al.* (2018) found that they are more consistently present and in larger numbers within the diamagnetic cavity (Section 1.3.2).

  Engelhardt *et al.* (2018) observed cold electrons at large heliocentric distances ($\gtrsim 3.5$ au), when no electron exobase was expected to form. The location of the electron exobase is typically defined as the scale height at which the distance from the surface of the comet is equal to the mean free path of the electrons, assuming a radial expansion. The observation of cold electrons outside of the region delimited by the exobase suggests that more electron-neutral collisions are taking place than would be expected for radially expanding electrons. This has been attributed to electron trapping by a potential well

around the nucleus, due to an ambipolar electric field. The ambipolar field is set up to ensure quasi-neutrality, attracting the electrons back towards the nucleus since their higher energies (therefore faster speeds) compared to the ions would cause a density gradient, and therefore a charge separation (Deca *et al.*, 2017). This trapping increases the path of electrons in the inner coma, allowing them to undergo more collisions with neutrals and to cool more effectively, as has now been shown through collision test-particle modelling (Stephenson *et al.*, 2022, Stephenson *et al.*, 2024). The ambipolar electric field is discussed in more detail in Section 2.3.2.

- *Suprathermal electrons* (> 15 eV) are so called because their energies are $> k_{\mathrm{B}}T_e$ where T_e is the mean temperature of the whole population. They are responsible for electron-impact ionisation (Galand *et al.*, 2016, Heritier, 2018) and Far UltraViolet (FUV) auroral emissions observed by the UV spectrograph Alice (Galand *et al.*, 2020, Stephenson *et al.*, 2021). Particle-in-cell (PiC) modelling (Deca *et al.*, 2017) has shown that for low outgassing comets these energetic electrons originate in the solar wind and are accelerated by the ambipolar field (Stephenson *et al.*, 2023).

The relative contribution of these three electron populations to the 'bulk electron temperature' depends on the outgassing, cometocentric distance, ionisation rate and electromagnetic field influences. For this reason, the electron temperature is very difficult to model and they do not follow a straightforward Maxwellian distribution. The radial profile of electron temperature is a key unknown and this is a particular problem for the determination of the ambipolar electric field (see Equation 2.44). In Section 2.4, I will discuss the different modelling approaches and the extent to which they are able to address this issue.

SECTION 2.3 KEY POINTS

- Cometary ions are accelerated along the **motional electric field** of the solar wind. To conserve momentum, the solar wind is slowed down and deflected. This effect is called **mass loading**.
- When the outgassing is high enough, the solar wind can be prevented from reaching the cometary nucleus, leaving a magnetic field free **diamagnetic cavity**.
- Inside the diamagnetic cavity, the only electric field term present in the Generalised Ohm's Law is the **ambipolar electric field** - set up by a gradient in the electron pressure.
- Rosetta observed a consistent population of **collisionally cooled electrons**.

2.4 Modelling approaches

As demonstrated in this chapter, the cometary plasma environment represents a complex and variable system that is influenced by interactions between the cometary and solar wind plasma populations. It is therefore valuable to complement the context-dependent data obtained by Rosetta and Giotto with models and simulations to explore the underlying physical processes. This section explores the various modelling techniques used to study cometary plasma, including magnetohydrodynamic (MHD, Section 2.4.1), kinetic (Section 2.4.2), and hybrid simulations (Section 2.4.3) highlighting their strengths, limitations, and regimes of applicability.

2.4.1 MHD

Magnetohydrodynamic (MHD) models take a fluid approach to plasma modelling. They are based on the assumption that the plasma is a single or multi fluid, with the ions and electrons moving together. The MHD equations (continuity, momentum, energy, and induction) are derived from the hydrodynamic equations of motion and Maxwell's equations, and are a set of coupled partial differential equations that describe the behaviour of the plasma. They are

solved on a grid, and the plasma is treated as a fluid that flows through the grid. A simplified version of the Generalised Ohm's law (Equation 2.31) is solved to determine the electric fields (just the convective term, in the case of ideal MHD).

MHD models are able to capture the large-scale behaviour of the plasma, and are used to study phenomena such as the solar wind, the Earth's magnetosphere, and the plasma environment around other planets. In application to cometary plasma, MHD has been used to study 1P/Halley during the flyby of the Giotto spacecraft in 1986 (e.g. Gombosi *et al.*, 1996, Benna and Mahaffy, 2007, Rubin *et al.*, 2014a). They are particularly useful for studying the interaction between the solar wind and cometary plasma. However, the small-scale behaviour of the plasma cannot be captured, since individual particles in the plasma are not resolved. This means that MHD models are not able to capture the effects of collisions between particles, or the effects of the electric and magnetic fields on individual particles. At lower outgassing comets such as 67P, these kinetic effects and collisions are more important than at Halley and cannot be neglected. This environment requires a more complex kinetic or hybrid approach.

2.4.2 Kinetic

Treating the effects of individual particle trajectories requires a kinetic approach to plasma modelling, and a common type of kinetic model is Particle-in-Cell (PiC). These do not enforce quasi-neutrality, instead deriving the electric and magnetic fields from the individual motions of electrons and ions, but this adds a new level of computational expense to the simulations. In order for the small gyro-period of the electrons to be resolved, the time step needs to be very short. It is common to artificially increase the electron-proton mass ratio in order to mitigate the issue.

A collisionless and fully kinetic model of the cometary plasma environment is described in Deca *et al.* (2017). This model self-consistently calculates the fields by treating the cometary and solar wind ions and electrons separately. The Generalised Ohm's law (Equation 2.31) is not enforced in the PiC model, and the self-consistently calculated fields have been used to assess the importance of its terms in Deca *et al.* (2019). Such analysis shows that the ambipolar

(Section 2.3.2) and Hall (Section 2.3.1) electric fields are important in shaping the trajectories of the cometary particles at the outgassing level of 67P.

A key shortcoming of the kinetic modelling applied so far to comets is the lack of collisional processes. Such collisional processes are clearly important in order to accurately describe the electron dynamics, as shown by the model of Stephenson *et al.* (2022), which does include electron-neutral collisions, in a test-particle approach. This method treats the electrons kinetically as they respond to a fixed background of electric and magnetic fields (supplied by the Deca *et al.* (2017) PiC model), therefore there is no direct feedback. This modelling showed that the cold electrons (see Section 2.3.3) observed at low outgassing can be explained by cooling through electron-neutral collisions, the rate of which is increased by trapping in the ambipolar potential well (Stephenson *et al.*, 2024). This test-particle model is revisited in Chapter 5, and adapted to model the cometary ion population.

The full kinetic and self-consistent treatment of collisions is computationally expensive, and has not yet been applied to cometary plasmas. Such a model would be able to capture the full range of electron and ion dynamics, and would likely go a long way to answering the remaining unanswered questions about the cometary ionosphere. In the meantime, a hybrid approach is a good compromise between the fluid and kinetic models.

2.4.3 Hybrid

In a hybrid simulation, the ions are treated kinetically and the electrons are treated as a fluid that moves in response to them, satisfying quasi-neutrality. This allows more dynamics to be captured than in the MHD case, but is less computationally expensive than a full kinetic model.

Puhl-Quinn and Cravens (1995) used a 1D hybrid model to demonstrate the kinetic ion effects present at the diamagnetic cavity boundary. Gyration of the cometary ions travelling out of the diamagnetic cavity and into the magnetised region stagnates the ion flow at the boundary and leads to enhanced recombination in this layer as observed by Giotto (Goldstein *et al.*, 1989).

For 67P, hybrid modelling has been used to study various ion phenomena. The ion pick-up

process (Section 2.3.1) is much more accurately modelled when the gyration of the ions is taken into account (Rubin *et al.*, 2014b). This allows the bow shock formation to be studied in more depth than with an MHD model (e.g. Koenders *et al.*, 2015, Gunell *et al.*, 2018, Alho *et al.*, 2019). The importance of charge exchange for these processes has also been highlighted (Simon Wedlund *et al.*, 2017, Simon Wedlund *et al.*, 2019).

These models have improved upon the capabilities of the MHD approach, but they still fail to capture the electron behaviour and the importance of electron collisions. Hybrid simulations will be discussed further in Chapter 5.

SECTION 2.4 KEY POINTS

- Different types of plasma simulation are applicable for different cometary outgassing rates - there is no 'one size fits all' approach.
- Magnetohydrodynamic (**MHD**) models treat the ions and electrons as magnetised fluids, work best for high outgassing comets such as 1P/Halley ($Q = 5 \times 10^{29}$ s^{-1}).
- **Kinetic** models treat the ions and electrons both as populations of particles, allowing their kinetic-scale behaviour such as gyro-motion to be studied. These simulations are very computationally expensive, especially if collisions are included.
- **Hybrid** models treat the ions as kinetic particles and the electrons as a neutralising fluid. They capture more ion dynamics than possible with MHD, but are less expensive than kinetic models.
- Both hybrid and kinetic models have been used to study weakly outgassing comets, such as 67P.

CHAPTER 3

ORIGIN AND TRENDS IN HIGH PROTON AFFINITY ION SPECIES

The high mass resolution of the ROSINA-DFMS instrument led to the detection of a wide and complex ion chemistry in the cometary environment (see Sections 1.2.1, 2.2). Of particular interest for ion dynamics is the presence of protonated high proton affinity (HPA) ion species. In order to form these ions, multiple ion-neutral chemical reactions need to occur, which is not possible without a sufficiently collisional coma. If the ions escape from the nucleus surface too quickly, the timescale for collisions becomes longer than the transport timescale, preventing new ion species from forming. Therefore, it is relevant to understand the complexity of the cometary ion environment and the factors that drive it, as it places an upper limit on the ion bulk velocity and constrain the ion acceleration processes.

In this chapter, I explore the variation in the detection of protonated high proton affinity ion species over the escort phase, and in the diamagnetic cavity near perihelion. The goal of this study is to confirm the source of NH_4^+ in the coma, and to understand what factors drive its abundance. I do this by exploiting the DFMS High Resolution ion mode dataset in depth over the 2-year escort phase of Rosetta. The majority of this chapter is taken from Lewis *et al.* (2023).

3.1 Interpretation of ion mass spectrometer data from DFMS

Ion mass spectrometer data used in this study are from ROSINA-DFMS (Balsiger *et al.*, 2007), described in detail in Section 1.2.1. Both the high and low resolution ion modes were used, though the HR mode is required to separate NH_4^+ from H_2O^+ (Beth *et al.*, 2016), since they both appear at 18 *m/z*, as illustrated in Figure 3.1.

The DFMS counts cannot be simply converted into ion number densities since the sensitivity of the instrument depends on other factors, such as the spacecraft potential and instrument field of view orientation with respect to the nadir direction (Schlaeppi, 2011). For this reason, I derived an empirical count sum as a proxy for the real ion densities and to determine whether or not the ion species has been detected for a given scan.

The process to derive these count sums is as follows. First, the counts were summed over a 0.02 *m/z* range away from where any mass peaks are expected ($17.94 - 17.96$ *m/z* for 18 *m/z*) to find a background count level. This level is then compared to the counts summed over a ± 0.01*m/z* window at the expected peak location (e.g. 18.03383 *m/z* for NH_4^+). The background is generally very low in HR mode at the lower mass/charge ratios (typically 2–6 counts at 18 *m/z*) but increases significantly at higher mass/charge ratios.

The DFMS dataset includes spectra from both channels of the instrument, A and B (see Section 1.2.1). Both channels should be materially identical, but in some cases one channel exhibited a much stronger peak than the other. Those spectra which had a $> 50\%$ difference in the count sums were disregarded. Otherwise, if the count sum at the peak was 5 times higher than the background level in both channels, I considered the ion species to be detected. Figure 3.2 summarises the variation in count sums between the two channels across the entire dataset, highlighting the spectra that have been removed due to low counts compared to the background (red) and to inconsistency between the two channels (light blue). Where count sums are referred to in the rest of this thesis, it refers to the peak count sum with the background subtracted. The count sums from channels A and B are added together, unless specified otherwise.

A rough estimate for the threshold ion density required for detection can be derived by

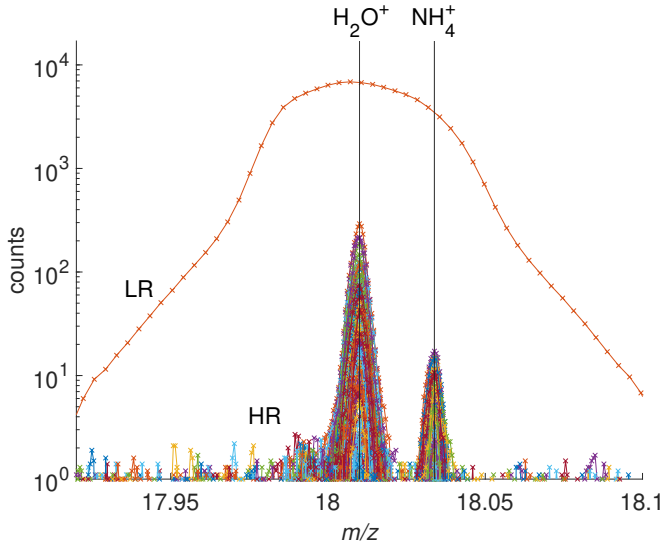

Figure 3.1: DFMS mass spectra from July 2015 (channel A), from the high resolution (HR) and low resolution (LR) demonstrating the separation of H_2O^+ and NH_4^+ in the high resolution mode. Credit: Lewis *et al.* (2023).

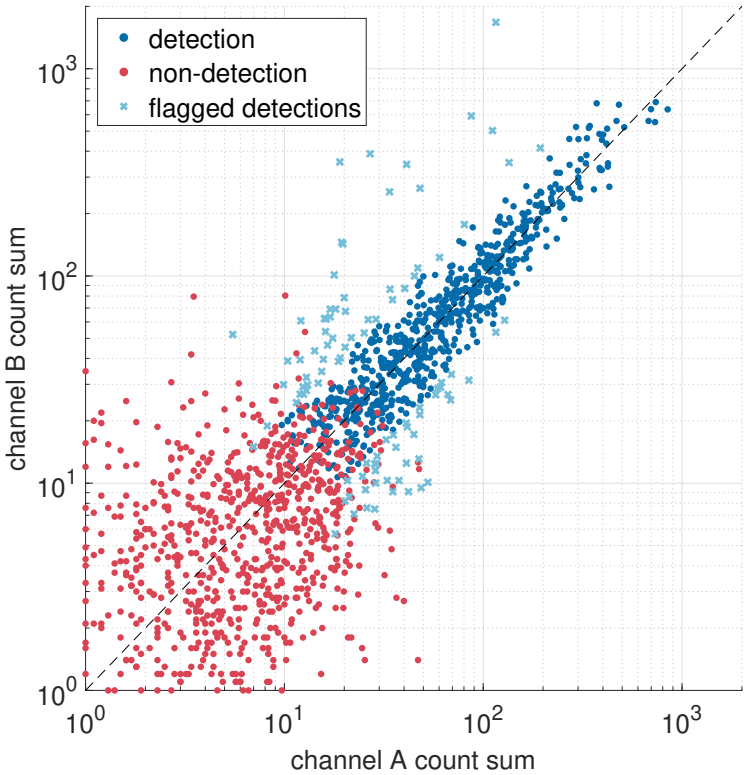

Figure 3.2: Count sums over the NH_4^+ peak from the two channels of DFMS (A and B), where red dots correspond to non-detections of the ion species and blue dots show identified detections. The light blue crosses show where detections have been discounted due to large ($> 50\%$) difference between the count sums from the two channels. Credit: Lewis *et al.* (2023).

considering the current of ions impinging on the instrument:

$$I_{\mathrm{coma}} = \frac{I_{det}}{S_i}, \tag{3.1}$$

where I_{coma} is the current of ions of a given mass, I_{det} is the current reaching the detector, and S_i is the sensitivity of DFMS to the ion species, i. The current generated by one ion impacting at the detector during the integration time dt (20 seconds) is given by

$$I_{det} = \frac{q}{dt} = \frac{1.6 \times 10^{-19}\mathrm{C}}{20\mathrm{s}} \approx 1 \times 10^{-20}\mathrm{A}. \tag{3.2}$$

Combining it with a typical sensitivity for 5 eV ions of $^{20}\mathrm{Ne}^{+}$ (of mass close to that of NH_4^+; Schlaeppi 2011), $S_i \approx 5 \times 10^{-4}$, gives the current from the coma: $I_{\mathrm{coma}} = nvqD \approx 2 \times 10^{-17}\mathrm{A}$, where n is the ion number density of the species of interest (here, NH_4^+), v is its bulk velocity and D is the collecting cross section of DFMS ($25.8\ \mathrm{mm}^2$, Balsiger *et al.*, 2007). As the bulk velocity of ions at 5 eV is:

$$v = \sqrt{\frac{2E}{m}} \approx \sqrt{\frac{2 \times 5\mathrm{eV}}{20u}} \approx 7\mathrm{km/s}, \tag{3.3}$$

the ion density is given by:

$$n = \frac{I_{\mathrm{coma}}}{vqD} \approx \frac{2 \times 10^{-17}\mathrm{A}}{7\mathrm{km/s} \times 1.6 \times 10^{-19}\mathrm{C} \times 25.8\mathrm{mm}^2} \approx 0.001\mathrm{cm}^{-3}. \tag{3.4}$$

As we require a count sum (counts summed $\pm 0.01 m/z$ on either side of the peak) of around 50 for a detection (see Figure 3.2), this corresponds to a minimum density of $0.05\ \mathrm{cm}^{-3}$.

Once the detections have been confirmed or ruled out from the individual DFMS scans, it is useful to use the occurrence frequency over multiple scans as given in Equation 1.4.

3.1.1 Spacecraft potential

When a spacecraft travels through a plasma, charged particles impact on the spacecraft surface and the incoming and outgoing currents need to balance in accordance with Kirchoff's current law. This leads to the spacecraft charging like a capacitor, and gaining a potential.

The spacecraft potential of Rosetta was usually negative, and only positive when either at a large cometocentric distance from the comet (for example during the excursion in March 2016), or when 67P was at a large heliocentric distances (Odelstad *et al.*, 2017). Highly negative spacecraft potentials are attributed to a large density of warm electrons, so it largely scales with the neutral density. However, within the diamagnetic cavity, the number density of cold electrons is higher than outside the cavity therefore the spacecraft potential is typically less negative in this region, as shown by combining observations from RPC–LAP and RPC–MAG (Odelstad *et al.*, 2018).

The less negative values of the spacecraft potential within the diamagnetic cavity present a challenge for understanding the ion composition in the cavity with ROSINA-DFMS. The negative potential accelerates ions towards the detector, which may push them out of the energy acceptance range (Heritier *et al.*, 2017a). This effect has a larger impact on heavier ions than it does on light ones, thereby altering their relative contributions to the overall ion composition as measured by DFMS, and affecting the validity of comparison between inside and outside the cavity.

Fully accounting for the spacecraft potential in the analysis of the DFMS data is difficult, and would require detailed modelling such as that performed for RPC–ICA by Bergman *et al.* (2020). Instead, I include qualitative 'checks' that the trends in $\mathrm{NH_4^+}$ cannot be purely explained by the spacecraft potential.

3.1.2 Spacecraft manoeuvres

Manoeuvres of the spacecraft may affect the DFMS ion data in multiple ways. Firstly, contamination by the propellant gas monomethylhydrazine ($\mathrm{CH_3NHNH_2}$, Schläppi *et al.*, 2010) from the spacecraft exhaust can result in false positive detections of $\mathrm{NH_4^+}$ (Beth *et al.*, 2016). This fuel is released during a wheel offloading manoeuvre, i.e. when the thrusters are fired to decelerate the reaction wheels. To mitigate the majority of this effect on the dataset used in this study, DFMS ion mode scans taken within 1 hour after a wheel offloading manoeuvre were flagged and subsequently removed.

During a spacecraft manoeuvre or rotation, the comet nucleus can move out of the field of

view of the instrument, leading to anomalous non-detection or unusually low counts from ion species that are in fact present in the cometary material. To account for this, I disregarded ion mode scans for which the field of view of DFMS is off nadir (nadir direction $< 10^{\circ}$ from the centre of the 20° field of view of DFMS).

3.1.3 Ammonium salts from dust grains: an alternative source of NH_4^+?

Aside from protonation of NH_3, which is the dominant pathway to NH_4^+ via ion-neutral chemistry 2.2.2, another possible source of NH_4^+ is the dissociation of ammonium salts embedded in dust grains (predominantly $NH_4^+SH^-$, but a host of others have been detected, Altwegg *et al.*, 2020). The exact mechanism by which the ammonium salts could directly lead to the formation of NH_4^+ is uncertain, but it is possible they could dissociate into a cation-anion pair either directly following sublimation or electron impact. In the case of measurements at comet 67P, this could either occur in the coma or inside the DFMS instrument itself (Hänni *et al.*, 2019). In both cases electric fields may be involved in separating the two. Dissociation into neutral NH_3 and H_2S is, however, more likely, and happens either during or after sublimation of the salt. The salts were identified from the detection of NH_3 peaks coinciding with H_2S peaks in the neutral mode of DFMS (Altwegg *et al.*, 2022) above the background coma level, thus it is not possible to directly relate them to individual detections of NH_4^+ in ion mode, which could not be operated at the same time. Detections of ammonium salts are also biased towards lower outgassing where there can be a clearer signal above the background. If sublimation of salts into cation and anion pairs was an important process, we would expect to see anions detected by IES, which is not the case, though they could be repelled by the negative spacecraft potential. A dust source for NH_4^+ can therefore not be excluded *a priori*. One of the goals of this study is to confirm whether the ion-neutral chemistry is the main contributor to NH_4^+ compared with the possible dust origin.

3.2 High Proton Affinity species across the escort phase

Using the methods discussed in Section 3.1, the occurrence frequency (Equation 1.4) could be assessed across the entire escort phase. Figure 3.3 summarises this analysis for the key ion species NH_4^+ and H_3O^+, along with those of other HPA species. The total counts over the NH_4^+ mass peaks are also displayed. Generally, the occurrence of NH_4^+ correlates with the local outgassing rate (Q). It reaches a peak in August 2015, when 67P was near perihelion. The increased outgassing results in a denser coma, leading to more frequent chemical reactions and richer ion chemistry with multiple protonated HPA species. Figure 3.3b depicts the detection of three other protonated HPA species: H_2COH^+, $CH_3OH_2^+$, and H_3S^+. H_2COH^+ and $CH_3OH_2^+$ require examination in the High Resolution mode of DFMS to distinguish them from other ions with the same mass-to-charge ratio (Beth *et al.*, 2020, Heritier *et al.*, 2017a). H_3S^+ is the only ion species at 35 *m/z*, allowing the use of the low resolution mode to benefit from its higher sensitivity. These ion species are primarily detected around perihelion in July, August, and September 2015, indicating more complex ion-neutral chemistry during this period (see Section 3.4.2). Figure 3.3c shows the mean count sum for NH_4^+ for each month, with the error bar showing the standard deviation. The count sums are highly variable, but in general they exhibit the same pattern as the detections in Figure 3.3a; the strongest signals appear around perihelion (July–September 2015).

An exception to the pattern of NH_4^+ occurrence frequency and mean count sum is observed in March 2015, which shows significantly higher values than expected for this period and heliocentric distance (2 au). HR ion mode data for this month is available for March 3rd, 4th, and 7th. After excluding detections potentially influenced by spacecraft outgassing, most remaining detections occur on March 3rd. As can be seen in Figure 3.3c, however, there was a significant discrepancy between channels A and B on this days. The high counts on this day remain unexplained, but will be discussed further in Section 3.5.

Figure 3.4 presents the NH_4^+ count sum relative to local outgassing, colour-coded by time throughout the mission. There is no clear correlation below $2 \times 10^{27} s^{-1}$. Above this threshold, the count sum generally increases with local outgassing. This indicates that around

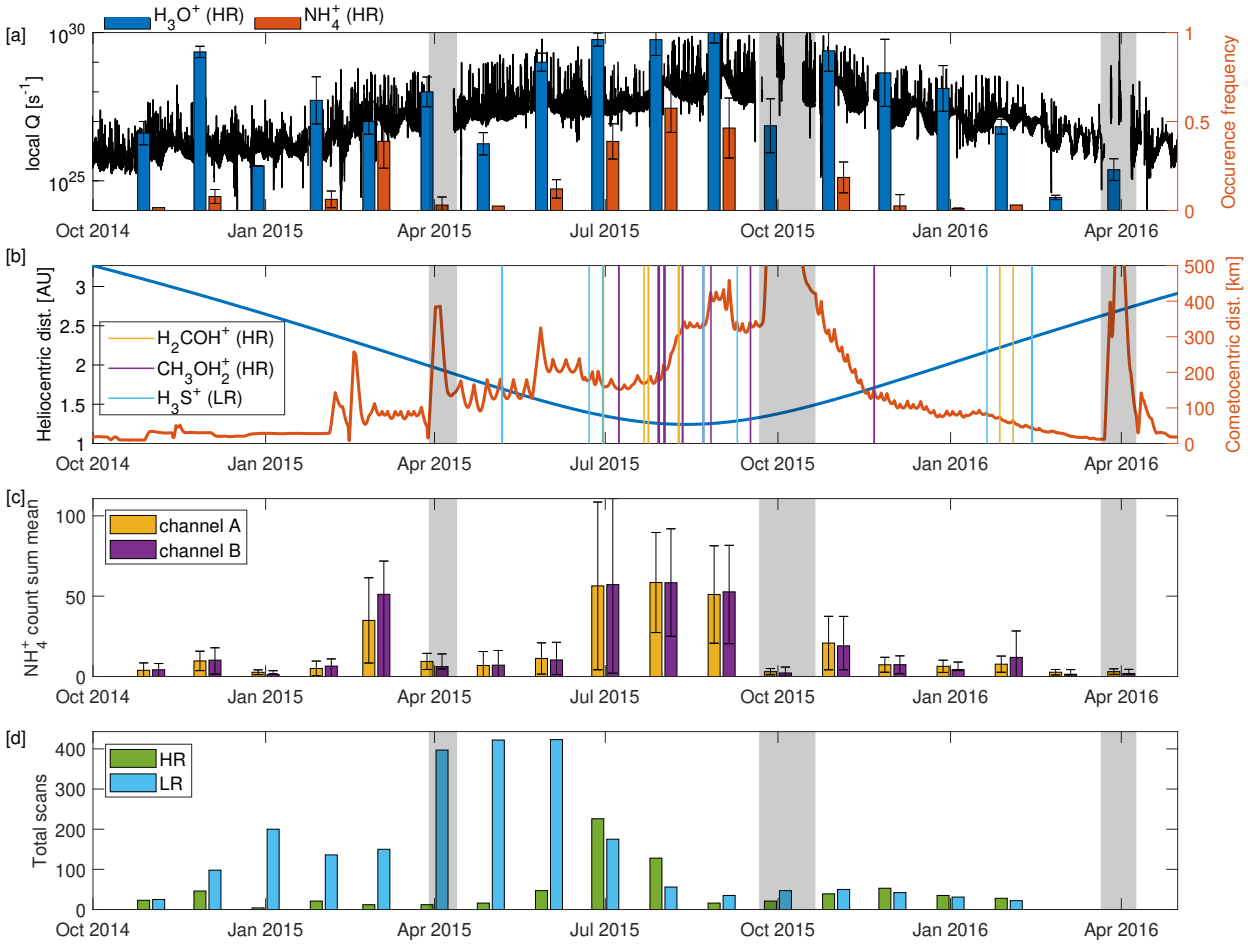

Figure 3.3: (**a**) Normalised occurrence frequency of H_3O^+ and NH_4^+ detections by ROSINA-DFMS per month during the escort phase, with local outgassing estimate from ROSINA-COPS. Error bars show the variation in the occurrence frequency as the detection threshold is altered. (**b**) Heliocentric (**black**) and cometocentric (**orange**) distance, during the escort phase with vertical lines representing the detection of three high proton affinity ions by ROSINA-DFMS. (**c**) Mean of the counts sum for NH_4^+ each month in the two channels of the detector. Error bars show the standard deviation. (d) Scans per month in High Resolution (HR) and Low Resolution (LR) modes of DFMS for context. Excursions (September/October 2015 and April 2016) and safe mode (April 2015) are shaded in **grey**. Credit: Lewis *et al.* (2023)

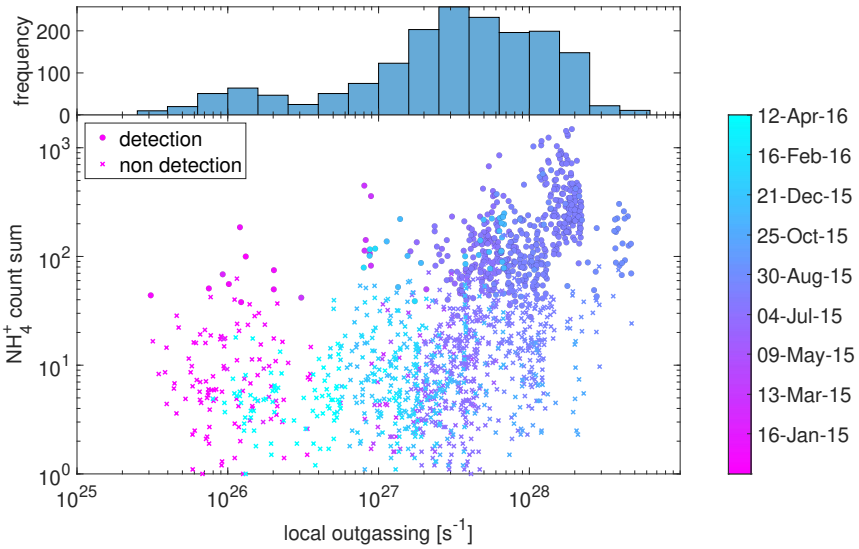

Figure 3.4: (**top**) Histogram showing number of points in each outgassing bin. (**bottom**) NH_4^+ count sum against local outgassing, with the **colour scale** showing the time along the mission. The **circles** show where NH_4^+ is considered to be detected, and the crosses show where it is not. Credit: Lewis *et al.* (2023)

perihelion, NH_4^+ is likely produced through coma chemistry driven by higher neutral densities or by dust grain impacts, which also increase with outgassing. High NH_4^+ count sums at lower outgassing levels mainly occur before or after perihelion and might be due to residual spacecraft outgassing (despite efforts to mitigate this by excluding data up to 1 hour after a wheel offloading manoeuvre) or more sporadic dust grain impacts. No dependence on cometocentric distance or DFMS channel was identified.

Figure 3.5a shows the same as in Figure 3.4 but for July and August 2015 only. It is evident that while there is an overall trend for higher NH_4^+ count sums at higher outgassing, on shorter timescale the count sums can vary highly for little change in outgassing. Figure 3.5b shows NH_4^+ count sum against NH_3 mixing ratio for the same time period; there is no clear trend. This suggests that the NH_4^+ production is at least in part driven by the local outgassing rate (and therefore the density and likelihood of ion-neutral collisions), rather than the amount of NH_3 present.

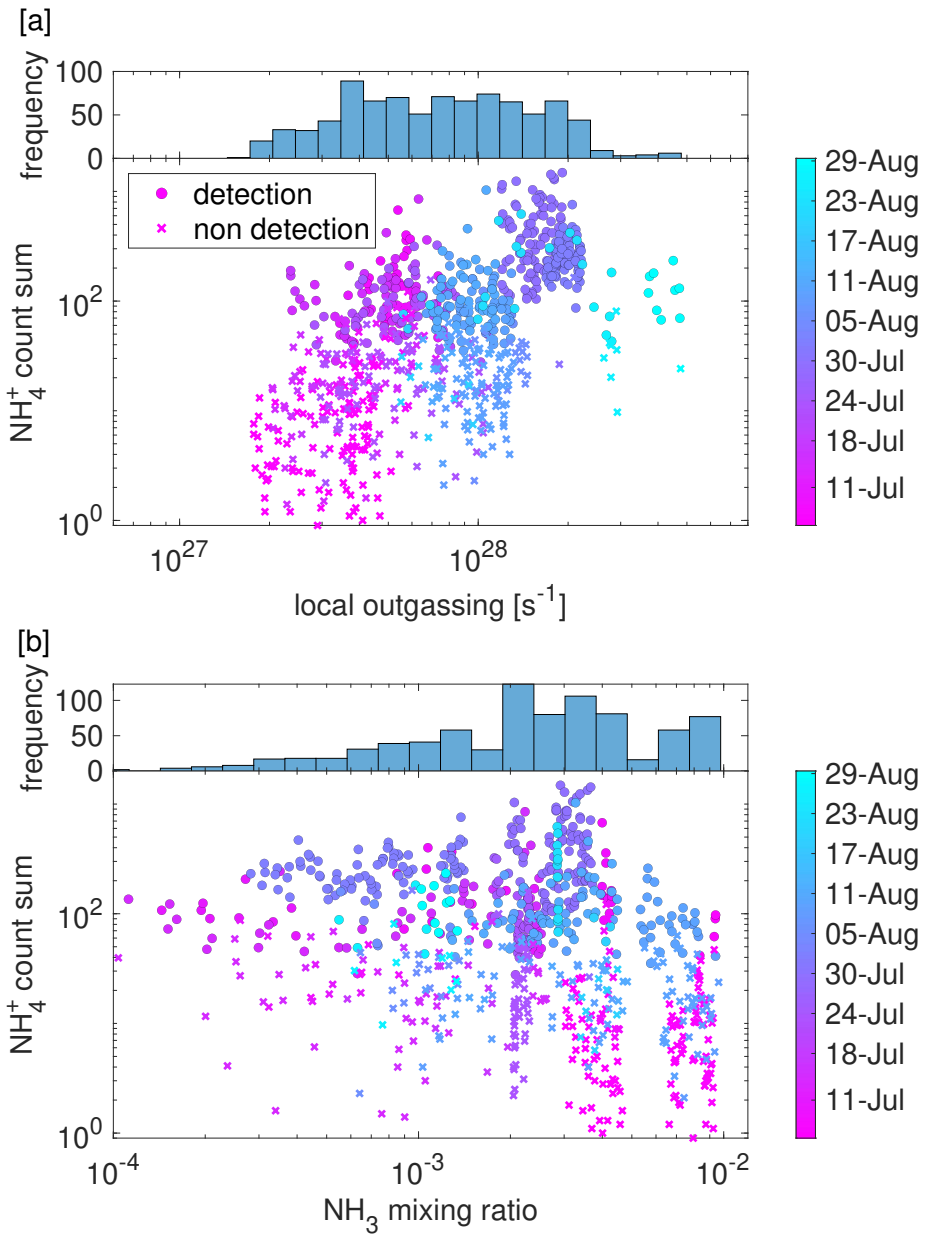

Figure 3.5: (**a**) (**Top**) Histograms showing the distribution of data in each local outgassing bin (**Bottom**) NH_4^+ count sum against local outgassing. (**b**) (**Top**) Histogram showing distribution of data in each NH_3 mixing ratio bin (**Bottom**) NH_4^+ count sum against NH_3 mixing ratios. Points are coloured by time, for July and August 2015. Credit: Lewis *et al.* (2023)

Table 3.1: Seasonal variations during the escort phase (Heritier, 2018)

Interval	**Season**	**Heliocentric dist. [au]**
01/08/2014 - 10/05/2015	NH summer/ SH winter	3.60 - 1.67
10/05/2015 - 04/09/2015	NH autumn/ SH spring	1.67-1.25, 1.25-1.27
04/09/2015 - 21/03/2016	NH winter/ SH summer	1.27 - 3.05

3.2.1 Latitudinal heterogeneities

Hemispheric heterogeneities in coma composition and outgassing of the surface of 67P have been observed (Le Roy *et al.*, 2015, Hässig *et al.*, 2015, Gasc *et al.*, 2017a) and are driven primarily by seasonal changes in solar insolation, as well as some inhomogeneity of the surface (Fougere *et al.*, 2016). Table 3.1 gives the dates of the seasons for the northern hemisphere (NH) and southern hemisphere (SH) of the comet during Rosetta's escort. I examine the variations in NH_4^+, comparing them to the mean NH_3 number density, and mean local outgassing. Figure 3.6 shows each of these quantities separated into latitudinal bins for the NH autumn/SH spring season described in Table 3.1.

NH autumn/SH spring (Figure 3.6) corresponds to the period around perihelion, and the highest detection rate of NH_4^+ is observed over both hemispheres. The southern hemisphere has up to 10 times higher local outgassing than the northern hemisphere, and also larger NH_3 number densities. The proportion of 18 *m/z* scans resulting in a detection of NH_4^+ is therefore also significantly higher above the southern hemisphere (see Figure 3.6a), as the higher neutral density permits more ion-neutral interactions (and also more dust impacts). The sharp drop in local outgassing at $-60°$ is due to an observational bias: latitudes of $-60°$ to $-80°$ were only passed over by Rosetta in July 2015, when 67P was at 1.5 au and the local outgassing was ~ 10 times less than in August 2015. When 67P was at perihelion (1.25 au), it flew over more equatorial regions.

The results presented in this section confirm that NH_4^+ is produced in the cometary coma, by showing its increasing prevalence as the outgassing increases near perihelion. It was also shown that other HPA species appear more frequently near perihelion, suggesting that the ion-neutral chemical reactions leading to production of these species, and ultimately to NH_4^+,

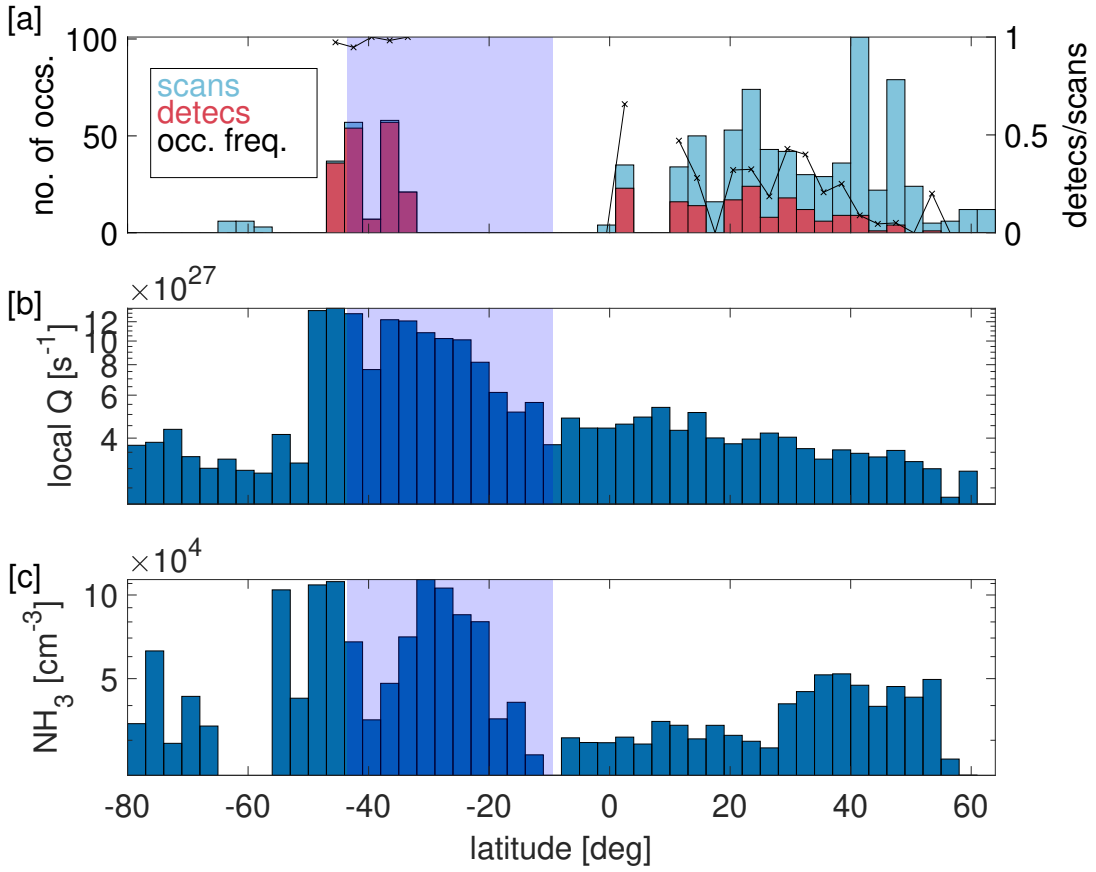

Figure 3.6: (**a**) Number of mass 18 *m/z* scans in HR by ROSINA-DFMS and NH_4^+ detections, (**b**) local outgassing and (**c**) mean NH_3 number density separated into latitudinal bins for the NH autumn/SH spring season (see Table 3.1). The **violet shaded region** shows the range of subsolar latitudes over the season. Credit: Lewis *et al.* (2023)

happen more readily at this time. However, from these data it cannot be concluded whether NH_4^+ production is driven more by ion-neutral chemistry or by impacting dust grains with ammonium salts embedded. Dust activity increases with outgassing, as does coma density and the possibility of ion-neutral chemistry.

3.3 NH_4^+ and the diamagnetic cavity

It is clear from the data presented in Section 3.2 that, to first order, the production of NH_4^+ is driven by increased local outgassing, with the highest rates of detection around perihelion over the southern hemisphere. I now focus on the period close to perihelion, during which the diamagnetic cavity was frequently detected (Goetz *et al.*, 2016a). The measured NH_4^+ count sums were compared with the magnetic field magnitude from RPC–MAG (see Section 1.2.1) in order to identify the main source of NH_4^+.

3.3.1 Case study: 29th July 2015

Figure 3.7 shows the spectra for all the scans of 18 *m/z* by ROSINA-DFMS in HR ion mode on 29th July 2015. This day was chosen for the case study as it was the day with the most HR ion mode data collected within the diamagnetic cavity (see Table 3.2). The cometocentric distance of Rosetta varied between 182–193 km during the time that the HR ion mode of DFMS was on (07:12–19:38 UTC), and Rosetta was above the southern hemisphere of 67P between -40° and -45° latitude. period was when the comet was around 2 weeks before perihelion, at a heliocentric distance of 1.26 au.

In Figure 3.7, the spectra are colour-coded by the mean absolute magnitude of the magnetic field (from RPC–MAG) during the integration time of ROSINA-DFMS (20 seconds), therefore the spectra taken within the cavity are shown in the darkest blue. This colour scheme reveals that the strongest NH_4^+ spectra are usually observed in or close to the diamagnetic cavity, where the magnetic field is low, and weaker signatures are mostly found where the magnetic field magnitude is higher ($|B| \geq 40$ nT).

In Figure 3.8, the first cavity crossing (shown with vertical violet shading) occurs at 13:21–

Table 3.2: List of cavity crossings with HR ion mode data available. Highlighted rows contain scans of 18 *m/z*. Cavity crossing list is from Goetz *et al.* (2016a).

Date	Start (hh:mm:ss)	End (hh:mm:ss)	Duration (mm:ss)	HR masses (*m/z*)
2015-07-08	17:15:50	17:22:36	06:46	34 -47
2015-07-29	**13:21:38**	**13:28:41**	**07:03**	**17-30**
	13:58:06	**13:58:58**	**00:52**	**18**
	14:19:00	**14:19:48**	**00:48**	**18**
	14:34:21	14:37:29	03:08	44-50
	14:57:31	**15:07:09**	**09:38**	**18, 13-27, 50**
	16:41:45	**16:45:51**	**04:06**	**17-24**
2015-08-09	10:22:50	10:24:33	01:43	29-32
2015-08-22	06:52:09	06:54:04	01:55	38-41
2015-11-21	07:28:49	07:30:35	01:14	25-27
	07:32:18	07:33:14	00:56	33
	07:37:55	07:38:57	01:02	45
	07:55:42	07:56:46	01:04	40-41
	08:04:43	**08:08:56**	**04:13**	**16-24**
	08:33:04	08:33:38	00:34	34
2015-11-25	**07:29:21**	**07:30:53**	**01:32**	**17-19**
	08:00:54	08:01:24	00:30	no full scans

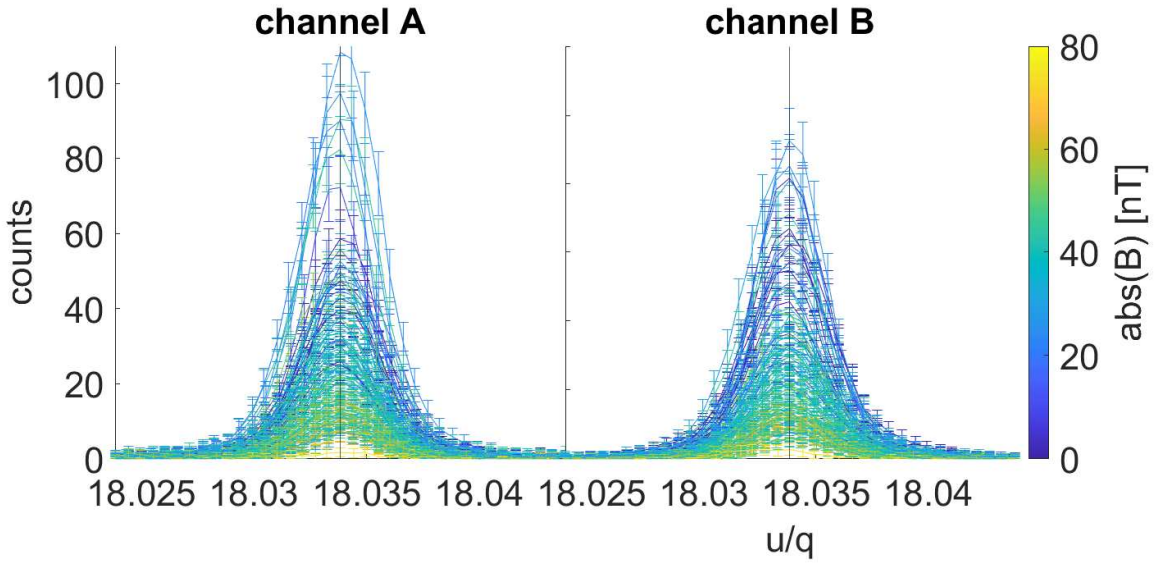

Figure 3.7: All HR ion mode spectra from ROSINA-DFMS at the location of NH_4^+ on 29th July 2015. The colour scale shows the mean magnetic field magnitude (in nT) from RPC–MAG over the 20s scan time. Credit: Lewis *et al.* (2023)

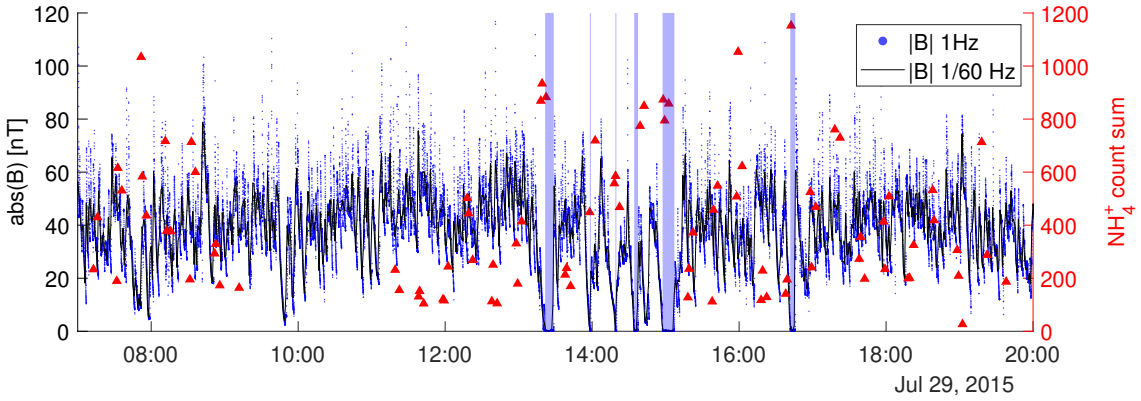

Figure 3.8: Time series (in UTC) of the RPC–MAG magnetic field magnitude (**blue dots** 1 Hz, resampled to **black line** 1/60 Hz) and ROSINA-DFMS NH_4^+ detections (**red triangles**) on 29th July 2015. Diamagnetic cavity crossings are highlighted with **violet vertical bars**. Credit: Lewis *et al.* (2023)

13:28, shortly before which there is a jump in the NH_4^+ counts, and afterwards the counts decrease again. The counts are then elevated again during the subsequent cavity boundary crossings at 13:58, 14:19, 14:34 and 14:57, and again at 16:41. However, there are several instances when Rosetta is outside the diamagnetic cavity, and there is no wheel offloading manoeuvre, sudden increase in local outgassing, or sudden change in cometocentric distance to explain the elevated counts.

Figure 3.9 shows the NH_4^+ count sums against magnetic field magnitude (a), cometocentric distance (b) and spacecraft potential (d), as well as the dependence of the spacecraft potential on the magnetic field (c). Figure 3.9a shows an apparent correlation between NH_4^+ count sum and magnetic field magnitude, with a correlation coefficient of 0.55, confirming the apparent trend in Figure 3.7. In particular, within the diamagnetic cavity ($B \approx 0$ nT), the count sum is very high (> 200), while it is low (< 100) for very high B magnitude ($B > 60$ nT). While Q was an important factor over large timescales (see Section 3.2), over this small range, no dependence is observed. The dependence of NH_4^+ count sum with magnetic field is also not biased by the cometocentric distance over this period, as illustrated in Figure 3.9b, even when local outgassing derived from ROSINA-COPS is taken into account.

Due to lower electron temperature in the diamagnetic cavity, the spacecraft potential has been shown to be less negative in this region (Odelstad *et al.*, 2018). Figure 3.9c demonstrates that this is indeed the case for the cavity crossings on the case study day, with potentials typically around -10 V where the magnetic field is zero, and otherwise lower. More negative values of the spacecraft potential observed outside the diamagnetic cavity may accelerate ions out of the energy acceptance range of DFMS, meaning the detectability of positive ions decreases (see Section 3.1.1). This could generate a bias leading to stronger NH_4^+ detection inside the diamagnetic cavity. However, Figure 3.9d shows that the NH_4^+ count sum is not correlated with the spacecraft potential. In particular, the data points are not organised in the same way as they are when plotted against the magnetic field (Figure 3.9a). Hence, the correlation in Figure 3.9a does not appear to be due purely to variation in the spacecraft potential, though it may be affecting the points at $\mathbf{B} \approx 0$ nT.

Another possible reason for the trend of NH_4^+ with the magnetic field could be the de-

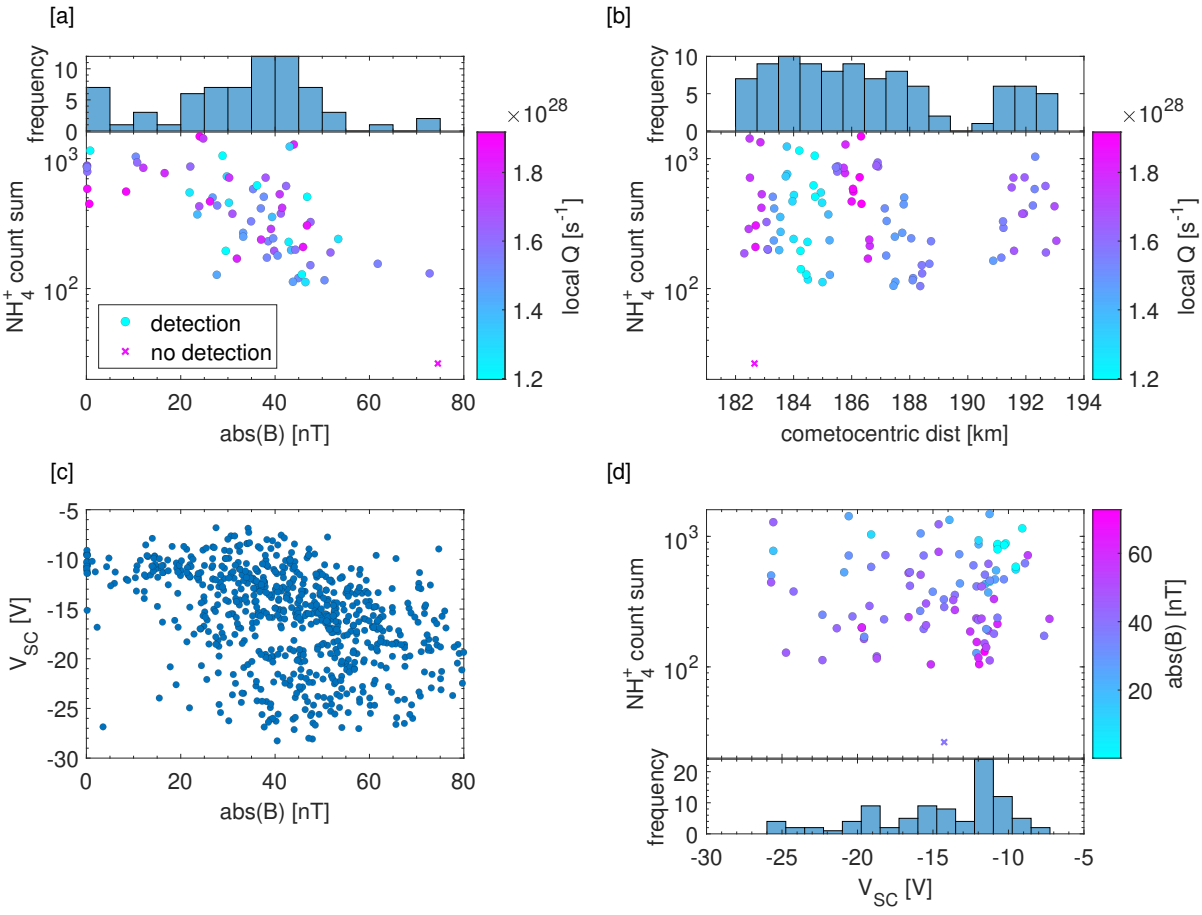

Figure 3.9: (**a**) ROSINA-DFMS NH_4^+ counts as a function of the magnetic field magnitude (RPC–MAG), and the colour scale shows the local outgassing Q. (**b**) NH_4^+ counts as a function of cometocentric distance. (**c**) Spacecraft potential as a function of magnetic field. All data is from 29th July 2015. (**d**) Counts as a function of spacecraft potential from RPC–LAP. Histograms for a, b, and d show the distribution of values for magnetic field, cometocentric distance and spacecraft potential respectively. Credit: Lewis *et al.* (2023)

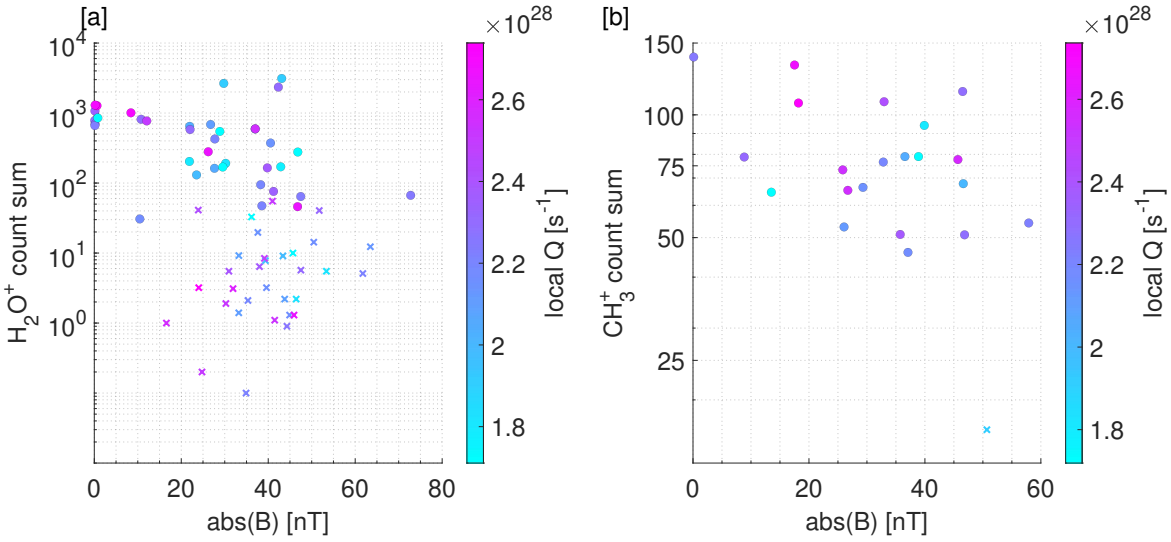

Figure 3.10: (**a**) Count sum against magnetic field magnitude with local outgassing colour scale for H_2O^+ and (**b**) CH_3^+ in HR ion mode. All data from 29th July 2015. Credit: Lewis *et al.* (2023)

flection of ions out of the field of view of DFMS due to the presence of a magnetic field outside the diamagnetic cavity. To rule this out, the count sums for two other ion species are examined, for which the number density should not be governed by the likelihood of ion-neutral collisions. Since they have similar masses, the effect of ion deflection would similarly affect all of these species, while trends due to a difference of ion chemistry should disproportionately affect NH_4^+.

The two ion species tested for this assessment were H_2O^+ and CH_3^+. H_2O^+ should generally be at photochemical equilibrium at low enough cometocentric distances (Galand *et al.*, 2016; Heritier *et al.*, 2017a). CH_3^+ does not undergo any significant ion-neutral chemical loss processes (Heritier *et al.*, 2017a, Beth *et al.*, 2020), and therefore its density should not vary systematically across the cavity boundary if the ion composition difference is due only to ion-neutral chemistry. Figure 3.10 shows the count sums against magnetic field magnitude for these two species, where the colour scale shows the local outgassing. Figure 3.10a shows that H_2O^+ has stronger than average counts inside the diamagnetic cavity, but there is no discernible trend with magnetic field strength as there is for NH_4^+. The correlation coefficient associated with H_2O^+ count sum for detected peaks vs the magnetic field strength is 0.17, compared to 0.55 for NH_4^+ in Figure 3.9a. This suggests that the trend in Figure 3.9a is not

driven purely by deflection out of the instrument field of view, as H_2O^+ and NH_4^+ have very similar masses, and one would therefore expect them to be affected similarly. This conclusion is confirmed by the absence of correlation between CH_3^+ counts and magnetic field strength (see Figure 3.10b). Note that since 15 *m/z* is scanned three times less frequently than 18 *m/z*, statistics are low and there is only one scan of 15 *m/z* inside the cavity (see Table 3.2).

3.4 Comparison with modelling

In this section, I compare the count sums of NH_4^+ with ion number densities predicted by ionospheric modelling. Although they cannot be compared like-for-like, analysis of the general trends can show to what extent the model assumptions are valid. The model is briefly described in Section 3.4.1, and then I describe the results of running this model for input conditions representing two periods of data observation by Rosetta (Section 3.4.2).

3.4.1 Ionospheric model

The model used in this section was first described in Heritier *et al.* (2017a) and solves a set of coupled continuity equations to find $n_j(r)$, the number density of ion species j at a given cometocentric distance, r. The continuity equations are set out in Section 2.2. The version used in this work was slightly adapted from the one in Heritier *et al.* (2017a) to include realistic photoionisation and electron impact rates for comparison with the Rosetta data (Galand *et al.* 2016, Stephenson *et al.* 2023).

The continuity equations are solved for spherical shells of the coma, starting at the shell adjacent to the cometary surface where there is no transport from below. The 1D model assumes no electric or magnetic fields (so the ions move radially and at the neutral speed), and non-radial ion dynamics are not included, hence it only applies within the diamagnetic cavity. The validity of these assumptions are discussed in Section 3.4.2. A full description of the model is given in Heritier (2018).

The Rosetta data sources for various terms of the continuity equation are illustrated in Figure 3.11. The grey arrows indicate iteration of the ion density for each species (n_j), which

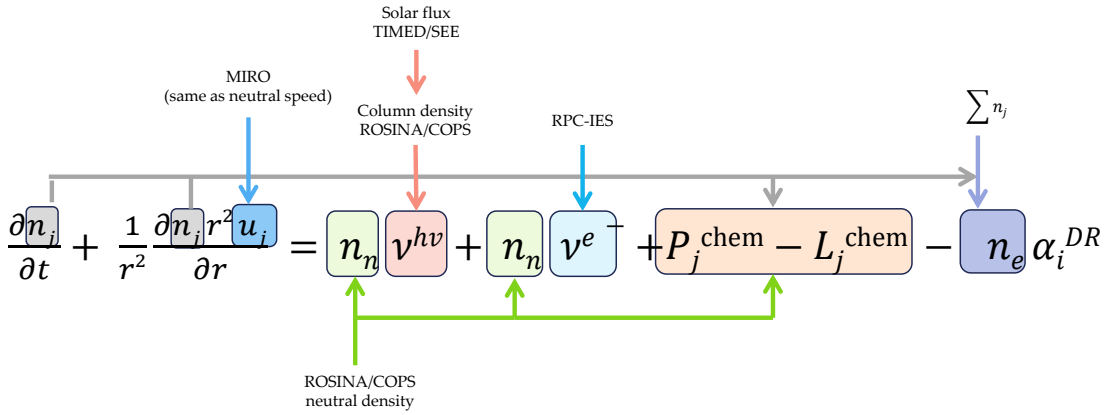

Figure 3.11: Figure showing the input data used for the ionospheric modelling in Section 3.4.2 and the continuity equation they are used to calculate (see Section 2.2). n_j represents the number density of ion species j

feeds back into the ion-neutral chemical production and loss terms (highlighted in orange), as well as the ion-electron dissociative recombination (in purple).

First, the neutral density and composition were filtered to remove data taken up to 30 minutes after a wheel offloading manoeuvre, or when the comet and solar aspect angles indicated off-nadir spacecraft (and hence DFMS) pointing. Then a median filter was applied to the COPS neutral density to remove remaining sharp peaks (due to, e.g. dust impacts). Means were taken over a 12.4 hour window, to smooth the effect of the comet rotation, and windows with insufficient data availability were removed. The model was first run for each 12.4 hour window with all ion-neutral reactions included (for the full list, see Heritier *et al.* 2017a). I then removed direct pathways to NH_4^+ from non-water species, to see the relative contribution of reactions of NH_3 with other protonated HPA species compared to those from H_2O^+ and H_3O^+ (see Section 2.2.2).

3.4.2 Two key periods

In this section the analysis performed for the case study in Section 3.3 is expanded to cover all the days in which HR ion mode was active during a diamagnetic cavity crossing (see Table 3.2).

Figure 3.12a shows the count sums of NH_4^+ as a function of the magnetic field magnitude, colour-coded by the local outgassing. This confirms the earlier findings from Section 3.3.1

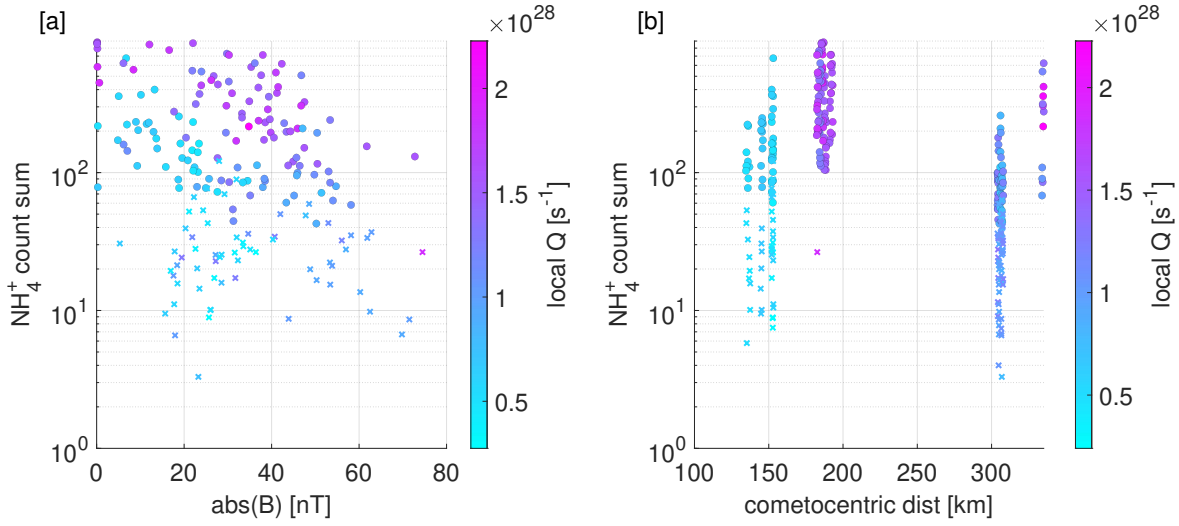

Figure 3.12: (**a**) NH_4^+ count sum as a function of magnetic field and (**b**) cometocentric distance, with the colour scale showing the local outgassing. The dataset is for the 6 days during which both DFMS was in HR ion data mode and a diamagnetic cavity was observed (see Table 3.2). Credit: Lewis *et al.* (2023)

(see Figure 3.9): the highest count sums of NH_4^+ are associated with lower magnetic field magnitude, for a given range of local outgassing (high outgassing with $Q > 2 \times 10^{28}\,s^{-1}$ and moderate outgassing, $Q < 2 \times 10^{28}\,s^{-1}$). As seen in Figure 3.9b, the count sum does not follow any trend in terms of cometocentric distance, even when the outgassing rate is taken into account.

With the link between NH_4^+ production and magnetic field established, I now focus on two separate periods in which the diamagnetic cavity was observed in combination with HR ion mass spectra: July–August and November 2015. The observed NH_4^+ count sum is compared to ion density calculated from the ionospheric model (as described in Section 3.4.1).

July–August 2015

The period of July–August 2015, which includes perihelion on 13th August 2015, has the most frequent scans of 18 *m/z* in HR ion mode. Figure 3.13 shows how NH_3 (b, black) NH_4^+ (c, black) detection varied over this period. It was autumn in the northern hemisphere (see Table 3.1). The local outgassing estimate (a, black) is higher over the southern hemisphere, as is the NH_3 number density.

Diamagnetic cavity crossings are shown by the vertical red dashed lines in Figure 3.13c:

the only scans of 18 *m/z* in high resolution ion mode inside the cavity took place on 29th July 2015. The NH_4^+ signal is particularly enhanced on this day, and the local outgassing does not appear to be the main driver. For example, when comparing July 29th with August 1st, the local outgassing and NH_3 density are similar but the NH_4^+ signal is much stronger when Rosetta was located within the diamagnetic cavity. In addition, in late August the NH_4^+ counts are very low, despite similar local outgassing to late July when the enhanced counts are observed. The counts peak again on August 22nd; on this day, Rosetta entered the diamagnetic cavity several times, though no HR scans of 18 *m/z* took place (see Table 3.2). Again, it seems that the presence of NH_4^+ near perihelion is driven by the location of Rosetta relative to the diamagnetic cavity boundary, confirming the finding from Section 3.3. Note however that due to the unstable nature of the boundary, we cannot know the actual distance of Rosetta from the boundary at a given time (Goetz *et al.*, 2016a).

The enhancement in the NH_4^+ counts on July 29th is also predicted by ionospheric modelling (Figure 3.13d) based on the ROSINA neutral density and composition at the Rosetta location (averaged over the 12.4 hour rotation period of the comet) showing approximately a factor 1.5 increase between July 28th and July 29th. The NH_4^+ density is predicted to remain high until 3rd August. The proportion of NH_4^+ produced by NH_3 reacting with water group ions also decreases during the enhancement. This suggests that NH_4^+ is being produced more readily through increased protonation of other HPA neutrals (e.g. H_2COH^+, $CH_3OH_2^+$, and H_3S^+), which is made possible by the higher local outgassing. More reactions can occur before the ion is lost through transport, so more chemical pathways are contributing to the production of NH_4^+. It is important to note that due to the field-free 1D radial nature of the model, it only captures ion composition driven by changes in local outgassing and neutral composition. It is therefore not sensitive to changing dynamics in different plasma interaction regions.

November 2015

Figure 3.14 shows the same information as Figure 3.13 but for November 2015, when the largest number of ammonium salt dust grain impacts were observed (Altwegg *et al.*, 2022).

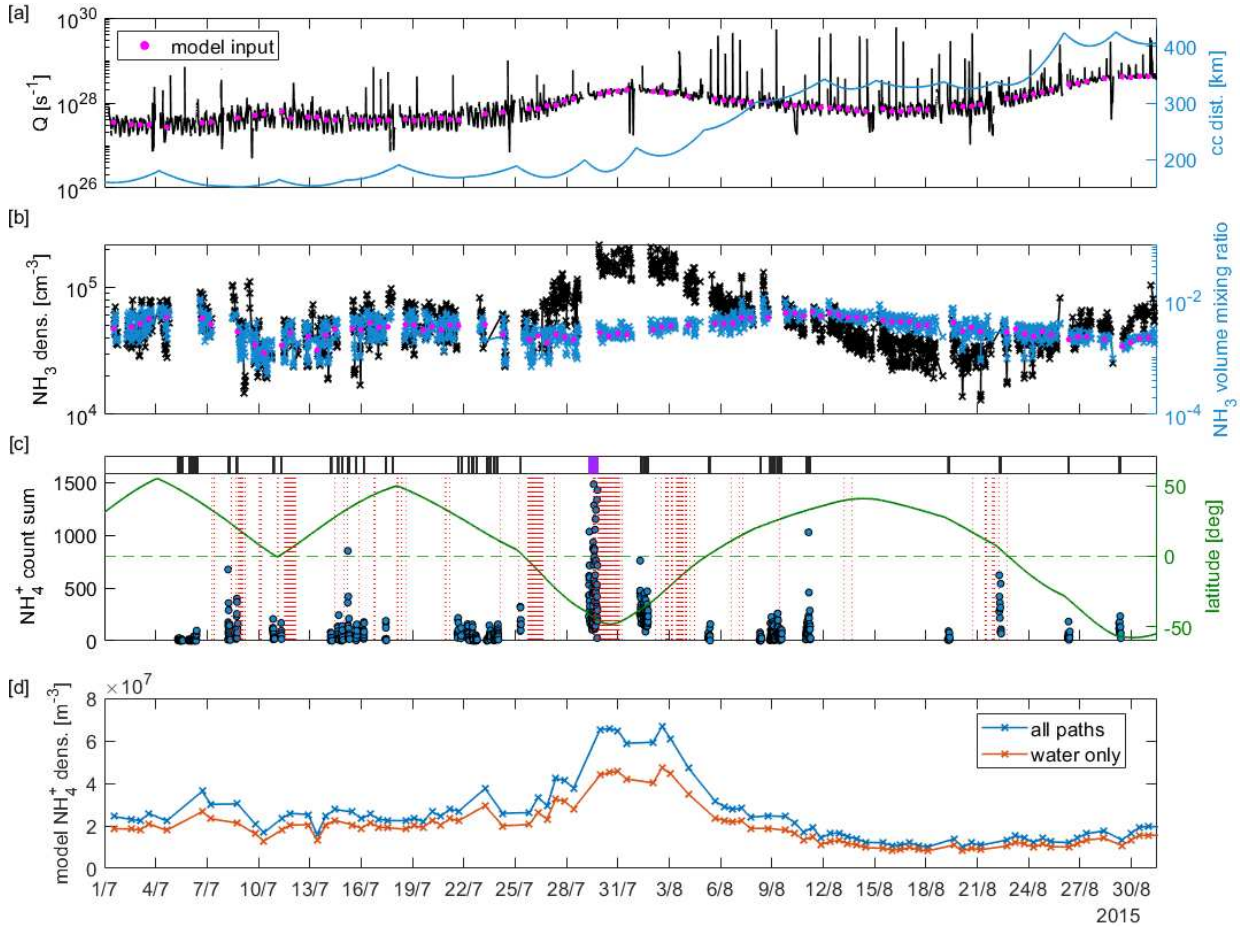

Figure 3.13: (**a**) Local outgassing from ROSINA-COPS (**black**), input outgassing used to generate model (**pink**), and cometocentric distance (**blue**). (**b**) NH_3 number density (**black**) and volume mixing ratio (**blue**, relative to total). Volume mixing ratio used as input to the model is shown in **pink**. (**c**) NH_4^+ count sum (**blue**), latitude (**green**), and diamagnetic cavity crossings (from RPC–MAG, **vertical red lines**). **Black lines** along the top show when DFMS HR ion mode is active, with purple highlighting 29th July 2015, on which the case study in Section 3.3.1 is based. (**d**) Modelled NH_4^+ ion density when all pathways to NH_4^+ (**blue**) and only water pathways (**red**) are 'switched on'. Credit: Lewis *et al.* (2023)

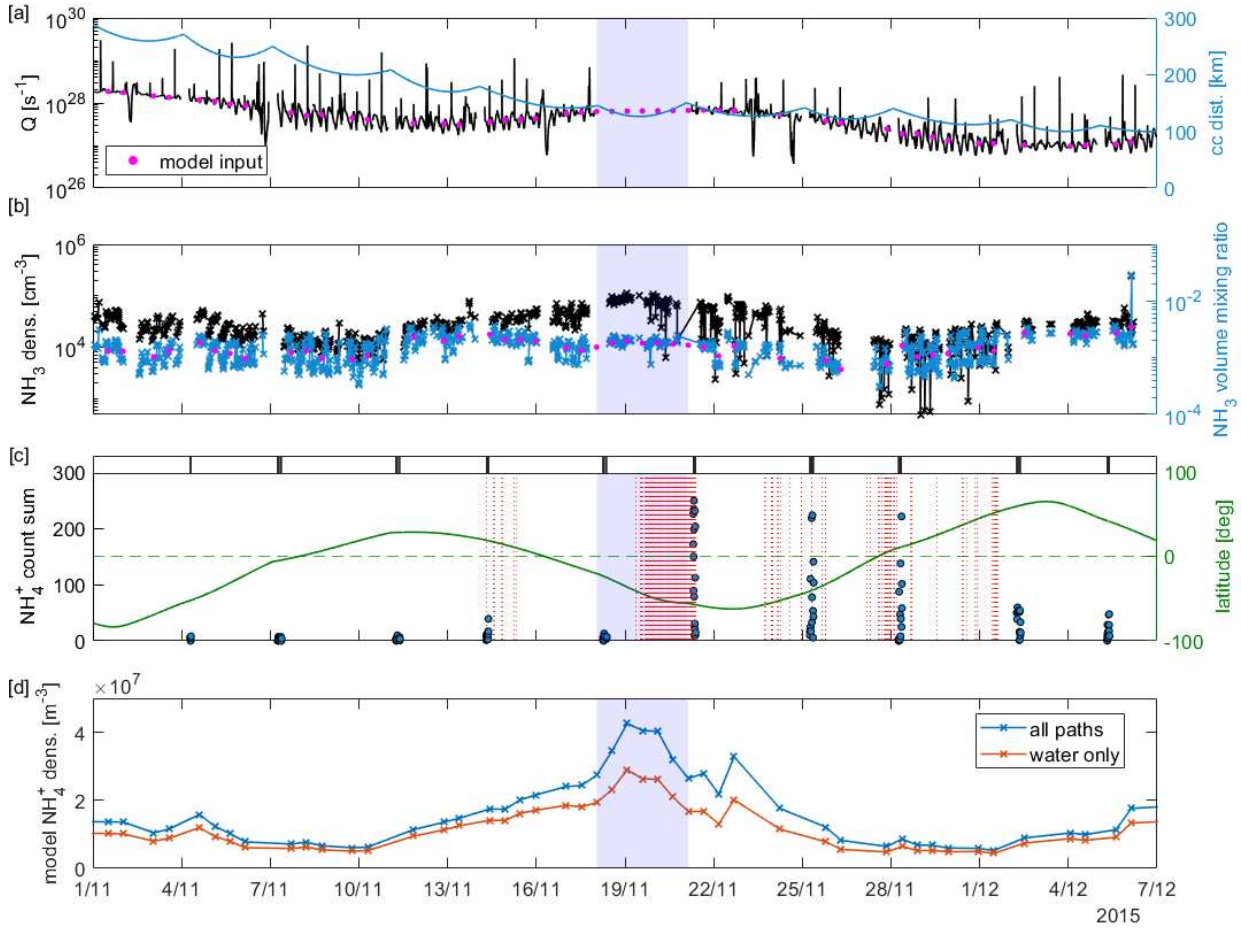

Figure 3.14: Same as Figure 3.13, but for November 2015. The shaded region indicates where the neutral density has been interpolated to generate the ionospheric model inputs. Credit: Lewis *et al.* (2023)

The signatures of NH_4^+ are generally weak or not present during this period but increase significantly on November 21st and remain high on the 25th and 28th, despite no particular increase in NH_3 number density or mixing ratio. On November 21th and 25, NH_4^+ measurements coincide with times when Rosetta was within the diamagnetic cavity and on November 28th, Rosetta was sporadically within the cavity, hence likely close to the boundary when in HR ion mode. The enhanced NH_4^+ seems to be more driven by the presence of the diamagnetic cavity than the outgassing or NH_3 prevalence.

Figure 3.14d shows the modelled NH_4^+ density for this period. The shaded region shows where the neutral density has been interpolated to fill the gap in the COPS coverage from 18th–21st November, assuming that the local outgassing is constant in this period. The NH_4^+

density then peaks on 19th November 2015, and begins to decrease on November 20th. The modelled density then remains low, but detected counts are still high on November 25th and 28th when the diamagnetic cavity is present again. The relative contribution of reactions with water family ions decreases during the peak modelled ion density, and the peak corresponds to an increase in both the local outgassing and the NH_3 number density (but not the NH_3 mixing ratio).

Detection of NH_4^+ appears to be more strongly driven by the diamagnetic cavity than high outgassing over the full period analysed. Since the ionospheric model only applies within the diamagnetic cavity as it assumes a radial flow of cometary ions, it is possible that the NH_4^+ count sum observed outside the cavity is reduced compared with the modelled density by increased acceleration and non-radial ion motion.

3.5 Discussion

In Section 3.2, I showed that over the full course of ion mode observations (1.25 au to 3.6 au), NH_4^+ detection frequency and count sums increase with local outgassing, and are most prevalent near perihelion, as are other high proton affinity ions. Around perihelion in July and August 2015, the detection is stronger over the southern hemisphere, which is in spring during this period, and therefore has higher outgassing and a greater density of NH_3, due to greater insolation. NH_4^+ therefore has a source within the coma, and its presence is not reduced to spacecraft manoeuvres only. There are two candidates for the NH_4^+ source in the coma: ion-neutral chemistry (through protonation) and ammonium salt dust grain impacts (see Section 3.1.3).

While ammonium salts detected from dust grains (sublimating after impact inside the DFMS ion source) are mostly observed during post-perihelion over the southern hemisphere, the majority of NH_4^+ detections happen around perihelion. The correlation between higher outgassing and NH_4^+ at perihelion is what we would expect from an ion-neutral chemistry source in the coma, and it remains the strongest candidate for the majority of detections observed. However, due to observational bias when looking for ammonium salts as a signal

over background noise, it is likely that dust impacts are also more prevalent at perihelion when outgassing is higher (Altwegg *et al.*, 2022). It is hence not possible to rule out that ammonium salt embedded in dust grains contributes as a source of NH_4^+ based on the analysis between its detection, local outgassing, and NH_3 (see Section 3.2).

In Section 3.3, we saw that for similar outgassing and cometocentric distances, the NH_4^+ signal is stronger inside the diamagnetic cavity than outside and appears to increase in prevalence with proximity to the diamagnetic cavity. More generally, the NH_4^+ count sum is found to increase with decreasing magnetic field strength (see Section 3.3.1). This trend is shown not to be driven by the less negative spacecraft potential inside the cavity. It is also not found for other ions of similar mass/charge which do not undergo ion-neutral chemistry (i.e. CH_3^+), or even for H_2O^+ (which is at photochemical equilibrium), suggesting that the effect is not due to ion deflection out of the field of view by a stronger magnetic field.

Through comparison with the ionospheric model, I determined that high NH_4^+ count sums appeared more driven by the location of Rosetta relative to the diamagnetic cavity than by favourable neutral conditions that increase the modelled NH_4^+ density (see Section 3.4.2). The model also predicts ion densities well above the estimated minimum detectable threshold of $5 \times 10^4\ \mathrm{m}^{-3}$ for July, August and November 2015. This suggests that, since the model only strictly applies inside the diamagnetic cavity (i.e. no magnetic field) with a radial outflow of cometary ions, it overestimates the NH_4^+ prevalence outside the cavity. There, the flow is more dynamic and less radial, allowing less time for ion-neutral chemistry to take place. This is consistent with 3D hybrid simulations of the coma (e.g. Koenders *et al.*, 2015), which show that the radial velocity dominates the flow inside the cavity, while there are more dynamics outside with a strong antisunward component.

I also found a strong presence of NH_4^+ in early March 2015 (Section 3.2), following an increase in outgassing of around an order of magnitude during February (see Figure 3.3a). The occurrence frequency and count sums are much higher in March than they are in May and June 2015, when the local outgassing is similar, with lower neutral density measured by COPS in May due to higher cometocentric distance. Running the ionospheric model for the mean conditions on 3rd March and 13th May 2015 predicts NH_4^+ ion densities of $1.40 \times 10^7\ \mathrm{m}^{-3}$

and 1.54×10^7 m^{-3}, respectively. These are similar in magnitude to the modelled densities predicted for July, August and November in Section 3.4.2, and suggests that detection is suppressed in May and June, rather than enhanced in March. It is possible that this is related to the presence or not of a diamagnetic cavity around the comet. The cavity was detected throughout May and June 2015, though all mass 18 observations by DFMS were made outside the cavity in this period. Based on our findings, the presence of a diamagnetic cavity would reduce the $\mathrm{NH_4^+}$ density outside of it. If the cavity was not formed yet in March 2015 (which is somewhat speculative but consistent with its non detection despite lower cometocentric distance in March than in May 2015), the cometary ion flow would be expected to be more uniformly radial, as derived from multi-instrument analyses at lower activity (e.g. Galand *et al.*, 2016, Heritier, 2018). In that case, we would expect higher $\mathrm{NH_4^+}$ density in March than in May/June. This does not explain why a similar effect in terms of $\mathrm{NH_4^+}$ was not observed in early 2016, when the comet moved away from perihelion again. There are, however, several detections of other HPA ions ($\mathrm{H_2COH^+}$ and $\mathrm{H_3S^+}$) in January–February 2016 which may suggest some equivalence to March 2015, and at a similar heliocentric distance. There could potentially also be additional loss processes for $\mathrm{NH_4^+}$ that are more efficient post perihelion and in May/June 2015 than at other times, such as charge exchange with neutral metals (Aikin, 1974) such as sodium (Beth *et al.*, 2020). These topics all require further study.

In conclusion, the link between the detection of $\mathrm{NH_4^+}$ and the local outgassing rate confirms that there is a source in the coma. While the protonation of $\mathrm{NH_3}$ is a confirmed pathway, it is not possible to rule out a contribution from the dissociation of ammonium salts embedded in cometary dust grains sublimating near DFMS. The trend between the $\mathrm{NH_4^+}$ count sum and the magnetic field strength suggests, however, that ion-neutral chemistry is the strongest driver at perihelion, and that the presence of $\mathrm{NH_4^+}$ is influenced by ion dynamics outside the diamagnetic cavity.

CHAPTER 3 SUMMARY

- High Proton Affinity ion species are a useful indicator of the collisionality of the cometary coma; they can only be produced where the timescale of proton transfer is faster than the transport timescale.
- High-resolution ion mass spectrometer data from the ROSINA-DFMS instrument were used to assess the trends in the HPA species, in particular the 'terminal ion' (NH_4^+) throughout the escort phase of Rosetta and across the diamagnetic cavity boundary.
- NH_4^+ detections and counts were found to peak around perihelion, as do those of other HPA ions.
- A link was identified for the first time between the prevalence of HPA ions and the presence of the diamagnetic cavity.
- This connection between the plasma environment and the ion chemistry suggests that ion-neutral chemistry within the comet's ionosphere is the predominant source of NH_4^+, though dissociation of ammonium salts embedded in dust grains may also be a contributing factor.

CHAPTER 4

CONSTRAINING ION TRANSPORT IN THE DIAMAGNETIC CAVITY

The ambipolar electric field that is thought to be responsible for ion acceleration in the inner coma of comet 67P near perihelion is poorly understood (see Section 2.3.2). Unlike at planets, the electron pressure gradient is driven by the energy difference between newly created ions and electrons rather than by the gravitational difference (e.g. Collinson *et al.*, 2019), and cannot be analytically constrained. There is also uncertainty in the ion velocity estimates derived from RPC–LAP and RPC–ICA data, due to the unconstrained thermal velocity as well as the influence of the spacecraft potential on the measured ion energies (see Section 1.3.3).

This chapter presents a new approach to constraining the ion bulk velocity and electric field strength, through ionospheric modelling. I developed a new ionospheric model based on the one described Heritier *et al.* (2017a) but that includes acceleration of the ions by a given ambipolar electric field, and moderated by the transfer of momentum through ion-neutral collisions. Three key ion species are modelled: H_2O^+, H_3O^+ and NH_4^+. This allows the sensitivity to the electric field of both the total plasma density and the ion composition to be explored, and to assess the strongest electric field that is compatible with the electron density measurements from RPC–MIP and RPC–LAP.

I focus on the diamagnetic cavity region so that radial transport can be assumed, allowing us to use a 1D model to assess the dynamics. In this region, the ion flow has been shown to be more consistently radial (see Section 1.3.3), and the only electric field term present is the ambipolar electric field since $\vec{B} = 0$ (Section 2.3.2). The more complex ion dynamics, outside the confines of the diamagnetic cavity, is explored in Chapter 5.

The model is described in Section 4.1. In Section 4.2 I then present the sensitivity of the ion composition to the electric field and to momentum transfer. Finally in Section 4.3 I compare the modelled total plasma density with electron density data from Rosetta, to constrain the ion bulk velocity and electric field strength within the diamagnetic cavity for two case studies. The majority of this chapter is taken from Lewis *et al.* (2024).

4.1 Ion Acceleration Model

The 1D ionospheric model presented and used in this chapter is based on the one described in Heritier *et al.* (2017a), restricted to the ion species H_2O^+, H_3O^+, and NH_4^+. I have updated it substantially to include acceleration of the ions above the neutral speed u_n by an ambipolar electric field. In the model, adapted coupled continuity equations are solved using a finite difference method for three ion species over logarithmically spaced spherical shells from the comet nucleus at $r = 2$ km up to $r = 1 \times 10^3$ km (300 bins).

In Section 4.1.1 I describe how the continuity equations first introduced in Section 2.2 are updated to include acceleration by an ambipolar electric field. Sections 4.1.2 and 4.1.4 cover the inclusion of momentum transfer and ion-neutral chemistry respectively, focussing on their practical application to the model. The ionisation is described in Section 4.1.4. The numerical scheme is described in Section 4.1.5. These three aspects of the model are validated separately against analytical solutions in Section 4.1.6.

4.1.1 Implementation of acceleration by an electric field

To model the ionosphere under constant acceleration from an electric field, the continuity equations presented in Section 2.2 need to be modified to allow the ion velocity to depend

on the distance travelled from their birthplace. The ion populations in the model are distinguished by their source location r_s as well as their species j. The modelled ions are born at the neutral speed and subsequently accelerated by an electric field as they travel radially outwards from the nucleus. This means that at a given shell r_q, the ion density is the sum of the populations from each source below and equal to it ($r_s \leq r_q$), which are all travelling with different bulk velocities.

The velocity profiles $u_{j,s}(r_q)$ are calculated before solving the continuity equations. I first define the electric field as

$$E(r_q) = E_c(r_c/r_q)^m, \tag{4.1}$$

where coefficient $m \in \{0, 1, 2\}$ is an integer and $E_c[\mathrm{V\ m^{-1}}]$ is the electric field at the comet surface (r_c). Conservation of energy then dictates that

$$\frac{1}{2}m_j u_{j,s}(r_q)^2 = \frac{1}{2}m_j u_n^2 + \int_{r_s}^{r_q} E_c(r_c)\left(\frac{r_c}{r}\right)^m dr \tag{4.2}$$

where $u_{j,s}(r_q)$ is the radial speed of the ions at r_q that were produced at r_s, either through ionisation, ion-neutral chemistry, or momentum transfer, and subsequently accelerated from the neutral speed u_n by the electric field. For example, for an electric field $E \propto r^{-1}$, this then leads to an ion velocity profile:

$$u_{j,s}(r) = \sqrt{u_n^2 + \frac{2E_c r_c}{m_j}\ln\frac{r_q}{r_s}}. \tag{4.3}$$

The three velocity profiles referred to in this chapter are given in Table 4.1.

The velocity profile is calculated for the ion population of species j produced at each shell r_s. The continuity equation is then solved for each population (j, s), and the production term $P_{j,s}$ is only non-zero in the source shells (located at r_s). The contributions from each source are then summed at each cometocentric distance shell to find the total density of each species:

$$n_j(r_q) = \sum_s n_{j,s}(r_q) \tag{4.4}$$

Table 4.1: Table showing the three electric field profiles (see Equation 4.1) used throughout this chapter, and the resulting radial speed at cometocentric distance r_q for a given species j born at r_s, calculated according to Equation 4.2.

m	Electric field	Velocity profile
0	$E(r_q) = E_c$	$u_{j,s}(r_q) = \sqrt{u_n^2 + \frac{2E_c}{m_j}(r_q - r_s)}$
1	$E(r_q) = E_c r_c / r_q$	$u_{j,s}(r_q) = \sqrt{u_n^2 + \frac{2E_c r_c}{m_j} \ln \frac{r_q}{r_s}}$
2	$E(r_q) = E_c r_c^2 / r_q^2$	$u_{j,s}(r_q) = \sqrt{u_n^2 + \frac{2E_c r_c^2}{m_j}\left(\frac{1}{r_s} - \frac{1}{r_q}\right)}$

where s varies to cover cometocentric distances from $r_s = r_c$ to $r_s = r_q$.

The bulk velocity of each species can then be calculated by summing over the sources

$$u_j(r_q) = \frac{\sum_s n_{j,s}(r_q) u_{j,s}(r_q)}{\sum_s n_{j,s}(r_q)} \tag{4.5}$$

and the total ion bulk velocity u_i is the weighted mean of all species $u_i = (\sum_j n_j u_j) / \sum_j n_j$.

Consider an ion population (j, s), of species j born at a cometocentric distance r_s. In 1D and spherical symmetry, the number density $n_{j,s}(r)$ of this species, along a given radial line, is then governed by the continuity equation

$$\frac{\partial n_{j,s}}{\partial t} + \frac{1}{r^2}\frac{\partial}{\partial r}(r^2 n_{j,s} u_{j,s}) = P'_{j,s} - R'_{j,s} n_{j,s} \tag{4.6}$$

where $u_{j,s}(r)$ is the bulk speed of the species (j, s) at r. $P'_{j,s}$ and $R'_{j,s}$ represent updated production and loss terms compared to those in Equation 2.26, and are discussed further in Section 4.1.2. All ions are produced initially at the neutral radial speed, so at $r = r_s$, $u_{j,s}(r) = u_n$.

Figure 4.1 portrays the implementation of the ion acceleration in the model. For a given ion species j. Each source population s is represented by a different colour, with its own velocity profile starting at u_n at the source shell. For each source, there is no production in the further shells, only transport and loss.

The production rate of the ion population (j, s) needs to be updated from 2.6 to account for the production through momentum transfer ions $P_{j,s}(r_q, t)$ is the production rate of the ion population at u_n (in $\mathrm{cm}^{-3}\ \mathrm{s}^{-1}$), such that

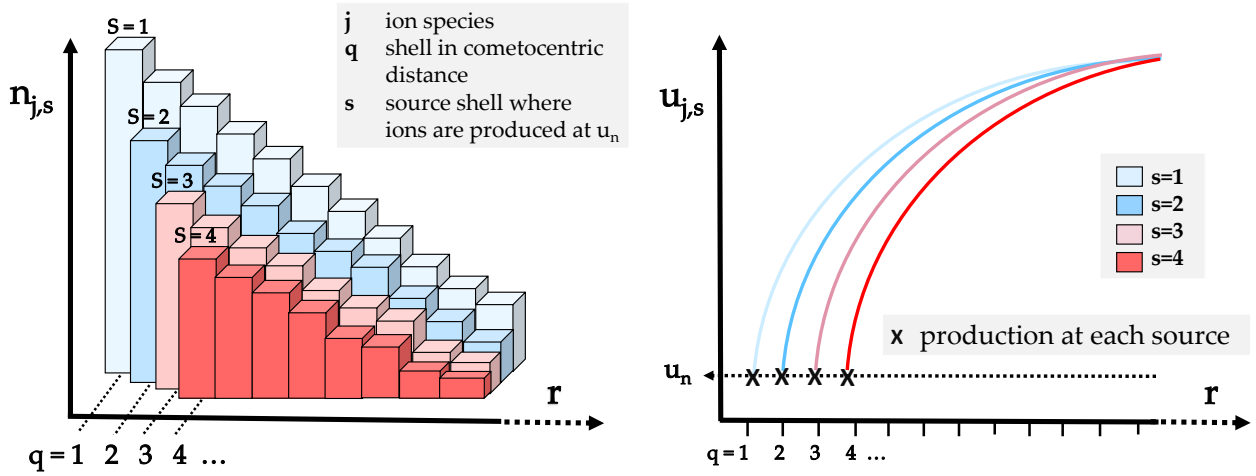

Figure 4.1: Diagrams showing the numerical scheme for implementing ion acceleration in the model for a given ion species j. Colours show different populations of ions that were produced at the neutral speed at a particular shell. Simplifications have been made for the schematic, for example Δr is not constant in the model but increases logarithmically with increasing r and n_j is shown to decrease with r which is not always the case.

$$P'_{j,s}(r_q) = P^{\text{ioni}}_{j,s}(r_q) + P^{\text{chem}}_{j,s}(r_q) + P^{\text{MT}}_{j,s}(r_q) \quad \text{for } q = s, \tag{4.7}$$

$$\text{and } P'_{j,s}(r_q) = 0 \quad \text{for } q \neq s.$$

Equivalently, the loss frequency $R_{j,s}(r_q, t)$ of the ion population (j, s) (in s^{-1}), now comprises losses due to both chemistry and momentum transfer:

$$R'_{j,s}(r_q) = R^{\text{chem}}_{j,s}(r_q) + R^{\text{MT}}_{j,s}(r_q) \tag{4.8}$$

4.1.2 Momentum transfer

The acceleration of ions can be interrupted by ion-neutral elastic collisions, where there is no change in ion species involved, but the momentum of the fast ion species is transferred to the slow neutral. For example, consider the collision between H_3O^+ and a neutral water molecule:

$$H_3O^{+\bigstar} + H_2O \rightarrow H_3O^+ + H_2O^{\bigstar}. \tag{4.9}$$

There is no change in ion species involved, but the momentum of the fast ion species is transferred to the neutral. This collision is assumed to be completely elastic, leaving the previously fast ion now at the neutral speed and the neutral at the accelerated ion speed (where 'fast' is identified by the black star ★ in Reaction 4.9).

Specific to the Ion Acceleration Model (compared to the previous continuity equation, Equation 2.26) the contribution of momentum transfer to the production rate of the ion population (j, s) (Equation 4.7) is

$$P^{\mathrm{MT}}_{j,s}(r_q) = \sum_{s'<s} L^{\mathrm{MT}}_{j,s'}(r_q) = \sum_{s'<s} F^{u_{j,s'}\rightarrow u_n}_{j,s'}(r_q) n_{j,s'}(r_q), \tag{4.10}$$

$$P^{\mathrm{MT}}_{j,s}(r_q) = 0 \text{ for } q \neq s,$$

where $L^{\mathrm{MT}}_{j,s'}(r_s)\,[\mathrm{cm}^{-3}\ \mathrm{s}^{-1}]$ is the momentum transfer loss rate and $F^{u_{j,s'}\rightarrow u_n}_{j,s'}\ [\mathrm{s}^{-1}]$ is the collision frequency for ions in population (j, s'), where $s' < s$. Put simply, this is the rate at which ions slowed down have been 'left behind' by their original population produced at $r_{s'}$ and will then contribute to the population (j, s) which were produced at r_s. This is represented schematically in Figure 4.2. All ions of all j and s are produced at the neutral speed u_n.

Conversely, the ions originally in population (j, s) and 'left behind' by the accelerating ions after undergoing an ion-neutral collision at radial distance r_q will then make up the momentum transfer loss frequency. They are produced at neutral velocity u_n. In this model I use simple constant collision rate coefficients $k^{\mathrm{MT}}_{j,n}\ [\mathrm{cm}^3\ \mathrm{s}^{-1}]$ (given in Appendix A) such that

$$R^{\mathrm{MT}}_{j,s}(r_q) = F^{u_{j,s}\rightarrow u_n}_{j,s}(r_q) = \sum_n k^{\mathrm{MT}}_{j,n} n_n(r_q). \tag{4.11}$$

4.1.3 Ion-neutral chemistry

Unlike in the full ionospheric model (see Section 3.4.2), the Ion Acceleration Model is restricted to only three key ion species: H_2O^+, H_3O^+ and NH_4^+. H_2O^+ is the only species that is directly

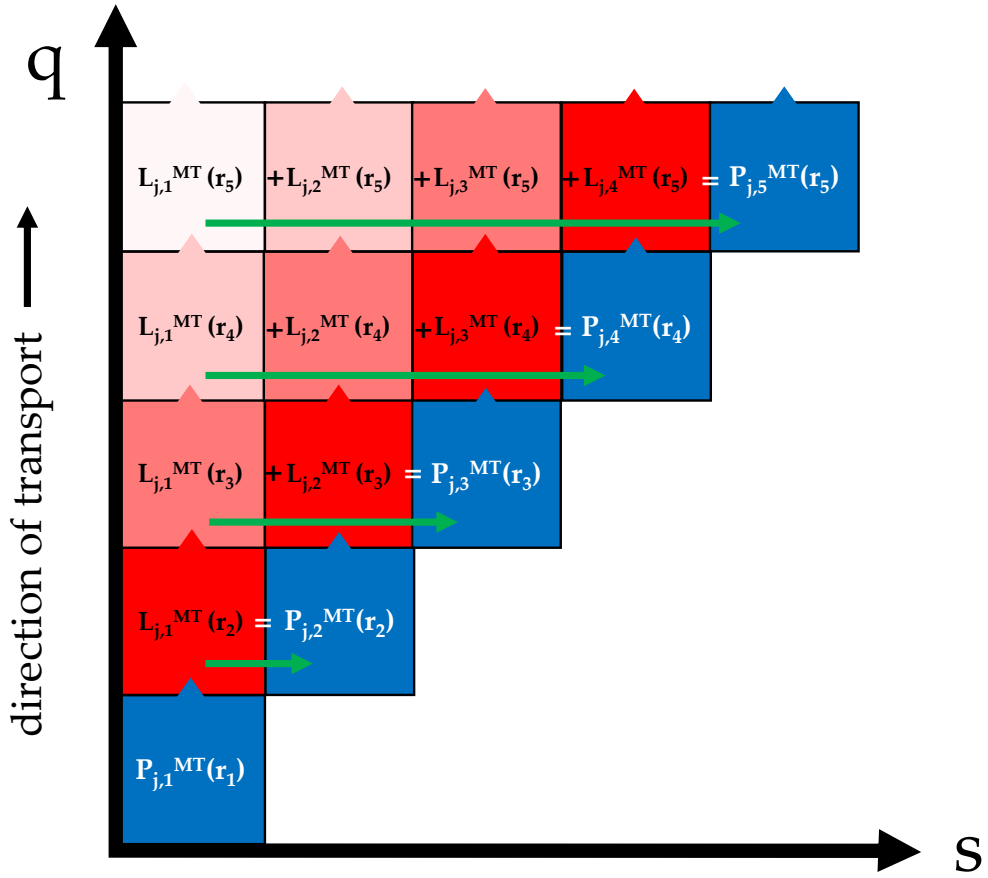

Figure 4.2: Schematic showing how the momentum transfer production rate $P_{j,s}^{\mathrm{MT}}(r_q)$ for each population j, s is calculated from the loss terms in Equation 4.10.

produced by ionisation, and the other two are produced in turn through protonation reactions. The interaction of the three ion species with each other and with the neutral species (only H_2O and NH_3 here) is summarised in Figure 4.3. The simplified neutral gas coma used (represented by green boxes in Figure 4.3) is comprised of a small fraction of NH_3 (f_{NH_3}) and the rest is water ($f_{H_2O} = 1 - f_{NH_3}$). For input values of f_{NH_3}, outgassing Q, and neutral speed u_n, the neutral density $n_n(r)$ of each species n is calculated using the simplified Haser model (see Section 2.1).

In the model, H_3O^+ can only be produced from the protonation of H_2O^+ and NH_4^+ can be produced from the protonation of either H_2O^+ or H_3O^+. This allows us to label H_2O^+, H_3O^+ and NH_4^+ as $j = 1, 2, 3$ and to solve their continuity equations in turn, since the dependence of each ion species on the next is unidirectional. Hence, in Equation 4.6 the production rate of each ion species j, produced at r_s is given by

$$P_{j,s}^{\text{chem}}(r_q) = \sum_{n,s',j'<j} k_{j',n\to j}^{\text{IN}} n_n n_{j',s'}(r_q) \quad \text{for } q = s, j \neq 1 \tag{4.12}$$

and

$$P_{j,s}^{\text{chem}}(r_q) = 0 \quad \text{for } q \neq s, j = 1.$$

The reaction rate coefficients k^{IN} that were used are given in Appendix A. Note that there is no ion-neutral chemical production for $j = 1$, since H_2O^+ is only produced directly through ionisation of the neutral water. Again, all ions of all j and s are produced at the neutral speed u_n.

The loss frequency introduced in Equation 4.6 is simply given by

$$R_{j,s}^{\text{chem}}(r_q) = \underbrace{\sum_{n,j'\neq j} k_{j,n\to j'}^{\text{IN}} n_n(r_q)}_{\substack{\text{ion-neutral} \\ \text{chemistry}}} + \underbrace{\alpha_j^{\text{DR}} n_e(r_q)}_{\substack{\text{dissociative} \\ \text{recombination}}}, \tag{4.13}$$

i.e. very similar to Equation 2.25 which was given in Chapter 2, but with the electron density $n_e(r_q)$ recalculated by summing over all the ion species j and source locations s at the end of a full model run (see Section 4.1.5).

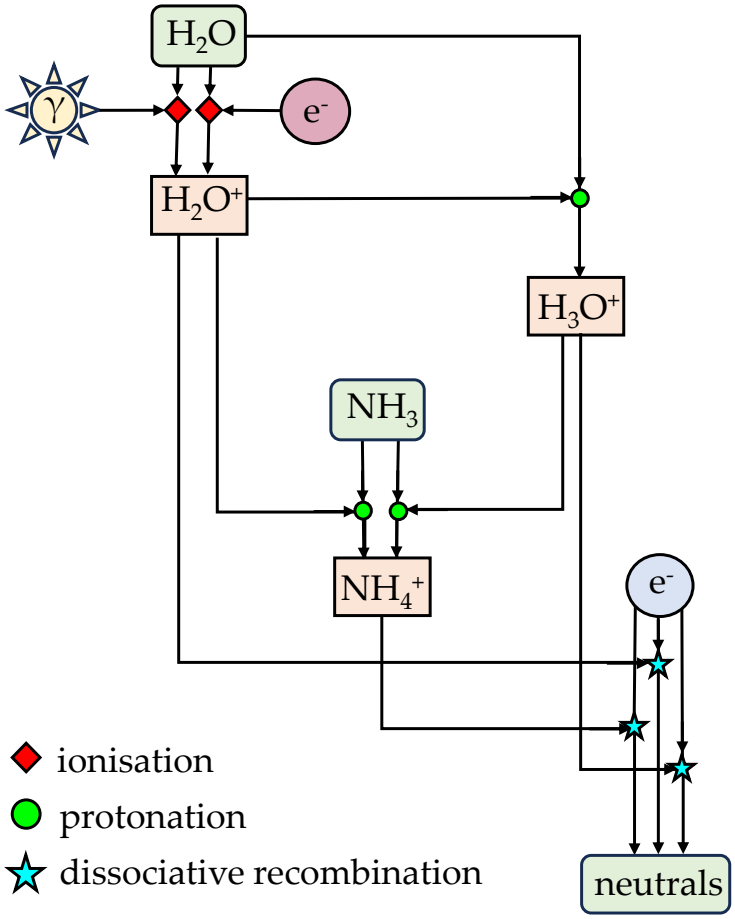

Figure 4.3: Schematic representation of the ionisation of a neutral species by solar photons γ or e^-, protonation, and dissociative recombination reactions included in the Ion Acceleration Model.

4.1.4 Ionisation

The two main ionisation sources for cometary ions are photoionisation and electron impact (Section 2.2.1). However, the importance of electron impact has been shown to be low at the location of Rosetta compared to photoionisation near perihelion when the outgassing is high (Stephenson *et al.*, 2023). Large electron-impact ionisation frequencies can be driven by acceleration of solar wind electrons (such as 67P away from perihelion, Madanian *et al.*, 2016a, Deca *et al.*, 2017, Galand *et al.*, 2020) or by absorption of X-rays at very large outgassing rates (such as 1P/Halley, Bhardwaj, 2003). Neither of these mechanisms are significant in the diamagnetic cavity of 67P near perihelion, so it is reasonable to neglect ionisation by

electron impact over the full range of r in the Ion Acceleration Model when it is applied to the diamagnetic cavity. Photoionisation of the most dominant neutral species, H_2O, is the most important ionisation reaction and results in the production of H_2O^+ at the same speed as the neutral coma (u_n).

The ionisation frequency $\nu_{n\to j}^{ioni}$ is calculated using the photoionisation cross sections for each neutral species $\sigma_{n\to j}^{ioni}(\lambda)$, combined with the attenuated solar EUV spectrum, calculated from the Lamber-Beer law using the unattenuated solar flux from TIMED/SEE (Woods *et al.*, 2005) adjusted to the heliocentric distance of the comet. A time shift is applied to correct for the difference in solar phase angle between the comet and the Earth (Galand *et al.*, 2016). The profiles of the photoionisation frequency with cometocentric distance, for the two case studies discussed in Section 4.3, are shown in Figure 4.4, attesting greater attenuation by the neutral coma when the outgassing is higher in July 2015 compared to November 2015.

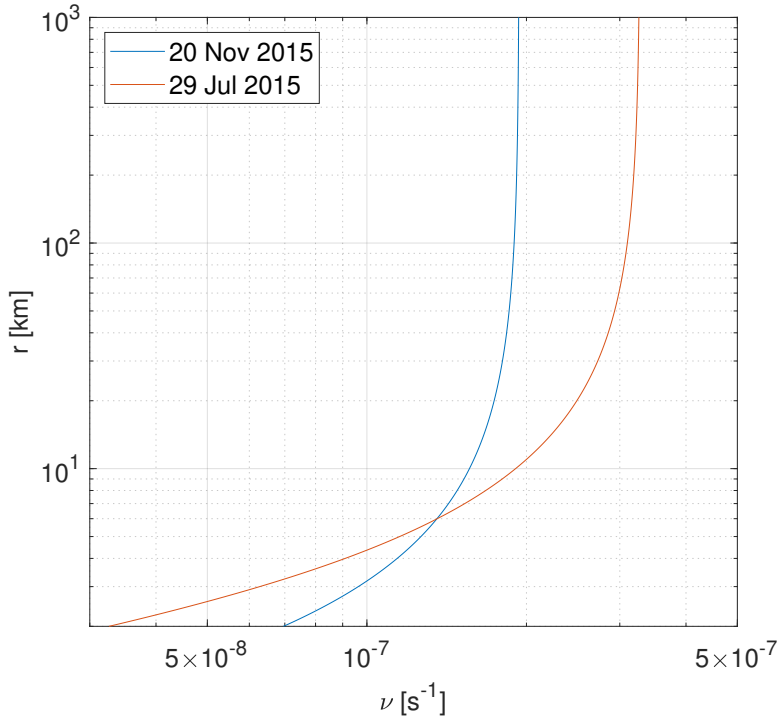

Figure 4.4: Photoionisation rate profiles for the two cases examined in Section 4.3 (see inputs in Table 4.3). Credit: Lewis *et al.* (2024)

4.1.5 Numerical scheme

The ion density profiles are computed by solving the continuity equation (Equation 2.26) for each ion species j and source location r_s, over finite volumes delineated by concentric spherical shells q (delimited by $r_q - \Delta r$ and r_q) around the nucleus. Time is divided into time steps Δt, and the ion density is assumed to be constant throughout each shell.

To find the change in ion density at each time step, Equation 2.26 is separated into an inhomogeneous equation with no transport (Equation 4.14) and a homogeneous pure transport equation (Equation 4.18).This approach is the same as that which was applied by Heritier *et al.* (2017a).

Inhomogeneous local equation

When transport is neglected, Equation (4.6) applied to the cometocentric distance r_q is reduced to the inhomogeneous equation:

$$\frac{\mathrm{d}n_{j,s}(r_q,t)}{\mathrm{d}t} + R_{j,s}(r_q,t)n_{j,s}(r_q,t) = P_{j.s}(r_q,t). \tag{4.14}$$

The general solution of the associated homogeneous equation is $n_{j,s}(r_q,t) = C(r_q,t_l)e^{-R_{j,s}(r_q,t_l)t}$ for $t \in [t_l, t_l + \Delta t]$, assuming that $R_{j,s}$ does not vary over the interval. Hence, a particular solution of Equation (4.14) is of the form:

$$n_j(r_q,t) = C(r_q,t)e^{-R_{j,s}(r_q,t_l)t}. \tag{4.15}$$

Integrating Equation (4.14) with this form between t_l and $t_l + \Delta t$ (and assuming that $R_{j,s}$ and $P_{j.s}$ don't vary over this interval) gives

$$C(r_q,t_l+\Delta t) = \frac{P_{j,s}(r_q,t_l)}{R_{j,s}(r_q,t_l)}e^{R_{j,s}(r_q,t_l)t_l}(e^{R_{j,s}(r_q,t_l)\Delta t} - 1) + C(r_q,t_l). \tag{4.16}$$

Combining Equation 4.15 and 4.16, we can then derive the solution of Equation 4.14 at $t_l + \Delta t$:

$$n_{j,s}(r_q, t_l + \Delta t) = n_{j,s}(r_q, t_l) + (1 - e^{-R_{j,s}(r_q,t_l)\Delta t}) \left(\frac{P_{j,s}(r_q, t_l)}{R_{j,s}(r_q, t_l)} - n_{j,s}(r_q, t_l) \right). \tag{4.17}$$

Homogeneous transport equation

When ion production, ion chemistry and momentum transfer are neglected, Equation 4.6 is reduced to a transport-only equation given by:

$$\frac{\partial n_{j,s}(r,t)}{\partial t} + \frac{1}{r^2}\frac{\partial}{\partial r}(n_{j,s}(r,t)r^2 u_{j,s}(r)) = 0. \tag{4.18}$$

As the ion velocity is always radially outwards, the density at each shell q is only affected by those below it. Between t_l and $t_l + \Delta t$, the change in ion density due to transport in each shell will therefore be composed of the difference between the amount of ions flowing out of it into the next shell up, and into it from below. It is required that $u_{j,s}(r_q)\Delta t < \Delta r$ for all r_q so that no ions may move further than the next shell $(q + 1)$ during each time step.

The volume of the spherical shell q, delimited by $r_{q-1} = r_q - \Delta r$ and r_q, is

$$\frac{4}{3}\pi(r_q^3 - (r_q - \Delta r)^3), \tag{4.19}$$

If the particles in the shell move at speed $u_{j,s}(r_q)$, then between t_l and $t_l + \Delta t$ they travel $u_{j,s}(r_q)\Delta t$. Therefore, the fraction of the shell that leaves the volume during Δt is

$$f_L(r_q) = \frac{r_q^3 - (r_q - u_{j,s}(r_q)\Delta t)^3}{r_q^3 - (r_q - \Delta r)^3}, \tag{4.20}$$

Similarly, the fraction entering from the shell below is

$$f_E(r_q) = \frac{(r_q - \Delta r)^3 - ((r_q - \Delta r) - u_{j,s}(r_{q-1})\Delta t)^3}{r_q^3 - (r_q - \Delta r)^3}. \tag{4.21}$$

therefore the net change in the ion density in the shell due to transport only is:

$$\Delta n_{j,s}(r_q) = n_{j,s}(r_q, t_l + \Delta t) - n_{j,s}(r_q, t_l) = f_E(r_q) n_j(r_q - \Delta r, t_l) - f_L(r_q) n_j(r_q, t_l). \quad (4.22)$$

Putting it together

The total net change at each time step is the sum of the homogeneous and inhomogeneous solutions, and is given by:

$$\begin{aligned} \Delta n_{j,s}(r_q, t_l) = (1 - e^{-R_{j,s}(r_q,t_l)\Delta t}) \left(\frac{P_{j,s}(r_q, t_l)}{R_{j,s}(r_q, t_l)} - n_{j,s}(r_q, t_l) \right) \\ + f_E(r_q) n_j(r_q - \Delta r, t_l) - f_L(r_q) n_j(r_q, t_l). \end{aligned} \quad (4.23)$$

The solution is also equivalent to the forward Euler method for small timesteps:

$$\begin{aligned} \Delta n_{j,s}(r_q, t_l) = P_{j,s}(r_q, t_l)\Delta t - R_{j,s} n_{j,s}(r_q, t_l)\Delta t \\ + f_E(r_q) n_j(r_q - \Delta r, t_l) - f_L(r_q) n_j(r_q, t_l). \end{aligned} \quad (4.24)$$

Since the flow of ions is entirely radial and directed outwards from the surface, there is no inflow from below the surface into the first shell and $f_E(r_c) = 0$, where r_c is the comet radius. The ion density, $n_{j,s}(r_q, t_l)$, is then computed until steady state is reached and the total ion density, n_j, for each species j calculated according to Equation 4.4. The condition for convergence is that $|\Delta n_j|/n_j < 10^{-8}$ for every r_q and j.

The electron density n_e (used to calculate R_j^{chem}, see Equation 4.13) is then recalculated by summing the total ion density over all the source populations:

$$n_e(r_q) = \sum_{j,s} n_{j,s}(r_q). \quad (4.25)$$

The solution is found again for every j and s and the process repeated until $\Delta n_e/n_e < 10^{-4}$ for all r_q.

4.1.6 Validation of the model

The Ion Acceleration Model is validated against analytical solutions for each of the three core components of the numerical scheme: momentum transfer (Model I), ion-neutral chemistry (Model II), and electric field acceleration (Model III). In all cases, dissociative recombination is neglected, the neutral speed $u_n = 1\ \mathrm{km\,s^{-1}}$, the photoionisation frequency $1 \times 10^7\ \mathrm{s^{-1}}$ and the comet radius $r_c = 2\ \mathrm{km}$. The aspects of the full model taken into account in each of the three analytical models are given in Table 4.2.

Table 4.2: Summary of the assumptions included in the three analytical models used to validate the Ion Acceleration Model in Section 4.1.6.

Analytical model	**I**	**II**	**III**
Extended source of ions	x	✓	✓
Ion acceleration	x	x	✓
Ion-neutral chemistry	x	✓	x
Momentum transfer	✓	x	x

Analytical model I: Momentum transfer

First, the momentum transfer numerical scheme is checked against a simple analytical model where a population of ions (single species) produced from the surface at a speed $u_i > u_n$ is considered. The ions are then transported radially outwards, undergoing momentum transfer collisions with the neutrals, but with no ion-neutral chemistry or dissociative recombination loss. Ions that have collided with a neutral have their speed reduced to the neutral speed. There are then two populations of ions, 'hot' ($n_H(r)$) and 'cold' ($n_C(r)$) at constant speeds u_i and u_n, respectively. The two populations follow the coupled continuity equations:

$$\frac{1}{r^2}\frac{d}{dr}(n_H(r)u_i r^2) = -k^{\mathrm{MT}} n_H(r) n_n(r) \tag{4.26}$$

$$\frac{1}{r^2}\frac{\mathrm{d}}{\mathrm{d}r}(n_C(r)u_n r^2) = k^{\mathrm{MT}} n_H(r) n_n(r) \tag{4.27}$$

which can be solved to find

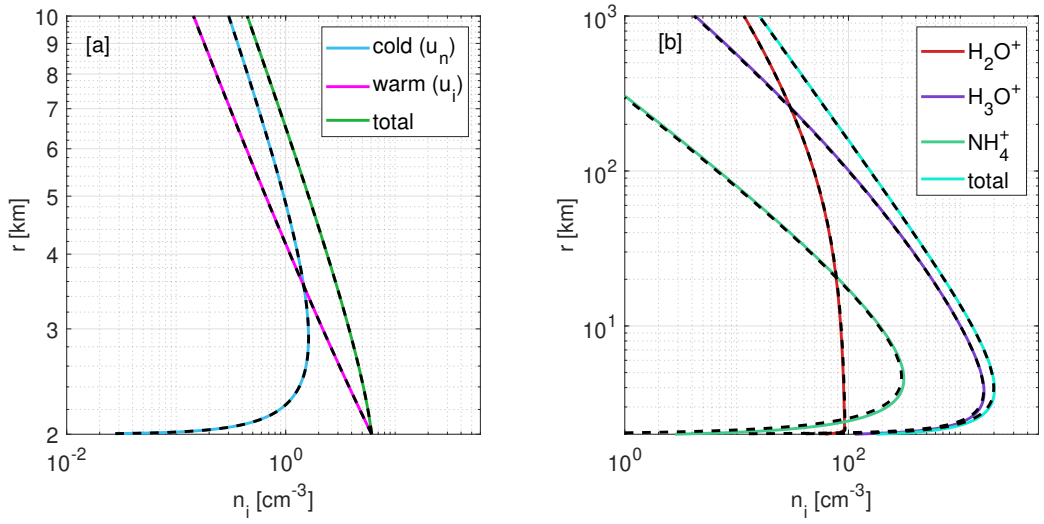

Figure 4.5: (**a**) Density profile of ions at u_i (**pink**) and u_n (**blue**) and the total density (**green**) for the present numerical model in comparison with analytical model I described in equations 4.29 and 4.28. (**b**) Density profile of H_2O^+ (red), H_3O^+ (**purple**) and NH_4^+ (**green**), as well as the total density (**cyan**) for the present numerical model in comparison with analytical model II. In both (a) and (b), the **coloured lines** show the numerical model, and the corresponding analytical model is shown by **black dashed lines**. Credit: Lewis *et al.* (2024)

$$n_H = \frac{n_H(r_c) r_c^2}{r^2} \exp\left(\frac{\mathrm{C}_0}{r} - \frac{\mathrm{C}_0}{r_c}\right) \tag{4.28}$$

$$n_C = \frac{n_H(r_c) r_c^2 u_i}{r^2 u_n} \left(1 - \exp\left(\frac{\mathrm{C}_0}{r} - \frac{\mathrm{C}_0}{r_c}\right)\right) \tag{4.29}$$

where $\mathrm{C}_0 = (k^{\mathrm{MT}} Q)/(4\pi u_n u_i)$. The results of comparison between Equations 4.29 and 4.28, and the numerical model with the same assumptions are given in Figure 4.5a, for $Q = 10^{27}\ \mathrm{s}^{-1}$ and $k^{\mathrm{MT}} = 5 \times 10^{-11}\ \mathrm{cm}^3\ \mathrm{s}^{-1}$. The numerical and analytical models show a very good agreement, with the maximum relative difference in the total ion density of 0.5% for the logarithmically spaced bins described in Section 4.1, and for $u_n = 1\ \mathrm{km\ s}^{-1}$ and $u_i = 3\ \mathrm{km\ s}^{-1}$. The difference results from the finite cell size in the numerical approach.

Analytical model II: Ion-neutral chemistry

Next, the implementation of ion-neutral chemistry in the model is validated. With acceleration, dissociative recombination and momentum transfer neglected, and considering a

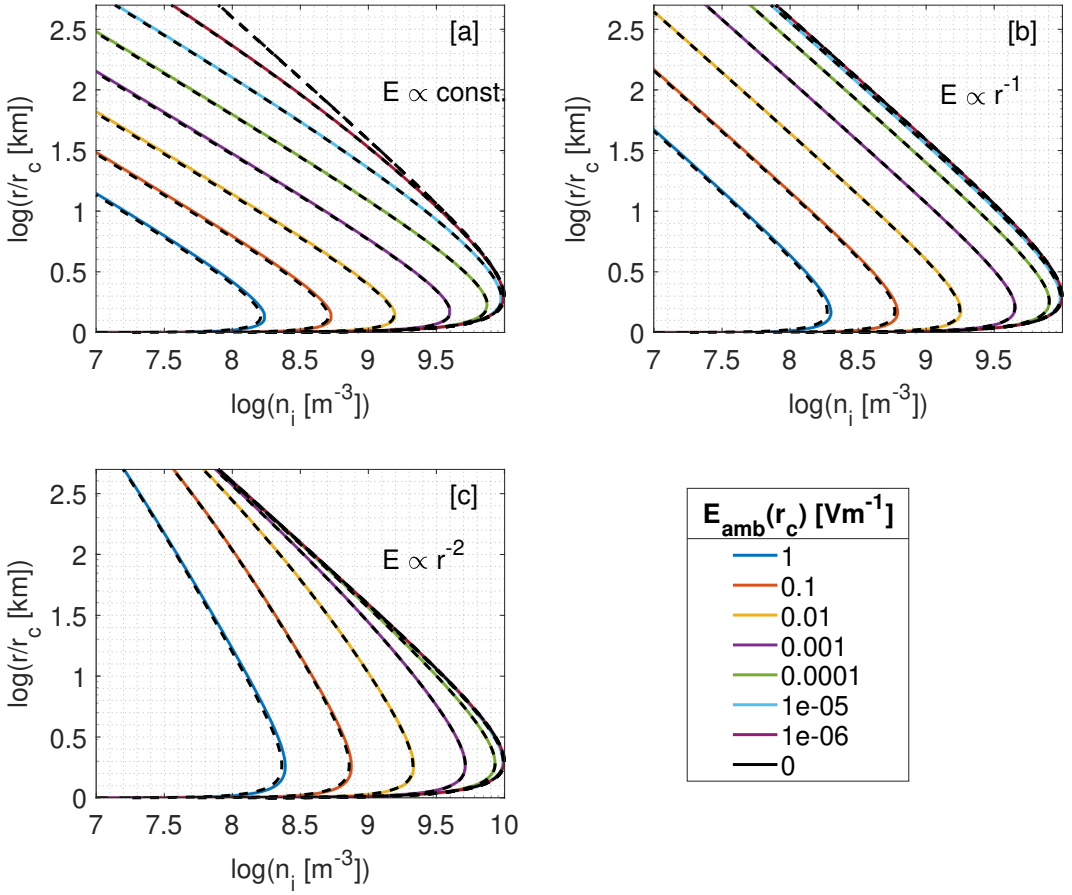

Figure 4.6: Total ion density profiles from the Ion Acceleration Model (**coloured lines**) compared to analytical model III (**black dashed lines**) for $Q = 10^{28}\mathrm{s}^{-1}$. Electric fields are of varying strengths and $\propto$ const. (**a**), $\propto r^{-1}$ (**b**), and $\propto r^{-2}$ (**c**). Credit: Lewis *et al.* (2024)

monoenergetic solar radiation at noon, it is possible to derive an analytical solution to the coupled continuity equations for three ion species (H_2O^+, H_3O^+, and NH_4^+):

$$\frac{1}{r^2}\frac{\mathrm{d}(n_{\mathrm{H_2O^+}}u_n r^2)}{\mathrm{d}r} = n_n^{\mathrm{tot}}(r)\left[\nu\exp\left(-\tau r_c/r\right) - (k_1 f_{\mathrm{H_2O}} + k_2 f_{\mathrm{NH_3}})n_{\mathrm{H_2O^+}}\right], \tag{4.30}$$

$$\frac{1}{r^2}\frac{\mathrm{d}(n_{\mathrm{H_3O^+}}u_n r^2)}{\mathrm{d}r} = n_n^{\mathrm{tot}}(r)\left[k_1 f_{\mathrm{H_2O}} n_{\mathrm{H_2O^+}} - k_3 f_{\mathrm{NH_3}} n_{\mathrm{H_3O^+}}\right], \tag{4.31}$$

$$\frac{1}{r^2}\frac{\mathrm{d}(n_{\mathrm{NH_4^+}}u_n r^2)}{\mathrm{d}r} = n_n^{\mathrm{tot}}(r)\left[k_2 f_{\mathrm{NH_3}} n_{\mathrm{H_2O^+}} + k_3 f_{\mathrm{NH_3}} n_{\mathrm{H_3O^+}}\right]. \tag{4.32}$$

where k_1, k_2 and k_3 are the relevant chemical rate coefficients (see Appendix A) and τ is the optical depth. The solutions to these equations are given in Lewis *et al.* (2024).

The analytical solutions are over-plotted in Figure 4.5b, with the result of the numerical model with the same assumptions and for $Q = 10^{27}\mathrm{s}^{-1}$, $f_{\mathrm{NH_3}} = 0.01$, $f_{\mathrm{H_2O}} = 0.99$, and $\tau = 0$ (optically thin coma at the surface). The two models show again very good agreement, with maximum variation 5%, for again the logarithmically spaced bins described in the introduction of Section 4.1.

Analytical model III: Electric field acceleration

Finally, the effect on the number density of the electric field can be validated analytically by the consideration of a single species model with no momentum transfer, no ion-neutral chemistry, and no dissociative recombination. The model is described in Lewis *et al.* (2024) and is compared to the present numerical model in Figure 4.6, for electric fields $\propto \mathrm{const.}$ (a), $\propto r^{-1}$ (b), and $\propto r^{-2}$ (c). Again, the maximum difference between the analytical model and the Ion Acceleration Model numerical scheme is around 5%.

4.2 Ion composition and ionospheric densities

In this section, I explore the sensitivity of the model output to momentum transfer and to the electric field. In order to assess the relative importance of different terms in the continuity equation, I compare the timescales for the various transport and chemical loss processes for each species. Processes occurring with a shorter timescale will dominate, while those with significantly longer timescales will only have a minor impact on the overall ion density profile.

The transport timescale $\tau_{trans,j}$ for an ion species j with density $n_j(r) = \sum_s n_{j,s}(r)$ and bulk velocity $u_j(r)$ (calculated according to Equation 4.5) can be derived from the transport term in the continuity equation (Equation 4.6) as:

$$\frac{1}{\tau_{trans,j}(r)} = \frac{1}{n_j(r)r^2}\frac{\mathrm{d}(n_j(r)u_j(r)r^2)}{\mathrm{d}r}. \tag{4.33}$$

Similarly, the dissociative recombination timescale $\tau_{DR,j}$ for species j is given by:

$$\frac{1}{\tau_{DR,j}(r)} = \alpha_{DR,j}n_e(r) \tag{4.34}$$

where $\alpha_{DR,j}$ is the recombination rate as defined in Equation 2.25. Finally, the proton transfer loss timescale $\tau_{PT,j}$

$$\frac{1}{\tau_{PT,j}(r)} = \sum_{n,j'\neq j} k^{\mathrm{IN}}_{j,n\rightarrow j'}n_n(r). \tag{4.35}$$

Figure 4.7 shows these timescales for each of the three ion species (right side) alongside the ion density profiles (left side) for input electric field profiles $\propto 1/r$ with three different surface field strengths: $0\ \mathrm{mV\ m^{-1}}$, $1\ \mathrm{mV\ m^{-1}}$ and $10\ \mathrm{mV\ m^{-1}}$. The density profile of H_2O^+ varies very little with the electric field strength (Figure 4.7a), owing to the proton transfer timescale that is always shorter than both the transport and dissociative recombination timescales (Figure 4.7b). As previously documented (e.g. Vigren and Galand, 2013), H_2O^+ is close to photochemical equilibrium at this outgassing rate ($10^{28}\ \mathrm{s^{-1}}$) and low cometocentric distances, such that $n_{\mathrm{H_2O+}}$ is mostly governed by the change in ionisation frequency. At

high cometocentric distance, the $10\ \mathrm{mV\ m^{-1}}$ case begins to exhibit a small departure from photochemical equilibrium, as the transport timescale is decreased such that it is more similar in magnitude to the proton transfer timescale.

H_3O^+ is only produced through the proton transfer from H_2O^+ (see Section 2.2.2) and is therefore more sensitive to the increasing electric field than H_2O^+ (See Figures 4.7c and 4.7d). With the strongest electric field ($10\ \mathrm{mV\ m^{-1}}$, red) the proton transfer has the shortest timescale below $10\mathrm{km}$, so loss of H_3O^+ to NH_4^+ dominates close to the nucleus. With no electric field (black), this continues up to $100\ \mathrm{km}$. Transport then takes over, reflected in the transport timescale becoming shorter than the proton transfer timescale, hence the ion density begins to decrease rapidly. In the prescence of an electric field, the H_3O^+ density profile reaches a slope in $1/r$ above $\sim 100\ \mathrm{km}$. When the electric field is applied, the dissociative recombination timescale is always at least an order of magnitude larger than the transport timescale, so this is not a significant loss process for this ion species.

NH_4^+ is the most sensitive of the three ion species to the increasing electric field, with the density over an order of magnitude lower at $100\ \mathrm{km}$ with a $10\ \mathrm{mV\ m^{-1}}$ electric field than when there is none. This means that the presence and strength of the ambipolar electric field may have important consequences for the formation and detectability of NH_4^+ within the diamagnetic cavity. The transport timescale is always shorter than the dissociative recombination timescale. The difference is particularly marked when the strong ($10\ \mathrm{mV\ m^{-1}}$) electric field is applied: transport dominates. This, combined with the lack of NH_4^+ production at high cometocentric distances, means that it is quickly transported away, and the ion density slope is in $1/r^2$ above $\sim\ 300\mathrm{km}$. This is the same as the pure transport solution (no production or chemical loss) to the continuity equation (Equation 2.26). With lower electric field, DR becomes increasingly important at high cometocentric distances and the slope of the NH_4^+ profile is between r^{-1} and r^{-2}.

Figure 4.8 shows the effect of including momentum transfer on the density of the three ion species as well as their sum. As anticipated, the addition of momentum transfer increases the ion density, since the acceleration process is interrupted, slowing the bulk ion speed and allowing the ionosphere to build up more before it is transported. H_2O^+, however, is

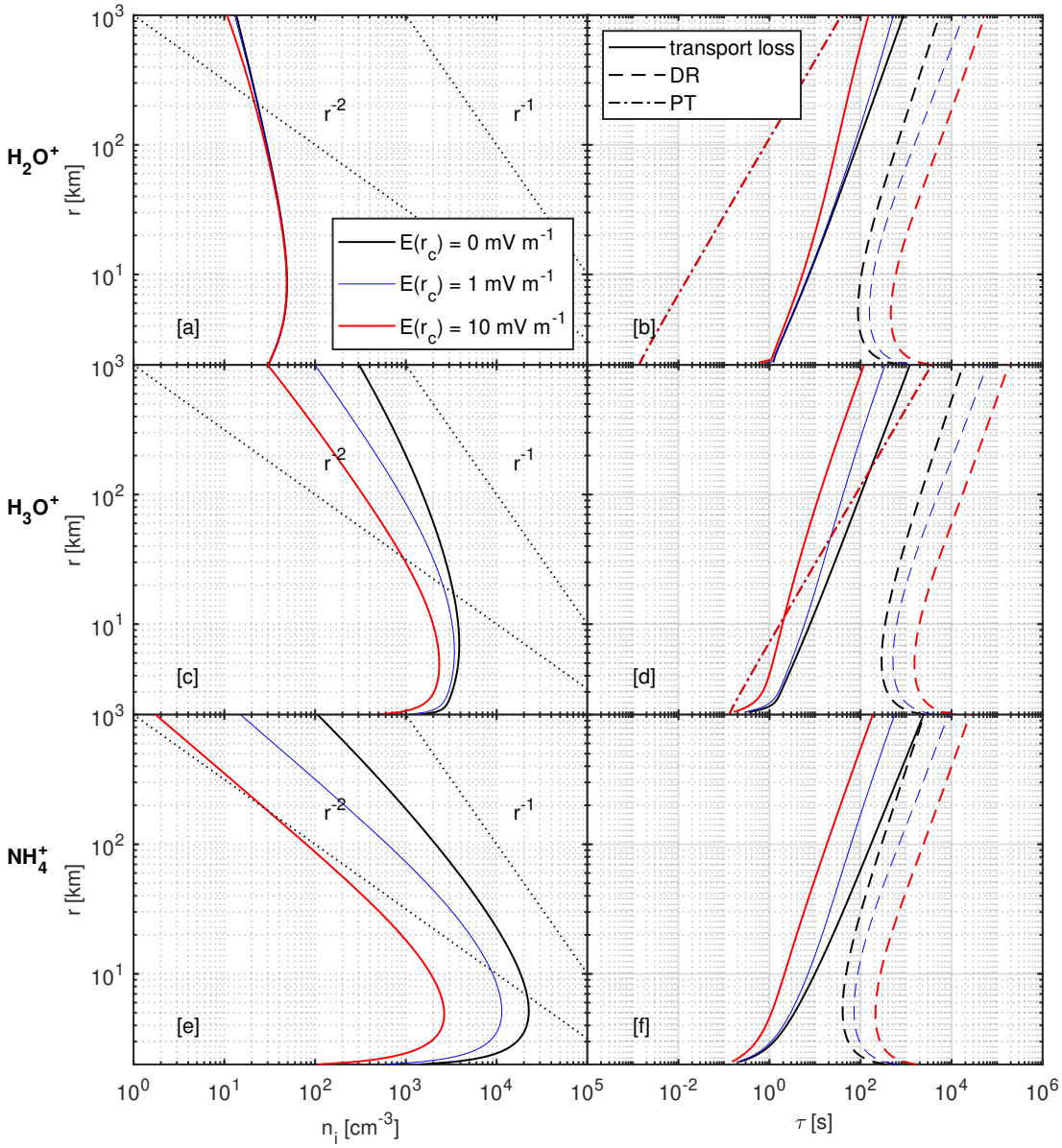

Figure 4.7: Ion density (**a,c,e**) and loss timescales (**b,d,e**) for H_2O^+ (**a,b**), H_3O^+ (**c,d**) and NH_4^+ (**e,f**). Three different electric field conditions are considered: no electric field (**black**), $E(r_c) = 1\text{mV m}^{-1}$ (**blue**) and $E(r_c) = 10\text{mV m}^{-1}$ (**red**). The three loss timescales are transport (Equation 4.33, **solid line**), dissociative recombination (DR, Equation 4.34, **dashed**) and proton transfer (PT, Equation 4.35, **dot-dashed**). The proton transfer timescales are overlapping. The electric field is assumed to be radial and proportional to $1/r$, the outgassing $Q = 10^{28}\text{s}^{-1}$, and the neutral composition to be 1% NH_3 and 99% H_2O. Credit: Lewis *et al.* (2024)

unaffected since it is close to photochemical equilibrium and therefore not sensitive to the transport timescale. Momentum transfer has the greatest impact on the NH_4^+ density, not only because of its decreased transport loss, but also because of its enhanced production. The slowing of H_3O^+ ions through ion-neutral collisions allows protonation to occur more readily.

The influence of both the electric field and momentum transfer on the total density and ion bulk speed is summarised in Figure 4.9, for electric field proportional to $1/r$ (a and b) and $1/r^2$ (c and d). In all cases, the total density is higher when momentum transfer is included, and the bulk speed is lower. Vigren *et al.* (2015) found for the case of an electric field decreasing as r^{-1}, in the absence of momentum transfer and for the case of water ions, the $n_i \propto 1/r$ relation is recovered above the density peak for all electric field strengths. I found that this remains valid for the case of three ions species with momentum transfer included.

4.3 Comparison with Rosetta data

I now focus on two key time periods during the Rosetta escort phase, comparing the total density derived from RPC–MIP and RPC–LAP inside the diamagnetic cavity with the total ion density from the Ion Acceleration Model for various electric field profiles. Doing so allows to determine the range of electric field strengths which are required in the model to explain the measurements from Rosetta. I also compare the predicted versus the measured NH_4^+ density with the same inputs and electric field strengths.

The first period I consider is 20th–21st November 2015, and a summary of the key data is given in Figure 4.10. Rosetta spent a significant amount of time inside the diamagnetic cavity (blue shaded vertical boxes) during this window, and there is strong coverage of the combined MIP/LAP dataset (black, bottom panel). On 21st November, the ROSINA-DFMS high resolution ion mode was briefly active, and captured signatures of NH_4^+ consistently (see Figure 4.10), hence this makes an interesting case study for comparison with the Ion Acceleration Model.

I also consider 29th–30th July 2015, two weeks before perihelion, which saw some of the strongest NH_4^+ signatures and many diamagnetic cavity crossings (see Figure 4.11). The

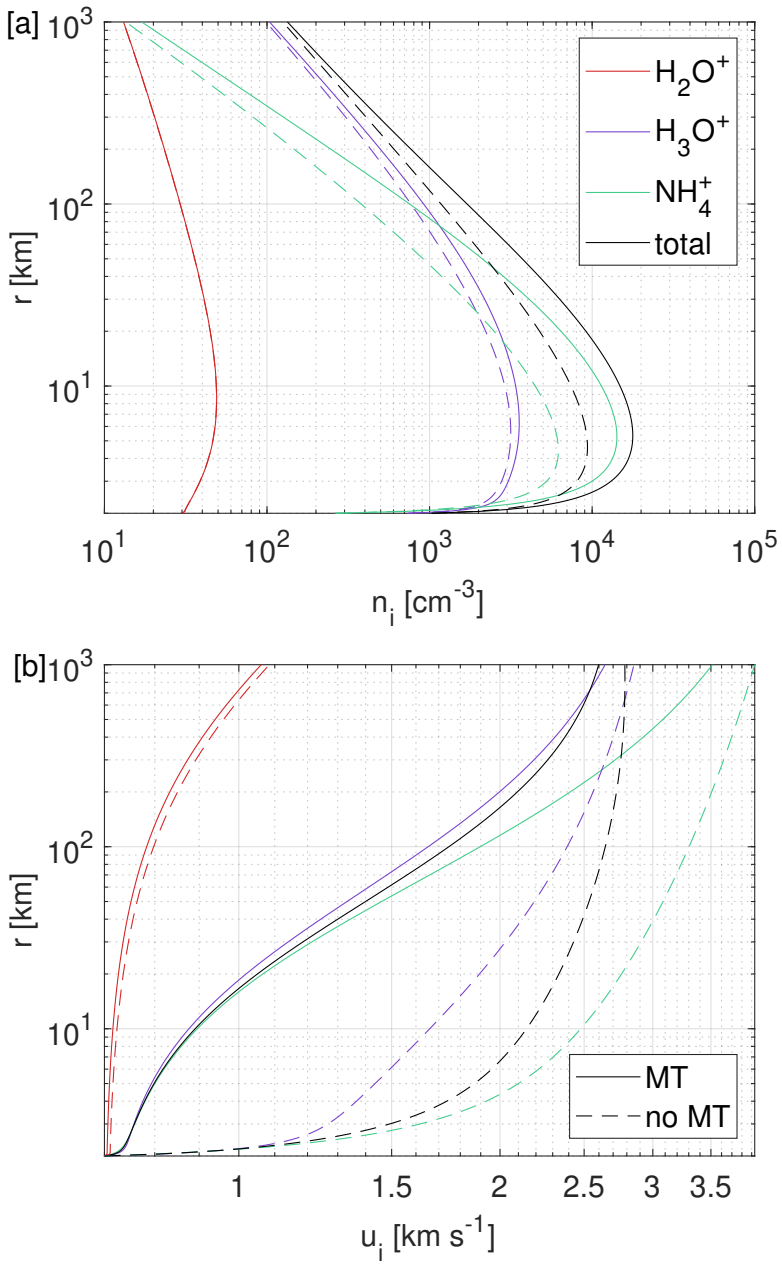

Figure 4.8: (**a**) Ion density for H_2O^+ (red), H_3O^+ (**purple**) and NH_4^+ (**green**), both with momentum transfer (**solid line**) and without (**dashed line**) momentum transfer. (**b**) Ion bulk speed for each ion shown in (a), calculated according to Equation 4.5. The electric field was assumed to be $E = 1 \times 10^{-3}(r_c/r)\mathrm{V\ m^{-1}}$, the outgassing $Q = 10^{28}\mathrm{s^{-1}}$, and the neutral composition to be $1\%NH_3$ and $99\%H_2O$. Credit: Lewis *et al.* (2024)

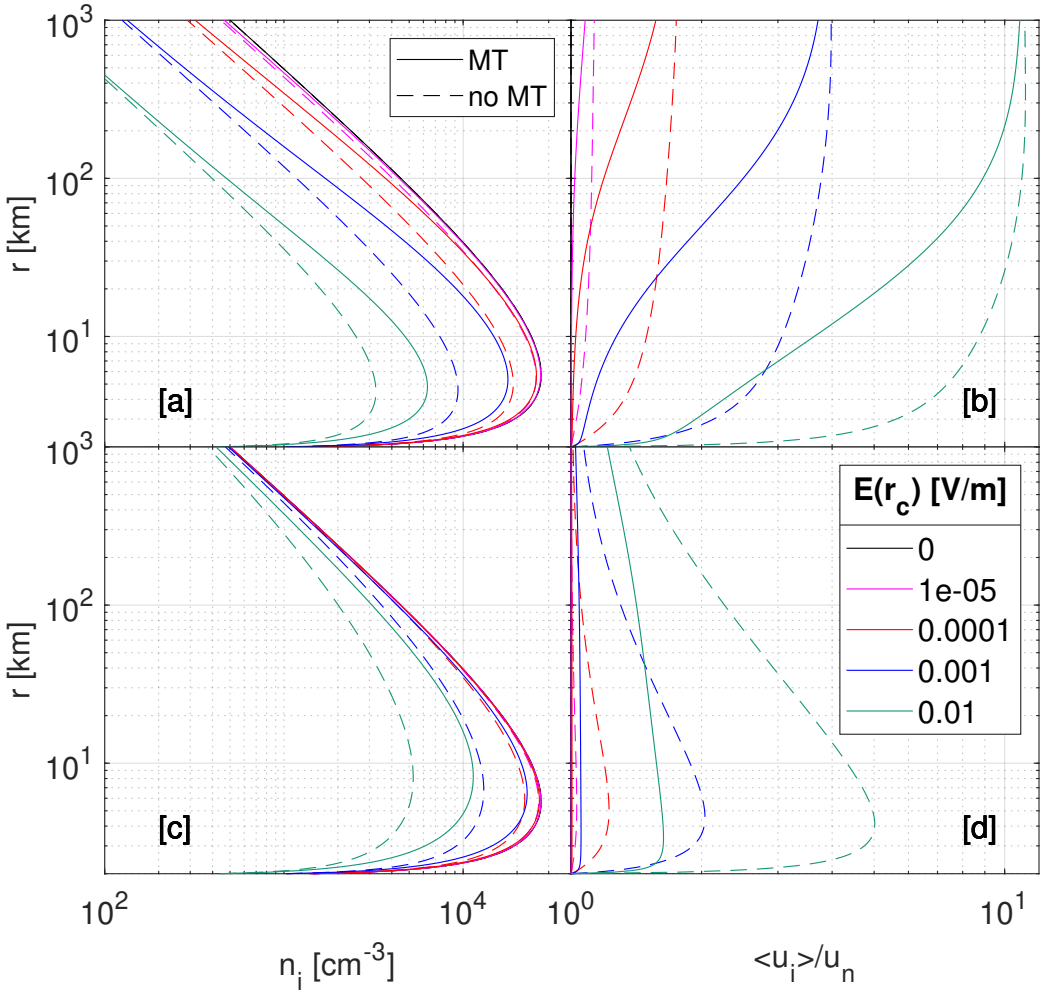

Figure 4.9: (**a**) Total ion density for different electric field strengths with $E \propto 1/r$, with (**solid line**) and without (**dashed line**) momentum transfer. (**b**) Ion bulk speed as a fraction of the neutral velocity for the case in (a). (**c**) Same as (a) but for $E \propto 1/r^2$. (**d**) Ion bulk speeds for case in (c). The outgassing used is $Q = 10^{28}\mathrm{s}^{-1}$, and the neutral composition is 1% $\mathrm{NH_3}$ and 99% $\mathrm{H_2O}$. Credit: Lewis *et al.* (2024)

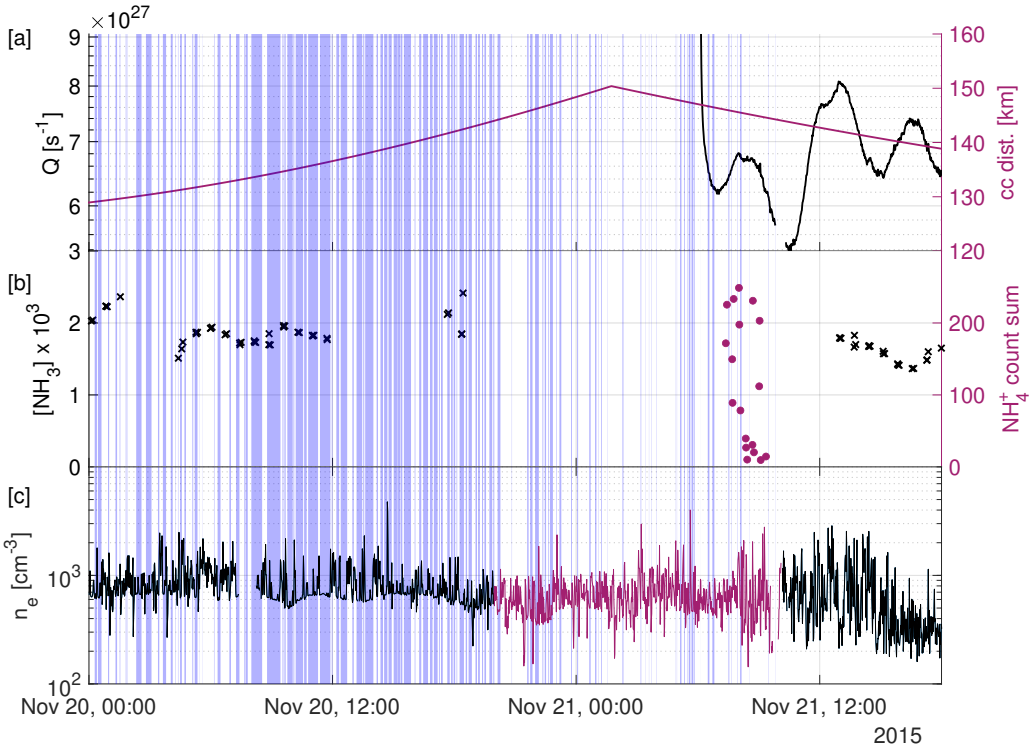

Figure 4.10: Time series of key data inputs into the model for November 20th–21st 2015. (**a**) Local outgassing from ROSINA-COPS with spikes from spacecraft thruster firings removed (**black**) and spacecraft-comet distance (**red**). (**b**) NH_3 volume mixing ratio from ROSINA-DFMS neutral mode (**black crosses**) and integrated counts from scans of NH_4^+ by ROSINA-DFMS (method described in Section 3.1) (**c**) Total electron density from the RPC–MIP/LAP combined dataset (**black**) or RPC–MIP only (**red**, Henri *et al.*, 2017) where RPC–LAP was unavailable. In all panels, **blue shaded regions** show when Rosetta was in the diamagnetic cavity, according to RPC–MAG data Goetz *et al.* (2016a). Credit: Lewis *et al.* (2024)

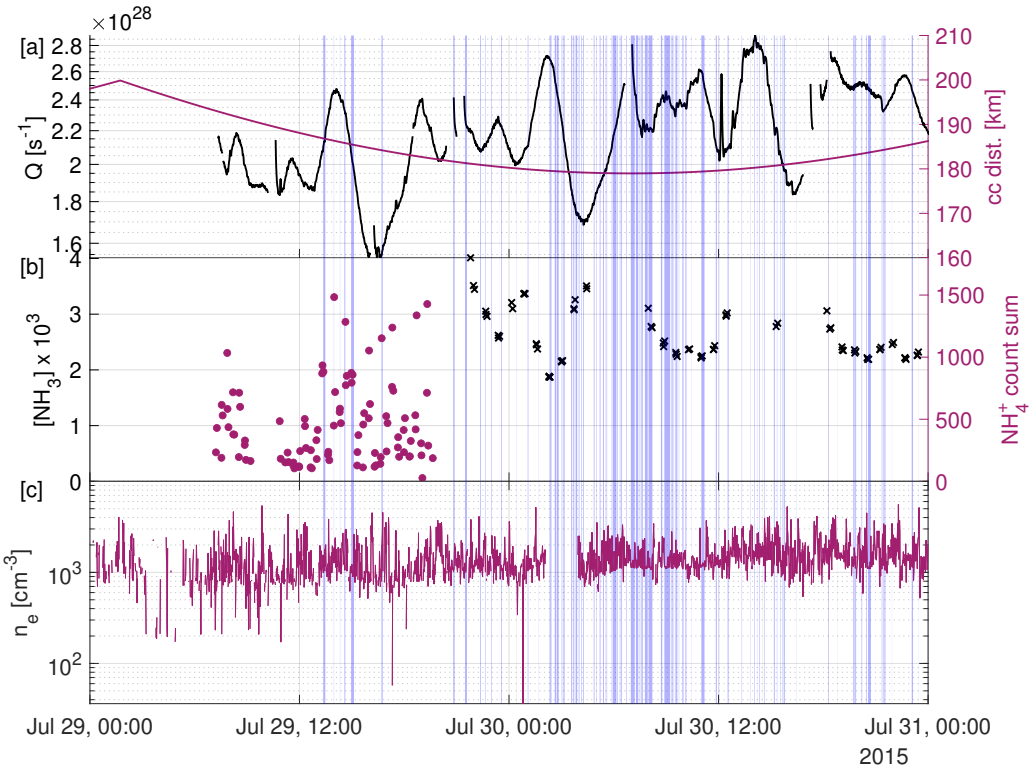

Figure 4.11: Same as Figure 4.10, but for July 29th–30th 2015. Credit: Lewis *et al.* (2024)

MIP/LAP combined dataset was not available for this period, so I use electron density data from RPC–MIP only (red, bottom panel).

The distribution of electron density measurements that were taken while Rosetta was inside the diamagnetic cavity for each time period is shown in the histograms in Figure 4.12. The data are similarly distributed, with less variation in November when more data were available. For comparison with the model, I take the range of electron densities one standard deviation on either side of the mean (indicated by the blue shaded regions), which was around twice as high in July 2015 (955.1–1517 cm^{-3}) compared to November 2015 (544.4–791.8 cm^{-3}).

A summary of the model inputs and range of electron densities for each period is shown in Table 4.3. The neutral speed was taken from Biver *et al.* (2019) (see Figure 2.1), and the outgassing Q was derived from this and the COPS neutral density (see Equation 2.1). It is worth noting that the data availability of COPS was limited for the November period, so only a best estimate of the average outgassing over the whole period can be used. The fraction of NH_3 was determined from the DFMS neutral mode data shown in Figures 4.10 and 4.11.

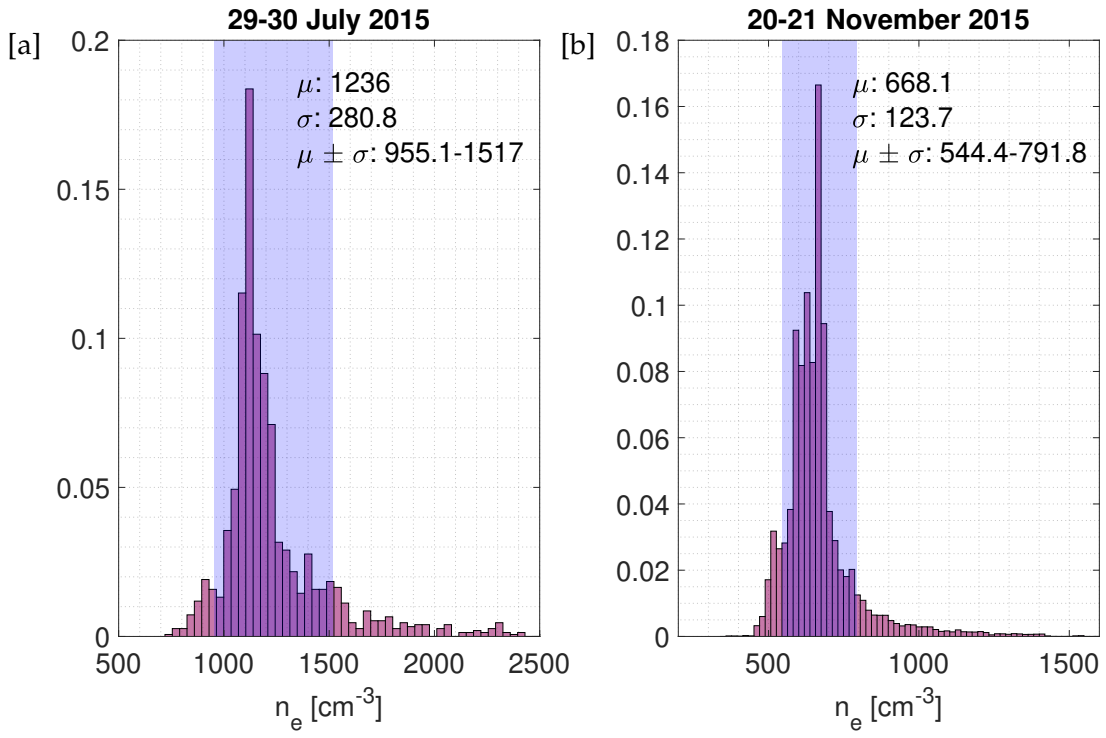

Figure 4.12: Histograms showing the spread of total electron density measurements within the diamagnetic cavity for (**a**) 29th–30th July 2015 and (**b**) 20th–21st November 2015. The shaded region shows the data one standard deviation either side of the mean. Credit: Lewis *et al.* (2024)

Table 4.3: Inputs in the model as used to represent the two time periods discussed in Section 4.3. Local outgassing rate (Q), cometocentric distance r of Rosetta and NH_3 mixing ratio are estimated from the data in Figures 4.10 and 4.11. The neutral speed u_n is taken from Biver *et al.* (2019), and the electron density range is as shown in Figure 4.12.

Input parameter		**29th–30th July 2015**	**20th–21st November 2015**	**Source**
Heliocentric dist. [au]		1.254	1.715	-
Q	$[s^{-1}]$	2.3×10^{28}	7×10^{27}	COPS
r	[km]	180	135	-
u_n	$[km\ s^{-1}]$	0.90	0.75	Biver *et al.*, 2019
NH_3	%	0.3	0.2	DFMS
n_e	$[cm^{-3}]$	955.1–1517	544.4–791.8	MIP/LAP

For a range of electric field surface strengths $E(r_c)$, the ionospheric model was run for the inputs in Table 4.3, for the time periods in November and July 2015. Figure 4.13a shows the modelled total ion density at the cometocentric distance of Rosetta for each electric field strength. The profiles are calculated for both $E \propto r^{-1}$ (solid lines) and $E \propto r^{-2}$ (dashed lines). The horizontal shaded regions in red and grey show the electron density data for July and November 2015, respectively (derived in Figure 4.12). The r^{-2} profiles are clearly unable to explain the measured electron densities and ion speeds, since an unreasonably high electric field would be required to reduce the electron density to the measured range at the Rosetta location. Hence, I use the r^{-1} profiles to derive the surface electric field strength range that would explain the measured electron density for each time period. I find electric field strengths for July and November of around $1.1 - 2.7\ \mathrm{mV\ m^{-1}}$ and $0.2 - 0.6\ \mathrm{mV\ m^{-1}}$, respectively. Stronger electric fields ($> 3\ \mathrm{mV\ m^{-1}}$) are found to reduce the plasma density to below the observed range, due to strongly enhanced ion transport.

Figure 4.13b then shows the predicted $\mathrm{NH_4^+}$ density corresponding to the total ion densities shown in Figure 4.13a. As discussed in Section 4.2, $\mathrm{NH_4^+}$ is more sensitive to the change in the electric field strength, and therefore varies over more orders of magnitude than the total ion density. For the total plasma densities measured in the two time periods, the model predicts that this would correspond to $20 - 40\,\mathrm{cm^{-3}}$ of $\mathrm{NH_4^+}$ on November 20th–21st 2015 and $50 - 110\,\mathrm{cm^{-3}}$ for July 29th–30th 2015.

As discussed in Chapter 3 Section 3.3, we know $\mathrm{NH_4^+}$ was consistently detected in the diamagnetic cavity during the two case study periods while the mass spectrometer was in ion mode (see Figures 4.11 and 4.10). However, the number density of $\mathrm{NH_4^+}$ cannot be inferred from the ROSINA-DFMS spectra with identified $\mathrm{NH_4^+}$ peaks. In Section 3.1, I derived an approximate threshold for detection of an ion with DFMS high resolution ion mode as about $0.05\,\mathrm{cm^{-3}}$. Therefore, it is likely that even the lowest modelled densities in Figure 4.13b would be detectable by the instrument in the high resolution mode. In addition, $\mathrm{NH_4^+}$ detection with DFMS is also dependent on the field-of-view and energy acceptance window of the instrument. Therefore, it is not possible to use the detection of $\mathrm{NH_4^+}$ to constrain the electric field in this way.

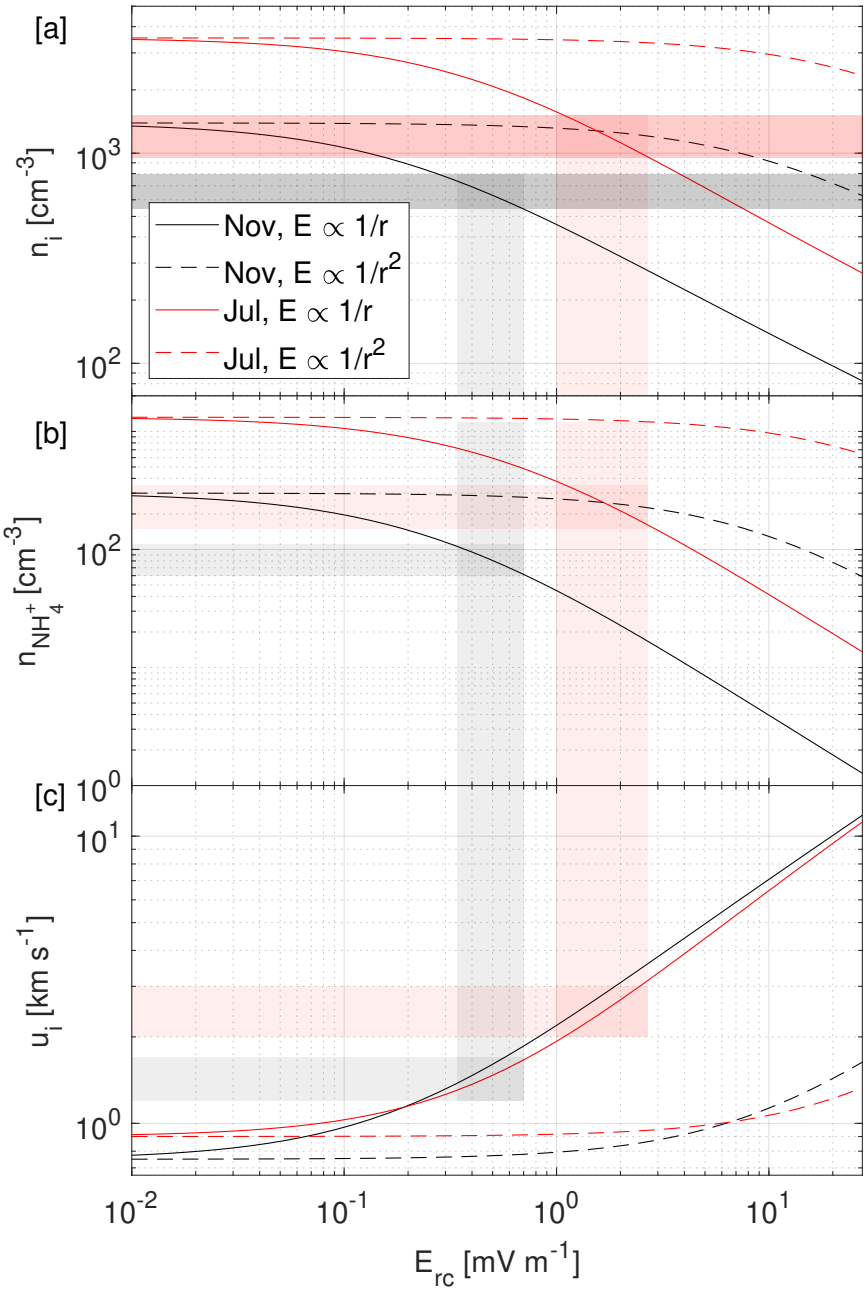

Figure 4.13: (**a**) Total plasma density, (**b**) NH_4^+ density, and (**c**) bulk ion velocity, for model runs for input conditions representing 29th–30th July 2015 (**red lines**) and 20th–21st November 2015 (**black lines**), as a function of electric field surface strength. Field profiles $\propto 1/r$ (**solid lines**) and $\propto 1/r^2$ (**dashed lines**) are shown. **Shaded red** and **grey** regions show how the NH_4^+ density is derived, ion bulk speed and electric field strength (when $E \propto 1/r$) that corresponds to the measured electron density from the RPC instruments over the two periods considered (see Table 4.3). Credit: Lewis *et al.* (2024)

Figure 4.13c shows the ion bulk speed corresponding to the model runs in Figures 4.13a and 4.13b. The bulk speeds are calculated according to Equation 4.5. For the lowest electric fields ($\approx 1 \times 10^{-5}$ V m^{-1}), the ions are not significantly accelerated above the neutral speed. When the electric field is high ($> 1 \times 10^{-2}$ V m^{-1}), the ions are further accelerated, up to 10 km s^{-1}. Such high speeds have been derived from RPC–ICA measurements (Bergman *et al.*, 2021a), but the present ionospheric modelling suggests that such a strong acceleration would lead to electron densities around 6 times lower than what have been measured by RPC–MIP and RPC–LAP. Instead, the observed densities are best explained by ion bulk speeds of $1.2 - 1.7$ km s^{-1} on 20th–21st November 2015 and $2 - 3$ km s^{-1} for July 29th–30th.

4.4 Discussion

The discussion of the results presented in this section is divided into three sections. First, in Section 4.4.1 I discuss the implications of cometary ion acceleration for the relative composition of the three key ion species included in the model. Section 4.4.2 focusses on the ion bulk speed, the uncertainties introduced by the approach, and the possible improvements that could be made to the method. Finally in Section 4.4.3 I discuss what we have learnt from this study about the nature of the ambipolar electric field at comet 67P and the ways in which the 'true' electric field is likely more complex than the simple model which I have assumed.

4.4.1 Ionospheric composition

One novelty of my approach is the inclusion of NH_4^+, the dominant ion species in the inner part of the ionosphere near perihelion. This does not have a significant impact on the total ion density, since the dissociative recombination rate coefficient is similar for all the species (Vigren and Galand, 2013), but it does reduce the density of H_3O^+ since loss through proton transfer to NH_3 happens very readily in a collisional coma at high outgassing rates. The NH_4^+ density is much more sensitive to the enhanced ion speed than the water ion species. However, it is not possible to directly compare modelled ion densities with counts from ROSINA-DFMS ion mode scans (see Section 3.1), limiting the possibility for using NH_4^+ detections with ion

mass spectrometer observations within the diamagnetic cavity to constrain the ambipolar electric field.

The density of H_2O^+ is resistant to changes in the electric field, since it is close to photochemical equilibrium (Galand *et al.*, 2016, Heritier *et al.*, 2017a) and therefore unaffected by the changing transport term in the continuity equation. As a result, it is also unaffected by the inclusion of momentum transfer in the model. For the other ion species, the momentum transfer has the impact of interrupting the process of ion acceleration, therefore reducing their transport loss and increasing the density. NH_4^+ is again more sensitive to momentum transfer than H_3O^+ in the presence of an electric field.

4.4.2 Ion bulk velocity

I compared the ionospheric simulation with total electron density data from RPC instruments (see Section 4.3). I find that to explain the measured plasma density in the diamagnetic cavity in November 2015, the model requires an ambipolar field of around $0.5\ \mathrm{mV\ m^{-1}}$, leading to a bulk ion speed of $\sim 1.2 - 1.7\ \mathrm{km\ s^{-1}}$ at the Rosetta location. On 29th–30th July 2015, I derive a stronger electric field, up to $1.5\ \mathrm{mV\ m^{-1}}$, leading to slightly faster bulk speeds of $\sim 2 - 3\ \mathrm{km\ s^{-1}}$. The ion speeds I derive are lower than those derived from RPC–ICA (e.g. Bergman *et al.*, 2021b, see Section 1.3.3) but are broadly consistent with the measured values from RPC–LAP and from the flux conservation method based on observations of the electron density around perihelion (Vigren and Eriksson, 2017).

To understand Figure 4.13 further, we return to the continuity equation (Equation 4.6), but now considering the total plasma density (i.e. $n_i(r) = \sum_{j,s} n_{j,s}$). By making the assumption that dissociative recombination is negligible (justified by its relatively long timescale, see Figure 4.7), then in steady state the equation reduces to

$$\frac{1}{r^2}\frac{\mathrm{d}}{\mathrm{dr}}(n_i r^2 u_i) = P^{\mathrm{ioni}} \tag{4.36}$$

where u_i is the bulk ion speed (Equation 4.5). This leads to the simple relation between the ion density n_i and the ion bulk speed u_i,

$$n_i u_i = \frac{\nu^{\text{ioni}} Q}{4\pi u_n r^2}(r - r_c), \tag{4.37}$$

showing that at a given cometocentric distance r, the modelled $n_i \propto 1/u_i$. The results of this section are therefore not dependent on what I assumed for the momentum transfer rate coefficients or on the included ion-neutral chemistry. The most critical assumptions are then regarding the neutral speed u_n and the ionisation frequency ν^{ioni}.

For the neutral speed, I have taken the values given by the power law fits given in Biver *et al.* (2019) (see Table 4.3), and I assumed that this speed is constant down to the surface of the nucleus. In reality, the neutral gas would be better described with an adiabatic expansion model (Heritier *et al.*, 2017a, Huebner and Markiewicz, 2000). I explored the sensitivity of my results to a slower neutral expansion velocity, taking $400\ \mathrm{m\ s^{-1}}$ as a lower limit - this is the surface speed used in Heritier *et al.* (2017a). For the same model runs as in Figure 4.13, I find this increases the bulk ion speed derived for July 29th–30th 2015 to $3 - 5\ \mathrm{km\ s^{-1}}$, and for November 20th–21st 2015 to $2 - 3\ \mathrm{km\ s^{-1}}$.

The ionisation frequency (see Figure 4.4) is derived from the appropriate TIMED/SEE dataset, adjusted to the heliocentric distance of 67P and time-shifted to account for the change in solar phase. The largest uncertainty in this approach is in the solar flux data themselves, which are up to 20% (Woods *et al.*, 2005). Repeating the analysis of Figure 4.13 to include maximum and minimum photoionisation frequencies (assuming a 20% uncertainty), leads to electric field estimates of $0.1 - 1\ \mathrm{mV\ m^{-1}}$ for 20th–21st November and $0.7 - 4\ \mathrm{mV\ m^{-1}}$ for 29th–30th July.

Any attenuation of the solar flux due to absorption from dust grains beyond the cometocentric distance of Rosetta (Johansson *et al.*, 2017) has been neglected. The effect of this attenuation on the model would be to decrease the photoionisation frequency, reducing the production of ions, meaning a lower bulk ion speed is required to produce the same plasma density (see Equation 4.5).

4.4.3 Nature of the ambipolar electric field

I find that the electric field following a r^{-1} dependence is most plausible (compared to r^{-2}, see Figure 4.13). This is however likely to not be the case at very large cometocentric distances as it would lead to an unbounded potential. Since the model is magnetic-field free, it is only valid within the diamagnetic cavity. It is clear that the electric field becomes more complex close to the boundary and outside of this region owing to the presence of the solar wind, and therefore a simple function of cometocentric distance is unlikely.

In addition, I assumed a constant electron temperature (10^4 K), while in reality it varies with cometocentric distance due to increased electron-neutral collisions in the dense coma close to the surface. A significant population of cold electrons (~ 0.1eV) has been observed through much of the escort phase of Rosetta (Engelhardt *et al.*, 2018, Wattieaux *et al.*, 2020, Henri *et al.*, 2017, Eriksson *et al.*, 2017). They dominate over the warm population particularly post-perihelion, and were observed to decrease with increasing cometocentric distance (though comet latitude also plays a key role; Gilet *et al.*, 2020) . These observations lead to the question of whether it is realistic to assume an ambipolar electric field in r^{-1}, or whether it would be better described with a decreasing or even zero electric field strength close to the surface. A difference in energy between the ions and electrons is necessary for an electron pressure gradient, and therefore an ambipolar electric field, to be set up. This possibility was examined in Vigren and Eriksson (2017), who implemented an electric field that abruptly 'switches on' at a radius of 100km, assuming that below this threshold the electrons are too cold to produce such a field. In contrast, it was assumed throughout this work that the ions are accelerated from the nucleus surface.

To test the impact of implementing a 'cold zone' with no ion acceleration on our results, Figure 4.14 shows ion density and bulk velocity profiles from the present model but with acceleration from 50 km (blue) and from 100 km (red). This treatment is nonphysical given that a decrease in the electric field strength towards the nucleus would be gradual and not abrupt, but it is the simplest approximation to make given the electron temperature profile at 67P is not well constrained. It allows the assessment of the sensitivity of the electron density when no electric field is present at the surface. In Figure 4.14, the ion bulk speed and ion

density converge to the same profile in all three cases by around $2r_E$, where r_E is the upper limit of the 'cold zone' and the start of the ion acceleration (see Figure 4.14). This result is not wholly unexpected when we consider Equation 4.3 in the case where acceleration is only from r_E to a distance r:

$$u_i(r) = \sqrt{u_n^2 + \frac{2E_c r_c}{m_i} \ln\left(\frac{r}{r_E}\right)}. \tag{4.38}$$

If $E_c r_c$ is held constant (i.e. the field starts with the same strength but from a different initial r), then in the limit $r \gg r_E$ there is no r_E dependence. At the cometocentric distances considered in Section 4.3 (135 km and 180 km, see Table 4.3) a cold, electric field-free zone is unlikely to significantly affect the ion bulk velocities derived in this study, unless it extends close enough to the spacecraft location. The electron exobase has been shown to be close to or even outside the diamagnetic cavity boundary (Henri *et al.*, 2017), but to explain the accelerated plasma speed observed beyond the neutral speed within this region, an ambipolar electric field must exist below this limit. Hence, although the cold electron population dominates within the cavity, the warm electron presence must be enough to set up a weak ambipolar field for at least some of the coma below the spacecraft location. Both cold and warm electron populations are indeed always observed with RPC–MIP (Wattieaux *et al.*, 2020).

For a higher outgassing comet such as 1P, the electrons are much colder compared with 67P and an ambipolar electric field is less likely to result within the diamagnetic cavity. Electron temperatures in the unmagnetised region at 1P/Halley during the Giotto flyby were calculated by solving coupled continuity, momentum, and energy equations by Korosmezey *et al.* (1987), finding values around $100\ \mathrm{K}$ (similar to the $0.01\ \mathrm{eV}$ cold population at Rosetta). In contrast, the total electron temperature (weighted mean of the warm and cold populations) in the diamagnetic cavity at 67P was on the order of $10^4\ \mathrm{K}$ [$\sim 1\ \mathrm{eV}$], according to spectra from RPC–MIP (Wattieaux *et al.*, 2020).

In the lower outgassing regime, such as 67P during the Rosetta escort at larger heliocentric distances, the coma is less dense and the cold electron population less significant than near perihelion (Gilet *et al.*, 2020). The ambipolar electric field has been shown to play a

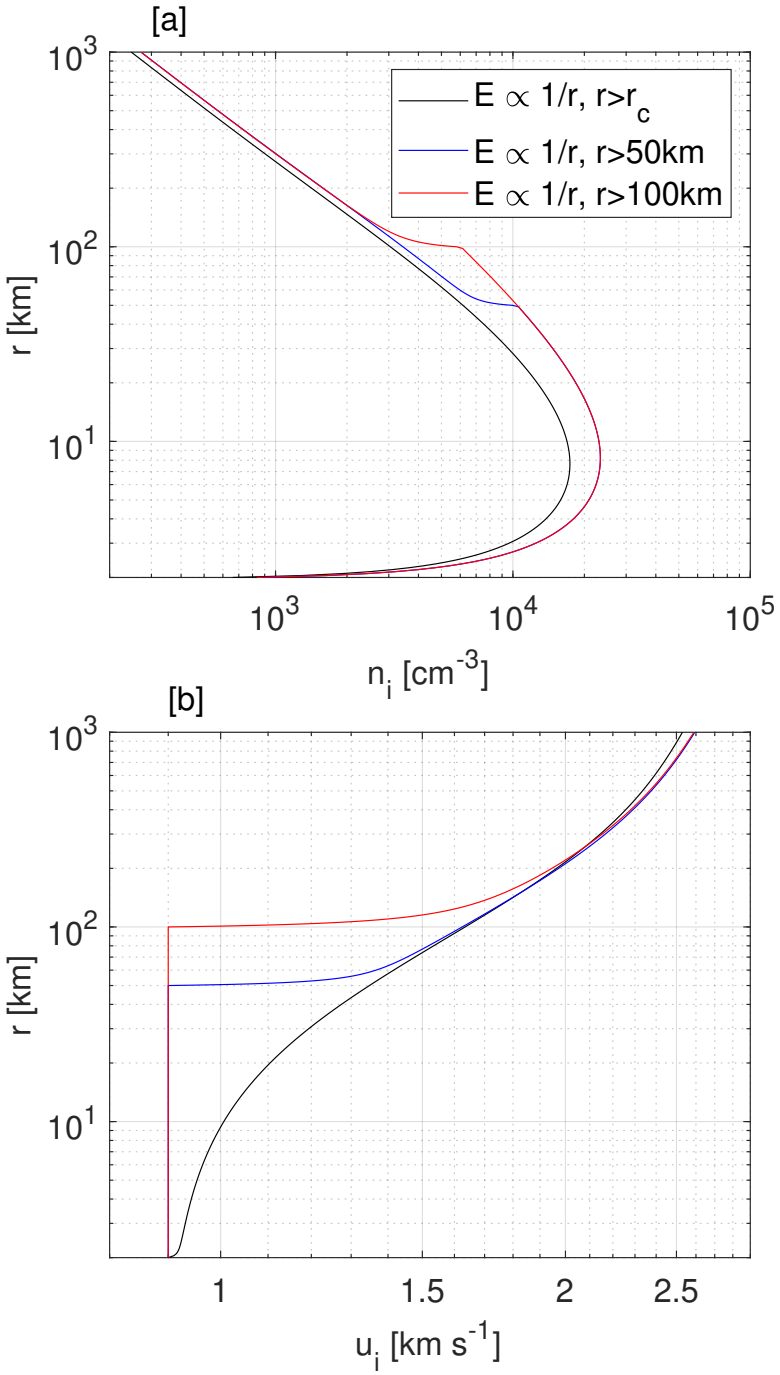

Figure 4.14: Ion density profiles (**a**) and ion bulk velocities (**b**) for runs of the model where an electric field $E = 10^{-3}\, r_c/r$ V m^{-1} is applied, starting at the surface (**black**), from $r = 50$ km (**blue**) and from $r = 100$ km (**red**). Credit: Lewis *et al.* (2024)

role in the plasma environment at these times, both through the presence of suprathermal electrons leading to UV aurora (Galand *et al.*, 2020, Stephenson *et al.*, 2021) and through trapping of electrons allowing them to be cooled despite the thin coma (Stephenson *et al.*, 2022, Stephenson *et al.*, 2024). However, the total electron density measured before January 2015 or from around February 2016 onwards is well explained even with the assumption that the ions travel at the neutral velocity (Galand *et al.*, 2016, Heritier, 2018, Vigren *et al.*, 2019), suggesting no acceleration of cometary ions by the ambipolar field. This could be explained by the low cometocentric distances explored by Rosetta during these times ($\lesssim 60\mathrm{km}$) not allowing for sufficient travel times for measurable acceleration, and by the flattening of the electric potential well as shown by test particle simulations (Stephenson *et al.*, 2023). These ideas will be explored further in Chapter 5.

CHAPTER 4 SUMMARY

- Assessed the effect of ion acceleration on ion densities in the presence of an electric field and momentum transfer, for three key ion species: H_2O^+, H_3O^+ and NH_4^+.
- **Ion acceleration by the ambipolar electric field increases the transport loss and therefore reduces the total ion density.**
- **High proton affinity ions, such as NH_4^+, are particularly sensitive** to the electric field, and where such ions are strongly present may be an indicator of limited ion transport (and vice versa).
- **Momentum transfer reduces the effect of the electric field**, by slowing down the accelerated ions through collisions with slower neutral molecules.
- I find that to reproduce the plasma densities measured by RPC inside the diamagnetic cavity of comet 67P near perihelion, our 1D ionospheric model requires an electric field in r^{-1} of around $2\ \mathrm{mV\ m^{-1}}$ at the surface, leading to bulk ion speeds at Rosetta of $1.4 - 3.0\ \mathrm{km\ s^{-1}}$.
- This contrasts 67P with the higher outgassing case of comet 1P/Halley during the Giotto flyby, during which the overall electron population was likely to be much colder preventing an ambipolar field from forming within the diamagnetic cavity (Gan and Cravens, 1990).

CHAPTER 5

MODELLING THE ION DYNAMICS IN 3D

The ion dynamics I have modelled so far have been exclusively one-dimensional and fluid, with only a radial electric field and no magnetic field to complicate the picture. As such, attention was focussed on the diamagnetic cavity, and the drivers of the ion composition, density and bulk velocity within it. In this Chapter, the previous studies are extended into a 3D and kinetic regime, out of the diamagnetic cavity, and to lower outgassing levels. In doing so, we aim to see the impact of a more complex set of electric and magnetic fields on the ion environment in the inner coma.

For this study, the collisional test-particle model originally used for the electron populations around the comet (Stephenson *et al.*, 2022) has been adapted to instead describe the ion environment. In Section 5.1, the model is described, with emphasis on the aspects of the code that were updated from the electron model. Section 5.2 then describes the hybrid simulations that provide the electric and magnetic fields to drive the ions. The model is validated in Section 5.3, first against the 1D Ion Acceleration Model from Chapter 4 (Section 5.3.1), and then against the collisionless hybrid simulation (Section 5.3.2).

In Section 5.4, the test-particle model is run for the diamagnetic cavity (radial electric field only) equivalent to the November 2015 case study from Chapter 4 (Section 4.3). This allows us to validate the 1D approach under these conditions, and understand its limitations.

Section 5.5 focuses on the cometary plasma environment around 67P at $2.5 - 3$ au, when the outgassing was lower and the diamagnetic cavity was not detected. The test-particle model in this case is driven by electric and magnetic fields from the hybrid model AMITIS (Fatemi *et al.*, 2017), as used in Moeslinger *et al.* (2024). The density and bulk velocity of H_2O^+, H_3O^+, and NH_4^+ are assessed, highlighting the extent to which each is driven by the changing ion transport and collisions.

Finally, I return to the RPC electron density measurements in Section 5.6, comparing the combined dataset from MIP/LAP with the results of the test-particle modelling in Section 5.5. The aim of this is to understand the drivers of the plasma density during the conditions used for the hybrid simulations, and to assess how well the simulation recreates them.

5.1 Collisional ion test-particle model

A test-particle model is one that simulates the trajectories of many single particles, which are assumed to behave independently of each other and without having a feedback effect on the background electric and magnetic fields which drive them. The test-particle model first described in Stephenson *et al.* (2022) was developed to assess the response of cometary and solar wind electron populations to electric and magnetic fields provided by a fully kinetic Particle-in-Cell (PiC) model (Deca *et al.*, 2017, Deca *et al.*, 2019). Crucially, the test-particle approach enabled study of the effect of collisions on the overall electron environment, which have not yet been incorporated into kinetic PiC models (Stephenson *et al.*, 2023, Stephenson *et al.*, 2024).

I have adapted the Stephenson *et al.* (2022) electron test-particle model to now model the cometary ion population. In this section, I describe the model briefly, focussing on the updates that have been made in order to model the ions. I consider the same three key ion species as in Chapter 4 (H_2O^+, H_3O^+, and NH_4^+) and the ion-neutral collisions that occur between them and the neutral gas (here, H_2O and NH_3 only).

The model is described by the flow chart in Figure 5.1. First, the ions are created, either as photo-ions (H_2O^+) or as secondary ions (H_3O^+, NH_4^+), which is described in Section 5.1.1. The

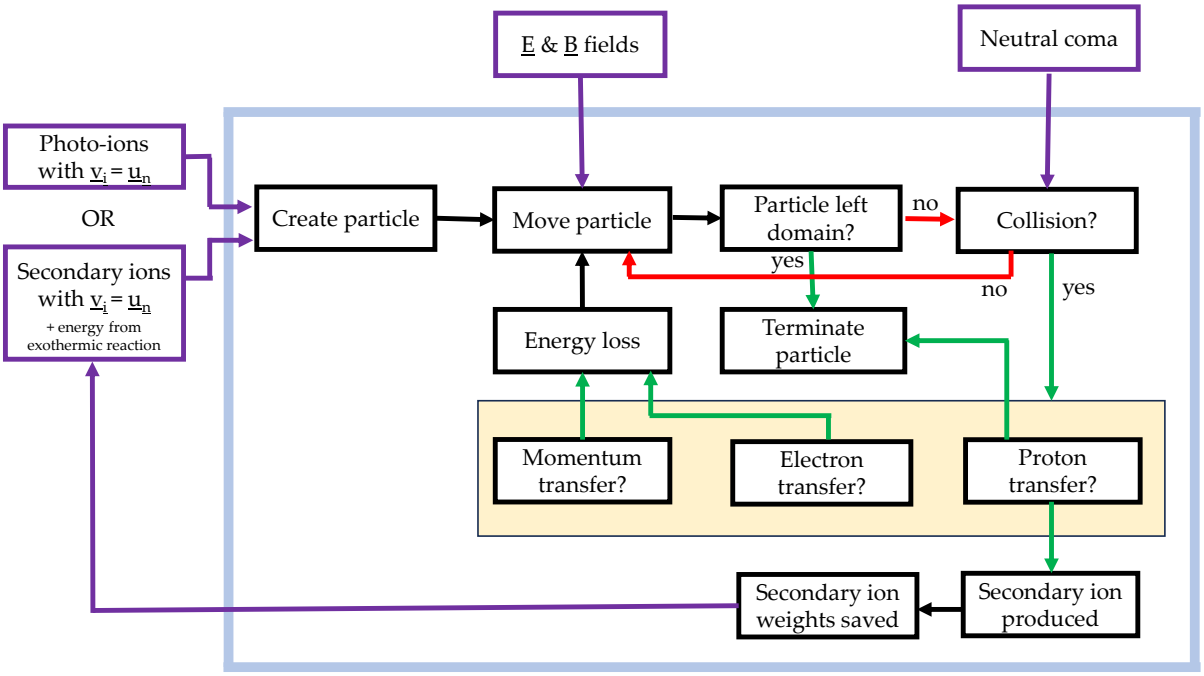

Figure 5.1: Flow chart representing the key elements of the ion test-particle model. The **blue** box separates processes happening inside the code, and the inputs controlled externally (in **purple boxes**). Adapted from Stephenson *et al.* (2022).

particles are then pushed through the background fields by the Lorentz force (Section 5.1.2). At each timestep, we check whether a collision has occurred, and if so, what type (Section 5.1.3). Particles are terminated when they either leave the domain, hit the nucleus, or undergo a proton transfer. Finally, the moments of the distributions can be calculated based on the trajectories of the particles, provided enough particles have travelled through each cell. For details of the moment calculation, see Stephenson (2022). The moments are calculated on a $(80 \times 60 \times 60)$ cell grid with the same resolution as the electric and magnetic fields (see Table 5.1).

5.1.1 Generation of ions

H_2O^+ ions are initialised in the model with a given velocity and position in the grid. Since these newly produced ions originate from the neutral coma, they are initially given the same velocity as the neutrals: $\vec{u_i} = u_n \hat{r}$. The total unattenuated ionisation frequency ν_{ioni}^{tot} is supplied as an input to the model and subsequently calculated in 3D taking photo-absorption

into account, using the Lambert-Beer law as described in Section 2.2.1.

The simulated ions, referred to as *macroparticles*, represent a flow of ions that follow the same trajectory through the fields. Macroparticles are assigned a 'weight' (W_p), based on the number of ions per second which follow the same path. This weight is dependent on the number of other ions produced within the same grid cell. It is given by

$$W_p = \frac{1}{N_p} \int_{\text{cell}} \nu_{\text{ioni}}^{\text{tot}}(\vec{x}) n_n(\vec{x}) d^3\vec{x} \tag{5.1}$$

where N_p is the number of macroparticles produced within the cell and $n_n(\vec{x})$ is the neutral density at the position $\vec{x}$ within the grid. The production grid comprises small boxes ($1\ \text{km} \times 1\ \text{km} \times 1\ \text{km}$) from the origin, where the comet nucleus is centred, up to $20\ \text{km}$ in each direction. The rest of the ($1000\ \text{km} \times 1000\ \text{km} \times 1000\ \text{km}$) domain is then filled with logarithmically spaced boxes such that there are 50 cells in the x-direction (the comet-Sun line) and 40 in the y- and z-directions.

After the run for the photo-ions (H_2O^+) has been completed, the secondary ions are generated from the weights that have been saved when proton transfer collisions occur.

5.1.2 Response of particles to electric and magnetic fields

The ion macroparticles are pushed through the simulation in response to electric and magnetic fields. The fields are considered as a stationary background input to the simulation, and the updated velocity and position of the particle is determined using the Boris algorithm (see Boris, 1970, Qin *et al.*, 2013, Carnielli *et al.*, 2019). A description of the electric and magnetic fields used in this study is given in Section 5.2. The full validation of the single particle trajectories is given in Stephenson (2022).

The timestep used for the Boris integrator is constant at 5×10^{-3} s. It was selected in order to fulfill the following criteria (Stephenson *et al.*, 2022):

(i) **Gyroradius**

The time step must be small compared to the gyroperiod $T_{\rm gyro}$ of the ions:

$$\mathrm{d}t < \mathrm{d}t_{\rm gyro} = T_{\rm gyro}/N_{\rm cycle}, \tag{5.2}$$

where $N_{\rm cycle}$ is a numerical factor, a value of 20 is typically sufficient (Carnielli *et al.*, 2019).

(ii) **E and B field grid size**

The ions may not move further than the resolution of the input magnetic and electric fields, $\mathrm{d}x_{\rm EB}$ (see Section 5.2):

$$\mathrm{d}t < \mathrm{d}t_{\rm EB} = \mathrm{d}x_{\rm EB}/2v_i. \tag{5.3}$$

(iii) **Moment grid resolution**

During one time step, the ions cannot travel further than the next cell on the grid over which the moments are calculated:

$$\mathrm{d}t < \mathrm{d}t_{\rm grid} = \mathrm{d}x_{\rm grid}/2v_i \tag{5.4}$$

Since I have used the same grid resolution for the moments and the fields, $dx_{\rm EB} = dx_{\rm grid}$, criteria (ii) and (iii) are equivalent. However, this is not a necessary condition to run the simulation.

(iv) **Collision probability**

This ensures that the total probability of collision within the time step is not larger than $P_{\rm max} = 0.01$, so that we can safely assume that the probability of more than one collision in the time step is very small. $\sigma_{\rm tot}$ is the total collision cross section (all collision types added together) and $n_n(\vec{x})$ is the neutral density at $\vec{x}$.

$$\mathrm{d}t < \mathrm{d}t_{\rm prob.} = -\frac{\log(1 - P_{max})}{n(\vec{x})\sigma_{tot}|\vec{v}_i|} \tag{5.5}$$

5.1.3 Treatment of collisions

Adapting the test-particle model to treat the cometary ion population requires a new set of cross sections. The full ion-neutral cross section set and references are presented in Appendix B, and shown graphically as a function of the relative energy between the reacting particles in Figure 5.2. In general, the cross sections increase with decreasing relative energy, but the experimental cross sections are only available down to 0.1 eV. For relative energies below this value, I linearly extrapolated in log space down to an approximate surface temperature of the neutrals of ~ 0.01 eV (Heritier *et al.*, 2017a, Marshall *et al.*, 2017). This rather crude approach is shown in Figure 5.2 and improved treatment could be included in future work.

Dissociative recombination is neglected, which is reasonable at the outgassing rates used in this study ($10^{26} - 10^{27}$ s^{-1}, reflecting January–March 2016 during Rosetta). Heritier *et al.* (2018) demonstrated that neglecting recombination in this regime introduces less than 20% error (for $T_e = 200$ K) in the total plasma density. This is likely to be even lower when acceleration of the ions by electromagnetic fields is taken into account (see the timescale analysis of Figure 4.7).

The probability of a given collision type c happening during a timestep $\mathrm{d}t$ is given by:

$$P_c(\mathrm{d}t) = 1 - \exp\left[-n_n(\vec{x})\ \mathrm{d}V_\sigma\right] \tag{5.6}$$

where $\mathrm{d}V_\sigma$ is the volume 'swept through' by the collision cross section in the frame of the neutral gas (of relevant species, n). This volume is given by

$$\mathrm{d}V_\sigma = \sigma_c(E_{\mathrm{rel}})\ w_{\mathrm{rel}}\ \mathrm{d}t \tag{5.7}$$

where v_{rel} is the relative speed between an ion and a neutral and the collision cross section is $\sigma_c(E_{\mathrm{rel}})$.

If we define $w_{\mathrm{rel}} = |\vec{v_i}(\vec{x}) - \vec{u_n}(\vec{x})|$, and $v_{n,th}^{mean}$ as the thermal speed corresponding to the mean speed in the frame of the neutral gas (assumed to have a Maxwellian velocity distribution) such that $v_{n,th}^{mean} = \sqrt{\frac{8k_BT_n}{\pi m_n}}$, then:

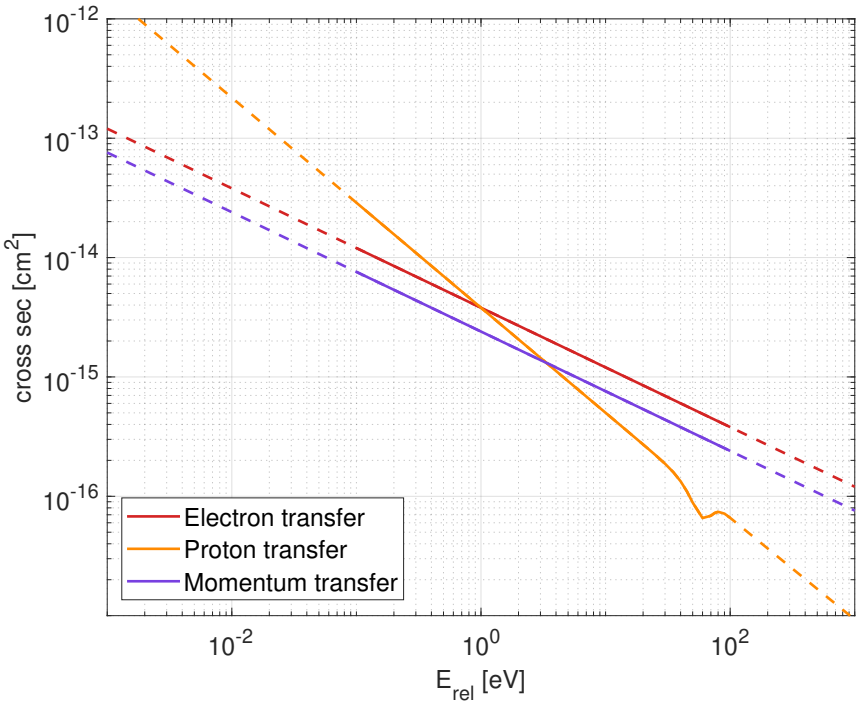

Figure 5.2: Cross sections for collisions used in the ion test-particle model, against relative energy between the ion and neutral. The **solid lines** are from published datasets (Appendix B) and **dotted sections of the lines** show where values have been extrapolated and are not included in the references.

- For $w_{rel} \gg v_{n,th}^{mean}$, the thermal speed can be neglected and $v_{rel} \approx w_{rel}$.
- For $w_{rel} \ll v_{n,th}^{mean}$, the relative speed is dominated by the thermal speed of the gas such that $v_{rel} \approx v_{n,th}^{mean}$.

However, when neither of these approximations apply, we must consider the general case. For a neutral gas with a Maxwell velocity distribution function $f_n(\vec{v_n})$, a bulk velocity $\vec{u}_n$, and a temperature T_n, the relative speed is defined as (Fahr and Mueller, 1967):

$$v_{\mathrm{rel}} = \iiint |\vec{v_i} - \vec{v}_n|\ f_n(\vec{v_n})\ \mathrm{d}^3\vec{v_n} \tag{5.8}$$

$$= \frac{v_{n,th}}{\sqrt{\pi}} \exp\left(-\frac{w_{\mathrm{rel}}^2}{v_{n,th}^2}\right) + w_{\mathrm{rel}} \left(1 + \frac{v_{n,th}^2}{2w_{\mathrm{rel}}^2}\right) \mathrm{erf}\left(\frac{w_{\mathrm{rel}}}{v_{n,th}}\right), \tag{5.9}$$

where $v_{n,th} = \sqrt{\frac{2k_B T_n}{m_n}}$ is the magnitude of the peak of the Maxwellian velocity distribution (in

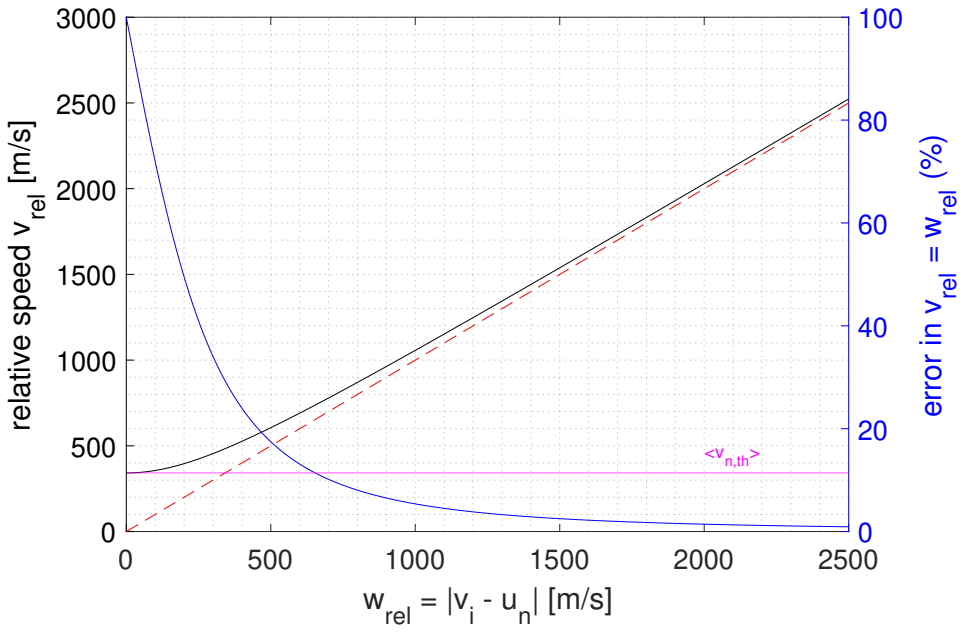

Figure 5.3: **Black line**: Relative speed of colliding ions and neutrals $v_{\rm rel}$ as a function of ($|\vec{v}_{rel} - \vec{u}_n| = u_{\rm rel}$). The neutral temperature is taken to be 100 K. **Red dotted line** indicates $v_{\rm rel} = u_{\rm rel}$. The **blue curve** corresponds to the % difference between $w_{\rm rel}$ and $v_{\rm rel}$. The **horizontal pink line** shows the thermal speed $v_{n,th}^{mean}$ associated with the mean of the distribution.

the frame of the gas), that is, the most probable speed. Equation 5.9 can be approximated as

$$v_{\rm rel} \approx \left(\frac{4v_{n,th}^2}{\pi} + w_{\rm rel}^2 \right)^{\frac{1}{2}} = \left((v_{n,th}^{mean})^2 + w_{\rm rel}^2 \right)^{1/2} \tag{5.10}$$

which is equivalent within 5% over all $w_{\rm rel}$ to Equation 5.9. In the limit where $|\vec{v}_i - \vec{u}_n| \gg v_{n,th}$, we recover $v_{rel} = w_{rel}$, and when $|\vec{v}_i - \vec{u}_n| \ll v_{n,th}$, we get $v_{rel} = v_{n,th}^{mean}$. Equation 5.9 (black) and the error from neglecting the thermal contribution to the relative velocity (blue) is given in Figure 5.3.

The v_{rel} can then be used to calculate the relative energy $E_{\rm rel}$ in order to find the cross section $\sigma_c(E_{\rm rel})$ using

$$E_{\rm rel} = \frac{1}{2} \frac{m_j m_n}{m_j + m_n} v_{\rm rel}^2 \tag{5.11}$$

with

$$m_{\mathrm{IN}} = \frac{m_j m_n}{m_j + m_n} \tag{5.12}$$

the reduced mass of the colliding ion and neutral particles.

Discounting the probability of multiple collisions in the same timestep, which is kept low by the timestep condition in Equation 5.5, the total collision probability is given by summing over all the collision processes c,

$$P(\mathrm{d}t) = \sum_c P_c. \tag{5.13}$$

To determine whether a collision occurs, a random number between 0 and 1 is generated at each timestep. The number is also used to determine the collision type and hence the continuation (or not) of the particle's trajectory (see the flow chart Figure 5.1).

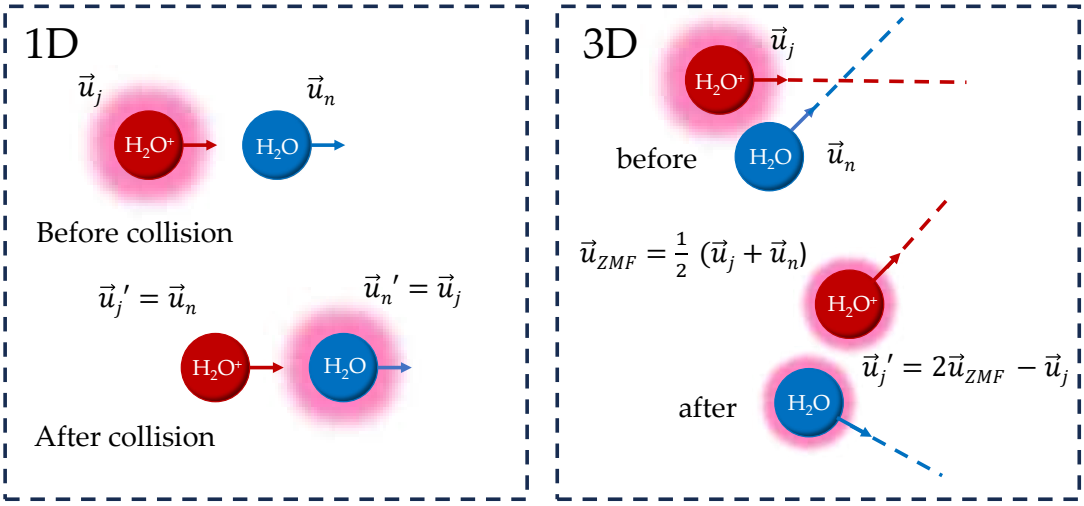

Figure 5.4: Diagram showing the different treatment of collisions in the 1D Ion Acceleration Model of Chapter 4 and in the 3D collisional test-particle model (Section 5.1). $\vec{u}_j$ and $\vec{u}_n$ are the initial ion and neutral velocities respectively, and the final velocities are $\vec{u}_j'$ and $\vec{u}_n'$. **Pink** indicates elevated velocity in the rest frame of the initial neutral gas velocity, but note that in the 3D case, $|\vec{u}_j| < |\vec{u}_n|$ is possible.

Figure 5.4 shows how the velocity of the ions after the collision is determined in the 3D case compared to the 1D model of Chapter 4. In both cases the collision is assumed to be elastic, but in 3D we account for elastic scattering.

The 3D model also allows us to account for the exothermic energy release from the protonation reaction (see Section 2.2.2). In this case, a component of velocity with a magnitude

equivalent to the 0.5 eV energy release is given to secondary ions (those newly produced through protonation) in a randomly generated direction.

5.2 Hybrid model - Electric and magnetic fields

The electric and magnetic fields used in this chapter are provided by simulations from two hybrid models (see Section 2.4). For validation of the test-particle model in the collisionless case (Section 5.3.2), we use the Hybrid model developed at Aalto University and applied to the cometary environment (Simon Wedlund *et al.*, 2017, Alho *et al.*, 2019). As well as comets, the model has been applied to a range of solar system bodies, such as Mars (Kallio and Janhunen, 2002), Venus (Jarvinen *et al.*, 2013, e.g.), and Mercury (Kallio *et al.*, 2022). For the application at intermediate outgassing and comparison with the Rosetta plasma dataset (see Section 5.5), fields from the AMITIS (Advanced Modelling InfrasTructure in Space simulations, Fatemi *et al.*, 2017) run presented in Moeslinger *et al.* (2024) are used [1]. AMITIS is a GPU-based 3D hybrid simulation that has also been applied to various solar system bodies.

The comparison between the parameters for the two hybrid simulations used here are given in Table 5.1, but the fundamental physical processes and assumptions are the same in both. Ion-neutral collisions are neglected in both, hence the need for a collisional test-particle model. Cometary ions in the hybrid simulations are produced through charge exchange with the solar wind, and through photo-ionisation of the cometary neutrals. Charge exchange with the solar wind is neglected in the ion test-particle model as it is a minor process below 1000 km from the nucleus (Simon Wedlund *et al.*, 2017).

As discussed in Section 2.4.3, a hybrid code treats the ions kinetically as macro particles and the electrons as a massless neutralising fluid. Since they are treated as particles, the motion of an ion of species j is driven by the Lorentz force:

[1] The E and B fields from AMITIS are provided in the supplementary material of Moeslinger *et al.* (2024) and can be found at Moeslinger and Gunell (2024). Input to the AMITIS model run was only provided as $Q\nu = 1.08 \times 10^{20}$ s^{-2}, I determined the relevant Q and ν from the COPS data and ionisation rates in Figure 2.5.

$$\frac{\mathrm{d}\vec{x}_j}{\mathrm{d}t} = \vec{v}_j \tag{5.14}$$

$$m_j \frac{\mathrm{d}\vec{v}_j}{\mathrm{d}t} = q_j(\vec{E} + \vec{v}_j \times \vec{B}) \tag{5.15}$$

where the electric field $\vec{E}$ and magnetic field $\vec{B}$ are computed using the generalised Ohm's law (2.31) and Faraday's law:

$$\frac{\partial \vec{B}}{\partial t} = -\nabla \times \vec{E}. \tag{5.16}$$

The electron thermal pressure p_e in the ambipolar electric field term of the generalised Ohm's law cannot be self-consistently calculated without the kinetic treatment of the electrons. For this reason, an electron temperature is usually imposed, either held constant or with a specific profile. Both the models of Kallio and Janhunen (2003) and Fatemi *et al.* (2017) assume adiabatic electrons, $p_e \propto n_e^{5/3}$, and impose the upstream solar wind electron temperature. This assumption is discussed further in Section 5.7.3.

Evolution of the current density $\vec{J}$ is given by Ampère's law with the displacement current neglected:

$$\vec{J} = \frac{\nabla \times \vec{B}}{\mu_0} \tag{5.17}$$

where μ_0 is the vacuum permeability ($4\pi \times 10^{-7}$ H/m), and the current density is the net contribution with all ion species (all singly charged here) and electrons taken into account, i.e.

$$\vec{J} = q_e \left(\sum_j n_j \vec{u}_j - n_e \vec{u}_e \right). \tag{5.18}$$

Equation 5.18 can be used to estimate the electron bulk velocity.

Table 5.1: Comparison of parameters for the two hybrid simulations used in this study.

Simulation	**Aalto model**	**AMITIS**
Reference	Kallio and Janhunen, 2002 (Kallio, E. private communication)	Fatemi *et al.*, 2017 (from Moeslinger *et al.*, 2024)
Q $[\mathrm{s}^{-1}]$	1×10^{27}	5.4×10^{26}
ν $[\mathrm{s}^{-1}]$	1.1×10^{-6}	2×10^{-7}
u_n $[\mathrm{kms}^{-1}]$	0.7	0.7
Simulation domain [km]	$4000 \times 4000 \times 4000$	$7000 \times 12000 \times 16000$
Grid resolution [km]	$15 - 250$ (variable) interpolated to 15 fixed grid	25
Heliocentric distance [au]	not specificed	$2.5 - 3$
Upstream n_{SW} $[\mathrm{cm}^{-3}]$	3.45	1
Upstream u_{SW} $[\mathrm{km\ s}^{-1}]$	400	430
Upstream $T_{e,\mathrm{sw}}$ [eV]	12	12
Upstream B_{IMF} [nT]	0.98	3

5.3 Validation of the ion test-particle model

In this section, I evaluate the accuracy and applicability of the ion test-particle model in two ways. First, in Section 5.3.1, the hybrid electric and magnetic fields are replaced by a radial test electric field, for validation of the collisions against the 1D numerical model introduced in Chapter 4. Second, in Section 5.3.2, the output of the model under collisionless conditions is compared to the results from the hybrid simulation.

5.3.1 Validation against the 1D fluid model

To validate the ion collisions in the ion test-particle model, the 3D model is compared against the 1D fluid Ion Acceleration Model described in Chapter 4 (Section 4.1). To do so, the hybrid electric and magnetic field inputs are replaced with $\vec{B} = \vec{0}$ everywhere in the simulation, and a radial electric field proportional to $1/r$, as given in Equation 4.1 with $m = 1$ and $E_c = 0.5 \times 10^{-3}$ V/m. The electric field is calculated over a $(1000 \times 1000 \times 1000)$ km grid with a 10 km spatial resolution in each direction. The field profile is shown in Figure 5.5.

For the collisions to be comparable to the Ion Acceleration Model, we need to use sim-

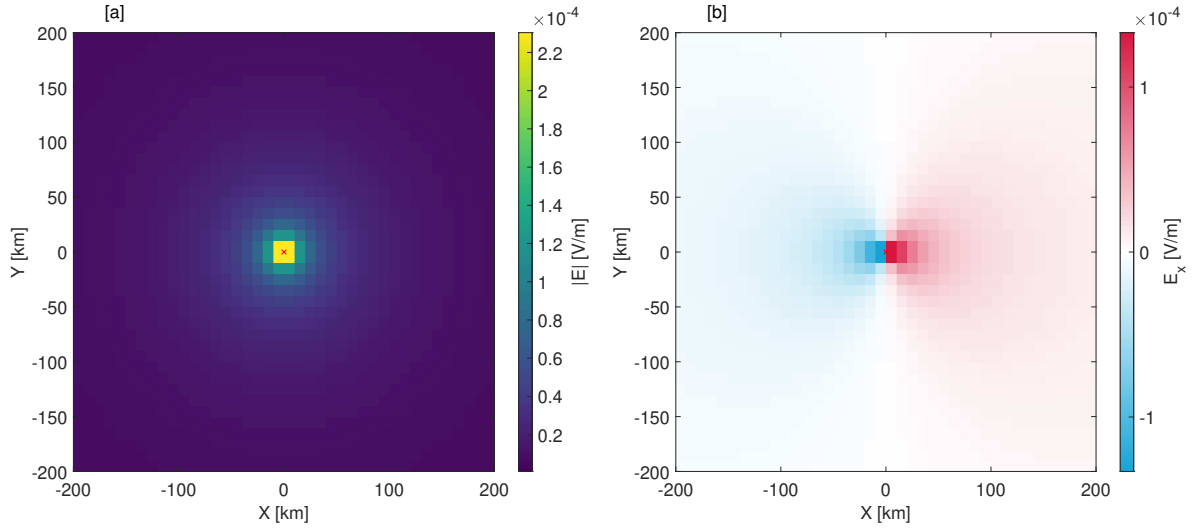

Figure 5.5: **[a]** Magnitude and **[b]** X-component of the radial electric field used for validation of the ion test-particle model in Section 5.3.1. The field is shown in the X-Y plane. The box used in the simulation run extends to 1000 km in each direction, but here is shown only up to 200 km.

Table 5.2: Inputs to the 1D ion acceleration and test-particle models for validation in Section 5.3.1. The case study used is the same as in Chapter 4, Section 4.3

Rosetta equivalent date	Q [s^{-1}]	ν [s^{-1}]	$\%NH_3$	u_n [km s^{-1}]	$E(r_c)$ [mV m^{-1}]
2015-11-21	7×10^{27}	2×10^{-7}	0.2	0.75	0.5

plified versions of the cross sections described in Section 5.1.3 such that the ion-neutral rate coefficients k_{IN} are held constant as they were for the 1D model. The reaction rates for momentum transfer and protonation can be related to energy-dependent cross-sections by writing the rate coefficient in terms of the cross section σ and the relative velocity, v_{rel}, between the ion and the neutral :

$$k^{\mathrm{IN}} = \sigma v_{\mathrm{rel}}. \tag{5.19}$$

This can then be rearranged to give the cross-section in terms of the relative energy E_{rel},

$$\sigma(E_{\mathrm{rel}}) = k^{\mathrm{IN}} \sqrt{\frac{m_{\mathrm{IN}}}{2E_{\mathrm{rel}}}} \tag{5.20}$$

where m_{IN} is the reduced mass of the ion and the neutral (Equation 5.12).

With these changes to the cross sections implemented into the ion test-particle model

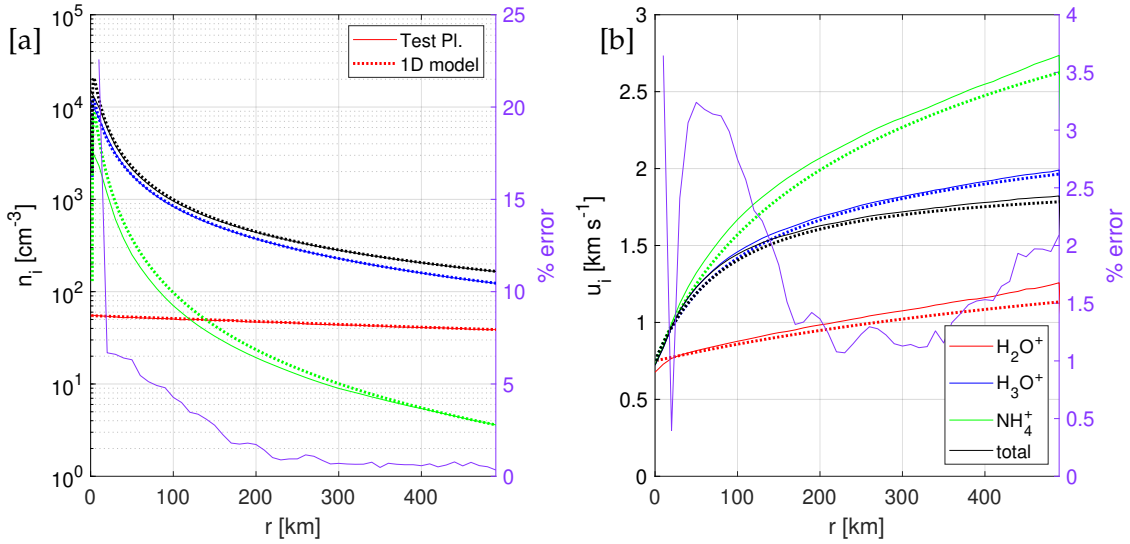

Figure 5.6: **[a]** H_2O^+ (**red**), H_3O^+ (**blue**), NH_4^+ (**green**) and total (**black**) density profiles from the 1D Ion Acceleration Model described in Section 4.1 (**solid lines**) compared with those from the test-particle model (**dotted lines**). **[b]** same as [a] but for the bulk ion velocity. Input parameters are given in Table 5.2

and run with the radial electric field shown in Figure 5.5, the resulting ion density and bulk velocity profiles can be properly compared against the 1D numerical Ion Acceleration Model. Figure 5.6 shows the outcome of this comparison, showing the density and velocity profiles averaged over 10 km radial bins for the three ion species, as well as the total. The percentage difference from the 1D model for the total density and bulk velocity are shown in purple. Over the 500 km range, the agreement is generally within 5%, with the best agreement between 20 and 200 km. The worst agreement is near the nucleus, since in the test-particle model the moments are calculated over a fixed grid ($10 \times 10 \times 10$ km in this instance) and the 2 km nucleus sits at an intersection between cells. In the 1D model, the densities are calculated over 1D logarithmically-spaced shells, allowing smaller resolution near the surface.

5.3.2 Validation with no collisions

Now, the test-particle model is compared to the hybrid collisionless simulation in order to validate the approach in the collisionless case. Figure 5.7 shows the result of this comparison along the comet-sun line (x). As there are no collisions considered, the only cometary ion species is H_2O^+. Input parameters of the runs are given in Table 5.1

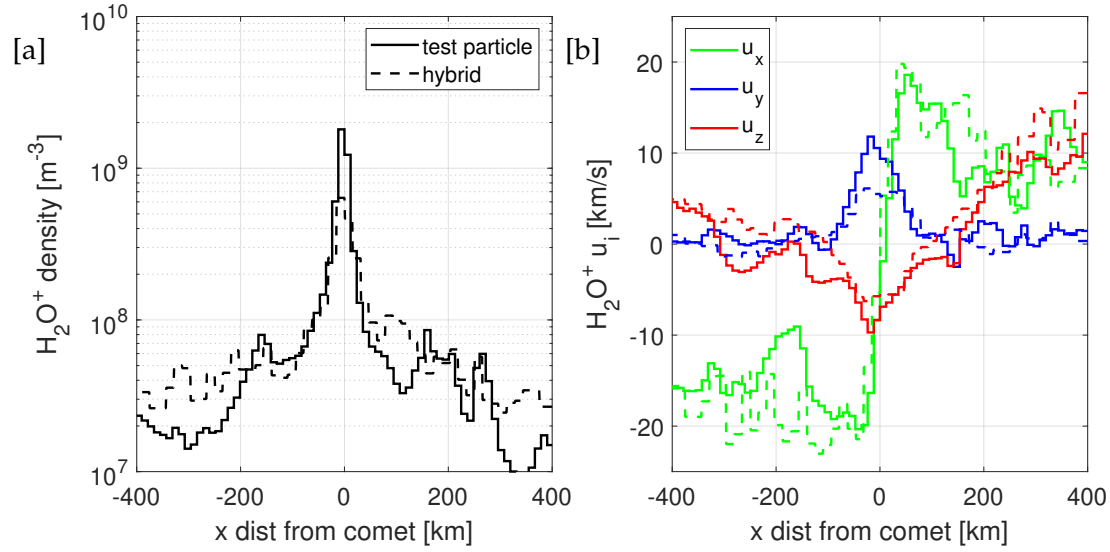

Figure 5.7: Comparison of the Aalto hybrid simulation and the ion test-particle model with no collisions, showing **[a]** the H_2O^+ density and **[b]** three components of the bulk velocity, both along the x (comet-sun) line. The Sun is in the +x direction.

The two models generally show a good agreement, with the largest discrepancy in the ion density near the nucleus. This is likely to be due to the different way that the comet itself is treated in the simulations. In the hybrid model, the comet is treated as a point source, whereas in the test-particle model there is no production below the 1.7 km radius.

5.4 Diamagnetic cavity: 1D fluid vs 3D kinetic collisions

I now use the 3D kinetic approach to assess the validity of the 1D fluid approach in Chapter 4. Comparison is made for the same case as in Section 5.3.1, with inputs given in Table 5.2. Since there is no magnetic field in this case, only a radial electric field, it continues to be valid only inside the diamagnetic cavity, and represents inputs similar to those seen on 21st November 2015 by Rosetta.

First, the 3D cross sections described in Section 5.1.3 need to be compared with the kinetic rates used for the 1D model in Chapter 4. Figure 5.8 shows the constant kinetic rates k and the equivalent σv_{rel} (Equation 5.19) against the ion speed. The momentum transfer and electron transfer kinetic rates are shown together as they are treated as the same process in the 1D model (having the exact same effect on the resulting ion). The momentum and electron

transfer cross sections result in a collision probability up to 3 times higher than given by the kinetic rates. The proton transfer cross section is less effective at high energies, but reaches up to 5 times higher collision rate than the 1D version at low energies.

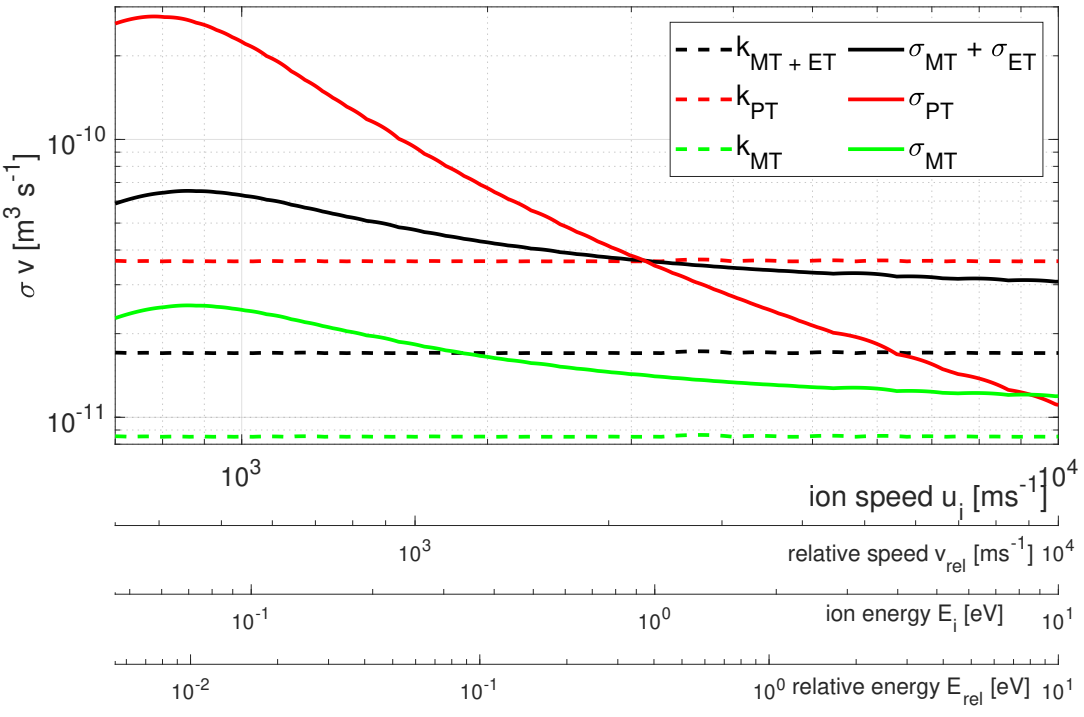

Figure 5.8: Comparison of the 3D cross sections (σ) presented in Section 5.1.3 and the 1D kinetic rates (k) used in Chapter 4. Proton transfer (PT), electron transfer (ET) and momentum transfer (MT) reactions between H_2O^+ and H_2O are shown.

The implication of these energy-dependent, 3D cross sections on the ion composition and velocity profiles is shown in Figure 5.9. Overall, the main effect of the new cross sections is to boost the proton transfer, reducing the H_2O^+ density and producing more NH_4^+. The total plasma density is increased by a factor of up to 1.3 in the 3D model thanks to more effective collisions, and the ion bulk velocity is up to 23% slower. However, as demonstrated in Section 4.4.2 (Equation 4.37), the product $n_i u_i$ for a given r is preserved, so the determination of the electric field strength and bulk velocity that are required to recreate the measured plasma density from RPC–LAP and RPC–MIP (Section 4.3) remains valid. In future 1D fluid models, increasing the kinetic rates by a factor of 5 for proton transfer, and 3 for momentum

and electron transfers, could account for this difference compared to the cross sections.

Figure 5.9 also shows the effect of a 0.5 eV exothermic energy release (see Section 2.2.2) during protonation. The difference is very small (in some cases not visible on the plots), only reducing the total plasma density by a maximum of 5%, and increasing the bulk velocity by up to 8%.

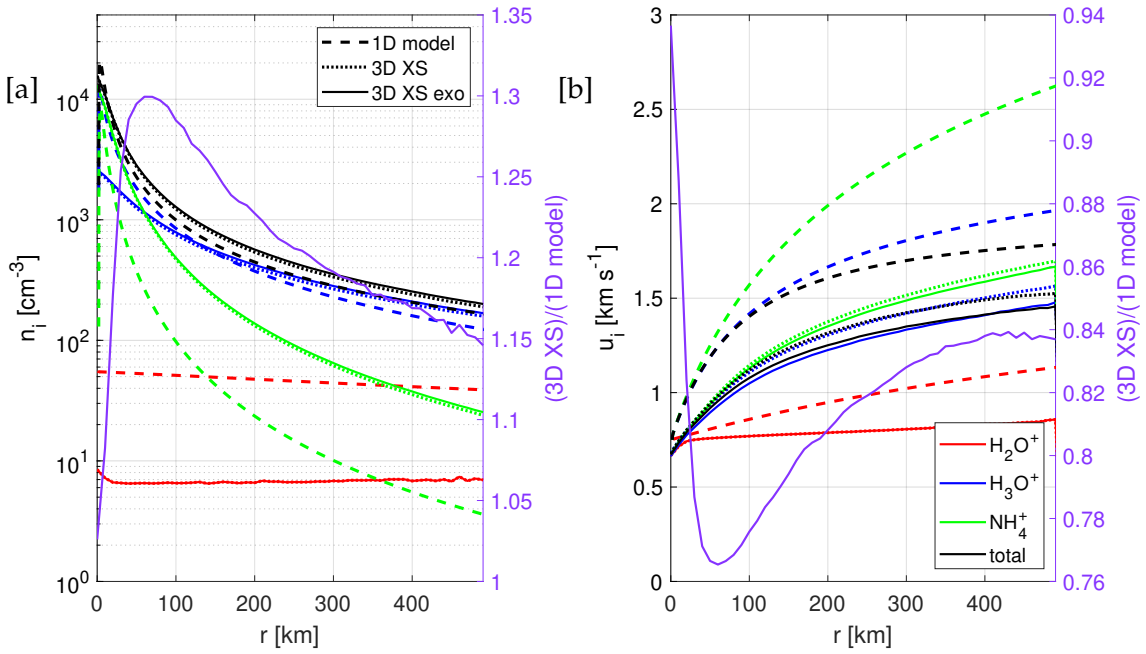

Figure 5.9: Comparison of 1D Ion Acceleration Model from Chapter 4 (**dashed lines**) with the 3D ion test-particle model with (**solid lines**) and without (**dotted line**) an exothermic energy release during protonation for [a] ion density and [b] ion bulk velocity. Profiles for H_2O^+ (**red**), H_3O^+ (**blue**) and NH_4^+ (**green**) are shown, alongside the total for all species (**black**). Right-hand axis shows the ratio between the two models for the total ion population (**purple**).

5.5 Application to intermediate outgassing

In this section, the ion test-particle model is run for the electric and magnetic fields from the AMITIS hybrid simulation (see Section 5.2), which represent the conditions encountered by Rosetta at 67P, $2.5 - 3.0$ au from the Sun (Table 5.1). Figure 5.10 shows the field magnitudes in the X-Y plane, where the X-axis points towards the Sun and the upstream IMF is along the Y-axis. This means that the convective electric field (Section 2.3.1), $\vec{E}_{\rm conv} = -\vec{u}_{\rm SW} \times \vec{B}_{\rm IMF}$ is in the +Z direction. The magnetic field piles up in front of the comet as the solar wind is slowed

down and mass-loaded by the obstacle, that is, the out-flowing cometary ions. Under these input conditions, there is no diamagnetic cavity formed, and the solar wind penetrates all the way to the surface.

5.5.1 3D simulated collisional ionosphere

Figure 5.12 shows the modelled ion density in the X-Y plane, with the Sun in the +X direction, Figure 5.13 shows the corresponding bulk velocity magnitude. Comparing Figure 5.12a and Figure 5.12b, the inclusion of collisions increases the total ion density, and the ions are slowed down (Figure 5.13b). However, even with collisions included, the velocities reached by the ions are significantly higher than those derived in Section 4.3 - around $10\ \mathrm{km\ s^{-1}}$ at $50\ \mathrm{km}$, compared to $2 - 3\ \mathrm{km\ s^{-1}}$. This will be discussed further in Section 5.6.The ion density is largest both close to the nucleus, as in the 1D case, but is also enhanced just inside the region of magnetic pile up (see Figure 5.10c). The cometary ions appear to stagnate in this area, which was also observed in the collisionless simulations of Moeslinger *et al.* (2024), but the addition of ion-neutral collisions reduces the piled-up density. Figure 5.11 shows the ratio between the total ion density in the collisional and non-collisional case, in all three planes. Collisions are shown to increase the total ion density by up to 4 times, with the greatest impact on the densities in the region of ion pile up, on the inner edge of the magnetic pile up region. It can also be seen in Figure 5.11b that the effect of collisions is more significant for -Z values. This is likely due to enhanced transport in the +Z direction by the motional electric field (Section 2.3.1).

When the ion density is separated into species (see Figure 5.12c-e), there is a clear difference in behaviour of the three key ion species. As expected from the ionisation (see Section 2.2.1) and protonation (see Section 2.2.2) processes, all three ion species are produced near the nucleus with a similar velocity to the neutral gas. However, all species are affected differently by the electric field. This is not simply because of different electromagnetic forces on them, since they all have the same charge ($+e$) and very similar masses ($18 - 19\ \mathrm{u\ q^{-1}}$). Instead, this confirms the findings of Chapter 4, that the different ion-neutral chemical timescales drives this variation.

H_2O^+ (Figure 5.12c) is around an order of magnitude less prevalent and significantly more homogenous than H_3O^+ (Figure 5.12d), with no clear enhancement in the pile up region. H_2O^+ has a very fast reaction with H_2O to form H_3O^+, therefore it has too little time to undergo significant acceleration by the electric field (see Figure 5.13c), as we saw with the 1D model in Section 4.2. H_2O^+ is at (or close to) photochemical equilibrium in regions close to the nucleus, and directly lost through transport far from the nucleus.

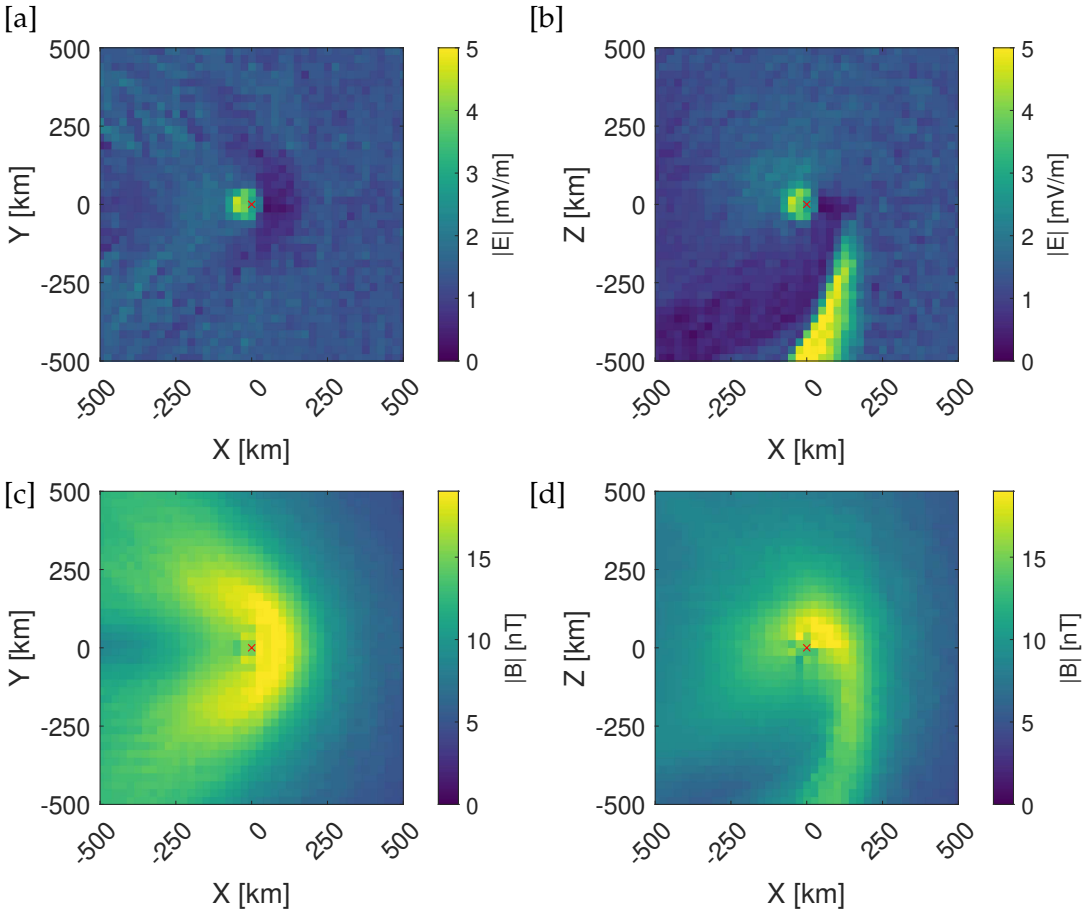

Figure 5.10: **[a]** and **[b]** Electric field and **[c]** and **[d]** magnetic field magnitudes from AMITIS (Fatemi *et al.*, 2017), used in the test-particle model for Section 5.5. (Moeslinger *et al.*, 2024, Moeslinger and Gunell, 2024)

NH_4^+ (Figure 5.12e) is produced in low densities (with similar magnitudes to H_2O^+) at its peak, but is concentrated more strongly near the nucleus and in the ion pile up region. This is because NH_4^+ is particularly sensitive to the increased ion transport further from the nucleus, and doesn't have time to be produced from ion-neutral chemistry when the bulk flow is too fast. NH_4^+ is also more strongly accelerated and reached higher velocities. However, at this

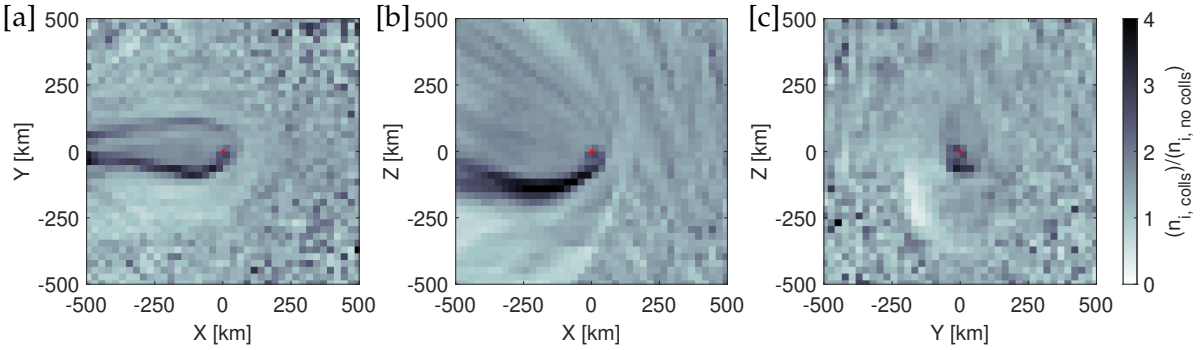

Figure 5.11: Ratio between the total ion densities calculated from the test-particle model with collisions included (as in Fig. 5.12a) and without (as in Fig. 5.12b). **Red cross** marks the location of the nucleus.

outgassing and outside the ion pile up region, the NH_4^+ density is low (Figure 5.13e), so the statistics for determination of the bulk velocity are poor. Cells for which the NH_4^+ density was less than $10^{-2}\ \mathrm{cm}^{-3}$ are blacked out in Figure 5.13e.

Figure 5.14 shows the total ion bulk velocity with arrows to show the direction of travel in each plane. Collisions are included for this simulation. Figures 5.14 [b], [d], and [f] show the same information as [a], [c] and [e], but focussed on the first $100\ \mathrm{km}$ from the nucleus. Panel [a] shows the bulk flow mainly diverted around the nucleus and tail-ward, with the radial motion only visible for $0 - 50\ \mathrm{km}$ from the nucleus. In the Y-Z plane (Figure 5.14f), where Rosetta was usually located, the radial flow extends over a larger region, up to 100 km. Figures 5.14 [c] and [e] show a strong component of the flow in the + Z direction, owing to the motional electric field.

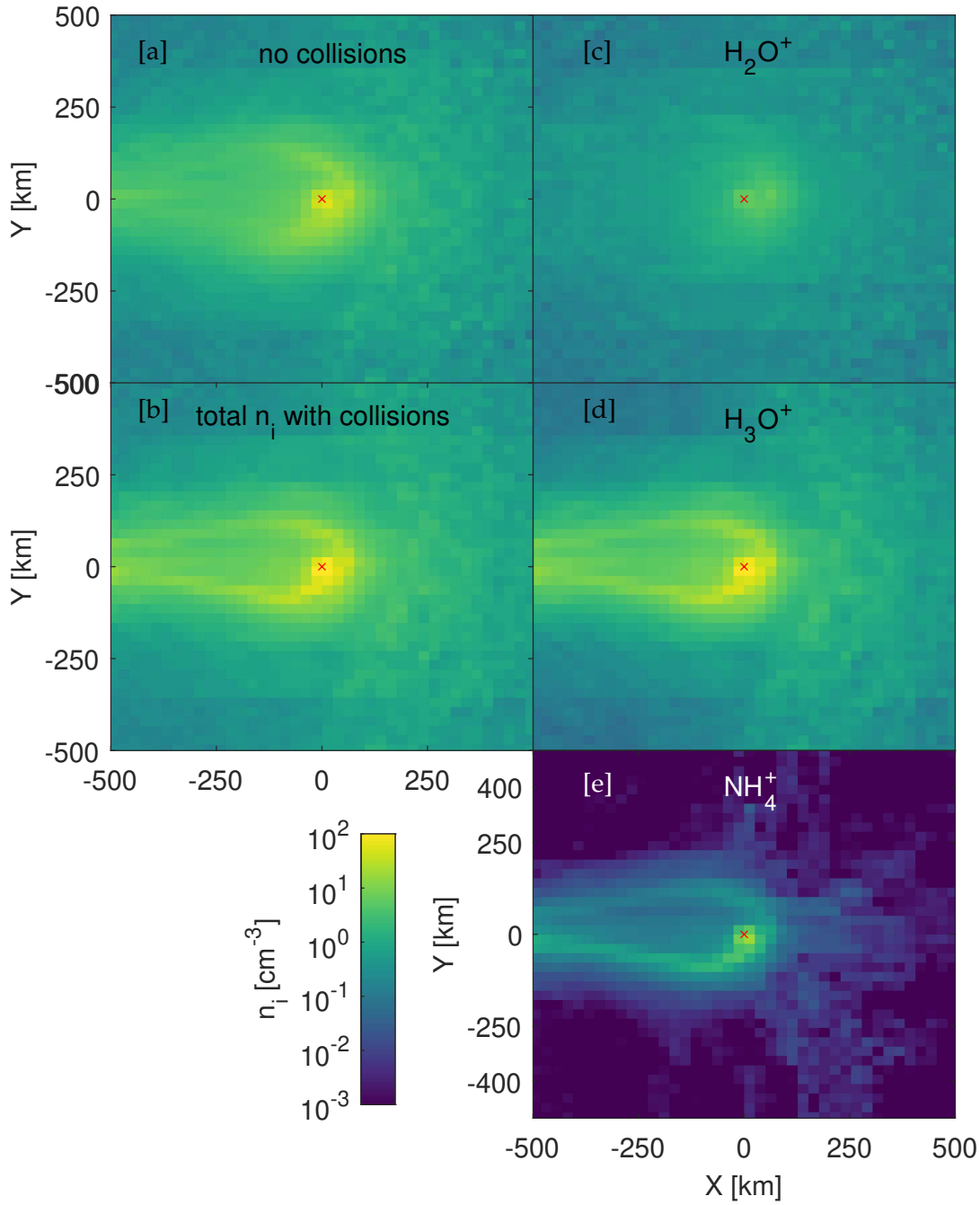

Figure 5.12: Ion density in the X-Y plane from the ion test-particle model, using the electric and magnetic fields from the AMITIS hybrid simulation (Table 5.1). **[a]** total ion density with no collisions, [b] total ion density with all collisions. For the collisional case, densities of **[c]** H_2O^+, **[d]** H_3O^+, and **[e]** NH_4^+ are given. The Sun is in the +X direction, and the comet nucleus is marked with a red cross.

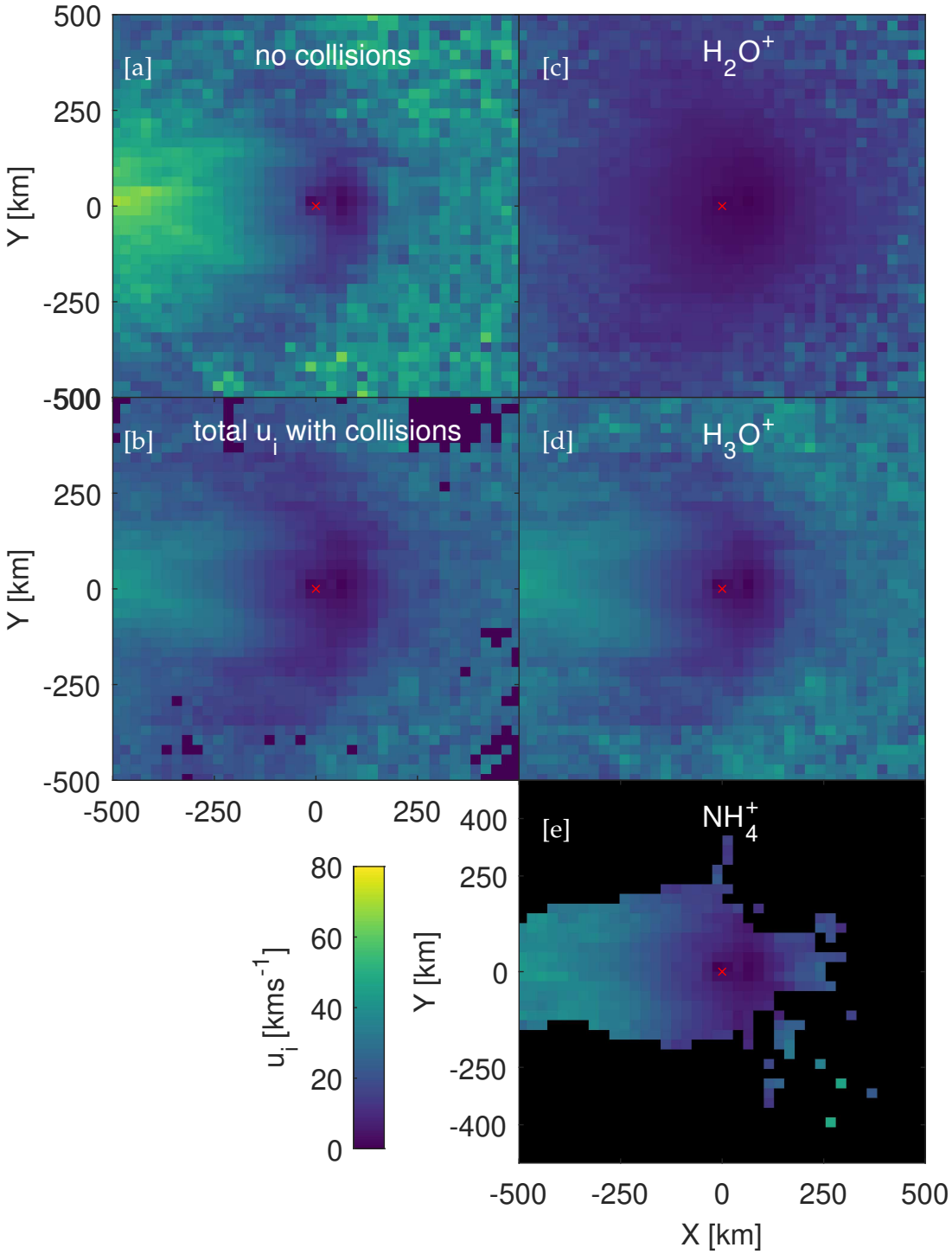

Figure 5.13: Same as Figure 5.12, but for the ion bulk speed. Cells in **black** are where the number density was too low ($< 10^{-2}$ cm^{-3}) to provide reliable statistics.

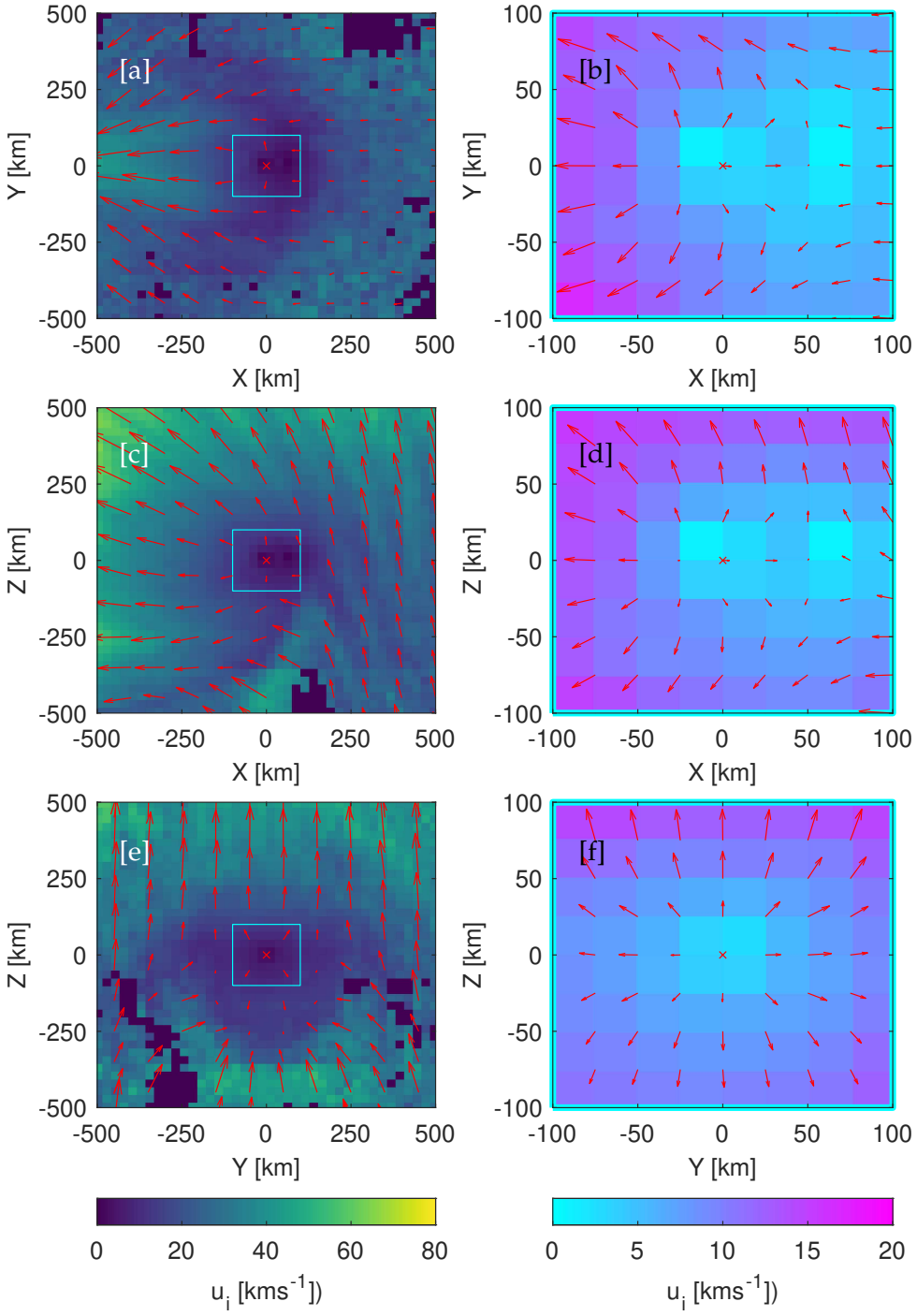

Figure 5.14: Ion bulk velocity magnitude (**colour scale**) and direction (**red arrows**) in the **[a, b]** X-Y plane, **[c, d]** X-Z plane, and **[e, f]** Y-Z plane. **Cyan box** in left column corresponds to the 100×100 inset, shown in the right column. The comet nucleus is marked with a **red cross**.

5.6 Comparison with plasma density data

In this section, the modelled ion density is compared to the data from RPC–MIP and RPC–LAP. This allows conclusions to be drawn about the validity of the assumptions in the hybrid simulation.

First, in Section 5.6.1, the full RPC–MIP/LAP combined dataset is compared against the plasma density calculated by the field-free, chemistry-free model (Equation 1.5) to verify where the model performs best over the Rosetta escort phase. This provides a reference case to compare with the ion-test particle model, to assess whether the plasma density can be constrained more accurately by the more complex model. In Section 5.6.2, the ion test-particle model run from Section 5.5 is compared against the MIP/LAP dataset and the field-free, chemistry-free model.

5.6.1 MIP/LAP data vs field-free chemistry-free model

The MIP/LAP electron density data (Johansson *et al.*, 2021) are first smoothed with a 1-minute rolling median to reduce noise and small-scale variations. Figure 5.15 shows the smoothed dataset sorted into $10\ \mathrm{km}$ bins of cometocentric distance and bins of width 0.1 of $\log_{10}(Q\nu^{\mathrm{tot}})$. The median of each bin (Figure 5.15a) is shown, as well as the 25th percentile, as this value is less sensitive to electron density spikes, and may capture the baseline plasma density better. The total ion production rate $Q\nu^{\mathrm{tot}}$ is calculated from the local outgassing Q (from COPS, Equation 2.2, and corrected for the neutral composition) and the total $\mathrm{H_2O}$ ionisation frequency (photoionisation and electron impact) from Stephenson *et al.* (2023) (see Figure 2.5).

Figure 5.15d then shows the field-free, chemistry-free model,

$$n_i(r) = \frac{Q\nu^{\mathrm{tot}}}{4\pi u_n^2 r^2}(r - r_c), \tag{5.21}$$

which is equivalent to Equation 1.5 using Equation 2.2 for the local outgassing Q. The bulk neutral velocity u_n is known to vary with heliocentric distance (Biver *et al.*, 2019, see Section 2.1.2) as well as with cometocentric distance (Heritier *et al.*, 2017a), but is assumed constant for Equation 5.21. A value of $u_n = 700\ \mathrm{km\ s^{-1}}$ is assumed, in line with the inputs to

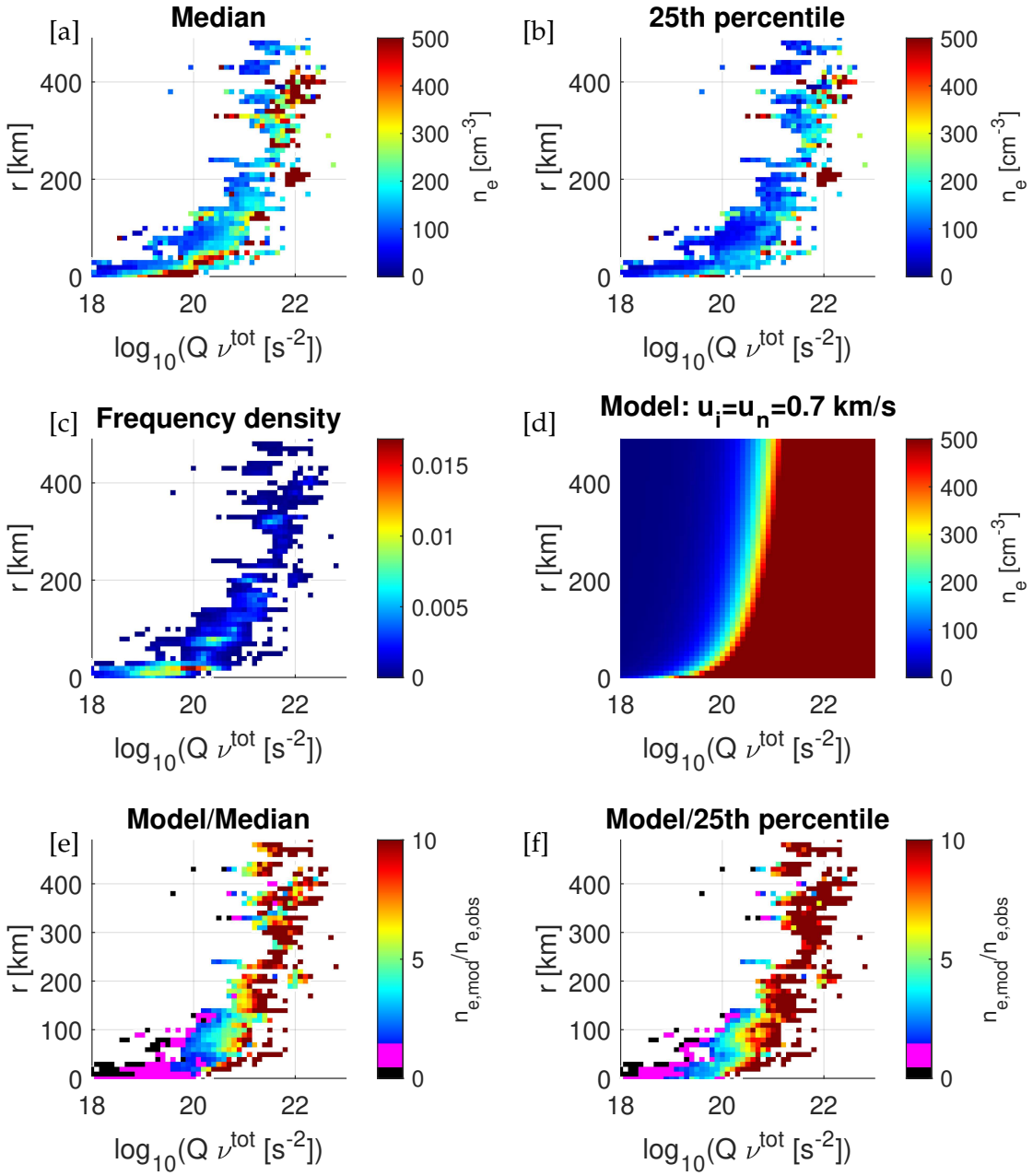

Figure 5.15: Heat maps showing the MIP/LAP combined dataset from the whole escort phase (covering August 2014– August 2016), binned by cometocentric distance r and total ion production rate $Q\nu^{\mathrm{tot}}$. **[a]** Shows the median electron density in each bin, **[b]** shows the 25th percentile. **[c]** shows, for context, the frequency density of data in each bin. **[d]** Shows the density as calculated by the 1D field-free model (Equation 5.21) and **[e]** and **[f]** the ratio between the field-free model and the MIP/LAP median and 25th percentiles respectively, with **magenta** indicating where the ratio is 0.5–1.5.

the ion test-particle model and hybrid simulation (Table 5.1). The colour scale in Figure 5.15d is capped at $500\ \mathrm{cm}^{-3}$.

Figure 5.15c highlights the limitations of the parameter space we have for the Rosetta data. Despite its extensive escort phase, practical limitations mean that the coverage for low cometocentric distances at high outgassing is limited, and vice versa. However, it is possible to draw several conclusions from the data we do have. Figures 5.15e and 5.15f show the overestimation of the field-free chemistry-free model (Equation 5.21) increases with ion production rate. At low outgassing, as predicted by Galand *et al.* (2016) and demonstrated in Galand *et al.* (2016) and Heritier *et al.* (2018), the field-free model performs well to explain the measured electron density. At high outgassing, the observed electron density is up to 40 times higher than is calculated (colour scale in Figure 5.15e and 5.15f capped at 10 for clarity). This has been previously reported in e.g. Vigren *et al.* (2019), but the full comparison over the whole escort phase is made here for the first time (see also Figure 1.13). Where the data are higher than field-free chemistry-free model (shown in black in Figure 5.15e and f), this may be due to the changes in neutral composition at low outgassing. The CO_2 component of the coma was found to increase significantly over the southern hemisphere beyond 3.1 au (Gasc *et al.*, 2017a), which was shown in Galand *et al.* (2016) to increase the photoionisation rate by up to 50%.

The coverage of the parameter space in Figure 5.15 by these previous studies is shown in Figure 5.16a, alongside the ion production rate $Q\ \nu^{\mathrm{tot}}$ used in this study (green line), and the instances of diamagnetic cavity crossings as detected by RPC–MAG (Goetz *et al.*, 2016a) (black crosses). Both the studies of Galand *et al.* (2016) (cyan triangles) and Heritier *et al.* (2018) (red squares) reported a good agreement between the field-free, chemistry-free model (Equation 5.21) and the electron density data[2] in the low outgassing cases (for which the model was developed). The study of Vigren *et al.* (2019) (blue squares) applied Equation 5.21 over a large time range post-perihelion, showing a transition from overestimation of the model near perihelion to good agreement at lower ion production rates. This result is well replicated in Figure 5.15, and generalised over the full dataset.

[2]Note that MIP and LAP were used separately in these studies as the combined MIP/LAP dataset (Johansson *et al.*, 2021) was not yet available.

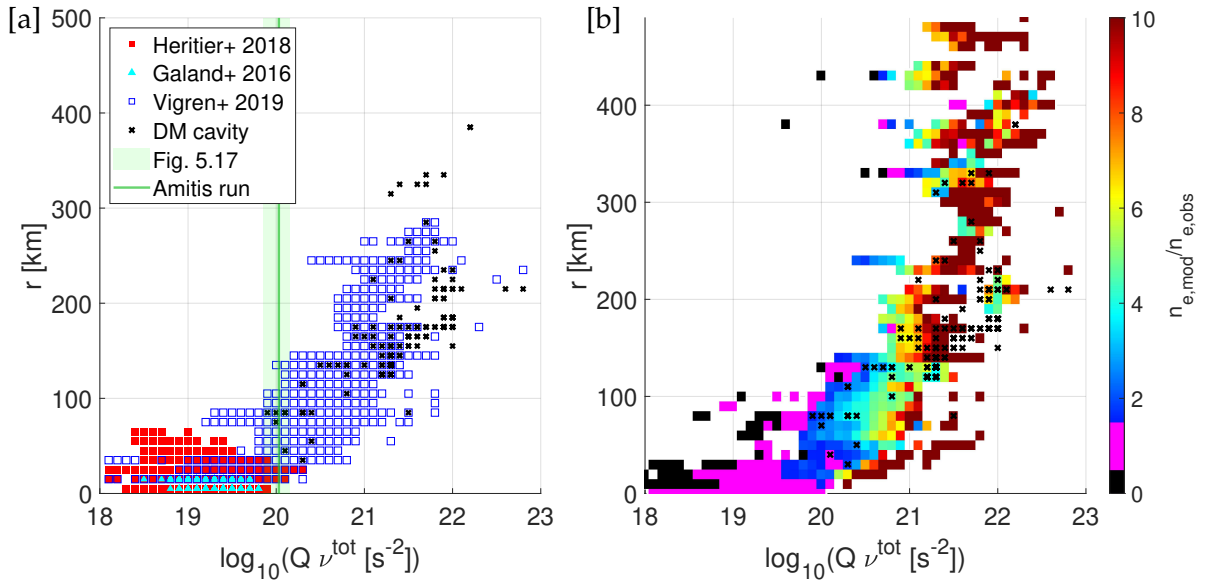

Figure 5.16: (**a**) Coverage of the parameter space in $Q\ \nu$ vs r (as in Figure 5.15), done by previous studies: Heritier *et al.*, 2018 (**red filled squares**), Galand *et al.*, 2016 (**cyan triangles**), and Vigren *et al.*, 2019 (**blue squares**). The ion production rate $Q\ \nu$ from the hybrid simulation run used in Section 5.5 is given by the **green line**, and the **green shaded region** is the data range used for MIP/LAP in Figure 5.15. The **black crosses** show diamagnetic cavity crossings as observed by RPC–MAG (Goetz *et al.*, 2016a) (**b**) Same as Figure 5.15e but with the diamagnetic cavity crossings marked with **black crosses**.

Figure 5.16b shows the location of the diamagnetic cavity boundary crossings as seen by RPC–MAG overlaid on Figure 5.15e. In general, the diamagnetic cavity has been observed for $Q\nu^{\mathrm{tot}} > 1 \times 10^{20}\ \mathrm{s}^{-2}$, where Equation 5.21 overestimates the plasma density. The larger the ion production rate, the further from the nucleus the cavity has been observed - however the data bias in the parameter space explored by Rosetta is probably artificially enhancing this trend.

The ion production rate $Q\nu^{\mathrm{tot}} = 1.08 \times 10^{20}\ \mathrm{s}^{-2}$ used in the simulation in Section 5.5.1 falls in an interesting region of the parameter space shown in Figure 5.16a. At cometocentric distances below 50 km, a generally good agreement with the field-free, chemistry-free model has been reported (Heritier *et al.*, 2018 and in Figure 5.15). However, diamagnetic cavity crossings have also been observed at other times when Rosetta was closer to 100 km for the same $Q\ \nu^{\mathrm{tot}}$. It is possible that this ion production rate reflects somewhat of a transition between the low outgassing regime, where the field-free chemistry-free model applies, and

where the ambipolar electric field becomes important and leads to increased transport at the Rosetta distance.

5.6.2 MIP/LAP data vs ion test-particle model

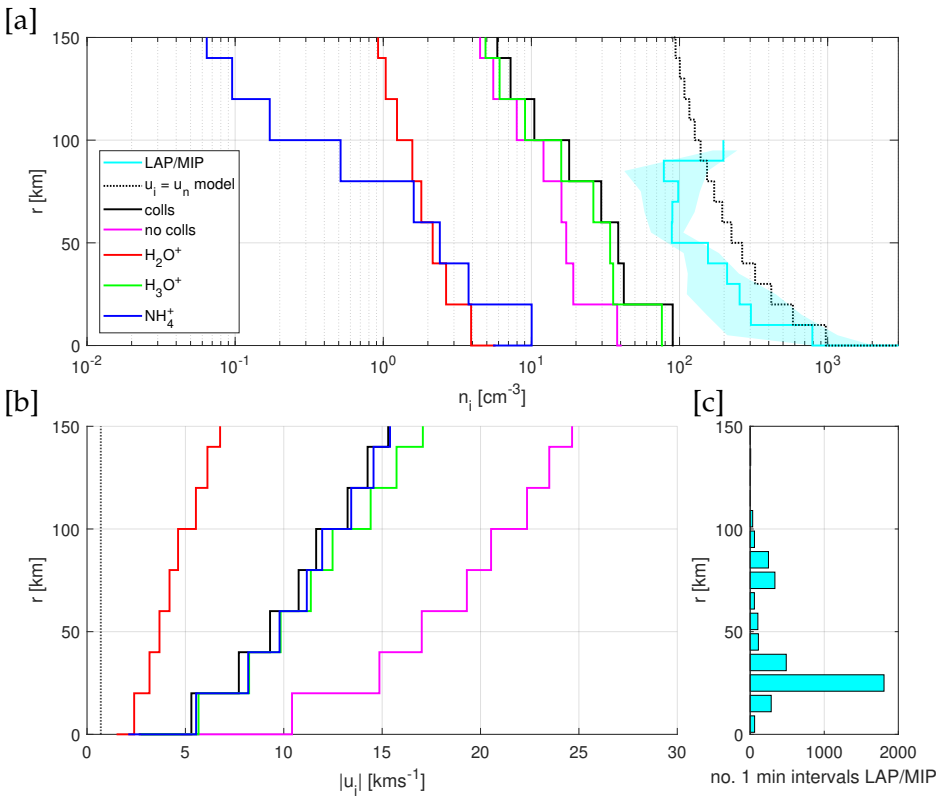

Figure 5.17: [a] Ion density averaged over 20 km cometocentric distance bins for the test-particle model in the terminator plane: Total with collisions (**black**), total without collisions (**pink**), H_2O^+ (**red**), H_3O^+ (**green**) and NH_4^+ (**blue**). The field-free, chemistry-free modelled density using Equation 5.21 is shown by the **black dashed line**. Cyan line shows the median in each radial bin from MIP/LAP for $19.85 < \log_{10}(Q\nu^{\mathrm{tot}}) < 20.15$. **Shaded region** shows the 25th-75th percentile range of the data in each bin. [b] same as [a] but for the ion bulk velocity from the test-particle model only. [c] Number of 1-minute intervals in each 10 km bin for the MIP/LAP dataset.

I now compare the plasma density from the ion test-particle model with the MIP/LAP combined dataset and the field-free chemistry-free model. The ion test-particle model in Section 5.5 was run with $Q\nu^{\mathrm{h}\nu,\mathrm{ioni}} = 1.08 \times 10^{20}$ s^{-2} (see Table 5.1). The ion test-particle model and the AMITIS hybrid simulation only treat photoionisation, and do not include the electron-impact ionisation frequency. To account for this shortcoming of the models,

both have artificially boosted the photoionisation frequency in accordance with the electron-impact ionisation frequency measured by RPC–IES (e.g., Stephenson *et al.*, 2023). The input parameters in Table 5.1 for the AMITIS model then represent the total ionisation frequency (ν^{tot}) for the $2.5 - 3.0$ au range. This total value is used in this Section for comparison with the Rosetta data, and the impact of this assumption is discussed further in Section 5.7.3. A more thorough implementation of electron-impact ionisation into the model is left for future work.

For comparison between the MIP/LAP data and the ion test-particle model run in Section 5.5, I take the simulated ions in the terminator (Y-Z) plane only. This is where Rosetta made the majority of its orbits around the comet, so is most applicable for data comparison. These simulated data are then averaged over $20\ \mathrm{km}$ radial bins and compared to the MIP/LAP data as presented in Figure 5.15, for $19.85 < \log_{10}(Q\nu^{\mathrm{tot}}) < 20.15$. The result is shown in Figure 5.17. Even with the collisions implemented, the resulting ion densities are consistently lower than the plasma density measured by the spacecraft, by 5-10 times. The measured densities lie between the $u_i = u_n$ model (Equation 5.21) and those calculated by the test-particle model, with good agreement between the data and the Equation 5.21 particularly below 30 km. The reasons for the too low densities obtained by the test-particle model are discussed in Section 5.7.3, but it is clear that the ions are transported too quickly in the hybrid model.

The ion bulk velocities for each of the species and the total from the test-particle model are shown in Figure 5.17b. It shows that the ions in the model are quickly accelerated to significantly above the neutral speed, even in the first 20 km from the surface. The inclusion of collisions in the model decreases the bulk ion speed from $20\ \mathrm{km\ s^{-1}}$ to $11\ \mathrm{km\ s^{-1}}$ at $100\ \mathrm{km}$. $\mathrm{NH_4^+}$ is the most strongly accelerated, reaching $20\ \mathrm{km\ s^{-1}}$ at $100\ \mathrm{km}$. Despite the deceleration due to collisions, these speed values remain high, leading to underestimation of the plasma density compared with the observations. The reason for the high ion speeds is discussed in Section 5.7.3.

5.7 Discussion

5.7.1 Impact of 1D fluid vs 3D kinetic collisions

In Section 5.4, the 3D test-particle model was applied to the radial electric field derived for the diamagnetic cavity crossings on 21st November 2015 in Chapter 4 (Section 4.3). I showed that the energy-dependent 3D cross sections make the ion environment more collisional at this outgassing, driving more proton transfer and increasing the prevalence of NH_4^+. However, since the total $n_i u_i$ at a given cometocentric distance is preserved according to Equation 4.37, the bulk velocity and electric field strengths required to reproduce the plasma density observed at Rosetta remain the same.

For the radial electric field case, the impact of the exothermic energy release during protonation was shown to be small but measurable, altering the total ion bulk speed by up to 8%. This is likely because the electric field and momentum transfer collisions quickly 'fix' the velocity back to being directed radially outwards from the nucleus. However, the exothermic energy release requires further study as it may have important implications for the ion dynamics at lower outgassing, when the electric field is weaker (Stephenson *et al.*, 2024), though collisions are also less likely in this regime.

5.7.2 Application to intermediate outgassing

Applying the test-particle model to the electric and magnetic fields from the hybrid simulation AMITIS in Section 5.5 confirmed the findings of Chapter 4, that the ion dynamics are different for individual ion species due to their different ion-neutral chemical pathways.

H_2O^+ is close to photochemical equilibrium, even at $2.5 - 3$ au, so is present in low amounts and not concentrated in any particular location (see Figure 5.12c). Conversely, H_3O^+ and NH_4^+ are more strongly affected by the electric fields, accumulating in greater numbers both near the nucleus and in the ion pile up region inside the magnetic pile up region (see Figure 5.12d-e). Collisions of all types are most effective in this ion pile up region, which extends into the comet tail. The chemistry is less complex in the +Z direction, that is, the direction of the motional electric field where transport is enhanced (see Figure 5.10).

It was previously assumed that the radial flow assumption was only valid in the diamagnetic cavity, when the only electric field term present was the ambipolar electric field. Figure 5.14 shows that within the first 100 km of the nucleus, radial motion dominates the flow in the Y-Z plane assessed by Rosetta (for conditions with no diamagnetic cavity). However, comparison with the MIP/LAP data suggests that the ions in the simulation may be accelerated too strongly, likely due to limitations of the hybrid model and the assumptions made about the electron temperature. This is discussed further in the next Section, 5.7.3.

Beyond 100 km, the flow is dominated upstream of the comet by the +Z component, accelerated by the motional electric field of the solar wind. On the anti-sunward side, the flow is tailward (-X), with the velocity direction in the -Z region corresponding to an electric field enhancement. This behaviour at large cometocentric distances is reported in detail by Moeslinger *et al.* (2024), so I focus mainly on the assessment of the cometary ion population at the spacecraft-comet distances covered by Rosetta at $2.5 - 3$ au. This is the focus of Section 5.7.3.

5.7.3 Comparison of the ion test-particle model and Rosetta data

In Section 5.6, I used the ion test-particle model to assess the impact of the electric and magnetic fields from the AMITIS hybrid simulation on the ion composition and density, and compared it to the equivalent plasma density observations from the combined MIP/LAP dataset. The input conditions used were representative of those witnessed by Rosetta at $2.5 - 3$ au post-perihelion (Table 5.1).

The key finding of this comparison is that the plasma density data at this outgassing level ($\sim 1 \times 10^{27}$ s^{-1}) are underestimated by the test-particle model, even with collisions slowing the acceleration by the electric fields. In fact, the bulk of the data lie somewhere between the profile calculated by the 3D model and the one calculated by the field-free, chemistry-free model (which assumes $u_i = u_i = 0.7$ km s^{-1}, Equation 5.21, see Figure 5.17). To understand the underestimation of the plasma density by the model, we need to reflect on the assumptions made in both the test-particle model and the hybrid electric and magnetic fields that drive it.

Electron-impact ionisation

In the hybrid simulations, photoionisation and charge exchange with the solar wind are considered. Electron-impact ionisation is not modelled, only treated by boosting the photoionisation, because its proper assessment requires the kinetic treatment of electrons. Stephenson *et al.* (2023) modelled the cometary electrons using the collisional test-particle model, showing that the electron-impact ionisation frequency at $Q = 1.5 \times 10^{27}$ s^{-1} was most strongly enhanced in the region extending 100 km upstream and 380 km downstream of the nucleus. In short, in an optically thin coma the photoionisation frequency is broadly constant with radial distance but this is not the case for the electron impact. This suggests that simple 'boosting' of the photoionisation frequency to account for electron impact (informed by the data from Stephenson *et al.* (2023) presented in Figure 2.5), is unlikely to capture the full radial profile of the ion production rate properly. However, since the comparison with the MIP/LAP data in Figure 5.17 is only available up to 100 km in the terminator plane, assuming a constant ionisation frequency is probably a reasonable assumption in this range. At $Q = 1.5 \times 10^{27}$ s^{-1}, Stephenson *et al.* (2024) showed that the electron cooling exobase was at ~ 100 km, suggesting that electron-neutral collisions would flatten the potential well within this region (Stephenson *et al.*, 2023).

Electron temperature

The collisionality of electrons observed near the nucleus raises further questions about the validity of the hybrid simulation and its fluid treatment of the electrons. As discussed in Section 5.2, the hybrid approximation requires an equation of state to be chosen for the electrons. In many cases (including the two simulations used in this chapter), this is assumed to be adiabatic, such that

$$p_e = n_\mathrm{e} k_B T_\mathrm{e} = \alpha n_e^\gamma \tag{5.22}$$

and

$$T_e = \frac{\alpha}{k_B} n_e^{\gamma - 1} \tag{5.23}$$

where p_e is the total thermal pressure of the electrons, and $\alpha = k_B n_{\mathrm{e},0}^{1-\gamma} T_{\mathrm{e},0}$ where $n_{\mathrm{e},0}$ and $T_{\mathrm{e},0}$ are the number density and temperature of the electrons in the solar wind, respectively (fixed in the inputs of the simulations). γ is the adiabatic index, assumed 5/3 (three degrees of freedom for monatomic gas). In the solar wind, or at low enough neutral density (i.e. sufficiently far from the nucleus), this treatment of the electrons as one population with a Maxwellian distribution may be reasonable, but is clearly an oversimplification in the inner coma. In this region, the cometary electrons have distinct populations according to the collisions and field acceleration they undergo (see Section 2.3.3), and, beside a warm e^- population ($\sim 5 - 10$ eV), a significant population of cold electrons was observed throughout the Rosetta escort (Gilet *et al.*, 2020).

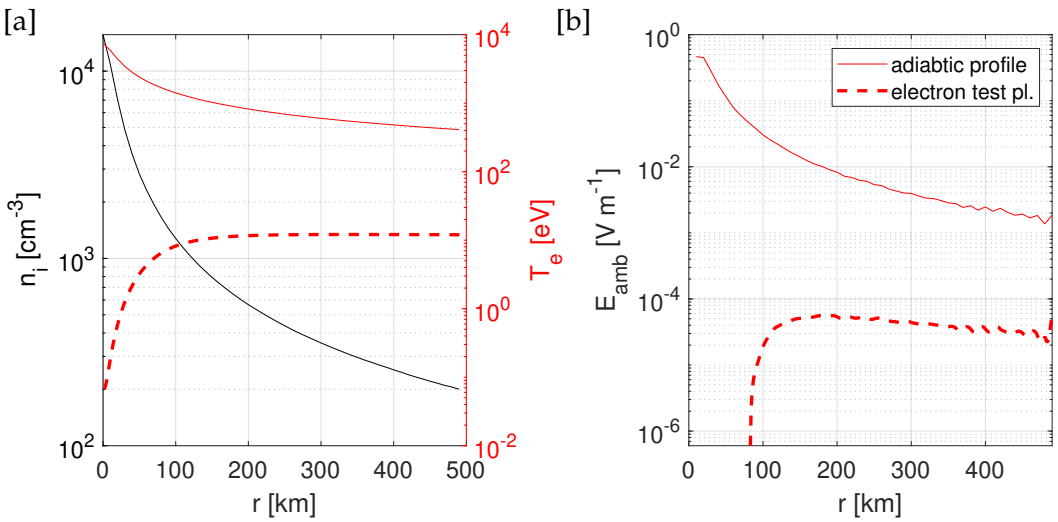

Figure 5.18: [a] **Black line**: the total ion density distribution from the ion test-particle model, for the radial electric field case in Section 5.4. **Red solid line**: Electron temperature calculated using the ion density profile (**black**) and the adiabatic temperature relation, Equation 5.22. **Red dashed line**: Electron temperature profile derived from the electron test-particle model of Stephenson *et al.* (2024) for $Q = 1 \times 10^{27}$ s^{-1}. Provided by P. Stephenson in private communication. [b] Ambipolar electric field $\vec{E}_{amb} = -\frac{1}{en_e}\nabla(n_e k_B T_e)$, calculated using the density profile in [a] and T_e from the (**solid red**) adiabatic and (**dashed red**) collisional electron test-particle model. Assuming quasi-neutrality $n_e = n_i$, upstream solar wind temperature 12 eV and density $n_{e,\mathrm{SW}} = 1$ cm^{-3}.

Stephenson *et al.* (2023) showed using their 3D electron test-particle model, that the electron-neutral collisions produce cold electrons and a 'flattened' potential well in the collisional region surrounding the nucleus. Figure 5.18a shows an electron temperature profile derived from their model for $Q = 1 \times 10^{27}\mathrm{s}^{-1}$. The drop in temperature within 100 km

of the nucleus contrasts with the adiabatic temperature profile (solid red line, calculated using Equation 5.23), which increases with increasing n_e. Figure 5.18b then shows, for illustrative purposes, the ambipolar electric field calculated from each of these temperature profiles, using the plasma density profile and the relation $\vec{E}_{\rm amb} = -\frac{1}{en_e}\nabla(n_e k_B T_e)$ (see Section 2.3.2). For the collisional electron case (red dotted line) this leads to a positive pressure gradient, and hence a negative ambipolar electric field, below $\sim 100\,\mathrm{km}$ where the temperature profile starts to flatten. In reality, there will be be a feedback on the plasma density from whatever electric field is acting upon it, and the final profile would need a self-consistent model. However I show these different electric field profiles, with significant caveats, to illustrate how critical the electron temperature is to the ion acceleration, and how this is a serious limitation of the hybrid simulations that are based on the adiabatic temperature assumption. Such an assumption leads to a very high $\vec{E}_{amb}$, hence high ion speeds and low ion densities. For the model runs in Section 5.6, a lower ambipolar electric field strength near the surface would result in less acceleration of the cometary ions. That is, slower bulk velocity and higher densities - perhaps closer to the measured plasma densities from MIP/LAP.

The collisionality of the electrons may therefore be key to understand why the radial $u_i = u_n$ model works so well at low outgassing. However, the impact of the electron-neutral collisions at higher outgassing cannot be determined without a fully kinetic and collisional 3D model of electrons and self-consistent fields.

CHAPTER 5 SUMMARY

- **Adapted the 3D collisional electron test-particle model** of Stephenson *et al.* (2022) to model the cometary ions in the inner coma of comet 67P.
- For a radial electric field (inside the diamagnetic cavity) the **3D collisional cross sections lead to up to** 20% **more collisions than the 1D kinetic rates** used in Chapter 4, but the same bulk velocity, hence the same ambipolar field, is required to explain the electron density measured by Rosetta.
- Increasing the fluid kinetic rates by a factor of 5 for proton transfer and 3 for momentum transfer would bring them more in line with the 3D kinetic cross sections.
- The **exothermic energy released in protonation reactions only plays a minor role in the ion dynamics near perihelion**, but may be more important when the electric fields are weaker.
- For lower outgassing ($Q = 5.4 \times 10^{26}\ \mathrm{s}^{-1}$), when no diamagnetic cavity has formed, **cometary ions are still moving predominantly radially, up to** $100\ \mathrm{km}$ **above the surface**.
- For outgassing rates as low as $Q = 5.4 \times 10^{26}\ \mathrm{s}^{-1}$, H_2O^+ **is close to photochemical equilibrium**, while H_3O^+ **and** NH_4^+ **are strongly affected by the strong electric and magnetic fields generated by the hybrid simulation**.
- Even with collisions, the **total plasma density derived by the test-particle model is low compared to the MIP/LAP data** at the same outgassing. This seems to result from the assumption of adiabatic electrons driving strong ambipolar electric fields in the hybrid simulations, and therefore overestimating the loss of ions through transport.
- Showed that **kinetic, collisional modelling of the cometary electrons are necessary to understand the ion dynamics and chemistry fully.**

CHAPTER 6

CONCLUSIONS

Rosetta sent its last data back to Earth in September 2016, making its final controlled landing onto the cometary surface and ending a decades-long endeavour (Figure 6.1). However, as I have aimed to demonstrate throughout this thesis, the wealth of data collected over the two-year escort phase is continuing to be analysed in new ways, and there is much still to be explored.

In Section 6.1, I summarise the findings of Chapters 3-5 and highlight the key themes that link them. In Section 6.2, I discuss remaining open questions and make suggestions for further research.

6.1 Summary

6.1.1 Ion composition

In Chapter 3 I evaluated the detections of protonated high proton affinity ion species, particularly NH_4^+, using the high resolution mode of the ROSINA–DFMS instrument. I showed that over the mission's timescale, the local outgassing rate was generally the strongest driver of NH_4^+ counts, since the denser coma allows more ion-neutral chemistry to take place before transport takes over (see Section 3.2). The counts of NH_4^+ correlate positively with the local

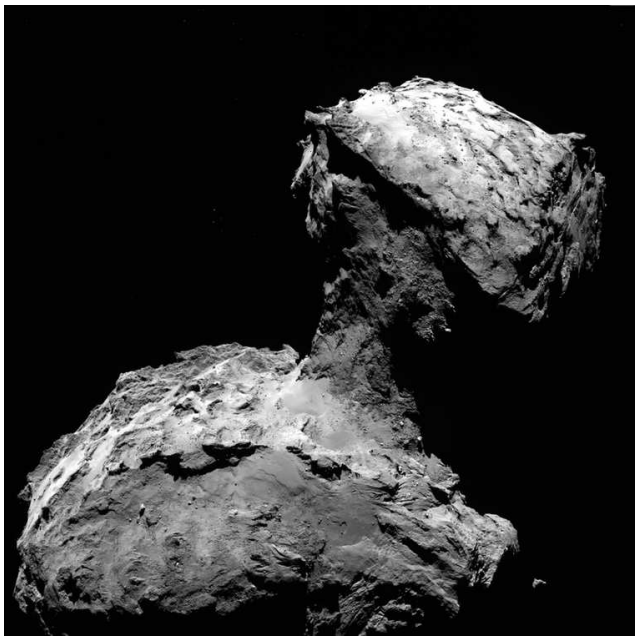

(a) Nucleus of 67P, taken on 27th September 2016 by the Wide Angle Camera

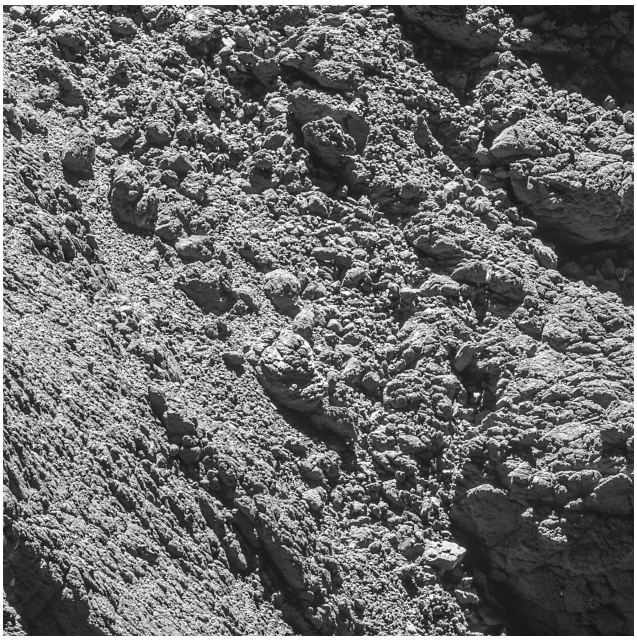

(b) Comet surface taken on 2nd September 2016 by the Narrow Angle Camera. On the right hand edge of the image, the Philae lander can be seen.

Figure 6.1: Images taken by OSIRIS on the final descent to the surface. Credit: ESA/Rosetta/OSIRIS

outgassing for $Q > 10^{27}$ s^{-1}. There are some detections at low outgassing, but these are more likely to be a result of released monomethylhydrazine during spacecraft manoeuvres (Section 3.1). Dissociation of ammonium salts imbedded in dust grains may also result in sporadic NH_4^+ detection, however it is more likely from the consistent counts and trend with outgassing that ion-neutral chemistry (specifically protonation) is the main source.

Although the trend of NH_4^+ with local outgassing was anticipated, more surprising was the observation that on a shorter timescale (over a few weeks near perihelion), the NH_4^+ counts were higher for lower values of the magnetic field (see Section 3.3). Although the study was limited by the fact that only 5 scans of mass-to-charge ratio 18 m z^{-1} took place when Rosetta was inside the diamagnetic cavity, detections were also elevated when the cavity boundary was expected to be nearby. Additionally, driving a 1D ionospheric model (assuming radial outflow and a constant ion bulk velocity) with the neutral density from COPS and the NH_3 mixing ratio was not sufficient to predict enhancements in NH_4^+ that coincided with a cluster of diamagnetic cavity crossings (see Section 3.4.2).

This link identified between the plasma dynamics and the prevalence of NH_4^+ was sup-

ported by modelling of ion acceleration in Chapter 4. By developing a 1D numerical model of the response of H_2O^+, H_3O^+, and NH_4^+ to an imposed radial ambipolar electric field, I showed that the latter is particularly sensitive to loss through transport. H_2O^+ is close to photochemical equilibrium, so varies less than other ion species both spatially and with increasing electric field. This was also seen in the 3D kinetic model of Chapter 5, which showed that even for the lower outgassing rate of $Q = 5.4 \times 10^{26}\ \mathrm{s}^{-1}$, and with no diamagnetic cavity present, H_2O^+ density decreases by less than an order of magnitude over the first 200 km from the surface in the terminator plane (see Section 5.5).

The strong detections of NH_4^+ (Chapter 3, Section 3.3) inside and near the diamagnetic cavity then imply some upper limit of the bulk ion velocity and electric field. It is likely that this upper limit is not consistent with the bulk ion velocities measured by the RPC instruments (Section 1.3.3), however it is hard to constrain it from the ROSINA-DFMS data, as the ion counts do not translate simply into number densities. The theoretical minimum for detection of an ion with DFMS is very low (around $5 \times 10^{-2}\ \mathrm{cm}^{-3}$, see Section 3.1), though in reality, spacecraft manoeuvres and the spacecraft potential may make this higher. With these uncertainties in mind, I turned to the total plasma density for comparison between the plasma transport models and the Rosetta data.

6.1.2 Ion dynamics

In Chapter 4, the Ion Acceleration Model of the ion acceleration allowed me to determine the changes in the ion density and bulk velocity when a given electric field profile was implemented. The 1D nature of the approach, however, meant the model was valid for the environment inside the diamagnetic cavity, but not outside it where non-radial flow would dominate. I showed that, under these radial conditions, increasing the ambipolar electric field increases the transport loss and therefore decreases the total ion density. However, the effect of the acceleration was mitigated by ion-neutral collisions, which act to slow some of the ions back to the outflowing neutral gas velocity.

In Section 4.3, I ran the Ion Acceleration Model for the conditions representative of two days with several diamagnetic cavity crossings (in July and November 2015, see Section 4.3),

varying the ambipolar electric field strength. This allowed me to find the electric field strength and corresponding bulk ion velocity that would provide the right balance of ion production and transport loss in the presence of collisions to reproduce the plasma densities measured by RPC–MIP. I found that the model reproduces the data best for an electric field proportional to r^{-1}, with r the cometocentric distance, and with a surface field strength of $\sim 2\ \mathrm{mV\ m^{-1}}$. This leads to bulk ion velocities at Rosetta of around $1 - 3\ \mathrm{km\ s^{-1}}$, demonstrating that the ion velocity does need to be faster than the neutrals (in this case $u_n \sim 0.7\ \mathrm{km^{-1}}$) in order to explain the plasma density near perihelion, inside the diamagnetic cavity.

Figure 6.2a illustrates the ion environment near perihelion, when the diamagnetic cavity was present. In this regime, the ion-neutral chemistry is complex, and the bulk flow of the cometary ions is radial until it reaches the diamagnetic cavity boundary, which variably lies between 70 and 400 km from the surface (Goetz *et al.*, 2016a). The cometary ions are accelerated by the ambipolar electric field inside the diamagnetic cavity, and the further they travel along this radial path, parallel to the radial field direction, the more efficient the acceleration. This increases the bulk velocity of the ions to above the neutral speed, though it is tempered by collisions (Section 4.3), and reduces the ion density with respect to the $u_i = u_n$ fluid model (Equation 5.21). A summary of the cometary ion properties in the different regimes studied is given in Table 6.1.

At low outgassing (Figure 6.2b), a simple transport-production balance (Equation 5.21) is sufficient to explain the total plasma density under the assumption that the ion bulk velocity is the same as the neutral velocity (Figure 1.13, Galand *et al.*, 2016, Heritier *et al.*, 2018). In light of the findings of Chapter 4, it is puzzling that the $u_n = u_i$ assumption works so well, where there is no diamagnetic cavity and the interplanetary magnetic field, motional electric field, and polarisation electric field are able to transport the ions (Section 2.3).

To explore this 3D environment where the radial ion flow approximation breaks down, in Chapter 5, I adapted a 3D collisional test-particle model to the ion population, to assess the behaviour of the cometary ions to 3D electric and magnetic fields from a hybrid simulation. I found that in the case where $Q = 5.4 \times 10^{26}\ \mathrm{s^{-1}}$, even when no diamagnetic cavity had formed and the solar wind was present all the way to the comet nucleus, the cometary

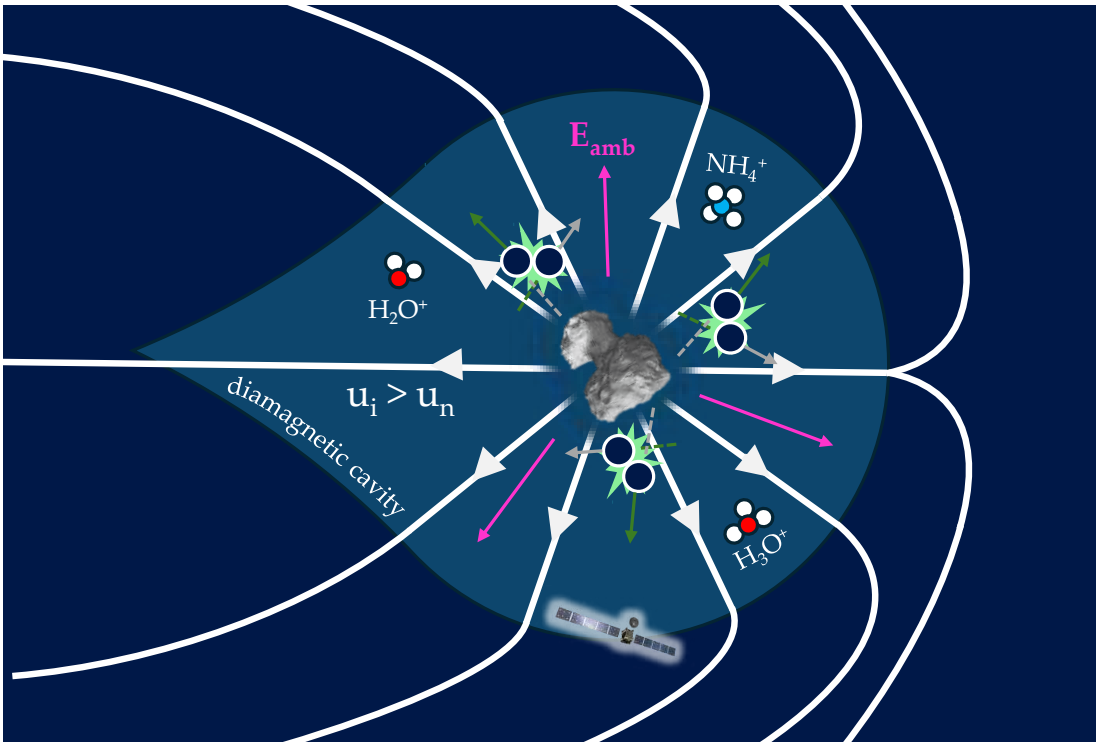

(a) Schematic summarising the behaviour of the cometary ions at high outgassing rate near perihelion. **White lines** represent the ion streamlines, flowing radially inside the diamagnetic cavity (**light blue shaded region**) and accelerated by the ambipolar electric field (**pink arrows**) to $u_i > u_n$. Acceleration is slowed by ion-neutral collisions (**green stars**).

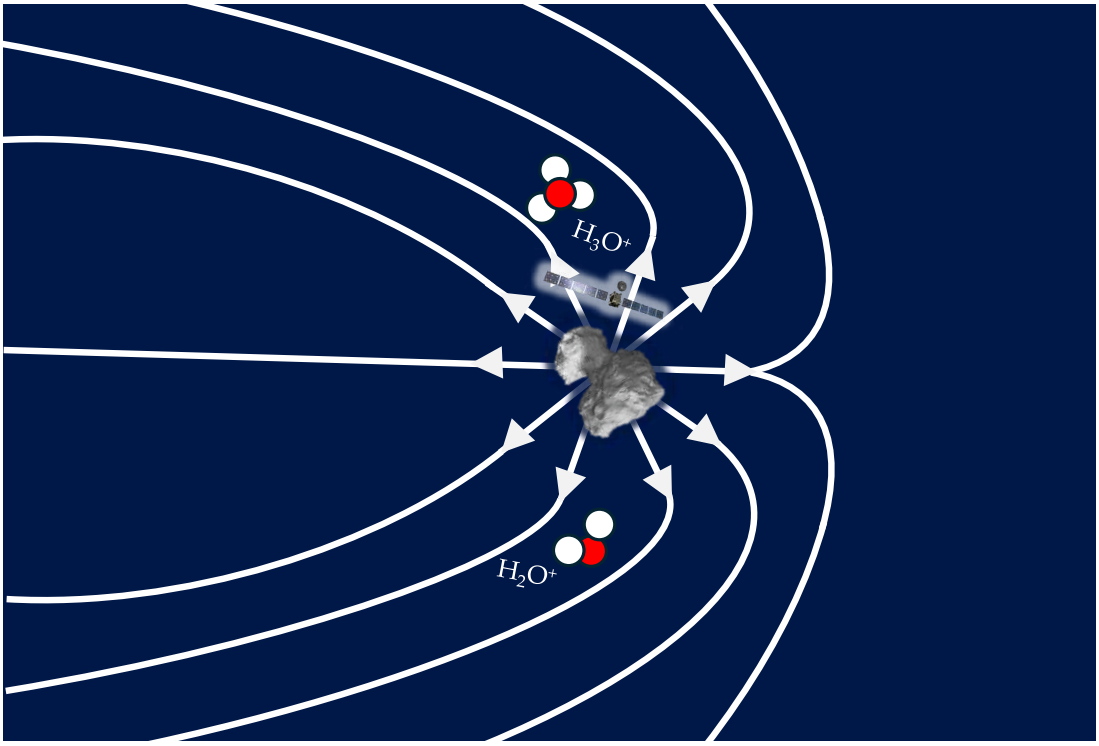

(b) Same as Figure 6.2a, but representing the case at low outgassing rate. Flow of ions (**white lines**) is initially radial (below at least 80 km where Rosetta was located)

Figure 6.2

ions continued to flow radially up to about $100\ \mathrm{km}$ from the surface. Part of the reason for this is that there is a significant number of ion-neutral collisions taking place at these low cometocentric distances, helping to couple the ions to the radially outflowing neutrals. Another reason, however, is that the ambipolar field term dominates the total electric field experienced by the ions in the inner coma. This is not necessarily realistic - the electrons in the hybrid simulation are assumed to be adiabatic and are therefore hotter with increased plasma density close to the comet. This leads to an unrealistically strong ambipolar electric field and rapidly accelerates the ions above the neutral velocity. The result is that the total simulated ion density is around 5 times lower than that which was measured by RPC–MIP and RPC–LAP (Section 5.6). Collisional test-particle modelling of the cometary electrons by Stephenson *et al.* (2022) has shown that the electrons are actually cooled through collisions with the neutrals, flattening the ambipolar potential well (Stephenson *et al.*, 2023) in the first 100 km near the nucleus (depending on the outgassing, Stephenson *et al.*, 2024). This would prevent significant acceleration of the ions close to the nucleus, and be consistent with the plasma density observations.

It is likely that the only way to fully understand the influence the electron cooling has on the cometary ions is to model the electrons kinetically. This is particularly the case since, for operational reasons, the data from Rosetta is biased towards lower cometocentric distances for lower outgassing, and vice versa. It seems to me most likely that the $u_i = u_n$ fluid model describes the plasma density so well at low outgassing *because* of this bias towards low altitudes. There is not time for the ions to undergo significant acceleration by the ambipolar electric field before reaching the spacecraft. However, the transition in Figure 1.13 where the $u_i = u_n$ model begins to become valid again post-perihelion, seems to coincide with the last diamagnetic cavity crossings that were observed by RPC–MAG. The diamagnetic cavity boundary, and its possible link to the electron exobase (see Section 1.3.2) may be key to a clearer understanding of the ion dynamics at this time.

Table 6.1: Overview of the different regimes and the applicability of the field-free, chemistry-free model (Equation 5.21) to describe the ion density and ion bulk velocity over the Rosetta escort phase. DM and HPA stand for 'diamagnetic' and 'high proton affinity' respectively.

Regime	**Low activity** (> 2 au) $Q\nu^{\mathrm{tot}} < 10^{20}\ \mathrm{s}^{-2}$	**Intermediate activity** $Q\nu^{\mathrm{tot}} \sim 10^{20}\ \mathrm{s}^{-2}$	**High activity inside DM cavity** $Q\nu^{\mathrm{tot}} > 10^{20}\ \mathrm{s}^{-2}$	**High activity outside DM cavity** $Q\nu^{\mathrm{tot}} > 10^{20}\ \mathrm{s}^{-2}$
Plasma density	Well explained by 1D fluid model up to 80km (Equation 5.21). Beyond this limited data from *Rosetta* at this activity level	Well explained by 1D fluid model up to ~ 30 km, then reduced density.	Simple fluid model not applicable (overestimate). Can be explained by 1D model including acceleration by ambipolar electric field.	Simple fluid model not applicable (overestimate) as non-radial plasma flow and complex E and B fields present.
Ion bulk velocity	Fluid model works with $u_i = u_n$ assumption (up to 80km)	Initially radial flow, $u_i = u_n$, then diverges and accelerates.	Radial flow. $\lvert u_i \rvert > \lvert u_n \rvert$ measured, and needed to explain plasma density.	$u_i > u_n$ and non radial
Ion composition	Limited ion-neutral chemistry	Some ion-neutral chemistry, small amounts of NH_4^+ produced	Effective protonation. More NH_4^+ (and other HPA) produced inside cavity boundary.	Rich ion-neutral chemistry, lots of HPA species detected.
References				
Fluid model	Galand *et al.*, 2016, Heritier *et al.*, 2018, Vigren *et al.*, 2019	Heritier *et al.*, 2018	**Chapter 4** (Lewis *et al.*, 2024), Vigren and Eriksson, 2017	-
Kinetic model	-	**Chapter 5, Section 5.5**	**Chapter 5**, **Section 5.4**	-
Ion composition measurements	**Chapter 3** (Lewis *et al.*, 2023), Beth *et al.*, 2020	**Chapter 3** (Lewis *et al.*, 2023), Beth *et al.*, 2020, Fuselier *et al.*, 2015	**Chapter 3** (Lewis *et al.*, 2023), Beth *et al.*, 2020	Heritier *et al.*, 2017a, Beth *et al.*, 2020, **Chapter 3** (Lewis *et al.*, 2023)
Ion bulk velocity measurements	-	-	Odelstad *et al.*, 2018, Bergman *et al.*, 2021b	Vigren *et al.*, 2017

6.2 Future work

It has now been ten years since Philae landed on the surface of 67P while Rosetta settled into its escort phase. The data they gathered has advanced our understanding of comets and the early solar system significantly, but, like all good science experiments, it has also raised new questions. In this section, I outline some of these questions that relate to the ion environment, the study of which would build upon the findings of this thesis.

Firstly, the impact of exothermic energy release during protonation on the energetics of the inner coma has not been assessed fully, and has usually been neglected in ionospheric models. A first step was made in Chapter 5, but this should be assessed over a larger range of outgassing rates. In addition, this process may have a feedback onto the ambipolar electric field, by adding energy to the newly produced high proton affinity ions.

Regarding the ambipolar electric field, it is unclear how it is shaped by cooled electrons near the nucleus. The hybrid assumption of an adiabatic electron profile is clearly not realistic, and a fully kinetic PiC model including electron-neutral collisions implemented would be required for full consistency. A better representation of the electric and magnetic fields focussed on the first 100 km from the nucleus is required to explain the observations of the ion population at low outgassing, as the ion transport appears to be overestimated in current models. Until collisions can be fully implemented into kinetic models at higher outgassing, the test-particle model developed in Chapter 5 could be fed simulated fields that capture the reduced electron temperature near the nucleus.

Finally, a question persists about the origin of the diamagnetic cavity at 67P and what forces are in balance at the boundary. The correlation identified with the electron exobase (Henri *et al.*, 2017) may suggest that collisional cooling of electrons plays a role. We also don't understand the origin of the instability in the boundary location.

Some of these questions could make use of the modelling tools developed in this thesis. Others require more advanced computer modelling than has been possible to date, and some may be understood through data gathered by Comet Interceptor and analysed over the coming decades.

BIBLIOGRAPHY

Accomazzo, A., K. R. Wirth, S. Lodiot, M. Küppers, and G. Schwehm (2010). "The flyby of Rosetta at asteroid Šteins – mission and science operations". en. In: *Planetary and Space Science* 58.9, pp. 1058–1065. ISSN: 00320633. DOI: 10.1016/j.pss.2010.02.004.

Aikin, A. C. (1974). "Cometary Coma Ions". In: *The Astrophysical Journal* 193, pp. 263–264.

Alfven, H. (1943). "On the existence of electromagnetic-hydro· dynamic waves." en. In: *Arkiv for Matematik, Astronomi och Fysik* 29.2.

Alfvén, H. (1957). "On the Theory of Comet Tails". en. In: *Tellus* 9.1, pp. 92–96. ISSN: 00402826, 21533490. DOI: 10.1111/j.2153-3490.1957.tb01855.x.

Alho, M., C. S. Wedlund, H. Nilsson, E. Kallio, R. Jarvinen, and T. I. Pulkkinen (2019). "Hybrid modeling of cometary plasma environments: II. Remote-sensing of a cometary bow shock". In: *Astronomy & Astrophysics* 630, A45. ISSN: 0004-6361, 1432-0746. DOI: 10.1051/0004-6361/201834863.

Altwegg, K., H. Balsiger, R. Goldstein, J. Geiss, W.-H. Ip, A. Meier, M. Neugehauer, H. Rosenbauer, and E. Shelley (1993). "The ion population between 1300km and 230000 km in the coma of comet 1P/Halley". In.

Altwegg, K., M. Combi, S. A. Fuselier, N. Hänni, J. De Keyser, A. Mahjoub, D. R. Müller, B. Pestoni, M. Rubin, and S. F. Wampfler (2022). *Abundant ammonium hydrosulfide embedded in cometary dust grains*. Tech. rep.

Altwegg, K., H. Balsiger, A. Bar-Nun, J.-J. Berthelier, A. Bieler, P. Bochsler, C. Briois, U. Calmonte, M. R. Combi, H. Cottin, J. De Keyser, F. Dhooghe, B. Fiethe, S. A. Fuselier, S. Gasc, T. I. Gombosi, K. C. Hansen, M. Haessig, A. Jäckel, E. Kopp, A. Korth, L. Le Roy, U. Mall, B. Marty, O. Mousis, T. Owen, H. Rème, M. Rubin, T. Sémon, C.-Y. Tzou, J. Hunter Waite, and P. Wurz (2016). "Prebiotic chemicals—amino acid and phosphorus—in the coma of comet 67P/Churyumov-Gerasimenko". en. In: *Science Advances* 2.5, e1600285. ISSN: 2375-2548. DOI: 10.1126/sciadv.1600285.

Altwegg, K., H. Balsiger, N. Hänni, M. Rubin, M. Schuhmann, I. Schroeder, T. Sémon, S. Wampfler, J. J. Berthelier, C. Briois, M. Combi, T. I. Gombosi, H. Cottin, J. De Keyser, F. Dhooghe, B. Fiethe, and S. A. Fuselier (2020). "Evidence of ammonium salts in comet 67P as explanation for the nitrogen depletion in cometary comae". In: *Nature Astronomy* 4.5, pp. 533–540. ISSN: 23973366. DOI: 10.1038/s41550-019-0991-9.

Anicich, V., J. Kim, and W. Huntress (1977). "Bimolecular reactions of positive ions in ammonia-water mixtures". en. In: *International Journal of Mass Spectrometry and Ion Physics* 25.4, pp. 433–438. ISSN: 00207381. DOI: 10.1016/0020-7381(77)80068-5.

Balsiger (1986). "Ion composition and dynamics at comet Halley". In.

Balsiger, H., K. Altwegg, P. Bochsler, P. Eberhardt, J. Fischer, S. Graf, A. Jäckel, E. Kopp, U. Langer, M. Mildner, J. Müller, T. Riesen, M. Rubin, S. Scherer, P. Wurz, S. Wüthrich, E. Arijs, S. Delanoye, J. De Keyser, E. Neefs, D. Nevejans, H. Rème, C. Aoustin, C. Mazelle, J. L. Médale, J. A. Sauvaud, J. J. Berthelier, J. L. Bertaux, L. Duvet, J. M. Illiano, S. A. Fuselier, A. G. Ghielmetti, T. Magoncelli, E. G. Shelley, A. Korth, K. Heerlein, H. Lauche, S. Livi, A. Loose, U. Mall, B. Wilken, F. Gliem, B. Fiethe, T. I. Gombosi, B. Block, G. R. Carignan, L. A. Fisk, J. H. Waite, D. T. Young, and H. Wollnik (2007). "Rosina - Rosetta orbiter spectrometer for ion and neutral analysis". In: *Space Science Reviews* 128.1-4, pp. 745–801. ISSN: 00386308. DOI: 10.1007/s11214-006-8335-3.

Behar, E., J. Lindkvist, H. Nilsson, M. Holmström, G. Stenberg-Wieser, R. Ramstad, and C. Götz (2016). "Mass-loading of the solar wind at 67P/Churyumov-Gerasimenko: Observations and modelling". In: *Astronomy & Astrophysics* 596, A42. ISSN: 0004-6361, 1432-0746. DOI: 10.1051/0004-6361/201628797.

Benna, M. and P. Mahaffy (2007). "Multi-fluid model of comet 1P/Halley". en. In: *Planetary and Space Science* 55.9, pp. 1031–1043. ISSN: 00320633. DOI: 10.1016/j.pss.2006.11.019.

Bergman, S., G. Stenberg Wieser, M. Wieser, F. L. Johansson, and A. Eriksson (2020). "The Influence of Varying Spacecraft Potentials and Debye Lengths on In Situ Low-Energy Ion Measurements". In: *Journal of Geophysical Research: Space Physics* 125.4. ISSN: 21699402. DOI: 10.1029/2020JA027870.

Bergman, S., G. Stenberg Wieser, M. Wieser, H. Nilsson, E. Vigren, A. Beth, K. Masunaga, and A. Eriksson (2021a). "Flow directions of low-energy ions in and around the diamagnetic cavity of comet 67P". In: *Monthly Notices of the Royal Astronomical Society* 507.4, pp. 4900–4913. ISSN: 13652966. DOI: 10.1093/mnras/stab2470.

Bergman, S., G. S. Wieser, M. Wieser, F. L. Johansson, E. Vigren, H. Nilsson, Z. Nemeth, A. Eriksson, and H. Williamson (2021b). "Ion bulk speeds and temperatures in the diamagnetic cavity of comet 67P from RPC-ICA measurements". In: *Monthly Notices of the Royal Astronomical Society* 503.2, pp. 2733–2745. ISSN: 13652966. DOI: 10.1093/mnras/stab584.

Besse, S., C. Vallat, M. Barthelemy, D. Coia, M. Costa, G. De Marchi, D. Fraga, E. Grotheer, D. Heather, T. Lim, S. Martinez, C. Arviset, I. Barbarisi, R. Docasal, A. Macfarlane, C. Rios, J. Saiz, and F. Vallejo (2018). "ESA's Planetary Science Archive: Preserve and present reliable scientific data sets". en. In: *Planetary and Space Science* 150, pp. 131–140. ISSN: 00320633. DOI: 10.1016/j.pss.2017.07.013.

Bessel, F. W. (1836). "Beobachtungen ¨uber die physische Beschaffenheit des Halley'schen Kometen und dadurch veranlasste Bemerkungen". In.

Beth, A. and M. Galand (2017). *Effects of the convective and ambipolar electric fields on weakly outgassing comets (preprint old version)*. Tech. rep., pp. 1–20.

Beth, A., K. Altwegg, H. Balsiger, J. J. Berthelier, U. Calmonte, M. R. Combi, J. De Keyser, F. Dhooghe, B. Fiethe, S. A. Fuselier, M. Galand, S. Gasc, T. I. Gombosi, K. C. Hansen, M. Hässig, K. L. Héritier, E. Kopp, L. Le Roy, K. E. Mandt, S. Peroy, M. Rubin, T. Sémon, C. Y. Tzou, and E. Vigren (2016). "First in situ detection of the cometary ammonium ion NH4+ (protonated ammonia NH3) in the coma of 67P/C-G near perihelion". In:

Monthly Notices of the Royal Astronomical Society 462, S562–S572. ISSN: 13652966. DOI: 10.1093/mnras/stw3370.

Beth, A., K. Altwegg, H. Balsiger, J. J. Berthelier, M. R. Combi, J. De Keyser, B. Fiethe, S. A. Fuselier, M. Galand, T. I. Gombosi, M. Rubin, and T. Sémon (2020). "ROSINA ion zoo at Comet 67P". In: *Astronomy and Astrophysics* 642. ISSN: 14320746. DOI: 10.1051/0004-6361/201936775.

Beth, A., M. Galand, and K. L. Heritier (2019). "Comparative study of photo-produced ionosphere in the close environment of comets". In: *Astronomy and Astrophysics* 630. ISSN: 14320746. DOI: 10.1051/0004-6361/201833517.

Bhardwaj, A. (2003). "On the solar EUV deposition in the inner comae of comets with large gas production rates". In: *Geophysical Research Letters* 30.24. ISSN: 00948276. DOI: 10.1029/2003GL018495.

Bieler, A., K. Altwegg, H. Balsiger, A. Bar-Nun, J.-J. Berthelier, P. Bochsler, C. Briois, U. Calmonte, M. Combi, J. De Keyser, E. F. Van Dishoeck, B. Fiethe, S. A. Fuselier, S. Gasc, T. I. Gombosi, K. C. Hansen, M. Hässig, A. Jäckel, E. Kopp, A. Korth, L. Le Roy, U. Mall, R. Maggiolo, B. Marty, O. Mousis, T. Owen, H. Rème, M. Rubin, T. Sémon, C.-Y. Tzou, J. H. Waite, C. Walsh, and P. Wurz (2015). "Abundant molecular oxygen in the coma of comet 67P/Churyumov–Gerasimenko". In: *Nature* 526.7575, pp. 678–681. ISSN: 0028-0836, 1476-4687. DOI: 10.1038/nature15707.

Biermann, L., B. Brosowski, and H. U. Schmidt (1967). *THE INTERACTION OF THE SOLAR WIND WITH A COMET*. Tech. rep.

Biermann, L. (1951). "Kometenschweife und solare Korpuskularstrahlung". In: *Zeitschrift fur Astrophysik* 29, p. 274. ISSN: 0372-8331.

Biver, N., D. Bockelée-Morvan, M. Hofstadter, E. Lellouch, M. Choukroun, S. Gulkis, J. Crovisier, F. P. Schloerb, L. Rezac, P. Von Allmen, S. Lee, C. Leyrat, W. H. Ip, P. Hartogh, P. Encrenaz, and G. Beaudin (2019). "Long-term monitoring of the outgassing and composition of comet 67P/Churyumov-Gerasimenko with the Rosetta/MIRO instrument". In: *Astronomy and Astrophysics* 630. ISSN: 14320746. DOI: 10.1051/0004-6361/201834960.

Boice, D. C., L. A. Soderblom, D. T. Britt, R. H. Brown, B. R. Sandel, R. V. Yelle, B. J. Buratti, Hicks, Nelson, Rayman, J. Oberst, and N. Thomas (2000). "[No title found]". In: *Earth, Moon, and Planets* 89.1/4, pp. 301–324. ISSN: 01679295. DOI: 10.1023/A:1021519124588.

Boris, J. (1970). *Relativistic plasma simulation-optimization of a hybrid code.*

Burch, J. L., R. Goldstein, T. E. Cravens, W. C. Gibson, R. N. Lundin, C. J. Pollock, J. D. Winningham, and D. T. Young (2007). "RPC-IES: The ion and electron sensor of the Rosetta plasma consortium". In: *Space Science Reviews* 128.1-4, pp. 697–712. ISSN: 00386308. DOI: 10.1007/s11214-006-9002-4.

Carnielli, G., M. Galand, F. Leblanc, L. Leclercq, R. Modolo, A. Beth, H. Huybrighs, and X. Jia (2019). "First 3D test particle model of Ganymede's ionosphere". en. In: *Icarus* 330, pp. 42–59. ISSN: 00191035. DOI: 10.1016/j.icarus.2019.04.016.

Carr, C., E. Cupido, C. G. Lee, A. Balogh, T. Beek, J. L. Burch, C. N. Dunford, A. I. Eriksson, R. Gill, K. H. Glassmeier, R. Goldstein, D. Lagoutte, R. Lundin, K. Lundin, B. Lybekk, J. L. Michau, G. Musmann, H. Nilsson, C. Pollock, I. Richter, and J. G. Trotignon (2007). "RPC: The Rosetta plasma consortium". In: *Space Science Reviews* 128.1-4, pp. 629–647. ISSN: 00386308. DOI: 10.1007/s11214-006-9136-4.

Churyumov, K. I. and S. I. Gerasimenko (1972). "Physical Observations of the Short-Period Comet 1969 IV". en. In: *Symposium - International Astronomical Union* 45, pp. 27–34. ISSN: 0074-1809. DOI: 10.1017/S0074180900006215.

Collinson, G., A. Glocer, S. Xu, D. Mitchell, R. A. Frahm, J. Grebowsky, L. Andersson, and B. Jakosky (2019). "Ionospheric Ambipolar Electric Fields of Mars and Venus: Comparisons Between Theoretical Predictions and Direct Observations of the Electric Potential Drop". In: *Geophysical Research Letters* 46.3, pp. 1168–1176. ISSN: 19448007. DOI: 10.1029/2018GL080597.

Cravens, T. (1986). "The physics of the cometary contact surface". In.

Cravens, T. E. (1987). *Theory and observations of cometary ionospheres*. Tech. rep. 12, p. 147.

— (1989). *A Magnetohydrodynamical Model of The Inner Coma of Comet Halley*. Tech. rep., pp. 25–40.

Cravens, T. E. (2004). *Physics of Solar System Plasmas*.

Deca, J., A. Divin, P. Henri, A. Eriksson, S. Markidis, V. Olshevsky, and M. Horányi (2017). "Electron and Ion Dynamics of the Solar Wind Interaction with a Weakly Outgassing Comet". In: *Physical Review Letters* 118.20. ISSN: 10797114. DOI: 10.1103/PhysRevLett.118.205101.

Deca, J., P. Henri, A. Divin, A. Eriksson, M. Galand, A. Beth, K. Ostaszewski, and M. Horányi (2019). "Building a Weakly Outgassing Comet from a Generalized Ohm's Law". en. In: *Physical Review Letters* 123.5, p. 055101. ISSN: 0031-9007, 1079-7114. DOI: 10.1103/PhysRevLett.123.055101.

Edberg, N., A. Eriksson, E. Vigren, H. Nilsson, H. Gunell, C. Götz, I. Richter, P. Henri, and J. De Keyser (2023). "Scale size of cometary bow shocks". In: *Astronomy & Astrophysics*. ISSN: 0004-6361. DOI: 10.1051/0004-6361/202346566.

Elsila, J. E., D. P. Glavin, and J. P. Dworkin (2009). "Cometary glycine detected in samples returned by Stardust". In: *Meteoritics and Planetary Science* 44, pp. 1323–1330. ISSN: 1086-9379. DOI: 10.1111/j.1945-5100.2009.tb01224.x.

Engelhardt, I. A., A. I. Eriksson, E. Vigren, X. Valliéres, M. Rubin, N. Gilet, and P. Henri (2018). "Cold electrons at comet 67P/Churyumov-Gerasimenko". In: *Astronomy and Astrophysics* 616. ISSN: 14320746. DOI: 10.1051/0004-6361/201833251.

Eriksson, A. I., R. Boström, R. Gill, L. Åhlén, S. E. Jansson, J. E. Wahlund, M. André, A. Mälkki, J. A. Holtet, B. Lybekk, A. Pedersen, and L. G. Blomberg (2007). "RPC-LAP: The Rosetta langmuir probe instrument". In: *Space Science Reviews* 128.1-4, pp. 729–744. ISSN: 00386308. DOI: 10.1007/s11214-006-9003-3.

Eriksson, A. I., I. A. Engelhardt, M. André, R. Boström, N. J. Edberg, F. L. Johansson, E. Odelstad, E. Vigren, J. E. Wahlund, P. Henri, J. P. Lebreton, W. J. Miloch, J. J. Paulsson, C. Simon Wedlund, L. Yang, T. Karlsson, R. Jarvinen, T. Broiles, K. Mandt, C. M. Carr, M. Galand, H. Nilsson, and C. Norberg (2017). "Cold and warm electrons at comet 67P/Churyumov-Gerasimenko". In: *Astronomy and Astrophysics* 605. ISSN: 14320746. DOI: 10.1051/0004-6361/201630159.

Fahleson, U. (1967). "Theory of electric field measurements conducted in the magnetosphere with electric probes". en. In: *Space Science Reviews* 7.2-3, pp. 238–262. ISSN: 0038-6308, 1572-9672. DOI: 10.1007/BF00215600.

Fahr, H. and K. G. Mueller (1967). "Ionenbewegung unter dem Einfluss von Umladungsstoessen". de. In: *Zeitschrift fur Physik* 200.4, pp. 343–365. ISSN: 1434-6001, 1434-601X. DOI: 10.1007/BF01326177.

Fatemi, S., A. R. Poppe, G. T. Delory, and W. M. Farrell (2017). "AMITIS: A 3D GPU-Based Hybrid-PIC Model for Space and Plasma Physics". In: *Journal of Physics: Conference Series* 837, p. 012017. ISSN: 1742-6588, 1742-6596. DOI: 10.1088/1742-6596/837/1/012017.

Fleshman, B. L., P. A. Delamere, F. Bagenal, and T. Cassidy (2012). "The roles of charge exchange and dissociation in spreading Saturn's neutral clouds". In: DOI: 10.1029/2011JE003996.

Fougere, N., K. Altwegg, J. J. Berthelier, A. Bieler, D. Bockelée-Morvan, U. Calmonte, F. Capaccioni, M. R. Combi, J. De Keyser, V. Debout, S. Erard, B. Fiethe, G. Filacchione, U. Fink, S. A. Fuselier, T. I. Gombosi, K. C. Hansen, M. Hässig, Z. Huang, L. Le Roy, C. Leyrat, A. Migliorini, G. Piccioni, G. Rinaldi, M. Rubin, Y. Shou, V. Tenishev, G. Toth, and C. Y. Tzou (2016). "Direct Simulation Monte Carlo modelling of the major species in the coma of comet 67P/Churyumov-Gerasimenko". In: *Monthly Notices of the Royal Astronomical Society* 462, S156–S169. ISSN: 13652966. DOI: 10.1093/mnras/stw2388.

Fuselier, S. A., K. Altwegg, H. Balsiger, J. J. Berthelier, A. Bieler, C. Briois, T. W. Broiles, J. L. Burch, U. Calmonte, G. Cessateur, M. Combi, J. De Keyser, B. Fiethe, M. Galand, S. Gasc, T. I. Gombosi, H. Gunell, K. C. Hansen, M. Hassig, A. Jackel, A. Korth, L. Le Roy, U. Mall, K. E. Mandt, S. M. Petrinec, S. Raghuram, H. Rème, M. Rinaldi, M. Rubin, T. Semon, K. J. Trattner, C. Y. Tzou, E. Vigren, J. H. Waite, and P. Wurz (2015). "ROSINA/DFMS and IES observations of 67P: Ion-neutral chemistry in the coma of a weakly outgassing comet". In: *Astronomy and Astrophysics* 583. ISSN: 14320746. DOI: 10.1051/0004-6361/201526210.

Galand, M., P. D. Feldman, D. Bockelée-Morvan, N. Biver, Y. C. Cheng, G. Rinaldi, M. Rubin, K. Altwegg, J. Deca, A. Beth, P. Stephenson, K. L. Heritier, P. Henri, J. W. Parker, C. Carr, A. I. Eriksson, and J. Burch (2020). "Far-ultraviolet aurora identified at comet 67P/Churyumov-

Gerasimenko". In: *Nature Astronomy* 4.11, pp. 1084–1091. ISSN: 23973366. DOI: 10.1038/s41550-020-1171-7.

Galand, M., K. L. Héritier, E. Odelstad, P. Henri, T. W. Broiles, A. J. Allen, K. Altwegg, A. Beth, J. L. Burch, C. M. Carr, E. Cupido, A. I. Eriksson, K. H. Glassmeier, F. L. Johansson, J. P. Lebreton, K. E. Mandt, H. Nilsson, I. Richter, M. Rubin, L. B. Sagnières, S. J. Schwartz, T. Sémon, C. Y. Tzou, X. Vallières, E. Vigren, and P. Wurz (2016). "Ionospheric plasma of comet 67P probed by Rosetta at 3 au from the Sun". In: *Monthly Notices of the Royal Astronomical Society* 462, S331–S351. ISSN: 13652966. DOI: 10.1093/mnras/stw2891.

Gan, L. and T. E. Cravens (1990). "Electron energetics in the inner coma of comet Halley". In: *Journal of Geophysical Research* 95.A5, p. 6285. ISSN: 0148-0227. DOI: 10.1029/ja095ia05p06285.

Gasc, S., K. Altwegg, H. Balsiger, J. J. Berthelier, A. Bieler, U. Calmonte, B. Fiethe, S. Fuselier, A. Galli, T. Gombosi, M. Hoang, J. De Keyser, A. Korth, L. Le Roy, U. Mall, H. Rème, M. Rubin, T. Sémon, C. Y. Tzou, J. H. Waite, and P. Wurz (2017a). "Change of outgassing pattern of 67P/Churyumov-Gerasimenko during the March 2016 equinox as seen by ROSINA". In: *Monthly Notices of the Royal Astronomical Society* 469, S108–S117. ISSN: 13652966. DOI: 10.1093/mnras/stx1412.

Gasc, S., K. Altwegg, B. Fiethe, A. Jäckel, A. Korth, L. Le Roy, U. Mall, H. Rème, M. Rubin, J. Hunter Waite, and P. Wurz (2017b). "Sensitivity and fragmentation calibration of the time-of-flight mass spectrometer RTOF on board ESA's Rosetta mission". In: *Planetary and Space Science* 135, pp. 64–73. ISSN: 00320633. DOI: 10.1016/j.pss.2016.11.011.

Gilet, N., P. Henri, G. Wattieaux, N. Traoré, A. I. Eriksson, X. Vallières, J. Moré, O. Randriamboarison, E. Odelstad, F. L. Johansson, and M. Rubin (2020). "Observations of a mix of cold and warm electrons by RPC-MIP at 67P/Churyumov-Gerasimenko". In: *Astronomy and Astrophysics* 640. ISSN: 14320746. DOI: 10.1051/0004-6361/201937056.

Glassmeier, K. H., I. Richter, A. Diedrich, G. Musmann, U. Auster, U. Motschmann, A. Balogh, C. Carr, E. Cupido, A. Coates, M. Rother, K. Schwingenschuh, K. Szegö, and B. Tsurutani (2007a). "RPC-MAG the fluxgate magnetometer in the ROSETTA plasma consortium". In:

Space Science Reviews 128.1-4, pp. 649–670. ISSN: 00386308. DOI: 10.1007/s11214-006-9114-x.

Glassmeier, K.-H., H. Boehnhardt, D. Koschny, E. Kührt, and I. Richter (2007b). "The Rosetta Mission: Flying Towards the Origin of the Solar System". en. In: *Space Science Reviews* 128.1-4, pp. 1–21. ISSN: 0038-6308, 1572-9672. DOI: 10.1007/s11214-006-9140-8.

Goetz, C., C. Koenders, K. C. Hansen, J. Burch, C. Carr, A. Eriksson, D. Frühauff, C. Güttler, P. Henri, H. Nilsson, I. Richter, M. Rubin, H. Sierks, B. Tsurutani, M. Volwerk, and K. H. Glassmeier (2016a). "Structure and evolution of the diamagnetic cavity at comet 67P/Churyumov–Gerasimenko". In: *Monthly Notices of the Royal Astronomical Society* 462.Suppl 1, S459–S467. ISSN: 0035-8711. DOI: 10.1093/mnras/stw3148.

Goetz, C., C. Koenders, I. Richter, K. Altwegg, J. Burch, C. Carr, E. Cupido, A. Eriksson, C. Güttler, P. Henri, P. Mokashi, Z. Nemeth, H. Nilsson, M. Rubin, H. Sierks, B. Tsurutani, C. Vallat, M. Volwerk, and K. H. Glassmeier (2016b). "First detection of a diamagnetic cavity at comet 67P/Churyumov-Gerasimenko". In: *Astronomy and Astrophysics* 588. ISSN: 14320746. DOI: 10.1051/0004-6361/201527728.

Goldstein, B. E., K. Altwegg, H. Balsiger, S. A. Fuselier, W.-H. Ip, A. Meier, G. Neugebauer, H. Rosenbauer, Schwenn, and R (1989). *Observations of a Shock and a Recombination Layer at the Contact Surface of Comet Halley*. Tech. rep. A12, pp. 251–268. DOI: 10.1029/JA094iA12p17251.

Gombosi, T. I., D. L. De Zeeuw, R. M. Hiiberli, and K. G. Powell (1996). *Three-dimensional multiscale MHD model of cometary plasma environments*. Tech. rep. A7, pp. 233–248.

Gulkis, S., M. Allen, P. Von Allmen, G. Beaudin, N. Biver, D. Bockelée-Morvan, M. Choukroun, J. Crovisier, B. J. R. Davidsson, P. Encrenaz, T. Encrenaz, M. Frerking, P. Hartogh, M. Hofstadter, W.-H. Ip, M. Janssen, C. Jarchow, S. Keihm, S. Lee, E. Lellouch, C. Leyrat, L. Rezac, F. P. Schloerb, and T. Spilker (2015). "Subsurface properties and early activity of comet 67P/Churyumov-Gerasimenko". en. In: *Science* 347.6220, aaa0709. ISSN: 0036-8075, 1095-9203. DOI: 10.1126/science.aaa0709.

Gunell, H., C. Goetz, C. S. Wedlund, J. Lindkvist, M. Hamrin, H. Nilsson, K. Llera, A. Eriksson, and M. Holmström (2018). "The infant bow shock: A new frontier at a weak activity

comet". In: *Astronomy and Astrophysics* 619. ISSN: 14320746. DOI: 10.1051/0004-6361/201834225.

Hänni, N., S. Gasc, A. Etter, M. Schuhmann, I. Schroeder, S. F. Wampfler, S. Schürch, M. Rubin, and K. Altwegg (2019). "Ammonium salts as a source of small molecules observed with high-resolution electron-impact ionization mass spectrometry". In: *Journal of Physical Chemistry A* 123.27, pp. 5805–5814. ISSN: 15205215. DOI: 10.1021/acs.jpca.9b03534.

Hansen, K. C., K. Altwegg, J. J. Berthelier, A. Bieler, N. Biver, D. Bockelée-Morvan, U. Calmonte, F. Capaccioni, M. R. Combi, J. De Keyser, B. Fiethe, N. Fougere, S. A. Fuselier, S. Gasc, T. I. Gombosi, Z. Huang, L. Le Roy, S. Lee, H. Nilsson, M. Rubin, Y. Shou, C. Snodgrass, V. Tenishev, G. Toth, C. Y. Tzou, and C. Simon Wedlund (2016). "Evolution of water production of 67P/Churyumov-Gerasimenko: An empirical model and a multi-instrument study". In: *Monthly Notices of the Royal Astronomical Society* 462, S491–S506. ISSN: 13652966. DOI: 10.1093/mnras/stw2413.

Haser, L. (1957). "Distribution d'intensité dans la tête d'une comète". In: *Bulletin de la Classe des Sciences de l'Académie Royale de Belgique* 43, pp. 740–750.

Hässig, M., K. Altwegg, H. Balsiger, A. Bar-Nun, J. J. Berthelier, A. Bieler, P. Bochsler, C. Briois, U. Calmonte, M. Combi, J. De Keyser, P. Eberhardt, B. Fiethe, S. A. Fuselier, M. Galand, S. Gasc, T. I. Gombosi, K. C. Hansen, A. Jäckel, H. U. Keller, E. Kopp, A. Korth, E. Kührt, L. Le Roy, U. Mall, B. Marty, O. Mousis, E. Neefs, T. Owen, H. Rème, M. Rubin, T. Sémon, C. Tornow, C.-Y. Tzou, J. H. Waite, and P. Wurz (2015). "Time variability and heterogeneity in the coma of 67P/Churyumov-Gerasimenko". en. In: *Science* 347.6220, aaa0276. ISSN: 0036-8075, 1095-9203. DOI: 10.1126/science.aaa0276.

Henri, P., X. Vallières, R. Hajra, C. Goetz, I. Richter, K. H. Glassmeier, M. Galand, M. Rubin, A. I. Eriksson, Z. Nemeth, E. Vigren, A. Beth, J. L. Burch, C. Carr, H. Nilsson, B. Tsurutani, and G. Wattieaux (2017). "Diamagnetic region(s): Structure of the unmagnetized plasma around Comet 67P/CG". In: *Monthly Notices of the Royal Astronomical Society* 469, S372–S379. ISSN: 13652966. DOI: 10.1093/mnras/stx1540.

Heritier, K. (2018). "Cometary ionosphere analysis from Rosetta multi-instrument dataset". PhD Thesis. London: Imperial College London.

Heritier, K. L., K. Altwegg, H. Balsiger, J. J. Berthelier, A. Beth, A. Bieler, N. Biver, U. Calmonte, M. R. Combi, J. De Keyser, A. I. Eriksson, B. Fiethe, N. Fougere, S. A. Fuselier, M. Galand, S. Gasc, T. I. Gombosi, K. C. Hansen, M. Hassig, E. Kopp, E. Odelstad, M. Rubin, C. Y. Tzou, E. Vigren, and V. Vuitton (2017a). "Ion composition at comet 67P near perihelion: Rosetta observations and model-based interpretation". In: *Monthly Notices of the Royal Astronomical Society* 469, S427–S442. ISSN: 13652966. DOI: 10.1093/mnras/stx1912.

Heritier, K. L., P. Henri, F. L. Johansson, A. Beth, A. I. Eriksson, X. Vallières, K. Altwegg, J. L. Burch, C. Carr, E. Ducrot, R. Hajra, and M. Rubin (2018). "Plasma source and loss at comet 67P during the Rosetta mission". In: *Astronomy and Astrophysics* 618. ISSN: 14320746. DOI: 10.1051/0004-6361/201832881.

Heritier, K. L., P. Henri, X. Vallières, M. Galand, E. Odelstad, A. I. Eriksson, F. L. Johansson, K. Altwegg, E. Behar, A. Beth, T. W. Broiles, J. L. Burch, C. M. Carr, E. Cupido, H. Nilsson, M. Rubin, and E. Vigren (2017b). "Vertical structure of the near-surface expanding ionosphere of comet 67P probed by Rosetta". In: *Monthly Notices of the Royal Astronomical Society* 469, S118–S129. ISSN: 13652966. DOI: 10.1093/mnras/stx1459.

Ho, P. Y. (2000). *Li, qi, and shu: an introduction to science and civilization in China*. eng. Mineola, NY: Dover Publications. ISBN: 978-0-486-41445-4.

Hoang, M., P. Garnier, H. Gourlaouen, J. Lasue, H. Rème, K. Altwegg, H. Balsiger, A. Beth, U. Calmonte, B. Fiethe, A. Galli, S. Gasc, A. Jäckel, A. Korth, L. Le Roy, U. Mall, M. Rubin, T. Sémon, C.-Y. Tzou, J. H. Waite, and P. Wurz (2019). "Two years with comet 67P/Churyumov-Gerasimenko: H_2 O, CO_2 , and CO as seen by the ROSINA/RTOF instrument of Rosetta". In: *Astronomy & Astrophysics* 630, A33. ISSN: 0004-6361, 1432-0746. DOI: 10.1051/0004-6361/201834226.

Houpis, H. L. F. and D. A. Mendis (1980). *Physicochemical and Dynamical Processes in Cometary Ionospheres. I. The Basic Flow Profile*. Tech. rep., pp. 1107–1118.

Huebner, W. F., J. J. Keady, and S. P. Lyon (1992). "Solar photo rates for planetary atmospheres and atmospheric pollutants". en. In: *Astrophysics and Space Science* 195.1, pp. 1–294. ISSN: 0004-640X, 1572-946X. DOI: 10.1007/BF00644558.

Huebner, W. F. and W. J. Markiewicz (2000). "The Temperature and Bulk Flow Speed of a Gas Effusing or Evaporating from a Surface into a Void after Reestablishment of Collisional Equilibrium". In: *Icarus* 148.2, pp. 594–596. ISSN: 00191035. DOI: 10.1006/icar.2000.6522.

Hunter, E. P. L. and S. G. Lias (1998). "Evaluated Gas Phase Basicities and Proton Affinities of Molecules: An Update". en. In: *Journal of Physical and Chemical Reference Data* 27.3, pp. 413–656. ISSN: 0047-2689, 1529-7845. DOI: 10.1063/1.556018.

Huntress, W. T. and R. F. Pinizzotto (1973). "Product distributions and rate constants for ion-molecule reactions in water, hydrogen sulfide, ammonia, and methane". en. In: *The Journal of Chemical Physics* 59.9, pp. 4742–4756. ISSN: 0021-9606, 1089-7690. DOI: 10.1063/1.1680687.

Itikawa, Y. and N. Mason (2005). "Cross Sections for Electron Collisions with Water Molecules". en. In: *Journal of Physical and Chemical Reference Data* 34.1, pp. 1–22. ISSN: 0047-2689, 1529-7845. DOI: 10.1063/1.1799251.

Ivezić, Ž. *et al.* (2019). "LSST: From Science Drivers to Reference Design and Anticipated Data Products". In: *The Astrophysical Journal* 873, p. 111. ISSN: 0004-637X. DOI: 10.3847/1538-4357/ab042c.

Jarvinen, R., E. Kallio, and S. Dyadechkin (2013). "Hemispheric asymmetries of the Venus plasma environment". en. In: *Journal of Geophysical Research: Space Physics* 118.7, pp. 4551–4563. ISSN: 2169-9380, 2169-9402. DOI: 10.1002/jgra.50387.

Johansson, F. L., A. I. Eriksson, N. Gilet, P. Henri, G. Wattieaux, M. G. G. T. Taylor, C. Imhof, and F. Cipriani (2020). "A charging model for the Rosetta spacecraft". In: *Astronomy & Astrophysics* 642, A43. ISSN: 0004-6361, 1432-0746. DOI: 10.1051/0004-6361/202038592.

Johansson, F. L., A. I. Eriksson, E. Vigren, L. Bucciantini, P. Henri, H. Nilsson, S. Bergman, N. J. T. Edberg, G. Stenberg Wieser, and E. Odelstad (2021). "Plasma densities, flow, and solar EUV flux at comet 67P: A cross-calibration approach". In: *Astronomy & Astrophysics* 653, A128. ISSN: 0004-6361, 1432-0746. DOI: 10.1051/0004-6361/202039959.

Johansson, F. L., E. Odelstad, J. J. Paulsson, S. S. Harang, A. I. Eriksson, T. Mannel, E. Vigren, N. J. Edberg, W. J. Miloch, C. Simon Wedlund, E. Thiemann, F. Eparvier, and L. Andersson

(2017). "Rosetta photoelectron emission and solar ultraviolet flux at comet 67P". In: *Monthly Notices of the Royal Astronomical Society* 469, S626–S635. ISSN: 13652966. DOI: 10.1093/mnras/stx2369.

Jones, G. H. *et al.* (2024). "The Comet Interceptor Mission". In: *Space Science Reviews* 220.1. ISSN: 15729672. DOI: 10.1007/s11214-023-01035-0.

Kallio, E. and P. Janhunen (2003). *Modelling the solar wind interaction with Mercury by a quasi-neutral hybrid model*. Tech. rep., pp. 2133–2145.

Kallio, E. and R. Jarvinen (2012). "Kinetic effects on ion escape at Mars and Venus: Hybrid modeling studies". In: *Earth, Planets and Space*. Vol. 64. Springer Berlin, pp. 157–163. DOI: 10.5047/eps.2011.08.014.

Kallio, E., R. Jarvinen, S. Massetti, T. Alberti, A. Milillo, S. Orsini, E. De Angelis, G. Laky, J. Slavin, J. M. Raines, and T. I. Pulkkinen (2022). "Ultra-Low Frequency Waves in the Hermean Magnetosphere: On the Role of the Morphology of the Magnetic Field and the Foreshock". en. In: *Geophysical Research Letters* 49.24, e2022GL101850. ISSN: 0094-8276, 1944-8007. DOI: 10.1029/2022GL101850.

Kallio, E. and P. Janhunen (2002). "Ion escape from Mars in a quasi-neutral hybrid model". en. In: *Journal of Geophysical Research: Space Physics* 107.A3. ISSN: 0148-0227. DOI: 10.1029/2001JA000090.

Keller, H. U., C. Arpigny, C. Barbieri, R. M. Bonnet, S. Cazes, M. Coradini, C. B. Cosmovici, W. A. Delamere, W. F. Huebner, D. W. Hughes, C. Jamar, D. Malaise, H. J. Reitsema, H. U. Schmidt, W. K. H. Schmidt, P. Seige, F. L. Whipple, and K. Wilhelm (1986). "First Halley Multicolour Camera imaging results from Giotto". In: *Nature* 321, pp. 320–326. ISSN: 0028-0836. DOI: 10.1038/321320a0.

Keller, H. U., C. Barbieri, P. Lamy, H. Rickman, R. Rodrigo, K.-P. Wenzel, H. Sierks, M. F. A'Hearn, F. Angrilli, M. Angulo, M. E. Bailey, P. Barthol, M. A. Barucci, J.-L. Bertaux, G. Bianchini, J.-L. Boit, V. Brown, J. A. Burns, I. Büttner, J. M. Castro, G. Cremonese, W. Curdt, V. D. Deppo, S. Debei, M. D. Cecco, K. Dohlen, S. Fornasier, M. Fulle, D. Germerott, F. Gliem, G. P. Guizzo, S. F. Hviid, W.-H. Ip, L. Jorda, D. Koschny, J. R. Kramm, E. Kührt, M. Küppers, L. M. Lara, A. Llebaria, A. López, A. López-Jimenez, J. López-Moreno, R.

Meller, H. Michalik, M. D. Michelena, R. Müller, G. Naletto, A. Origné, G. Parzianello, M. Pertile, C. Quintana, R. Ragazzoni, P. Ramous, K.-U. Reiche, M. Reina, J. Rodríguez, G. Rousset, L. Sabau, A. Sanz, J.-P. Sivan, K. Stöckner, J. Tabero, U. Telljohann, N. Thomas, V. Timon, G. Tomasch, T. Wittrock, and M. Zaccariotto (2007). "OSIRIS – The Scientific Camera System Onboard Rosetta". en. In: *Space Science Reviews* 128.1-4, pp. 433–506. ISSN: 0038-6308, 1572-9672. DOI: 10.1007/s11214-006-9128-4.

Keller, H. U., S. Mottola, B. Davidsson, S. E. Schröder, Y. Skorov, E. Kührt, O. Groussin, M. Pajola, S. F. Hviid, F. Preusker, F. Scholten, M. F. A'Hearn, H. Sierks, C. Barbieri, P. Lamy, R. Rodrigo, D. Koschny, H. Rickman, M. A. Barucci, J.-L. Bertaux, I. Bertini, G. Cremonese, V. Da Deppo, S. Debei, M. De Cecco, S. Fornasier, M. Fulle, P. J. Gutiérrez, W.-H. Ip, L. Jorda, J. Knollenberg, J. R. Kramm, M. Küppers, L. M. Lara, M. Lazzarin, J. J. Lopez Moreno, F. Marzari, H. Michalik, G. Naletto, L. Sabau, N. Thomas, J.-B. Vincent, K.-P. Wenzel, J. Agarwal, C. Güttler, N. Oklay, and C. Tubiana (2015). "Insolation, erosion, and morphology of comet 67P/Churyumov-Gerasimenko". en. In: *Astronomy & Astrophysics* 583, A34. ISSN: 0004-6361, 1432-0746. DOI: 10.1051/0004-6361/201525964.

Koenders, C., K. H. Glassmeier, I. Richter, U. Motschmann, and M. Rubin (2013). "Revisiting cometary bow shock positions". In: *Planetary and Space Science* 87, pp. 85–95. ISSN: 00320633. DOI: 10.1016/j.pss.2013.08.009.

Koenders, C., K. H. Glassmeier, I. Richter, H. Ranocha, and U. Motschmann (2015). "Dynamical features and spatial structures of the plasma interaction region of 67P/Churyumov-Gerasimenko and the solar wind". In: *Planetary and Space Science* 105, pp. 101–116. ISSN: 00320633. DOI: 10.1016/j.pss.2014.11.014.

Korosmezey, A., T. E. Cravens, T. I. Gombosi, A. F. Nagy, D. A. Mendis, and K. Szeg6 (1987). *A New Model of Cometary Ionospheres*. Tech. rep. A7.

Läuter, M., T. Kramer, M. Rubin, and K. Altwegg (2019). "Surface localization of gas sources on comet 67P/Churyumov-Gerasimenko based on DFMS/COPS data". In: *Monthly Notices of the Royal Astronomical Society* 483.1, pp. 852–861. ISSN: 13652966. DOI: 10.1093/mnras/sty3103.

Le Roy, L., K. Altwegg, H. Balsiger, J.-J. Berthelier, A. Bieler, C. Briois, U. Calmonte, M. R. Combi, J. De Keyser, F. Dhooghe, B. Fiethe, S. A. Fuselier, S. Gasc, T. I. Gombosi, M. Hässig, A. Jäckel, M. Rubin, and C.-Y. Tzou (2015). *Inventory of the volatiles on comet 67P/Churyumov-Gerasimenko from Rosetta/ROSINA*. Tech. rep.

Lewis, Z. M., A. Beth, K. Altwegg, M. Galand, C. Goetz, K. Heritier, L. O'Rourke, M. Rubin, and P. Stephenson (2023). "Origin and trends in NH4+observed in the coma of 67P". In: *Monthly Notices of the Royal Astronomical Society* 523.4, pp. 6208–6219. ISSN: 13652966. DOI: 10.1093/mnras/stad1787.

Lewis, Z. M., A. Beth, M. Galand, P. Henri, M. Rubin, and P. Stephenson (2024). "Constraining ion transport in the diamagnetic cavity of comet 67P". In: *Monthly Notices of the Royal Astronomical Society* 530.1, pp. 66–81. ISSN: 13652966. DOI: 10.1093/mnras/stae856.

Lishawa, C. R., R. A. Dressler, J. A. Gardner, R. H. Salter, and E. Murad (1990). "Cross sections and product kinetic energy analysis of H2O+–H2O collisions at suprathermal energies". en. In: *The Journal of Chemical Physics* 93.5, pp. 3196–3206. ISSN: 0021-9606, 1089-7690. DOI: 10.1063/1.458852.

Madanian, H., T. E. Cravens, J. Burch, R. Goldstein, M. Rubin, Z. Nemeth, C. Goetz, C. Koenders, and K. Altwegg (2016a). "PLASMA ENVIRONMENT AROUND COMET 67P/CHURYUMOV-GERASIMENKO AT PERIHELION: MODEL COMPARISON WITH ROSETTA DATA". In: *The Astronomical Journal* 153. DOI: 10.3847/1538-3881/153/1/30.

Madanian, H., T. E. Cravens, A. Rahmati, R. Goldstein, J. Burch, A. I. Eriksson, N. J. T. Edberg, P. Henri, K. Mandt, G. Clark, M. Rubin, T. Broiles, and N. L. Reedy (2016b). "Suprathermal electrons near the nucleus of comet 67P/Churyumov-Gerasimenko at 3 AU: Model comparisons with Rosetta data". en. In: *Journal of Geophysical Research: Space Physics* 121.6, pp. 5815–5836. ISSN: 2169-9380, 2169-9402. DOI: 10.1002/2016JA022610.

Marshall, D. W., P. Hartogh, L. Rezac, P. Von Allmen, N. Biver, D. Bockelée-Morvan, J. Crovisier, P. Encrenaz, S. Gulkis, M. Hofstadter, W.-H. Ip, C. Jarchow, S. Lee, and E. Lellouch (2017). "Spatially resolved evolution of the local H_2 O production rates of comet 67P/Churyumov-Gerasimenko from the MIRO instrument on Rosetta". In: *As-*

tronomy & Astrophysics 603, A87. ISSN: 0004-6361, 1432-0746. DOI: 10.1051/0004-6361/201730502.

Massironi, M., E. Simioni, F. Marzari, G. Cremonese, L. Giacomini, M. Pajola, L. Jorda, G. Naletto, S. Lowry, M. R. El-Maarry, F. Preusker, F. Scholten, H. Sierks, C. Barbieri, P. Lamy, R. Rodrigo, D. Koschny, H. Rickman, H. U. Keller, M. F. A'Hearn, J. Agarwal, A.-T. Auger, M. A. Barucci, J.-L. Bertaux, I. Bertini, S. Besse, D. Bodewits, C. Capanna, V. Da Deppo, B. Davidsson, S. Debei, M. De Cecco, F. Ferri, S. Fornasier, M. Fulle, R. Gaskell, O. Groussin, P. J. Gutiérrez, C. Güttler, S. F. Hviid, W.-H. Ip, J. Knollenberg, G. Kovacs, R. Kramm, E. Kührt, M. Küppers, F. La Forgia, L. M. Lara, M. Lazzarin, Z.-Y. Lin, J. J. Lopez Moreno, S. Magrin, H. Michalik, S. Mottola, N. Oklay, A. Pommerol, N. Thomas, C. Tubiana, and J.-B. Vincent (2015). "Two independent and primitive envelopes of the bilobate nucleus of comet 67P". en. In: *Nature* 526.7573, pp. 402–405. ISSN: 0028-0836, 1476-4687. DOI: 10.1038/nature15511.

Mendis, D. A. and W. .-. Ip (1977). "The Ionospheres and Plasma Tails of Comets". In: *Space Science Reviews* 20, pp. 145–190. ISSN: 0038-6308. DOI: 10.1007/BF02186863.

Millar, T. J., C. Walsh, M. Van De Sande, and A. J. Markwick (2024). "The UMIST Database for Astrochemistry 2022". In: *Astronomy & Astrophysics* 682, A109. ISSN: 0004-6361, 1432-0746. DOI: 10.1051/0004-6361/202346908.

Moeslinger, A., H. Gunell, H. Nilsson, S. Fatemi, and G. Stenberg Wieser (2024). "Explaining the Evolution of Ion Velocity Distributions at a Low Activity Comet". en. In: *Journal of Geophysical Research: Space Physics* 129.9, e2024JA032757. ISSN: 2169-9380, 2169-9402. DOI: 10.1029/2024JA032757.

Moeslinger, A. and H. Gunell (2024). *Particle Tracing Code*. DOI: 10.5281/ZENODO.10973547.

Moreels, G., M. Gogoshev, V. A. Krasnopolsky, J. Clairemidi, M. Vincent, J. P. Parisot, J. L. Bertaux, J. E. Blamont, M. C. Festou, T. Gogosheva, S. Sargoichev, K. Palasov, V. I. Moroz, A. A. Krysko, and V. Vanyšek (1986). "Near-ultraviolet and visible spectrophotometry of comet Halley from Vega 2". en. In: *Nature* 321.S6067, pp. 271–273. ISSN: 0028-0836, 1476-4687. DOI: 10.1038/321271a0.

Murad, E. and P. Bochsler (1987). "Speculations about the origin of H3O+ seen in cometary mass spectra". en. In: *Nature* 326.6111, pp. 366–367. ISSN: 0028-0836, 1476-4687. DOI: 10.1038/326366a0.

Neubauer, F. M. (1988). "The ionopause transition and boundary layers at comet Halley from Giotto magnetic field observations". In: *Journal of Geophysical Research* 93.A7, p. 7272. ISSN: 0148-0227. DOI: 10.1029/ja093ia07p07272.

Neubauer, F. M., K. H. Glassmeir, M. Pohl, J. Raeder, M. H. Acuna, L. F. Burlaga, N. F. Ness, G. Musmann, F. Mariani, M. K. Wallis, E. Ungstrup, and H. U. Schmidt (1986). *First results from the Giotto magnetometer experiment at comet Halley*. Tech. rep., pp. 356–361.

Nilsson, H., H. Gunell, T. Karlsson, N. Brenning, P. Henri, C. Goetz, A. I. Eriksson, E. Behar, G. Stenberg Wieser, and X. Vallières (2018). "Size of a plasma cloud matters: The polarisation electric field of a small-scale comet ionosphere". In: *Astronomy and Astrophysics* 616. ISSN: 14320746. DOI: 10.1051/0004-6361/201833199.

Nilsson, H., R. Lundin, K. Lundin, S. Barabash, H. Borg, O. Norberg, A. Fedorov, J. A. Sauvaud, H. Koskinen, E. Kallio, P. Riihelä, and J. L. Burch (2007). "RPC-ICA: The ion composition analyzer of the Rosetta plasma consortium". In: *Space Science Reviews* 128.1-4, pp. 671–695. ISSN: 00386308. DOI: 10.1007/s11214-006-9031-z.

Nilsson, H., G. Stenberg Wieser, E. Behar, C. Simon Wedlund, E. Kallio, H. Gunell, N. J. Edberg, A. I. Eriksson, M. Yamauchi, C. Koenders, M. Wieser, R. Lundin, S. Barabash, K. Mandt, J. L. Burch, R. Goldstein, P. Mokashi, C. Carr, E. Cupido, P. T. Fox, K. Szego, Z. Nemeth, A. Fedorov, J. A. Sauvaud, H. Koskinen, I. Richter, J. P. Lebreton, P. Henri, M. Volwerk, C. Vallat, and B. Geiger (2015). "Evolution of the ion environment of comet 67P/Churyumov-Gerasimenko: Observations between 3.6 and 2.0 AU". In: *Astronomy and Astrophysics* 583. ISSN: 14320746. DOI: 10.1051/0004-6361/201526142.

Nilsson, H., G. S. Wieser, E. Behar, H. Gunell, M. Wieser, M. Galand, C. Simon Wedlund, M. Alho, C. Goetz, M. Yamauchi, P. Henri, E. Odelstad, and E. Vigren (2017). "Evolution of the ion environment of comet 67P during the Rosetta mission as seen by RPC-ICA". In: *Monthly Notices of the Royal Astronomical Society* 469, S252–S261. ISSN: 13652966. DOI: 10.1093/mnras/stx1491.

Novotný, O., H. Buhr, J. Stützel, M. B. Mendes, M. H. Berg, D. Bing, M. Froese, M. Grieser, O. Heber, B. Jordon-Thaden, C. Krantz, M. Lange, M. Lestinsky, S. Novotny, S. Menk, D. A. Orlov, A. Petrignani, M. L. Rappaport, A. Shornikov, D. Schwalm, D. Zajfman, and A. Wolf (2010). "Fragmentation Channels in Dissociative Electron Recombination with Hydronium and Other Astrophysically Important Species". In: *The Journal of Physical Chemistry A* 114.14, pp. 4870–4874. ISSN: 1089-5639. DOI: 10.1021/jp9104097.

Odelstad, E., A. I. Eriksson, F. L. Johansson, E. Vigren, P. Henri, N. Gilet, K. L. Heritier, X. Vallières, M. Rubin, and M. André (2018). "Ion Velocity and Electron Temperature Inside and Around the Diamagnetic Cavity of Comet 67P". In: *Journal of Geophysical Research: Space Physics* 123.7, pp. 5870–5893. ISSN: 21699402. DOI: 10.1029/2018JA025542.

Odelstad, E., G. Stenberg-Wieser, M. Wieser, A. I. Eriksson, H. Nilsson, and F. L. Johansson (2017). "Measurements of the electrostatic potential of Rosetta at comet 67P". In: *Monthly Notices of the Royal Astronomical Society* 469, S568–S581. ISSN: 13652966. DOI: 10.1093/mnras/stx2232.

Öjekull, J., P. U. Andersson, M. B. Någård, J. B. Pettersson, A. M. Derkatch, A. Neau, S. Rosén, R. Thomas, M. Larsson, F. Österdahl, J. Semaniak, H. Danared, A. Källberg, M. A. Ugglas, and N. Marković (2004). "Dissociative recombination of NH4+ and ND 4+ ions: Storage ring experiments and ab initio molecular dynamics". In: *Journal of Chemical Physics* 120.16, pp. 7391–7399. ISSN: 00219606. DOI: 10.1063/1.1669388.

Puhl-Quinn, P. and T. E. Cravens (1995). "One-dimensional hybrid simulations of the diamagnetic cavity boundary region of comet Halley". In: *Journal of Geophysical Research: Space Physics* 100.A11, pp. 21631–21644. DOI: 10.1029/95ja01820.

Qin, H., S. Zhang, J. Xiao, J. Liu, Y. Sun, and W. M. Tang (2013). "Why is Boris algorithm so good?" en. In: *Physics of Plasmas* 20.8, p. 084503. ISSN: 1070-664X, 1089-7674. DOI: 10.1063/1.4818428.

Rees, M. H. (1989). *Physics and Chemistry of the Upper Atmosphere*. 1st ed. Cambridge University Press. ISBN: 978-0-521-32305-5 978-0-521-36848-3 978-0-511-57311-8. DOI: 10.1017/CBO9780511573118.

Rosen, S., S. A. Derkatch, J. Semaniak, A. Neau, A. Al-Khalili, A. Le Padellec, L. Vikor, R. Thomas, H. Danared, M. af Ugglasd, and M. Larssona (2000). "Recombination of simple molecular ions studied in storage ring : dissociative recombination of H 2 O'". In: *Farday Discussions* 115, pp. 295–302. DOI: 10.1039/a909314a.

Rosseland, S. (1924). "Electrical State of a Star". en. In: *Monthly Notices of the Royal Astronomical Society* 84.9, pp. 720–729. ISSN: 0035-8711, 1365-2966. DOI: 10.1093/mnras/84.9.720.

Rubin, M., M. R. Combi, L. K. Daldorff, T. I. Gombosi, K. C. Hansen, Y. Shou, V. M. Tenishev, G. Tóth, B. Van Der Holst, and K. Altwegg (2014a). "COMET 1P/halley multifluid mhd model for the giotto fly-by". In: *Astrophysical Journal* 781.2. ISSN: 15384357. DOI: 10.1088/0004-637X/781/2/86.

Rubin, M., K. C. Hansen, M. R. Combi, L. K. Daldorff, T. I. Gombosi, and V. M. Tenishev (2012). "Kelvin-Helmholtz instabilities at the magnetic cavity boundary of comet 67P/Churyumov-Gerasimenko". In: *Journal of Geophysical Research: Space Physics* 117.6. ISSN: 21699402. DOI: 10.1029/2011JA017300.

Rubin, M., C. Koenders, K. Altwegg, M. R. Combi, K. H. Glassmeier, T. I. Gombosi, K. C. Hansen, U. Motschmann, I. Richter, V. M. Tenishev, and G. Tóth (2014b). "Plasma environment of a weak comet - Predictions for Comet 67P/Churyumov-Gerasimenko from multifluid-MHD and Hybrid models". In: *Icarus* 242, pp. 38–49. ISSN: 10902643. DOI: 10.1016/j.icarus.2014.07.021.

Rubin, M., K. C. Hansen, T. I. Gombosi, M. R. Combi, K. Altwegg, and H. Balsiger (2009). "Ion composition and chemistry in the coma of Comet 1P/Halley—A comparison between Giotto's Ion Mass Spectrometer and our ion-chemical network". In: *Icarus* 199.2, pp. 505–519. ISSN: 0019-1035. DOI: 10.1016/J.ICARUS.2008.10.009.

Schlaeppi, B. (2011). "PhD Thesis". PhD Thesis. Universitaet Bern.

Schläppi, B., K. Altwegg, H. Balsiger, M. Hssig, A. Jäckel, P. Wurz, B. Fiethe, M. Rubin, S. A. Fuselier, J. J. Berthelier, J. De Keyser, H. Rme, and U. Mall (2010). "Influence of spacecraft outgassing on the exploration of tenuous atmospheres with in situ mass spectrometry". In: *Journal of Geophysical Research: Space Physics* 115.12. ISSN: 21699402. DOI: 10.1029/2010JA015734.

Schulz, R., H. Sierks, M. Küppers, and A. Accomazzo (2012). "Rosetta fly-by at asteroid (21) Lutetia: An overview". en. In: *Planetary and Space Science* 66.1, pp. 2–8. ISSN: 00320633. DOI: 10.1016/j.pss.2011.11.013.

Schunk, R. and A. Nagy (2009). *Ionospheres: Physics, Plasma Physics, and Chemistry*. 2nd ed. Cambridge Atmospheric and Space Science Series. Cambridge: Cambridge University Press. ISBN: 978-0-521-87706-0. DOI: 10.1017/CBO9780511635342.

Simon Wedlund, C., M. Alho, G. Gronoff, E. Kallio, H. Gunell, H. Nilsson, J. Lindkvist, E. Behar, G. Stenberg Wieser, and W. J. Miloch (2017). "Hybrid modelling of cometary plasma environments: I. Impact of photoionisation, charge exchange, and electron ionisation on bow shock and cometopause at 67P/Churyumov-Gerasimenko". In: *Astronomy and Astrophysics* 604. ISSN: 14320746. DOI: 10.1051/0004-6361/201730514.

Simon Wedlund, C., D. Bodewits, M. Alho, R. Hoekstra, E. Behar, G. Gronoff, H. Gunell, H. Nilsson, E. Kallio, and A. Beth (2019). "Solar wind charge exchange in cometary atmospheres: I. Charge-changing and ionization cross sections for He and H particles in H2O". In: *Astronomy and Astrophysics* 630. ISSN: 14320746. DOI: 10.1051/0004-6361/201834848.

Smith, D., N. G. Adams, and M. J. Henchman (1980). "Studies of the binary reactions of H3O+(H2O)0,1,2 ions and their deuterated analogues with D2O, H2O, and NH3". en. In: *The Journal of Chemical Physics* 72.9, pp. 4951–4957. ISSN: 0021-9606, 1089-7690. DOI: 10.1063/1.439781.

Snodgrass, C. and G. H. Jones (2019). *The European Space Agency's Comet Interceptor lies in wait*. DOI: 10.1038/s41467-019-13470-1.

Stephenson, P., A. Beth, J. Deca, M. Galand, C. Goetz, P. Henri, K. Heritier, Z. Lewis, A. Moeslinger, H. Nilsson, and M. Rubin (2023). "The source of electrons at comet 67P". In.

Stephenson, P., M. Galand, J. Deca, and P. Henri (2024). "Cold electrons at a weakly outgassing comet". In: *Monthly Notices of the Royal Astronomical Society* 529.3, pp. 2854–2865. ISSN: 13652966. DOI: 10.1093/mnras/stae695.

Stephenson, P., M. Galand, P. D. Feldman, A. Beth, M. Rubin, D. Bockelée-Morvan, N. Biver, Y. C. Cheng, J. Parker, J. Burch, F. L. Johansson, and A. Eriksson (2021). "Multi-instrument

analysis of far-ultraviolet aurora in the southern hemisphere of comet 67P/Churyumov-Gerasimenko". In: *Astronomy and Astrophysics* 647. ISSN: 14320746. DOI: 10.1051/0004-6361/202039155.

Stephenson, P. (2022). "Origin, evolution and impact of electrons at comet 67P". PhD Thesis. Imperial College London.

Stephenson, P., < M. Galand, J. Deca, P. Henri, and G. Carnielli (2022). "A collisional test-particle model of electrons at a comet". In: *MNRAS* 511, pp. 4090–4108. DOI: 10.1093/mnras/stac055.

Tao, C., R. Kataoka, H. Fukunishi, Y. Takahashi, and T. Yokoyama (2005). "Magnetic field variations in the Jovian magnetotail induced by solar wind dynamic pressure enhancements". en. In: *Journal of Geophysical Research: Space Physics* 110.A11. ISSN: 2156-2202. DOI: 10.1029/2004JA010959.

Taylor, M. G. G. T., N. Altobelli, B. J. Buratti, and M. Choukroun (2017). "The Rosetta mission orbiter science overview: the comet phase". en. In: *Philosophical Transactions of the Royal Society A: Mathematical, Physical and Engineering Sciences* 375.2097, p. 20160262. ISSN: 1364-503X, 1471-2962. DOI: 10.1098/rsta.2016.0262.

Trotignon, J. G., J. L. Michau, D. Lagoutte, M. Chabassière, G. Chalumeau, F. Colin, P. M. Décréau, J. Geiswiller, P. Gille, R. Grard, T. Hachemi, M. Hamelin, A. Eriksson, H. Laakso, J. P. Lebreton, C. Mazelle, O. Randriamboarison, W. Schmidt, A. Smit, U. Telljohann, and P. Zamora (2007). "RPC-MIP: The mutual impedance probe of the Rosetta plasma consortium". In: *Space Science Reviews* 128.1-4, pp. 713–728. ISSN: 00386308. DOI: 10.1007/s11214-006-9005-1.

Vančura, J. and Z. Herman (1991). "Hydroxonium ion formation in collisions of H2O+ + D2O and D2O+ + H2O: a crossed-beam scattering study". en. In: *Chemical Physics* 151.2, pp. 249–259. ISSN: 03010104. DOI: 10.1016/0301-0104(91)80106-R.

Vigren, E., M. André, N. J. T. Edberg, I. A. D. Engelhardt, A. I. Eriksson, M. Galand, C. Goetz, P. Henri, K. Heritier, F. L. Johansson, H. Nilsson, E. Odelstad, M. Rubin, G. Stenberg-Wieser, C.-Y. Tzou, and X. Vallì Eres (2017). "Effective ion speeds at 200-250 km from

comet 67P/Churyumov-Gerasimenko near perihelion". In: *MNRAS* 469, pp. 142–148. DOI: 10.1093/mnras/stx1472.

Vigren, E., K. Altwegg, N. J. T. Edberg, A. I. Eriksson, M. Galand, P. Henri, F. Johansson, E. Odelstad, C.-Y. Tzou, and X. Valliéres (2016). "MODEL-OBSERVATION COMPARISONS OF ELECTRON NUMBER DENSITIES IN THE COMA OF 67P/CHURYUMOV–GERASIMENKO DURING 2015 JANUARY". In: *The Astronomical Journal* 152.3, p. 59. ISSN: 00046256. DOI: 10.3847/0004-6256/152/3/59.

Vigren, E., N. J. T. Edberg, A. I. Eriksson, M. Galand, P. Henri, F. L. Johansson, E. Odelstad, M. Rubin, and X. Valliéres (2019). "The Evolution of the Electron Number Density in the Coma of Comet 67P at the Location of Rosetta from 2015 November through 2016 March". In: *The Astrophysical Journal* 881.1, p. 6. ISSN: 15384357. DOI: 10.3847/1538-4357/ab29f7.

Vigren, E. and A. I. Eriksson (2017). "A 1D Model of Radial Ion Motion Interrupted by Ion–Neutral Interactionsin a Cometary Coma". In: *The Astronomical Journal* 153.4, p. 150. ISSN: 1538-3881. DOI: 10.3847/1538-3881/aa6006.

Vigren, E. and M. Galand (2013). "Predictions of ion production rates and ion number densities within the diamagnetic cavity of comet 67P/churyumov-gerasimenko at perihelion". In: *Astrophysical Journal* 772.1. ISSN: 15384357. DOI: 10.1088/0004-637X/772/1/33.

Vigren, E., M. Galand, A. I. Eriksson, N. J. Edberg, E. Odelstad, and S. J. Schwartz (2015). "ON the ELECTRON-TO-NEUTRAL NUMBER DENSITY RATIO in the COMA of COMET 67P/CHURYUMOV-GERASIMENKO: GUIDING EXPRESSION and SOURCES for DEVIATIONS". In: *Astrophysical Journal* 812.1. ISSN: 15384357. DOI: 10.1088/0004-637X/812/1/54.

Wattieaux, G., P. Henri, N. Gilet, X. Vallières, and J. Deca (2020). "Plasma characterization at comet 67P between 2 and 4 AU from the Sun with the RPC-MIP instrument". In: *Astronomy and Astrophysics* 638. ISSN: 14320746. DOI: 10.1051/0004-6361/202037571.

Whipple, F. L. (1950). "A comet model. I. The acceleration of Comet Encke". en. In: *The Astrophysical Journal* 111, p. 375. ISSN: 0004-637X, 1538-4357. DOI: 10.1086/145272.

Woods, T. N., F. G. Eparvier, S. M. Bailey, P. C. Chamberlin, J. Lean, G. J. Rottman, S. C. Solomon, W. K. Tobiska, and D. L. Woodraska (2005). "Solar EUV Experiment (SEE):

Mission overview and first results". In: *Journal of Geophysical Research: Space Physics* 110.A1. ISSN: 21699402. DOI: 10.1029/2004JA010765.

APPENDIX A

ION-NEUTRAL REACTION RATES INCLUDED IN THE ION ACCELERATION MODEL

The rate coefficients for dissociative recombination, momentum transfer and ion-neutral proton transfer are given. The dissociative recombination and ion-neutral chemical reaction rates are taken from the UMIST database (Millar *et al.*, 2024) and their accuracy is within 25 %.

A.1 Protonation

Table A.1: Ion-neutral chemical reaction rates for reactions included in the ion Acceleration Model.

Reaction	**Rate coefficient** $k^{IN}_{j,n\rightarrow j'}$ $[\mathrm{cm^3\ s^{-1}}]$	**Temp. range** [K]	**Reference**
$H_2O^{+\bigstar} + H_2O \rightarrow H_3O^+ + OH^{\bigstar}$	$2.10 \times 10^{-9}(300/T_n)^{0.5}$	10-41000	Huntress and Pinizzotto 1973
$H_3O^{+\bigstar} + NH_3 \rightarrow NH_4^+ + H_2O^{\bigstar}$	$2.20 \times 10^{-9}(300/T_n)^{0.5}$	10-41000	Smith *et al.* 1980
$H_2O^{+\bigstar} + NH_3 \rightarrow NH_4^+ + OH^{\bigstar}$	$9.45 \times 10^{-10}(300/T_n)^{0.5}$	10-41000	Anicich *et al.* 1977

A.2 Dissociative recombination

Table A.2: Ion-electron dissociative recombination rate coefficients used in the Ion Acceleration Model. T_e is the electron temperature in K.

Reaction	**Kinetic rate coefficient** α_j^{DR} $[\mathrm{cm^3\ s^{-1}}]$	**Temp. range** [K]	**Reference**
$H_2O^+ + e^- \rightarrow O + H_2$	$3.9 \times 10^{-8}(300/T_e)^{0.5}$	10-41000	Rosen *et al.* 2000
$H_2O^+ + e^- \rightarrow O + H + H$	$3.05 \times 10^{-7}(300/T_e)^{0.5}$	10-1000	Rosen *et al.* 2000
$H_2O^+ + e^- \rightarrow OH + H$	$8.6 \times 10^{-8}(300/T_e)^{0.5}$	10-1000	Rosen *et al.* 2000
$H_3O^+ + e^- \rightarrow H_2O + H$	$7.09 \times 10^{-8}(300/T_e)^{0.5}$	10-1000	Novotný *et al.* 2010
$H_3O^+ + e^- \rightarrow O + H_2 + H$	$5.60 \times 10^{-9}(300/T_e)^{0.5}$	10-1000	Novotný *et al.* 2010
$H_3O^+ + e^- \rightarrow OH + H_2$	$5.37 \times 10^{-8}(300/T_e)^{0.5}$	10-1000	Novotný *et al.* 2010
$H_3O^+ + e^- \rightarrow OH + H + H$	$3.05 \times 10^{-7}(300/T_e)^{0.5}$	10-1000	Novotný *et al.* 2010
$NH_4^+ + e^- \rightarrow NH_2 + H_2$	$4.72 \times 10^{-8}(300/T_e)^{0.6}$	10-2000	Öjekull *et al.* 2004
$NH_4^+ + e^- \rightarrow NH_2 + H + H$	$3.77 \times 10^{-8}(300/T_e)^{0.6}$	10-2000	Öjekull *et al.* 2004
$NH_4^+ + e^- \rightarrow NH_3 + H$	$8.49 \times 10^{-7}(300/T_e)^{0.6}$	10-2000	Öjekull *et al.* 2004

A.3 Momentum transfer

Table A.3: Ion-neutral collision coefficients for processes included in the model, assumed to be entirely elastic. The star (★) denotes a fast ion or neutral.

Reaction	**Collision rate coefficient** k^{MT} $[\mathrm{cm^3 s^{-1}}]$	**Reference**
$H_2O^{+\bigstar} + H_2O \rightarrow H_2O^+ + H_2O^{\bigstar}$	1.7×10^{-9}	Gombosi *et al.* 1996
$H_3O^{+\bigstar} + H_2O \rightarrow H_3O^+ + H_2O^{\bigstar}$	5.04×10^{-10}	Schunk and Nagy 2009
$NH_4^{+\bigstar} + H_2O \rightarrow NH_4^+ + H_2O^{\bigstar}$	5.25×10^{-10}	Schunk and Nagy 2009

APPENDIX B

ION-NEUTRAL CROSS SECTIONS FOR THE COLLISIONAL TEST-PARTICLE MODEL

Table B.1: Ion-neutral collision cross sections, as used in Chapter 5.

Reaction type	**Equation**	**Cross section** $[10^{-16}\ \mathrm{cm}^2]$	**Range [eV]**	**Reference**
Proton transfer	$H_2O^+ + H_2O \rightarrow H_3O^+ + OH$	$\sigma(E_{\mathrm{rel}}) = 38E_{\mathrm{rel}}^{-0.88} - 0.39\exp\left[-0.5(\frac{E_{\mathrm{rel}}-57}{12})^2\right]$	0.1 - 100	Fleshman *et al.*, 2012
Proton transfer	$H_2O^+ + NH_3 \rightarrow NH_4^+ + OH$	$\sigma(E_{\mathrm{rel}}) = 38E_{\mathrm{rel}}^{-0.88} - 0.39\exp\left[-0.5(\frac{E_{\mathrm{rel}}-57}{12})^2\right]$	0.1 - 100	Fleshman *et al.*, 2012
Proton transfer	$H_3O^+ + NH_3 \rightarrow NH_4^+ + H_2O$	$\sigma(E_{\mathrm{rel}}) = 38E_{\mathrm{rel}}^{-0.88} - 0.39\exp\left[-0.5(\frac{E_{\mathrm{rel}}-57}{12})^2\right]$	0.1 - 100	Fleshman *et al.*, 2012
Momentum transfer	$H_2O^+ + H_2O \rightarrow H_2O^+ + H_2O$	$\sigma(E_{\mathrm{rel}}) = 24E^{-0.5}$	Not given	Vigren and Eriksson, 2017
Momentum transfer	$H_3O^+ + H_2O \rightarrow H_3O^+ + H_2O$	$\sigma(E_{\mathrm{rel}}) = 24E_{\mathrm{rel}}^{-0.5}$	Not given	Vigren and Eriksson, 2017
Momentum transfer	$NH_4^+ + H_2O \rightarrow NH_4^+ + H_2O$	$\sigma(E_{\mathrm{rel}}) = 24E_{\mathrm{rel}}^{-0.5}$	Not given	Vigren and Eriksson, 2017
Electron transfer	$H_2O^+ + H_2O \rightarrow H_2O^+ + H_2O$	$\sigma(E_{\mathrm{rel}}) = 38E_{\mathrm{rel}}^{-0.5}$	0.1 - 100	Fleshman *et al.*, 2012